Development of Scalable Pathways for Addressing Constraints of Emerging Manufacturing Processes

by

Ikenna Henry Ozofor

A dissertation submitted in partial fulfillment
of the requirements for the degree of
Doctor of Philosophy
(Chemical Engineering)
in the University of Michigan
2023

Doctoral Committee:

Professor L. Jay Guo, Co-Chair
Professor Ronald Larson, Co-Chair
Professor Bryan Goldsmith
Professor Xiwen Gong

Ikenna H. Ozofor

hiozofor@umich.edu

ORCID iD: 0000-0002-9775-6319

Acknowledgements

I return my unreserved gratitude and praise to the Almighty God for the gift of life and grace.

Table of Contents

List of Tables

List of Figures

List of Abbreviations

AlGaAs: Aluminum gallium arsenide

AlGaInP: Aluminum indium gallium phosphide

Alq_3: Tris (8-hydroxyquinoline) aluminum

Alumina: Al_2O_3

BCP: 2,9-dimethyl-4,7-diphenyl-1,10-phenanthroline

BL: Boundary layer

Bphen: 4,4,4 -tris (N-carbazolyl) triphenylamine

C_{60}: Fullerene

C545T: Coumarin 545T

CCFL: Cold cathode fluorescent lamp

CFD: Computational fluid dynamic

CGU: Charge generating unit

CLO: chemical lift off

CRT: Cathode ray tube

Cs_2CO_3 : Caesium carbonate

CsF: Cesium fluoride

CsN_3: Cesium azide

CuPc: Copper phthalocyanine

DCM: 4-(Dicyanomethylene)-2-methyl-6-(4-dimethylaminostyryl)-4*H*-pyran

DMQA: N,N'-Dimethylquinacridone

DNA: Deoxyribonucleic acid

EIL: Electron injection layer

ELOG: Epitaxial lateral overgrowth

EML: Emissive layer

EQE: External quantum efficiency

ERF: Electrophoretic retardation force

ETL: Electron transport layer

F_4-TCNQ: Tetrafluorotetracyanoquinodimethane

F_{16} CuPc: Copper hexadecafluorophthalocyanine

GaAsP: Gallium arsenide phosphide

GaN: Gallium nitride

GaP: Gallium phosphide

HIL: Hole injection layer

HOMO: Highest occupied molecular orbital

HTL: Hole transport layer

HUD: Head-up display

InGaN: Indium gallium nitride

IPA: Isopropyl alcohol

Ir(piq)3: Tris(1-phenylisoquinoline)iridium(III)

ITO: Indium tin oxide

J-V: Current density-voltage

LEAP: laser enhanced advanced placement

LCD: Liquid-crystal display

LED: Light emitting diode

LiF: Lithium fluoride

LiQ: 8-Hydroxyquinolinolato-lithium

LLO: laser lift off

LT: Lifetime

LUMO: Lowest unoccupied molecular orbital

LW: Lifshitz- van der Waals

MADN: 2-methyl-9,10-bis(naphthalen-2-yl) anthracene

Micro-LED: Micro-light emitting diode

MgO: Magnesium oxide

MPRT: Moving picture response time

MoO_3: 4,40,4-tristriphenylamine and molybdenum trioxide

MUE: Material utilization efficiency

NPB: N,N'-bis(naphthalen-1-yl)-N,N'-bis(phenyl)-benzidine

NPD: N,N'-Di(1-naphthyl)-N,N'-diphenyl-(1,1'-biphenyl)-4,4'-diamine

OLED: Organic light emitting diode

OVPD: Organic vapor phase deposition

PPI: Pixels per inch

PVD: Physical vapor deposition

QD: Quantum dots

R2R: Roll to roll

Rubrene: 5,6,11,12-tetraphenyltetracene

SAG: Selective-area growth

SiC: Silicon carbide

SCCM: Standard cubic centimeters per min

SSL: Solid state lighting

TAPC: 1,1-Bis[(di-4-tolylamino)phenyl]cyclohexane

TBP: 4-*tert*-Butylpyridine   :

TPBi: 2,2',2"-(1,3,5-Benzinetriyl)-tris(1-phenyl-1-H-benzimidazole)

TPD: N,N'-bis(3-methyl phenyl)-N,N'-bis(phenyl)-benzidine

UV: Ultraviolet

VDWE: van der Waals epitaxy

VTE: Vacuum thermal evaporation

WOLED: White organic light emitting diode

WO_3: Tungsten trioxide

ZnSe: Zinc selenide

Nomenclature

A: Absorbance, A.U

A_{ch}: Chamber cross sectional area, m^2

A_s: Exposed substrate area, m^2

A_{132}: Hamaker constant of the system, J

CM: Clausius-Mossotti factor

C_o: Ion concentration, mol/m^3

C_p: Heat capacity at constant pressure,

c: Speed of light in vacuum, m/s

$\dot{c}$, molar concentration, mol/m^3

C_i: Concentration of species i, mol/m^3

ς : Dimensionless random distributing number

D: Effective displacement, m

D: Dielectric model parameter

D_i : Diffusivity of species i, m^2/s

ΔS : Entropy change, J/K

δ_{iw}^{+}: Acidic polarity ratio

δ_{iw}^{-}: Basic polarity ratio

δ_T: Thickness of thermal boundary layer

δ_T: Thickness of hydrodynamic boundary layer

E: Band gap energy, eV

E: Photon energy, eV

E: Electric field strength, V/m

$\dot{\varepsilon}$: molar absorption coefficient

ε_o: Permittivity of free space

ε_m: Relative permittivity of medium

F_R: Effective resistive force, N

γ_i^+: Acidic polar surface energy parameter of surface i, J/m^2

γ_i^-: Basic polar surface energy parameter of surface i, J/m^2

γ_i^{LW}: Apolar (Lifshitz –van der Waals) surface energy parameter of surface i, J/m^2

γ_L^+: Acidic polar energy parameter of liquid L, J/m^2

γ_L^-: Basic polar energy parameter of liquid L, J/m^2

γ_L^{LW}: Apolar (Lifshitz –van der Waals) energy parameter of liquid L, J/m^2

γ_w^+: Acidic polar energy parameter of surface i, J/m^2

γ_w^-: Basic polar energy parameter of surface i, J/m^2

γ_L: Surface tension of liquid L, J/m^2

h: Planck's constant, J-s

I_0: Incident light

I: Transmitted light

J_e: Externally generated current density

J_i : Flux of species i, mol/m^{2}s

λ: Wavelength of emitted light, m

$\bar{l}$: Mean free path, m

l: Optical path length, m

Kn: Knudsen number

κ: Thermal conductivity, W/m-K

K_B: Boltzmann constant, J/K

μLED: Micro-LED

M: Molecular weight, g/mol

μ: Gas/vapor viscosity, $N \cdot s/m^2$

N_A: Avogadro's constant, 1/mol

n_i: Number of moles of species i, mol

n_{io}: Number of ions of type i in bulk solution per unit volume

n_o: Bulk ion concentration, mol/m^3

η: Medium viscosity, $N \cdot s/m^2$

n_p: Number of particles

Pr: Prandtl number

P: Pressure, Pa

ρ: Local net charge density, C/m^3

ρ: Fluid density, kg/m^3

Φ: Dimensionless electrostatic potential

Φ: Electrostatic potential, V

σ: Charge density, C/m^2

φ_s: Surface potential, V

Pe: Peclet number for mass transfer

q: heat flux, W/m^2

Re: Reynolds number

R_i : Radius of sphere i

t_D: Diffusion time within the boundary layer

T: Temperature, K

Θ : Contact angle, degree

T (%): Transmittance

τ : Time required to transport the vapors downstream

T_s: Stage temperature, K

T_∞: Bulk (mainstream) temperature, K

u: Velocity vector, m/s

$u_{m,i}$: Mobility of species i,

U_z: Velocity with which fluid enters the boundary layer, m/s

U_∞: Bulk (mainstream) fluid velocity, m/s

$\bar{v}$: molecular speed

V_{ER}: Effective volume

$\dot{V}$: Carrier gas flow rate

x_i: Mole fraction of species i

z_i, ion charge number

ζ: Zeta potential, V

Z_{mix} : Axial distance needed for effective vapor mixing, m

Abstract

The goal of this Ph.D. study was to apply first-principle physics, computational fluid dynamic (CFD) simulation, scientific experimentation, model development and process design to develop scalable pathways for addressing critical constraints of emerging manufacturing processes, which can benefit semiconductor, specialty chemicals and pharmaceutical industries. This goal was accomplished by studying four research projects to investigate four key objectives, including development of a model for boosting material utilization efficiency (MUE) in organic vapor phase deposition (OVPD), scalable hardware design for effective vapor mixing and substrate heating management in OVPD, development of a pathway for cost-effective micro-LED assembling and understanding interactions energies and numerical demonstration of electrically directed particle trapping on a charged line. To develop a pathway for boosting utilization efficiency in OVPD, an MUE model was developed, the model insights were numerically and experimentally tested and corroborated. Based on the results, area ratio (substrate to chamber) drives MUE and utilization efficiency can be boosted by engineering thermal boundary layer in additional planes. This film deposition by thermal boundary layer engineering was experimentally demonstrated on practically useful substrates. Therefore, a system configuration that can deliver >75% MUE in OVPD was proposed. Scalable hardware design method was developed by analytically and numerically investigating the effects of process conditions on vapor transport, allowing for assessment of criteria needed for effective vapor mixing and substrate heating management. Based on the results, a scalable method for predicting hardware aspect ratio needed to realize effective vapor mixing

was proposed. Pathways for cost-effective microparticle assembling were developed by identifying and quantifying physical interactions acting on the particles in suspension, investigating the dependence of these energies on particle shape (sphere and cubic), chip size (0.2 - 50.2 µm) and fill factor (0.25 - 0.95) as well as their relative contributions to the overall free energy change. These energies were determined by using analytical and numerical methods. The results show interactions due to electrostatics and entropy of mixing to dominate those of Lifshitz-van der Waals and gravitational energies for different chip size and shapes. Free energy values from thermodynamic assessment of the process reveal surface energies and surface potential on the receiving cavities as clear pathways for chip assembling, leveraging dominance of interfacial Lewis acid-base interaction and entropic contribution, respectively. Thus, these findings and developed pathways can inform engineering chip-processing system for cost-effective assembling. To understand interaction energies during electrically directed particle trapping of particles to a charged line (which models binding of proteins to deoxyribonucleic acid (DNA) strand), energies of interactions, including Lifshitz-van der Waals (LW), Brownian, electrostatics, entropic contribution and gravity, were analytically and numerically quantified to assess overall thermodynamic feasibility of the process. Based on the results, comparative assessment of the energies reveals electrostatic interaction and entropic contribution are dominant contributors, which are both tunable by potential applied on the nanowire. Further, to capture the trajectories of the particles during the process, electrophoretic behavior of the particle under all four relevant competing forces (gravity, drag, electric and Brownian) was modeled under different system settings. The dynamic confinement of particles to charged lines was both numerically and experimentally demonstrated. In conclusion these original contributions from this Ph.D. present pathways for addressing constraints of emerging manufacturing processes.

Chapter 1 Introduction and Backgspherical

1.1 Technology Landscape for Display and General Illumination

The goal of this Ph.D. study is to develop fundamental solutions for addressing constraints of emerging optoelectronics fabrication processes. The theoretical, computational, and experimental works of this thesis aim to address the constraints of emerging manufacturing processes for next-generation light, display, and colloidal products. In this chapter, we review the history of different illumination and flat panel display technologies, and then analyze features of organic light-emitting diode (OLED) light and micro-light-emitting diode (micro-LED) display that make them suitable as the emerging solid-state lighting technology and display technology. In chapter 2, we describe different experimental techniques utilized in this study, and then discuss motivations and results of four research projects we studied in chapters 3 through 6. In chapter 7, we summarize contributions from this study and recommend future research directions.

In this section, we discuss different technologies for making devices for provision of ambient light (general illumination) as well as for visual presentation of information (display).

Technologies for general illumination find residential as well as commercial applications to provide light both indoors within a building (as backgroundlight) and outdoors like in car parks, walkways, streets, and roadways. These technologies include incandescent lighting, halogen

lighting, discharge lighting (fluorescent lighting and compact fluorescent lighting), light-emitting diode (LED) lighting, and the emerging organic light-emitting diode (OLED) lighting.

Incandescent light technology works by producing visible radiation from joule heating of wire filament. Typically, the glowing filament is protected from oxidation by housing it in a bulb under vacuum or in an inert environment. Incandescent lamps were among the earliest artificial light sources [1], and were particularly attractive due to low-cost, safe and mature manufacturing methods. However, the drawbacks of incandescent light technology include low energy efficiency, massive heat generation and short lamp lifetime. Since the brightness of radiation produced from incandescent bulb scale with the temperature of the heated filament, materials of high thermal stability are best suited as use as filaments. Tungsten, having an extremely high melting point and low evaporation rate is an excellent metal for this purpose [1], and is commonly used as filament material in incandescent bulbs.

Halogen light technology uses same working principle as incandescent bulb, but in addition small amounts of halogen element (bromine or iodine) are contained in the lamps to decrease the consumption rate of the tungsten as the filament burn thereby considerably improving the energy efficiency, brightness, and lifetime of the bulb. Mechanistically, this enhancement is due to redeposition of vaporized tungsten on the filament, reducing fraction of the vaporized metal coating the interior of the bulb [2], which results in improved brightness and lamp lifetime. Nevertheless, since halogen lamps also produce light by filament burning, this technology is substantially less energy efficient.

Discharge lighting is another lighting technology, and it is applied in manufacturing fluorescent and compact fluorescent lamps. This technology works by combining two processes, including production of ultraviolet light by electric discharge generated in a tube containing argon gas or mercury vapor, and conversion of the UV-light to visible light by film of special phosphors coated on the bulb interior. Discharge lamps are mainly fluorescent bulbs and compact fluorescent bulbs, which differ only on the nature of their sources as the former is linear source while the latter is point source [3]. Thus, in fluorescent bulbs, the luminous flux between light source and illuminated object scales inversely to the separation distance to a first order, while in compact fluorescent lamps, this decay of luminous flux scales inversely with cubic of the separation distance [3, 4]. Because of the point-source nature of compact fluorescent bulbs, they can be used on existing sockets built for incandescent lamps, and they are generally referred to as "energy saving bulbs" since they can deliver same light output with only a quarter of the power an incandescent lamp would require [3]. Generally, compared to incandescent bulbs, fluorescent and compact fluorescent lamps are attractive as they are more energy efficient and have a longer lifetime. Nevertheless, incandescent bulbs have less cost. Further, LED bulbs (discussed in the next paragraph) can have longer light span than both fluorescent and compact fluorescent bulbs [3].

LED lighting technology applies the principle of electroluminescence to produce light from a diode. Due to the narrow wavelengths of photons produced from carrier recombination during electroluminescence, LEDs typically produce lights of high color purity. Colors and wavelengths of light from common LED materials are discussed in detail in section 1.3. Further, since LEDs emit lights of high color purity, they can be engineered to realize white light by phosphor coating of the casein interior and RGB method[3]. Since general illumination requires white light, LED

white lights are realized by either using specialized phosphor-coated casing or by combining multiple LED chips of different colors in a single device. In terms of applications, LEDs used for lighting can be either be larger than 200 microns or between 100 and 200 microns. The former is the traditional broad-area LEDs which have been established in general illumination, display backlighting, signaling and outdoor displaying while the latter is termed mini-LEDs, which are used for backlighting flexible display [5], and high-dynamic-range display [6].

Conclusively, the lighting industry has witnessed significant progress and advancements throughout its history, ranging from development of incandescent lamps through halogen lamps, discharge lamps, to the current state of the art lighting technology, light emitting diode. Though these established lighting technologies have unique attractive features, each of them also has significant downsides as summarized in Table 1.1. To meet the quality and economic needs of emerging light applications, optimum combination of quality, stability, freeform and cost-competitiveness is critical. As a result, OLED lighting can be the next generation illumination technology. We will discuss this technology in detail in section 1.2.

Table 1.1: Traditional lighting technologies, their status of adoption, attractive features and challenges

Lighting technology || Status of adoption	Attractive features	Challenges
Incandescent lighting || Commercial (Commercialized 1881 [7])	Low-cost	Short lamp lifetime and poor energy

		inefficiency due to filament burning
Halogen lighting || Commercial (Commercialized 1959 [8])	Low-cost	Energy inefficiency due to filament. Short light span
Discharge lighting (Fluorescent and Compact fluorescent) || Commercial (Commercialized 1938 [9])	More energy efficient than incandescent bulb	More expensive than incandescent bulb. Lamps have shorter lifetime than LED bulbs
Light emitting diode (LED) lighting || Commercial (Commercialized 1968 [10])	Low-cost. Durable lamps with long lifetime. Miniaturized	Susceptible to damage by high voltage and current

Display technologies, on the other hand, enable visual presentation of information in several electronics like televisions, computer monitors, billboards, mobile phones, wearable electronics, smart glasses, etc. These technologies include cathode-ray tube (CRT) display, liquid-crystal display (LCD), plasma display, organic light emitting diode display, and the emerging micro-LED display.

CRT display technology was the pioneer display technology, which was first demonstrated by Karl Ferdinand Braun in 1897 [11]. The technology gained popularity by 1920s [12] and subsequently, by mid 1950s, phosphors for CRT display were commercialized [13]. CRT works by producing images from electrons fired by electron guns onto phosphor-coated screens. Because earlies CRT could only produce monochromatic output, they were used black and white televisions and oscilloscopes. Nevertheless, the development of shadow-mask cathode ray tube, among other system improvement enabled the production of first commercial color CRT in 1954 [14]. In addition to being the pioneer display technology, CRT was attractive because of the ability to deliver good reproducible, no-motion blurred images [15] with low latency [16]. However, bulkiness, inefficient power consumption, heat generation, low contrast ratio and the use of hazardous materials [12, 17] were important limitations of CRT technology, leading to their relegation as the dominant display technology.

Due to bulkiness, inefficient power consumption, use of hazardous materials and heat generation, alternative display technology was desired. Thus, liquid crystal display (LCD) technology was developed and being a portable and high-power-efficient technology, it addressed the bulkiness and high-power consumption issues of the CRT technology. Liquid crystal display is a non-emissive technology that works by combining processes of color filtering, polarization, and modulating properties of liquid crystal to produce colored images. Typically, light from backlight source is polarized and propagated through a liquid crystal, filtered and polarized to convert white light into red, green, blue color [18, 19].

Depending on the nature of backlight used, LCD can be based on cold cathode fluorescent lamp (CCFL) (CCFL-LCD) or on LED (LED-LCD). CCFL-LCD utilizes cold cathode fluorescent lamp (CCFL) as the backlight, and it is attractive because it produces images of more uniform color.

However, low energy efficiency limits the use of CCFL as LCD backlight. On the other hand, LED-LCD uses LED as the backlight source. Backlight for LCD is typically provided by broad-area LEDs (size: > 200 micron) or mini-LEDs (size: between 100 and 200 microns). By using LEDs for backlighting, LED-LCD delivers higher brightness and more efficient power usage than CCFL-LED as well as images of superior color quality.

While LCD technology addressed significant drawbacks of the CRT technology, the former has substantial issues. These issues include slow response time, color saturation, limited conversion efficiency and significant amount of light generated being wasted [18]. Further, use of backlight in LCD limits flexibility and form factor [20]. Hence, researchers and innovators pursuit of better display alternative culminated in the development of organic light emitting diode technology.

Another display technology is plasma display, and it works by utilizing ionized gas, known as plasma, to excite phosphors, whose emitted light illuminate pixels that create display output. Unlike in LCD technology where backlight is required to create display output, in plasma display technology, collisions among atoms of the ionized gas (plasma) releases light which excites the pixel. Advantages of plasma display include low energy consumption, ease of manufacturing, wide viewing angle, fast response [21], and ability to produce display output of more uniform quality than LCD. Nevertheless, plasma display technology is limited by susceptibility to glare, screen burn in, heavy in weight and suboptimal energy utilization.

Beyond the maturity stages of cathode ray tube display, plasma display technology and liquid crystal display technology, research and innovation led to the development of a new display technology; the OLED technology. OLED technology is an emissive technique that utilizes principle of electroluminescence to generate light from passage of electric current through

emissive organic layer(s). A typical OLED device comprises layers of thin films sandwiched between a cathode and an anode. At least one of the anode or cathode is coated or imprinted on a transparent substrate to enable outcoupling of light from the device. The sandwiched layers are (from cathode to anode) electron injection layer (EIL), electron transport layer (ETL), emissive layer (EML), hole transport layer (HTL), hole injection layer (HIL). Hence by this structure, on application of voltage, cathode injects electrons into the EML through EIL and ETL while holes are injected from the anode through HIL and HTL. The holes and electrons recombine at the emissive layer and give off photons. The color and intensity of the emitted light are controlled by nature of the emissive materials and magnitude of current passed through the electrodes.

For each component layer of OLED device, materials are chosen to meet a certain criterion [22-24]. For example, common substrate materials for OLED include glass and flexible plastic since they meet the requirements of transparency and high resistance to acidic and basic attacks. Cathode materials for OLED are required to have low work function, thus commonly used cathode materials are magnesium oxide (MgO) and alumina (Al_2O_3). Anode material should be conductive and transparent. Thus, indium thin oxide and graphene are common OLED anode materials [24]. EIL should have high electron affinity and substantially block hole, and a common example is lithium fluoride (LiF) while ETL materials should have high receptivity to negative charges, high electron affinity and ability to substantially block hole, such that common ETL materials are tris (8-hydroxyquinoline) aluminum (Alq_3) and 2,9-dimethyl-4,7-diphenyl-1,10-phenanthroline (BCP).On the other hand, common HIL materials are copper phthalocyanine (CuPc), 4,40,4-tristriphenylamine and molybdenum trioxide (MoO_3) and they meet the requirements of allowing high mobility and good electron blocking ability. To be used as an HTL, material needs to have low affinity for electron and ability to easily allow hole mobility, such that common HTL materials

are N,N'-bis(3-methyl phenyl)-N,N'-bis(phenyl)-benzidine (TPD), N,N'-bis(naphthalen-1-yl)-N,N'-bis(phenyl)-benzidine (NPB) [22-24], and N,N'-Di(1-naphthyl)-N,N'-diphenyl-(1,1'-biphenyl)-4,4'-diamine (NPD). Materials used as EML are generally organic small molecules, conjugated polymers, and transition metal complexes capable of allowing electroluminescence over a substantial lifetime.

OLED display technology is attractive since it offers fast respond rate, broad viewing angle, efficient power usage, no-requirement for backlight unit [18, 25], freeform factor and thin profile. Thus, OLED technology has been widely adopted in many applications, including but not limited to foldable display products televisions, smart electronics as well as mobile phones. Nevertheless, OLED technology is limited by issues like suboptimal color purity, burn in (which results from non-uniform degradation of emissive OLED pixels), and short device lifetime.

Summarily, the display industry has witnessed significant advancements throughout its history, ranging from development of cathode ray tube display through back-lit liquid crystal display, plasma display to the current state of the art display, organic light emitting display. While all these established display technologies have attractive features, each of them also has significant drawbacks as summarized in Table 1.2. To meet the quality and economic needs of emerging display applications, excellent mix of quality, stability, freeform and cost-competitiveness is critical. An emerging display technology, which has shown best prospects for meeting these needs is the micro-LED display technology, and we discuss this technology in detail in section 1.3.

Table 1.2: Traditional display technologies, their status of adoption, attractive features, and challenges.

Display technology || Status of adoption	Attractive features	Challenges
Cathode-ray tube (CRT) display || Commercial (Commercialized 1954 [14])	No-motion blurred images. Low latency	Inefficient power consumption, heat generation, bulkiness, heavy, low contrast ratio, use of hazardous materials
Cold cathode fluorescent lamp-liquid-crystal display (CCFL-LCD) display || Commercial (Commercialized 1970 [26])	Portable, light weight and efficient power usage	Slow response time, color saturation and limited conversion efficiency
Plasma display || Commercial (Commercialized 1997 [27])	Fast response, wide viewing angle and ease of manufacturing	Susceptible to burn in, glare, suboptimal energy utilization and heavy
Light-emitting diode-liquid crystal (LED-LCD) display || Commercial (Commercialized 1970 [26])	Portable, light weight and	Slow response time, color saturation and

	efficient power usage	limited conversion efficiency
Organic light-emitting diode (OLED) display || Commercial (Commercialized 1997 [28])	Freeform enabling fabrication into different shapes, fast response, broad viewing angle, self-emitting requiring no backlight and efficient power usage	Suboptimal color purity, burn in and short device lifetime

1.2 Emerging Illumination Technology: OLED Light

Lighting devices have become part of our daily technologies with their application growing across sectors (residential, industrial, transportation, security, entertainment, etc.). These devices account for 20% of US electricity consumption [29-31]. As a result, the development of efficient, safe, and

cost-effective devices has become the goal of academic and industrial research. Solid-state lighting (SSL) technology is at the forefront of research to meet these needs.

The primary SSL technologies LED and OLED. These devices are superior to incandescent lamps and fluorescent lamps due to better heat management, resulting in higher efficiency. OLED devices have higher power efficiencies than incandescent lamps, which translates to potential significant energy savings since lighting accounts for over 20% of electricity produced in the United States further positioning OLED technology as the future of solid-state lighting [31]. Additionally, SSL devices are more durable, secure, long-lasting and produce unidirectional light emission [29].

In terms of how OLEDs compare to LED lights, while LEDs are currently cheaper, higher in lifespan and efficiency, OLED lights are promising for several reasons. OLED devices are attractive because of their flexibility to be made into any shape, more environmentally friendly as its materials are biodegradable, lower power consumption, high color purity and more quality light that can be healthier to the eye [32]. Thus, OLEDs' ability to deliver high quality stable light as well as compatibility on flexible substrate make them attractive, and already a success for display applications, and promising for general illumination [33].

As an emerging solid state lighting product, white organic light emitting diode (WOLED) has received significant attention, and this WOLED architecture can be realized in many ways, including solution-processed WOLEDs (realized by coating a solution of blended chromophores on a transparent anode followed by vacuum deposition of metal cathode), vacuum deposition of

multiple emissive layers, utilization of excimer and exciplex emission, use of multiple doped emissive layers [31] and tandem structure of red, green and blue electroluminescence units.

To be suitable for lighting applications, OLED devices are expected to meet important requirements, including brightness, lifetime, and cost criteria. Specifically, high brightness ($\sim$ 5000 $\frac{Cd}{m^2}$) required for lighting is to be met by OLEDs [33]. It is important to note that this brightness is about 10 times that required in display OLEDS. One way to meet this requirement is to increase current density through the device. However, OLED device stability in terms of lifetime decays sharply with increase in current density such that increasing the latter by a factor of 10 (to meet brightness requirement for lighting application) results to decay in the former by a factor of 100 [33]. Further, OLEDs for SSL must deliver this high brightness of at least 5,000 cd/m^2 over a substantial lifetime of at least 50,000 hours [34]. One way to realize high brightness in conventional OLED is by increasing the current density through the device. However, this strategy is not sustainable as high current density triggers material decomposition, excessive heating, and coulombic degradation [34-41] thereby drastically reducing device lifetime [13]. Further, increasing current density in view of realizing high brightness also makes thin film transistor used to drive OLED backplane susceptible to damage. Hence, for solid state lighting, OLEDs that can deliver high brightness at low current density over a long lifetime are desired [34]. As a result, tandem OLED and white organic light emitting diode (WOLED) devices have been developed as promising alternatives that can deliver better performance.

A tandem OLED comprises more than one electroluminescence units that are in series electrical connection with charge generating layer as the intermediate connector [34, 42]. Each

electroluminescence unit consists of an electron transport layer, emissive layer and a hole transport layer. Further, with tandem OLED (against patterned structure used for display application), a given brightness can be obtained at relatively low current density, thereby reducing the decay of device lifetime [43]. Also, more color stability is achieved with tandem OLED due to the elimination of energy transfer problem in different emitters [43]. Also, by having this structure, tandem OLEDs having electrically connected N electroluminescence units can potentially produce N photons for a given pair of injected electrons and hole. Thus, compared to conventional one electroluminescence unit OLED, tandem OLEDs deliver superior performance, including higher luminance efficiency and power efficiency (that scale with number of electroluminescence units), longer operational lifetime, enhanced light output due to elimination of plasmon quenching as well as freedom to achieve different color combinations [34].

Since the charge generating unit plays a critical role in determining the performance of tandem OLEDs, we now discuss requirements and common materials and compositions of materials used in the charge generating layer. The layer functioning as charge generating unit must meet both the optical and electrical requirements for the tandem OLED to realize design performance [34]. A good charge generating unit (CGU) should be optically transparent and have the capability of generating charge with minimal extra voltage drops [42, 44-55].

Charge generating layers comprise of either doped or non-doped materials, which are classified under three categories, organic/organic heterojunction, bulk heterojunction, and organic/metal (oxide) heterojunction [56]. Such that, in one typical charge generating unit structure, there is a p-n heterojunction between an n-doped electron transport layer (ETL) and a p-doped hole transport

layer (HTL), which can result in hole generation at the highest occupied molecular orbital (HOMO) of the p-type HTL and electron generation at the lowest unoccupied molecular orbital (LUMO) of n-doped ETL [52, 57, 58]. Another charge generating unit structure that is being recently studied is a p-doped HTL/deep-lying LUMO material/n-doped ETL [50, 57, 59-61].

Conventional charge generating units are doped in nature, which are typically structured as organic-metal (oxide) bilayer or organic-organic bilayer to meet both the optical transparency and electrical requirements needed for CGU. Organic-organic junctions are obtained using n-doped electron transport layer and p-doped hole transport layer while organic-metal oxide junctions are achieved using n-doped electron transport layer and transition metal oxide. Common structures of these doped CGUs are summarized in Table 1.3. However, there are significant downsides to doped charge generating units, which make non-doped CGUs attractive. Compared to doped charge generating units, non-doped charge generating units are attractive since degradation of device stability due to dopant's diffusion into organic layers is reduced for non-doped CGUs, and it is less complicated to fabricate non-doped CGUs, eliminating the need for co-evaporation and deposition, thereby reducing manufacturing cost [62]. Common non-doped charge generating units that have been developed are summarized in Table 1.4.

Though OLED is promising as the next generation solid state lighting technology, significant technical and economic barriers currently limit WOLED, and tandem OLEDs intended for general illumination. Addressing the technical and economic challenges would improve the overall device performance while making OLED economically viable and attractive as a next generation SSL technology. These technical challenges limit overall device performance, and they include need to

maintain material purity, boost device brightness and realize device of long operational lifetime [31] as well as voltage division of charge generating units, which limits power efficiency of tandem OLEDS [63]. Nevertheless, identified approach that can be utilized to address the technical challenges include development of blue emitters with longer lifetime and improved efficiency, development of efficient p-type charge generating interface and development of tandem OLEDs based on exciplex emission [34].

On the other hand, a key economic barrier limiting commercialization of OLED for SSL is high manufacturing cost resulting from suboptimal material utilization efficiency and film production throughput. To this end, this study contributes to advancing efforts in reducing manufacturing cost of OLEDs intended for general illumination by developing scalable pathway on how organic vapor phase deposition (OVPD) can be efficiently used to deposit organic materials at > 75% MUE. Details on the motivation, methodology as well as the obtained results are provided in Chapters 3 and 4 of this dissertation.

Table 1.3: Common doped charge generating units developed for tandem organic light-emitting diodes.

Structure of doped charge generating unit ‖ Structure chemical symbol and thickness	References
1,4,5,8,9,11-hexaazatriphenylene hexacarbonitrile/ 1,4,5,8,9,11-hexaazatriphenylene hexacarbonitrile-4,4′-cyclohexylidenebis[N,N-bis(4-methylphenyl)benzenamine] (TAPC)/ 1,4,5,8,9,11-hexaazatriphenylene	[64]

hexacarbonitrile || HAT-CN (10 nm)/HAT-CN : TAPC (2 : 1, 20 nm)/TAPC (40 nm)	
1,4,5,8,9,11-hexaazatriphenylene hexacarbonitrile/ 1,4,5,8,9,11-hexaazatriphenylene hexacarbonitrile-4,4′-cyclohexylidenebis[N,N-bis(4-methylphenyl)benzenamine] (TAPC)/ 1,4,5,8,9,11-hexaazatriphenylene hexacarbonitrile || HAT-CN (20 nm)/HAT-CN : TAPC (2 : 1, 10 nm)/ TAPC (40 nm)	[64]
Molybdenum oxide/ Aluminum/ Caesium carbonate || MoO_3 (8 nm)/Al (1 nm)/Cs_2CO_3 (0.5 nm)	[65]
Tetrafluorotetracyanoquinodimethane: 4,4',4"-tris (N-1-naphtyl-N-phenylamino-triphenylamine/Lithium: 1,3,5-tri(phenyl-2-benzimidazole)-benzene || 1-TNATA: F_4-TCNQ/TPBi:Li. P-doped and n-doped thicknesses: 1- 20 nm	[58]
4,4,4 -tris (N-carbazolyl) triphenylamine:Cesium azide/Aluminum/1,4,5,8,9,11-hexaazatriphenylene-hexacarbonitrile || Bphen:CsN_3, (17%, 10 nm)/Al (1 nm)/HAT-CN (15 nm)	[66]

Table 1.4: Common non-doped charge generating units developed for tandem organic light-emitting diodes.

Structure of non-doped charge generating unit || Structure chemical symbol and thickness	References
Lithium fluoride/Aluminum/1,4,5,8,9,11-hexaazatriphenylene hexacarbonitrile || (LiF (1 nm)/Al (1 – 7 nm) /HAT-CN (20 nm))	[67]
Lithium fluoride/ Aluminum/ Molybdenum oxide || LiF (1 nm)/Al (5 nm)/MoO$_3$ (20 nm)	[62]
Lithium fluoride/ Aluminum/1,4,5,8,9,11-hexaazatriphenylene hexacarbonitrile (HAT-CN$_6$) || LiF (1 nm)/Al (1 nm)/HAT-CN6 (10 nm)	[68]
Cesium azide/Aluminum/1,4,5,8,9,11-hexaazatriphenylene-hexacarbonitrile || CsN$_3$, (1 nm)/Al (1 nm)/HAT-CN (15 nm)	[69]
Aluminum/tungsten trioxide/gold || Al (2 nm)/ WO$_3$ (3 nm)/ Au (16 nm)	[70]
Lithium fluoride/Calcium/Silver || LiF (1 nm)/ Ca (25 nm)/Ag (15 nm)	[71]
Lithium fluoride/Aluminum/Gold || LiF (1 nm)/ Al (3 nm)/Au (15 nm)	[71]
Lithium fluoride/Aluminum/Fullerene/1,4,5,8,9,11-hexaazatriphenylene-hexacarbonitrile/ N,N'-diphenyl-N,N'-bis(1-naphthyl)-1,1'-biphenyl-4,4'-diamine || LiF (1 nm) /Al (5 nm) /C$_{60}$ (5 nm) /HAT-CN (15 nm) /NPB (40 nm)	[63]
Aluminum/1,4,5,8,9,11-hexaazatriphenylene-hexacarbonitrile/Copper (II) phthalocyanine || Al (1 nm)/HAT-CN (10 nm)/CuPc (20 – 35 nm)	[72]

Lithium fluoride/Aluminum/Fullerene/4,4',4''-tris (N-3-methylphenyl-N-phenyl-amino) triphenylamine || LiF (1 nm)/Al (3 nm)/C_{60} (3 – 10 nm)/m-MTDATA (10 nm)	[73]
Copper hexadecafluorophthalocyanine /Copper phthalocyanine || F_{16} CuPc (5 nm) /CuPc (5 nm)	[74]

1.3 Emerging Display Technology: Micro-LED Display

Micro-LED technology is being considered as a superior alternative to other technologies, as micro-LED devices have the potential to deliver higher brightness, efficiency, longer lifetime and less power consumption than other display technologies, making it a promising technology for emerging display products like smart glasses, head-up displays and smart watches.

Micro-LEDs, being microscopic arrays of LEDs, are made of groups III-V elements, typically including a combination of two or three of boron, gallium (Ga), aluminum (Al), nitrogen (N), arsenic (As), phosphorus (P) and antimony (Sb). The wavelength and consequently color of the emitted light of the resultant semiconductor can be tuned by varying the composition of the constituent materials, and common colors and wavelengths of light emitted by different micro-LED materials include green ($492 < \lambda < 570$): gallium nitride (GaN) and indium gallium nitride (InGaN); violet ($400 < \lambda < 455$): indium gallium nitride (InGaN); blue ($450 < \lambda < 500$): indium gallium nitride (InGaN), silicon carbide (SiC), and zinc selenide (ZnSe); yellow ($570 < \lambda < 600$): gallium arsenide phosphide (GaAsP), aluminum indium gallium phosphide (AlGaInP), and

gallium phosphide (GaP); orange (590 < λ < 625): gallium arsenide phosphide (GaAsP), aluminum indium gallium phosphide (AlGaInP), and gallium phosphide (GaP); and red (610 < λ < 760): gallium arsenide phosphide (GaAsP), aluminum gallium arsenide (AlGaAs), aluminum indium gallium phosphide (AlGaInP), and gallium phosphide (GaP).

The corresponding band gap energy (E in eV) for the corresponding wavelength of the emitted light can be obtained using Eq. 1.1:

$$E = \frac{hc}{\lambda} \qquad\qquad 1.1$$

Where h is Planck's constant (= 4.1357 * 10^{-15} eV. s), c, speed of light in vacuum (= 299,792,458 m/s) and λ, the wavelength of emitted light (m).

In terms of fabrication method, Micro-LEDs can be fabricated by micro-scale etching (dry) of LED film or non-etch processes [75]. For fabrication by micro-scale etching, etching process and chip singulation expose and damages active layers thereby necessitating repair strategies like wet chemical treatment, passivation layer deposition, etc. These repair methods are important strategies for recovering degradation in device quantum efficiency caused during dry etching [75] and singulation. For wet chemical treatment, the strategy involves passivating or treating the damaged area by exposing the dice LED in chemical solutions like ammonium sulphide [76], potassium hydroxide and ammonium sulfide [75], and octadecyl thiol [77] while for passivation layer deposition, the approach is to treat or remedy these damages by deposition of passivation layers using materials like alumina and silica [78].

In addition to the above etch-method, micro-LEDs can also be fabricated using non-etch methods. Techniques based on the latter that have been demonstrated include selective-area growth (SAG) and epitaxial lateral overgrowth (ELOG) methods where micro-LED units are grown on predetermined sections on the substrate [75].

For the rest of this section, we discuss different features that make micro-LED attractive for emerging applications.

Firstly, micro-LED display technology utilizes a self-emissive mechanism to convert flow of electrical charges into emitted light at subpixel level, thereby eliminating the need for backlight. This emissive nature of micro-LED, and micron size of micro-LED chips allow for compact design as well as realization of portable and flexible display. Flexible displays are attractive for emerging applications since they enable the development and fabrication of light, foldable, brittle-resistant electronic and bioelectronic display units of different shapes. Further, flexible displays can be made on cost-effective plastics, which are compatible with continuous manufacturing mode [79] thereby resulting in economic benefits in terms of material cost and operating costs as well as reduction in contamination level [80]. Thus, like organic light emitting diode display, micro-LEDs can be made into different foldable and rollable forms suited for emerging applications.

Other features that make micro-LED a befitting technology for emerging display is the capability to be made as high pixel density display (up to 30,000 pixels per inch (PPI)) that can deliver output of ultrahigh contrast ratio. These features are critically important in display as display quality and resolution are greatly enhanced for high PPI display products while ultrahigh contrast ratio enable

delivery of brighter and more distinct display output. This ability to make micro-LED display to have high PPI and ultrahigh contrast ratio make micro-LED technology well suited for emerging display applications like (smart glasses, HUD display, etc.), which are used in near-proximity to the eye allowing for true-state visualization of display outputs even in daytime. In terms of how micro-LED displays compare with OLED and LCD counterparts on these features, micro-LEDs offer superior contrast ratio, which is about 100 times better than OLED and 200 times better than LCD. Specifically, while LCD and OLED can achieve contrast ratio of 5000:1 and 10,000:1, respectively, micro-LED can deliver > 1,000,000:1 ratio [6]. Further, micro-LED display can have density of 30,000 PPI (with minimum pixel size of < 1 micron) compared to the 1433 PPI and 806 PPI for OLED (minimum pixel size of 18 micron) and LCD (minimum pixel size of 32 micron), respectively [6].

Response time is another important feature for emerging displays since ultralow response time reduces blurring and allows for better experience in visualizing dynamic display output. For context, micro-LEDs have ultrafast response rate corresponding to response time of nanoseconds compared to microseconds and milliseconds for OLED and LCD, respectively [6]. Nevertheless, while micro-LEDs have faster response rate, it cannot be assumed that micro-LEDs will deliver better viewing experience since moving picture response time (MPRT) is also affected by frame rate [20, 81].

Further, large view angle, long lifetime and high resistance to environmental degradation further make micro-LED well suited for emerging display. Specifically, while OLED and LCD can have view angle up to 89°, micro-LED display allows for wider viewing angle of up to 180° [6] thereby

enabling higher quality visualization of display outputs from different locations. Further, micro-LEDs have higher stability and longer lifetime (LT: > 100, 000) than OLED (LT: 10, 000) and LCD (LT: 30, 000 – 60,000) [6] further making micro-LED suitable for emerging display where significant usage is needed before product replacement.

Nevertheless, while micro-LEDs show these excellent quality capabilities, its wider adoption and commercialization have been limited by complexity in manufacturing and assembling processes [82] resulting in exorbitant device cost. These manufacturing complexities are largely due to suboptimal micro-LED chip mass transfer yield and assembling rate. We therefore discuss different technologies that have been developed to advance assembling yield and throughput in chapter 5.

Chapter 2 Experimental Techniques

2.1 Overview

This chapter describes major experimental techniques used in this study. Working principles of the techniques are described, while demonstrating proof of concept by fabricating a green OLED device.

2.2 Vacuum Thermal Evaporation

Vacuum thermal evaporation (VTE) is the conventional physical vapor deposition technique for coating thin film of materials unto substrates. As shown in Figure 2.1, VTE system works by utilizing joule heating under hard vacuum (10^{-6} Torr) to vaporize source materials, causing the vapors to move with long mean free path before condensing on the substrate as thin film. The used Joule heating is produced from exposing the resistive boat to enormous direct current while the source boat is typically made of metals of excellent thermal stability and high melting point like Tungsten.

In terms of applications, VTE can be used to process several materials, at different operating vacuum pressures, co-deposition of materials as well as fabrication of multilayer unit without breaking vacuum. Source materials processable in VTE range from small molecular organic materials that can be readily vaporized and deposited unto substrate, to metals, alloys and

compounds whose melting points are substantially less than the melting point of the source boat material.

Long mean free path of vapors in VTE is due to the extreme low-pressure condition, which are typically in the order of 10^{-4} - 10^{-8} Torr. The corresponding mean free paths at these pressures can be estimated from kinetic theory of gases using the Eq. 2.1 below, and they are in centimeters and hundreds of meters.

$$\bar{l} = \frac{\mu}{P}\sqrt{\frac{\pi RT}{2M}}$$

2.1

Where M is source molecular weight, μ, viscosity at temperature, T and pressure, P.
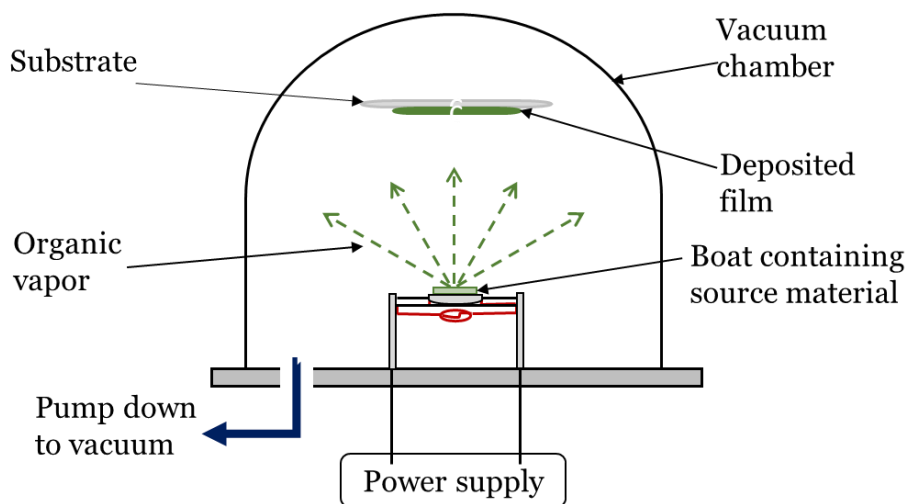
Figure 2.1: Schematic of a vacuum thermal evaporation system.

2.3 Organic Vapor Phase Deposition

Organic vapor deposition (OVPD) is an emerging physical vapor deposition technique developed to allow for more controllable film coating under low pressure. Figure 2.2 shows schematic of OVPD, with its controllable variables highlighted as well as the critical response variables including film deposition rate and material utilization efficiency. Typically, in OVPD, source material is thermally vaporized from source cell and carrier gas is simultaneously fed through the source tube to support vapor transport towards the substrate.

$\dot{V}$: carrier gas flow rate; P_{ch}: chamber pressure;
T_t: tube temperature; T_s: stage temperature
R_{dep}: film deposition rate
MUE: material utilization efficiency;

Figure 2.2: Schematic of organic vapor phase deposition system.

While OVPD shares common features with VTE, the former technique also differs significantly from the latter. In terms of similarity, both VTE and OVPD are physical vapor deposition

techniques, and they utilize thermal energy at conditions below atmospheric pressure to vaporize materials, allowing their vapor to condense on the substrate as film.

However, OVPD differs from VTE in three key areas, which makes the former a more controllable physical vapor deposition technique. These three areas include: i) decoupling of source evaporation from vapor transport, ii) more directional flow of source vapor, and iii) controllability of operating deposition variables.

Compared to VTE (operated at 10^{-4} - 10^{-8} Torr), OVPD, which operates at low pressure (0.01-10 Torr) produces source vapor with shorter mean free path (<5 mm for OVPD) than VTE (mean free path > 20 cm for VTE). Practically, OVPD can be operated at other sub-atmospheric pressures (10 - 600 Torr). Unlike in VTE, where a vapor molecule makes it from the source boat to the substrate under few random walks, vapor molecules in OVPD having shorter mean free path embark in multiple random walks before condensing on the substrate. Thus, the decoupling of evaporation from transport in OVPD is due to many random walks undertaken by molecules, which also potentially allows more vapor mixing enroute to the substrate.

More directional flow of source vapor is the second distinction that OVPD offers, and this feature is due to short mean free path of vapor species as well as the directional transport support provided by carrier gas used in OVPD.

The last distinct feature that OVPD offers is more controllability of operating deposition variables. Specifically, unlike in VTE, each chamber temperature, pressure, carrier gas flow rate as well as stage temperature can be independently controlled.

In terms of application relevant to this study, though VTE is sufficient for making OLEDs for small-area display application, its usage is hampered by limited material utilization, restrictive process operation [83, 84] and poor control at high deposition rate. On the other hand, OVPD offers flexible operating conditions that can be potentially maximized to produce OLED at fast rate with enhanced material utilization. Some of these features have been demonstrated by earlier studies on OVPD.

Baldo et al. first demonstrated that OVPD can be used to fabricate OLED on both rigid and flexible substrates [85], which confirmed OVPD's suitability for roll-to-roll processing of organic semiconductor devices. Consequently, Baldo et al. [86] showed that multiple materials can be co-deposited in OVPD thereby allowing for controllable doping of low concentration emitters in host matrix. Furthermore, film growth in OVPD can be optimized by controlling process variables to improve deposition rate. It has been demonstrated that OVPD can achieve relatively high deposition rate up to 12 angstrom/sec [87]. Nevertheless, it is important to note that at high growth rate more defects form on the emissive film with resultant decrease in device performance [88]. Further, in chapters 3 and 4 of this study, we will also show that OVPD can be conveniently scaled to realize > 75% material utilization efficiency [89] thereby making it a promising processing technique for tandem OLEDs for lighting application.

2.4 Ellipsometry

Ellipsometry is an optical technique for determining properties of optically reflective surfaces by utilizing models to analyze changes in polarization of reflected light (refer to Figure 2.3). These properties include thickness, absorption coefficient, conductivity, porosity, composition, and refractive index [90], and can be used for characterizing both reflective inorganic surfaces and organic films coated on the former. Further, ellipsometry is an attractive film characterization as it is also fast and non-destructive technique [91] that can be used to analyze film of wide range of thickness (nanometer to micrometer) in both single layer and multilayer structure films [90].

Figure 2.3 illustrates the working principle of an ellipsometer, which comprises polarization of light before it is incident on the sample, and collection of change in polarization data of the reflected beam, which are mathematically analyzed to obtain film properties.

To use ellipsometry to characterize film for abovementioned properties, the ratio of amplitude of two perpendicularly polarized beams is used to determine the change in polarization of reflect light [90]. These ellipsometry data must then be mathematically analyzed in order to obtain relevant film properties [91], with its first essential theory emanating from the works of Fresnel [92]. After which significant progresses have been recorded in the development of ellipsometry theory and instrumentation [93]. Among these theories, mathematical analyses of ellipsometry data are essential in relating data to film properties. Procedures for these mathematical analyses have been reviewed by Jellison Jr. [91] and typically include construction of near-surface region model and selection of a method to determine the complex Fresnel reflection coefficients, selection of spectroscopic optical functions used in the model, and fitting of ellipsometry data to model to

determine fitting parameters. In this work, we used ellipsometric technique to determine thickness of deposited film.
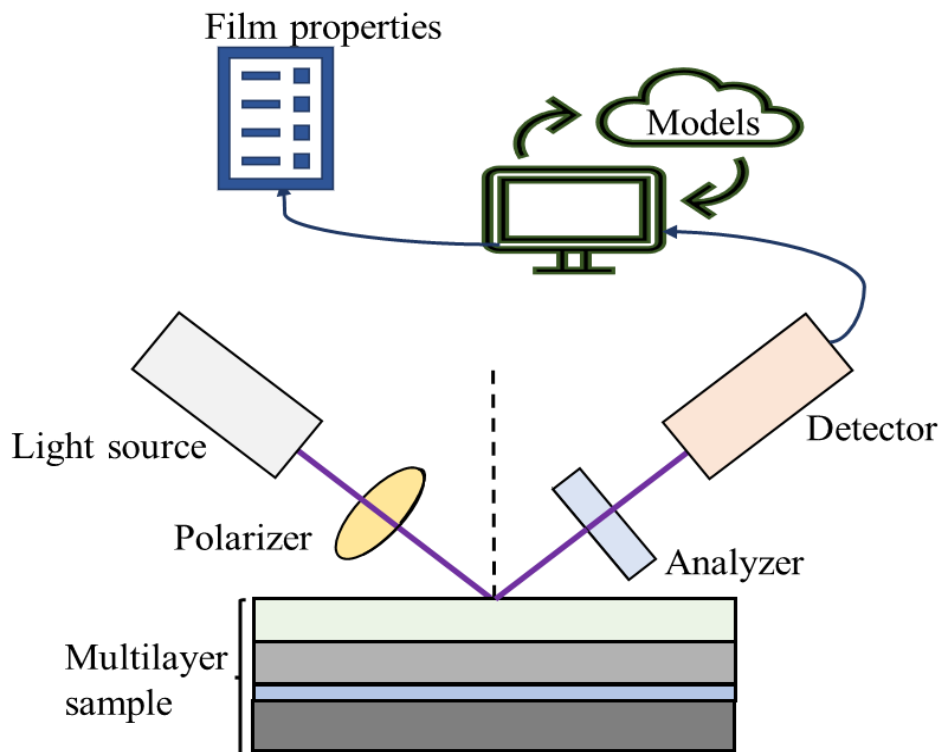
Figure 2.3: Illustration of working principle of an ellipsometer used in characterizing film properties.

2.5 Spectrophotometry

Spectrophotometry is an analytical technique for determining properties of material by determining the amount of light it absorbs at a given wavelength. Spectrophotometry is used for identification of a species, quantification of species concentration, and detection of chemical structure, and this technique is widely applied in several industries, including but not limited to water, food and beverage, petrochemical, pharmaceutical, medical and research and development institutions.

Figure 2.4 illustrates the schematic of a spectrophotometer, showing how principles of spectrometry and photometry are used by the instrument to determine the amount of absorbed by the sample being investigated. Spectrometer serves to produce light of desired wavelength while photometry measures the intensities of the light produced (and absorbed by the sampled). Production of light of desired wavelength consists of, in sequence, generation of straight beams of light from source light by the collimator, splitting of light as lights of distinct different wavelengths, and then followed by transmission of lights of desired wavelength, which pass through the sample under analysis.

The working principle of a spectrophotometer is based on Beer-Lambert's law. By the Beer-Lambert's law, the amount of light absorbed (or transmitted) by a sample is proportional to the sample's properties, its concentration and path length, as described by Eq. 2.2:

$$a = \dot{\varepsilon}\dot{c}l \qquad\qquad 2.2$$

Where a is absorbance, $\dot{\varepsilon}$, molar absorption coefficient representing the sample property, $\dot{c}$, molar concentration, and l the optical path length.

The absorbance, a of the studied sample at a given wavelength is obtained from the sample's transmittance (T in %), which relates the intensities of incident light (I_0) to that of transmitted light (I) (refer to Eq. 2.3).

$$a = -\log_{10}T = -\log_{10}\left(\frac{100 * I}{I_0}\right) \qquad\qquad 2.3$$

Therefore, from Eq. 2.2, spectrophotometry utilizes dependence of absorbance on the molar absorption coefficient, ε to identify presence of species in the analyte solution. Similarly, the dependence of absorbance on molar concentration at a given wavelength is used by the instrument to quantify the sample concentration in the analyte solution (see Eq. 2.3). In this work, we utilized spectrophotometric technique to determine the MUE during organic vapor phase deposition.
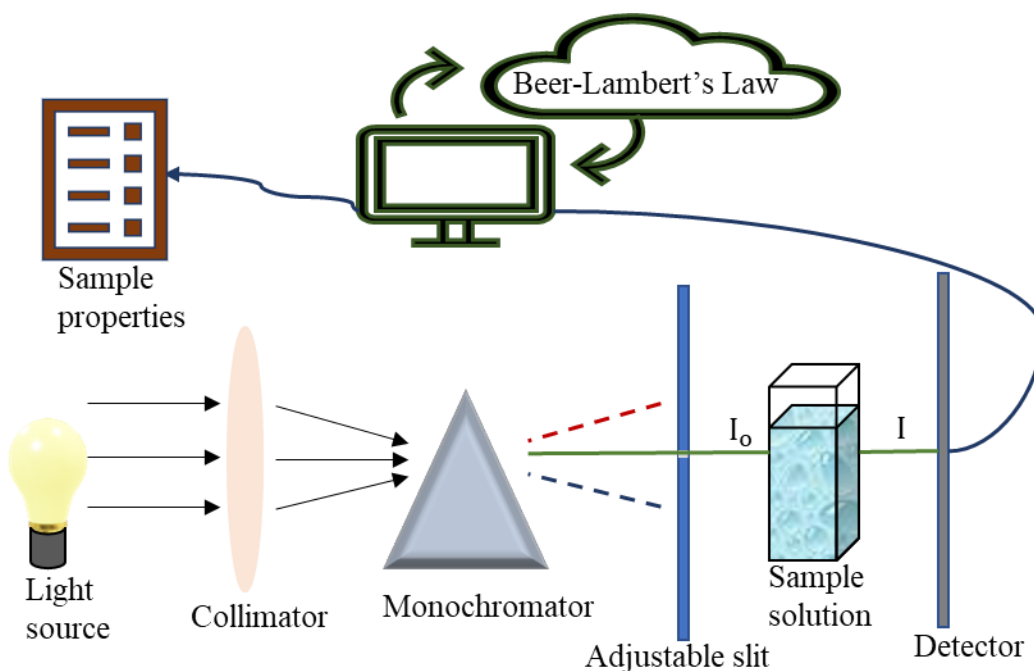
Figure 2.4: Illustration of working principle of a spectrophotometer used in characterizing sample solution.

2.6 Proof of Concept: Fabrication of a Green OLED Device

2.6.1 Overview and acknowledgement

In this section, we demonstrate proof of concept by fabricating a green OLED device. The author conducted this experiment with Binyu Wang. The author acknowledges Boning Qu and Brian Lezzi for their assistance during the experiment.

2.6.2 Materials

Materials used for this demonstration (*and their functions*) include glass (*substrate*), indium tin oxide (ITO) (*anode*), molybdenum trioxide (MoO_3) (*hole injection*), N,N'-Di(1-naphthyl)-N,N'-diphenyl-(1,1'-biphenyl)-4,4'-diamine (NPD) (*hole transport*), tris(8-hydroxyquinoline)aluminum(III) AlQ_3 (organic emitter and electron transport), lithium fluoride (*hole injection)*, and Aluminum (cathode).

2.6.3 Methods

The structure of OLED device fabricated is like that made by Zou, et al. [94] with the thickness of each layer illustrated in Figure 2.5. A 25×75×1.1mm indium tin oxide (ITO)-coated glass (Delta Technologies, USA) is the substrate, with the ITO as the anode. Prior to deposition the substrate is cleaned in four different solvents in the order of soapy water, deionized water, acetone, and finally isopropyl alcohol (IPA). For each cleaning, the substrate is rinsed and then sonicated in the solvent for 15 mins at 40°C. After which the cleaned substrate is boiled in fresh IPA from 180 to 215°C for 3 minutes. The substrate is then dried with an inert gas with the help of a nitrogen gun. Finally, the substrate is treated in ultraviolet ozone for a minute, and it is then ready for deposition.

Subsequently, the substrate is loaded in a glove box of inert environment (maintained by constant circulation of nitrogen) with both oxygen and moisture concentrations less than 50 parts per million (ppm). The deposition system is a vacuum thermal evaporation system (Angstrom Engineering, Canada), which is directly connected to the glovebox to ensure inert environment is maintained. To load substrate on the deposition chamber, the latter is brought up to atmospheric pressure, substrate holder is unloaded, and the substrate is firmly mounted on the holder, and reloaded back to the system. The chamber is then pumped down to vacuum before deposition commences. Different layers of the device are then grown according to the thickness and order illustrated in Fig. 2.5 (from bottom layer to top layer, excluding the cathode). After deposition of these layers, the device is unloaded to mount a mask to selectively create sections for cathode deposition. Cathode mask is then mounted, and the device is reloaded to deposition chamber. Aluminum cathode is then deposited to complete the device making process. The device is unloaded from the chamber and subsequently from the glove box and prepared for testing. Finally, the fabricated OLED device is successfully tested (refer to Fig. 2.5) using a semiconductor parameter analyzer (Hewlett-Packard) and then analyzed for J-V and EQE, thereby demonstrating proof of concept.

Material (thickness(nm))	Function
Al (150)	Cathode
LiF (1)	Electron injection layer
Alq$_3$ (60)	Emitting and electron transport layer
NPD (80)	Hole transport layer
MoO$_3$ (5)	Hole injection layer
ITO	Anode

(A)

(B)

Fabricated OLED device: Before and during testing
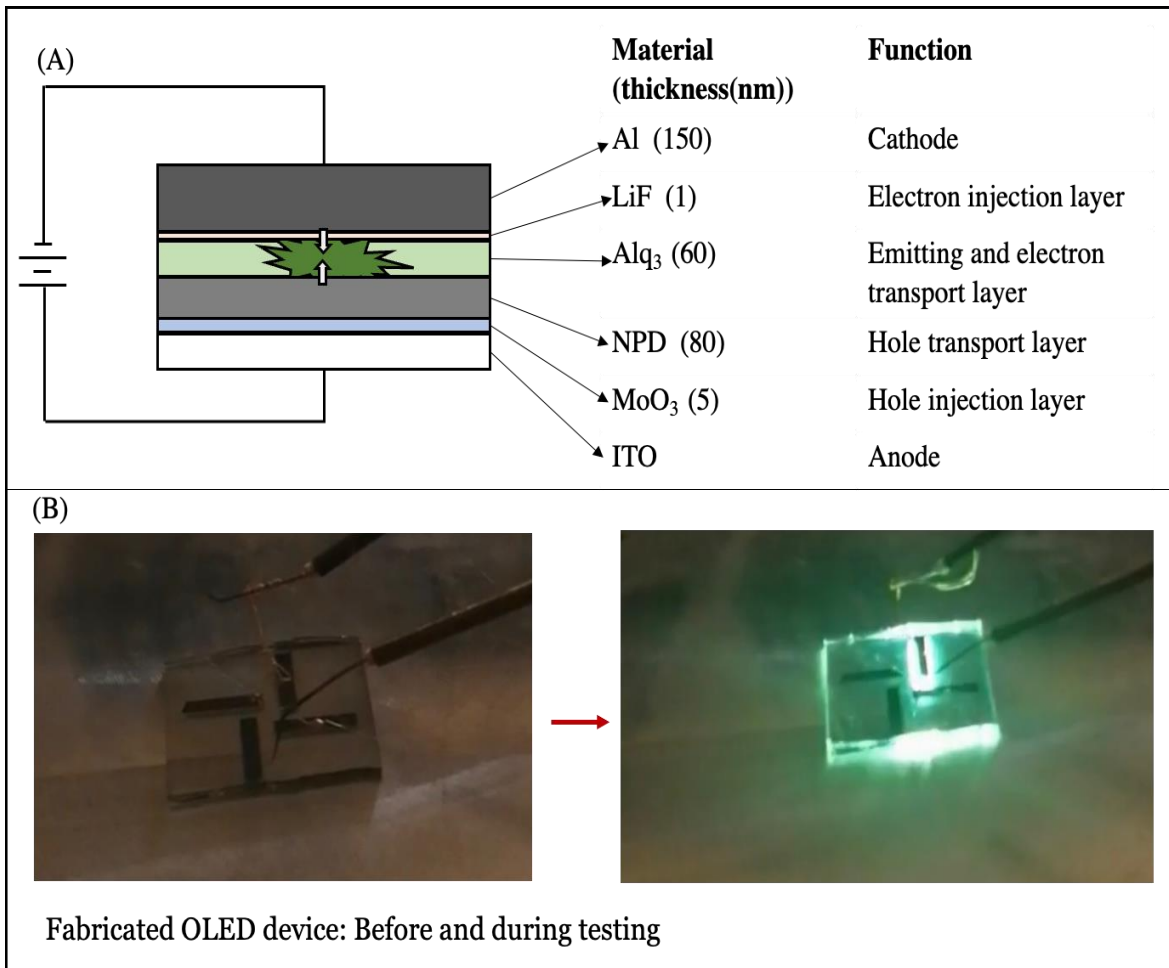
Figure 2.5: Structure of fabricated green OLED device with thickness and function of each film layer outlined (A). Picture of fabricated device before and during testing shown in figure B.

Chapter 3 Development of Model for Boosting Material Utilization in Organic Vapor Phase Deposition

3.1 Preface:

This chapter is a moderately modified version of the original work published in the Journal of Materials Research and has been reproduced here with the permission of the copyright holder. First published in the Journal of Materials Research, 38, pages 2327–2338 (2023) by Springer Nature. Reproduced with permission from Springer Nature.

3.2 Abstract: Statement of Research Gaps, Hypothesis and Original Contribution

Organic vapor phase deposition (OVPD) is a promising technique for cost-effective manufacture of organic electronic devices. Maximizing utilization of the active organic source materials is essential for manufacturing organic light emitting devices (OLEDs) intended for general lighting, especially for tandem OLEDs where multilayers of these emissive materials are used to meet the brightness requirement. Further, the ability to predict MUE is crucial for economic analyses prior to process scaling since it allows for yield projections, material requirements, and cost modeling. To develop pathway for boosting material utilization efficiency (MUE) in OVPD, we hypothesize that if the relative contributions of organic species flow and system configuration to film growth are understood, a model that predicts MUE for OVPD can be developed. We therefore apply a combination of first-principle physics, computational fluid dynamic (CFD) simulation, model development and experimentation to develop a pathway for boosting MUE beyond reported

values. The developed model was theoretically tested for different process conditions including chamber pressures (0.1 – 400 Torr), evaporation temperatures (200 – 400 °C) and substrate size, relative chamber cross-section. Our theoretical and experimental results reveal area ratio (substrate to chamber) as the key driving variable for MUE. We further show that material utilization efficiency can be further boosted by engineering thermal boundary layer in additional planes, which was experimentally demonstrated on practically useful substrates. Based on original contributions, we propose a system configuration that can deliver > 75% MUE in OVPD.

3.3 Introduction and Motivation

In this section, we introduce organic vapor phase deposition (OVPD) and discuss practical motivations for project 1, which is to develop a model for boosting material utilization efficiency in OVPD.

Physical vapor deposition (PVD) is an essential coating technique that is applied across industries to produce thin film layers unto substrates, especially for applications where the source materials naturally exist in solid state. Common types of PVD include sputter deposition [95], electron-beam deposition [96], pulsed laser deposition [97], and evaporation deposition. Among the PVD techniques, evaporation PVD is attractive where high deposition rate and simple operating procedures are desired, and its main types are vacuum thermal evaporation (VTE) and organic vapor phase deposition (OVPD). Other simple coating techniques are the solution-based processes, which are attractive due to low-cost, low-material wastage and ability to be used for large-area film deposition, and significant research efforts are being invested towards improving performance of solution-processed devices [98-100]. However, solution-based processes lack the capability of

multilayer deposition, precise control of film thickness and deposition rate, which are critical features desired in OLED fabrication. While VTE is capable of multilayer deposition with precise control of film thickness and deposition rate, it is limited by suboptimal material utilization efficiency (MUE) and difficulty in creating uniform films over large area substrate. Since VTE system works by utilizing joule heating under hard vacuum (10^{-4} - 10^{-8} Torr) to vaporize source materials, vapors move with long mean free path before condensing on the substrate as thin film (see Figure 1A). This line-of-sight nature of vapor transport contributes to the suboptimal MUE obtainable in VTE.

On the other hand, in OVPD (Figure 1B), source materials are thermally vaporized in low-pressure (0.01 - 10 Torr) from source cells with carrier gas simultaneously fed through the sourc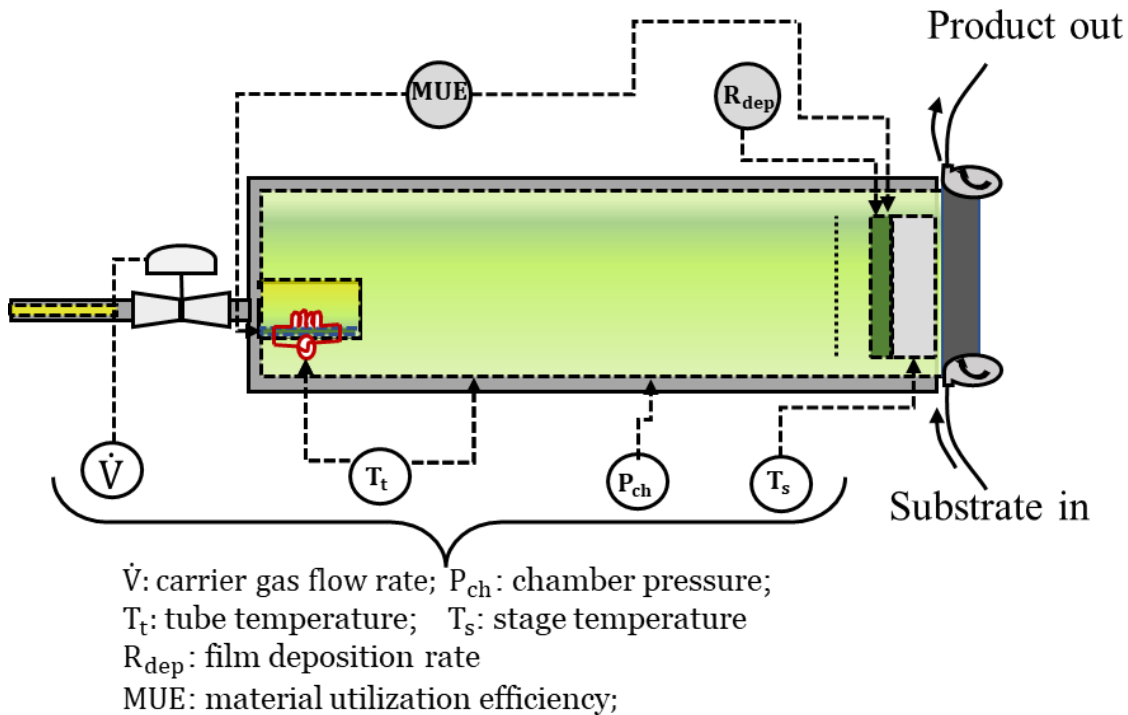e tube to support vapor transport towards a cooled substrate where they condense. Thus, in OVPD, vapors have shorter mean free path allowing for control in vapor flow direction, and consequently process flexibility to enhance MUE.

Organic vapor phase deposition (OVPD) is attractive for high volume production of organic semiconductor devices, circumventing several trade-offs of vacuum thermal evaporation (VTE). The latter is traditionally used for depositing the layers comprising organic light emitting devices (OLEDs), but is subject to a natural trade-off between, e.g., host-dopant mixing effectiveness and the fraction of source material that is usefully coated on the substrate (MUE). To ensure even dopant distribution, the distance from source to substrate should be large relative to the distance between the sources. Increasing the distance, however, causes more of the evaporated material to be lost at the edges of the substrate, such that source material utilization efficiency scales with the

width of the reel. Placing sources more proximally to each other in the transport direction to encourage host-dopant mixing, on the other hand, increases the risk of cross-contamination. Point evaporation sources are limited to < 5 % MUE [83, 84], while line source systems achieve on the order of 50 %. [101] Complex mechanical designs and/or batch production could mitigate these issues, but at the expense of capital equipment cost and amortization rate, and still suffer from significant downtime for cleaning.

Further, for emerging OLEDs intended for general illumination, MUE is a critical economic metric as material expenditure is a significant component of the overall device cost, especially for tandem OLEDs where multilayers of organic materials are used to meet the brightness requirement. Thus, earlier studies have studied how some process regimes could affect material utilization in OVPD. Lunt, et al. [102] obtained theoretical MUE at different carrier gas flow rates (> 100 SCCM) and pressures with maximum experimental value of 46 %. Their numerical approach assumed a fixed inlet organic concentration, which in some transport regimes can impact MUE. However, determination of inlet organic vapor concentration has significant uncertainties. Similarly, Rolin, et al. [103] found that MUE is inversely related to flow rate and only weakly dependent on pressure. They also derived an Eq. that describes MUE as a function of temperature and Reynolds number (Re). In principle, Reynolds number (Re) increases with flow velocity, while the diffusion coefficient increases with temperature, favoring deposition. However, the model used by Rolin and coworkers employed two empirical parameters (geometric constant, *a*, and a function of temperature, *b*) as inputs. Values for empirical inputs can be process-dependent, thus requiring significant extensive experimentation to obtain robust input values. Thus, a model that requires

fewer number of empirical inputs is desirable since it can be easily adapted to predict MUE for different systems and process conditions.

Also, the ability to conveniently predict material utilization efficiency in OVPD process facilitates informed apparatus design, yield projections, forecasting of material requirements as well as cost modeling. Therefore, to advance knowledge in OVPD, in project 1, we develop a simple model that predicts MUE in OVPD, and further demonstrate a scalable pathway on how OVPD can deliver > 75% MUE.

3.4 Chapter Objectives for Project 1 on Development of model for boosting material utilization in organic vapor phase deposition.

The research objectives of this project are summarized below:

- Develop a model for predicting material utilization (MUE) during organic vapor phase deposition.
- Numerically and experimentally test the developed model.
- Leverage model insights and obtained results to propose system configuration that can deliver > 75% MUE.

3.5 Methodology

The OVPD process involves 3 main stages: 1) evaporation of active material(s), 2) carrier-gas supported transport of the vapor, and 3) deposition onto a cooled substrate. To develop a model for boosting MUE, we focus on step 3. We utilize a combination of first-principle physics, model development, theoretical analyses and experimentation for this purpose.

Because apparatus dimensions substantially exceed the molecular mean free path in the pressure range of interest (e.g., 0.1 – 10 torr), continuum fluid mechanics is expected in OVPD, such that conservation of momentum is modeled by Navier-Stokes (Eq. 3.1) and energy conservation of Eq. 3.2. It is important to state that, while the Navier-Stokes Eq.s are commonly used to model viscous liquid flow processes [104, 105], they are also appropriate for modeling gaseous and vapor flow processes where the operating conditions justify the continuum assumptions, especially at high temperatures and low pressures where their viscosities are enhanced.

$$\rho(\mathbf{u} \cdot \nabla)\mathbf{u} = \nabla \cdot (-p\mathbf{I} + \mathbf{K}) + \mathbf{F} + \rho\mathbf{g} \qquad\qquad 3.1$$

$$\rho C_p \mathbf{u} \cdot \nabla T \;\; + \nabla \cdot \mathbf{q} \;\; = \;\; Q \qquad\qquad 3.2$$

where ρ is fluid density, C_p, heat capacity at constant pressure, and T, absolute temperature. Bold letters denote vector quantities where $\mathbf{u}$, velocity vector, $\mathbf{q}$ is heat flux due to conduction. Q is heat input rate from other heat sources, $\mathbf{F}$ is volume force vector, $\mathbf{K}$ vector accounting for constitutive relation between conservation of mass and momentum. Eq. (3.1) is based on the combined conservation of mass and momentum and Eq. (3.2) on conservation of heat energy. Physical properties of the fluid are those of nitrogen adjusted for temperature: viscosity $\mu = \frac{1.73 \times 10^{-5} T}{300}$ [kg/m-s] and thermal conductivity $\kappa = \frac{0.025 T}{300}$ [W/m-K] [102]. We used COMSOL Multiphysics®

(COMSOL 5.5) to solve the above Equations. Boundary conditions included slip along the chamber walls, the walls held at the same temperature as the vapor inlet temperature (evaporation temperature), and the substrate maintained at 15 °C.

In a diffusion-limited regime, species flux in cylindrical coordinate is given by Eq. 3.3, and organic vapor in the boundary layer (BL) is either deposited on the substrate, deposited on the chamber walls, or pumped out along with the carrier gas. The chamber wall is typically heated to minimize parasitic deposition. In such configuration, determining MUE is analogous to estimating a reaction yield in a continuously stirred tank reactor, where an effective volume and residence time are estimated based on flow conditions. The BL has an effective volume, $V_{ER} = A_{ch}\delta_T$, where in the upper limit, A_{ch} is the cross-sectional area of the chamber. The molar flow rate of organic species in the BL is given as Eq. 3.4. Under axisymmetric flow behavior and dominant axial concentration gradient ($\frac{\partial C_i}{\partial z} \gg \frac{\partial C_i}{\partial r}$), it can be shown that the rate of organic species deposition is proportional to the product of substrate area and organic flux due to concentration gradient to concentration (see Eq. 3.5):

$$J_i = -D_i \left\{ \frac{\partial C_i}{\partial r} + \frac{1}{r}\frac{\partial C_i}{\partial \theta} + \frac{\partial C_i}{\partial z} \right\} \qquad\qquad 3.3$$

Molar flow rate of organic in the BL: $\dot{V}C_i{}^{BL}$ 　　　　　　　　　　　　　　 3.4

Organic species deposition rate: $K \dfrac{D_i A_s C_i{}^{BL}}{\delta_T}$ 　　　　　　　　　　 3.5

where $\dot{V}$ is flow rate and $C_i{}^{BL}$ is concentration of organic species in the thermal boundary layer of thickness, δ_T, and K is a dimensionless parameter that links flow in upstream zone to downstream zone as defined in Eq. 3.6, while D_i ($= \frac{\overline{v}\overline{l}}{3}$) is the diffusion coefficient of organic species, and A_s is substrate area. An assumption of Eq. 3.5 is that concentration gradient across the boundary is linear, with $C_i{}^{BL} \gg C_i{}^{sub}$ such that $C_i{}^{BL} - C_i{}^{sub} \approx C_i{}^{BL}$ is the instantaneous organic vapor concentration on the substrate. The ratio of outflow rate from upstream zone to flow rate in downstream zone gives expression for K as shown in Eq. 3.6:

$$K = \frac{t_d U_z A_{ch}}{V_{ER}} \qquad\qquad 3.6$$

U_z is the velocity with which fluid enters the BL. By using parameter K we have assumed that the exposed area of the substrate is parallel to chamber cross section.

In steady state, no accumulation is expected upstream, hence organic species evaporated from source zone successfully traverse the upstream before entering the boundary layer, such that steady state MUE is given by Eq. 3.7:

$$MUE = \frac{\text{Mass deposited per unit time}}{\text{Mass evaporated per unit time}} = \frac{\text{Mass deposited per unit time}}{\text{Mass entering the BL per unit time}} \qquad 3.7$$

By combining Eqs. (3.1 – 3.7), we introduce a model that predicts OVPD material utilization efficiency, MUE as shown in Eq. (3.8):

$$MUE = \frac{t_d U_z D_i A_s}{\dot{V}\,\delta_T{}^2} = \frac{t_d U_z D_i A_c}{\dot{V}\,\delta_T{}^2} \qquad\qquad 3.8$$

A_c is the area of cooled stage exposed to vapor flow. Eq. 3.8 presents a convenient means for predicting material utilization in OVPD, as it does not require the organic concentration as an input, thereby eliminating errors associated with uncertainty in determining organic vapor

43

concentration. To accurately use Eq.3.8 for MUE prediction, the carrier gas flow rate must be scaled to operating temperature and pressure, and temperature input for t_d and U_z must be taken as the average gas temperature within the boundary layer.

To experimentally test the model insights, films of Alq_3 were grown in a tubular, hot-walled deposition chamber on 675 µm silicon wafer and 100 µm thick polyimide in two substrate configurations. In one, the substrate was mounted perpendicular to chamber axis using the system described in [106], at 0.16 Torr chamber pressure, 20 standard cubic centimeter per minute (SCCM) carrier gas flow rate, and 250 °C source temperature. The MUE was measured by weighing the Si substrate before and after film growth to determine the mass of deposited film and comparing this with the change in the mass of source material. The deposition rate was determined post growth by measuring the film thickness by variable angle ellipsometry using $50 - 70$-degree incident angles with the data analyzed by Cauchy model. In the second configuration, the substrate was mounted on a 12.5 cm x 3.8 cm cold finger oriented parallel to the chamber axis and gas flow, at 8.00 Torr chamber pressure, 20 SCCM carrier gas flow rate, and 300 °C source temperature. The polyimide substrate was also coated in this configuration to experimentally determine MUE. The mass of deposited Alq_3 was determined by dissolving it from the substrate in acetonitrile and measuring the concentration of the resulting solution by comparing its optical absorbance to that from solutions of known concentration.

3.6 Results and Discussion

Figure 3.1 shows dependence of species mean free path on chamber base pressures (10^{-8} to 10^1 Torr), with the corresponding Knudsen numbers and flow regimes illustrated in the insert. These flow regimes include molecular flow (at VTE conditions), transition flow, and continuum flow at

44

OVPD conditions. As shown in Figure 3.1, the mean free path decreases exponentially with increase in base pressure such that at hard vacuum (10^{-8} to 10^{-4} Torr), organic vapors travel hundreds and thousands of meters before colliding with another vapor. This line-of-sight nature of vapor transport causes significant parasitic deposition on walls of VTE. At OVPD pressures (0.01 – sub atmospheric Torr), vapor mean free paths are short enough to allow for mixing of species on transit prior to deposition, hence the intrinsic OVPD process flexibility in for boosting MUE.

The continuum nature of flow in OVPD allows for modeling with the Navier-Stokes Equations, and we illustrate the schematics and settings used for modeling in Figure 3.2. As discussed in section 3.4, we have developed the model below for predicting MUE in OVPD

$$\text{MUE} = \frac{t_d U_z\, D_i A_s}{\dot{V}\, \delta_T{}^2} = \frac{t_d U_z\, D_i A_c}{\dot{V}\, \delta_T{}^2} \qquad\qquad 3.8$$

Use of the above model requires the knowledge of $\mathbf{U_z}$, and $\boldsymbol{\delta_T}$, which are species velocity when it enters the boundary layer and thickness of boundary layer. These parameters can be determined numerically as illustrated in Figure 3.3. For OVPD conditions, our results show that thickness of the thermal boundary layer > thickness of the hydrodynamic boundary layer, with the former having value of ~ 10 cm (compared with ~ 7cm for the latter).

To further check the accuracy of the thermal boundary layer thickness, δ_T is calculated using Prandtl number, Pr and hydrodynamic boundary layer thickness, δ_h. For flow over flat plate where $0.6 \leq \text{Pr} \leq 50$, consistent with Pohlhausen's correlation [107], thermal thickness, δ_T can be determined when the hydrodynamic thickness, δ_h and Pr are known, using Eq. 3.9 [107]:

$$\frac{\delta_T}{\delta_h} = Pr^{-\frac{1}{3}}$$

<div align="right">3.9</div>

Using 7 cm as δ_h (from Figure 3.3), we calculate δ_T = 7.8 cm, which shows that both result from Figure 3.3 (10 cm) and the calculated result from Eq. 3.9 confirm that thickness of the thermal boundary layer is greater than the hydrodynamic boundary layer. In practice, the behavior may deviate somewhat from flow over a flat plate, accounting for the discrepancy between the results obtained from Fig. 3.3 and Eq. 3.9. Thus, the thermal boundary layer is used to obtain the relevant inputs needed for MUE prediction.
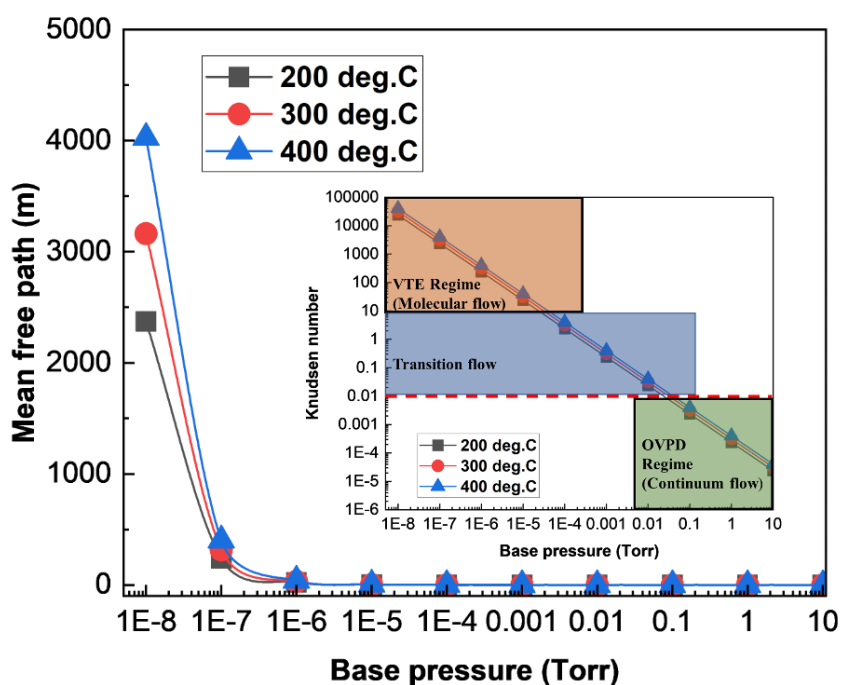
Figure 3.1: Dependence of organic vapor mean free path on base pressure with insert illustrating corresponding flow regimes, including molecular flow, transition and continuum flow. The model organic material is tris (8-hydroxyquinolinato) aluminum (AlQ_3).

(A)

δ_{BL}: Thickness of boundary layer near cooled substrate

δ_{BL}

(B)

u_{in}

$$\mathbf{u} \cdot \mathbf{n} = 0$$
$$\mathbf{K_n} - (\mathbf{K_n} \cdot \mathbf{n})\mathbf{n} = 0$$

P_{ch}

(1);(2)

(3)

T_{evap}

T_{sub}

25 °C

(1). Conservation of mass at steady state $\rho\nabla \cdot \mathbf{u} = 0$

(2). Conservation of momentum at steady state (Navier-Stokes equation) $\rho(\mathbf{u} \cdot \nabla)\mathbf{u} = \nabla \cdot (-p\mathbf{I} + \mathbf{K}) + \mathbf{F} + \rho\mathbf{g};$ $\mathbf{K} = \mu(\nabla\mathbf{u} + (\nabla\mathbf{u})^{\mathbf{T}})$

(3). Energy conservation at steady state $\rho C_p \mathbf{u} \cdot \nabla T + \nabla \cdot \mathbf{q} = Q$
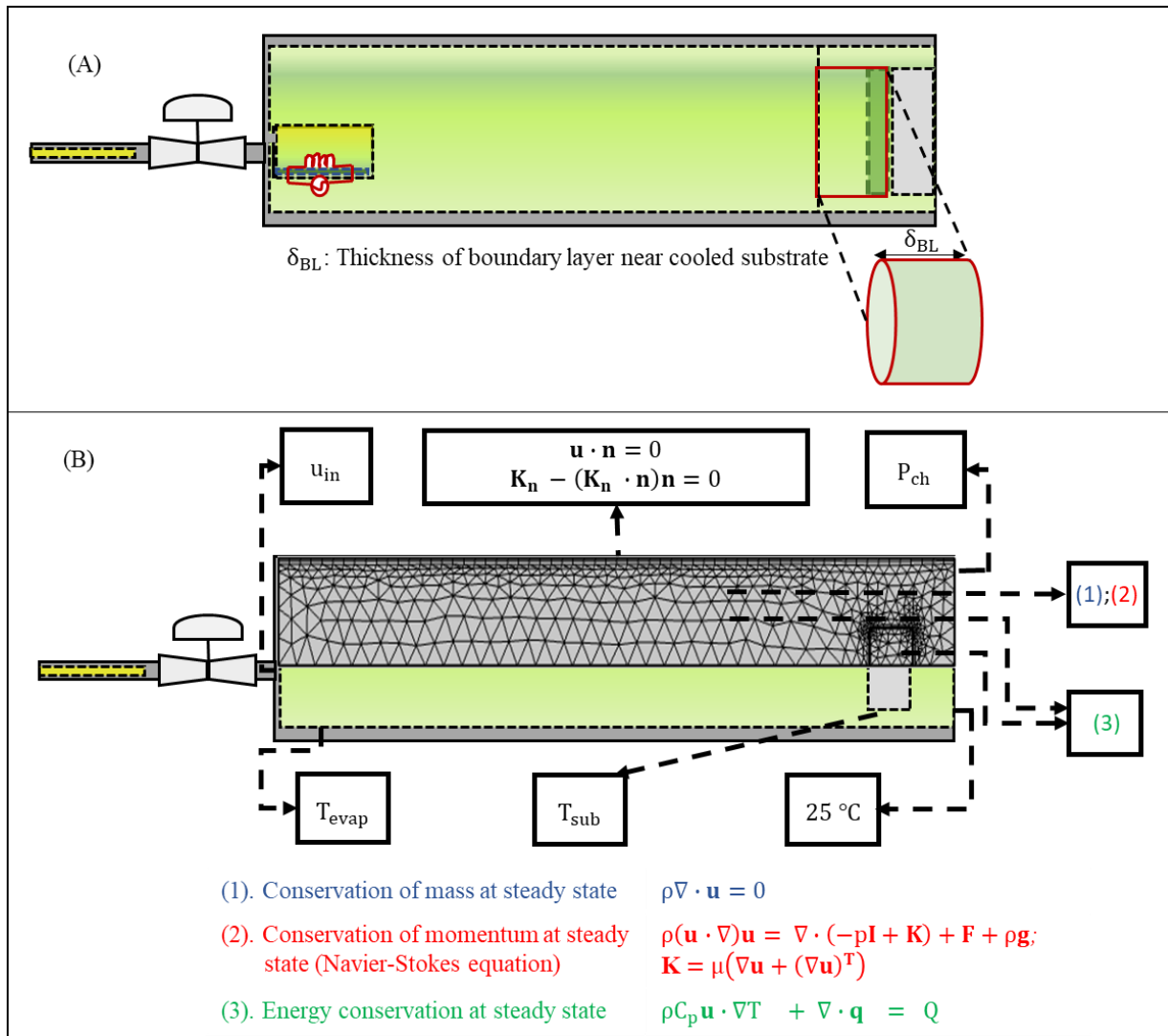
Figure 3.2: Schematic of OVPD with effective reactor volume near cooled substrate illustrated in 3.2 A, and physics and settings implemented on the domains and boundaries of the simulated system highlighted in 3.2B.
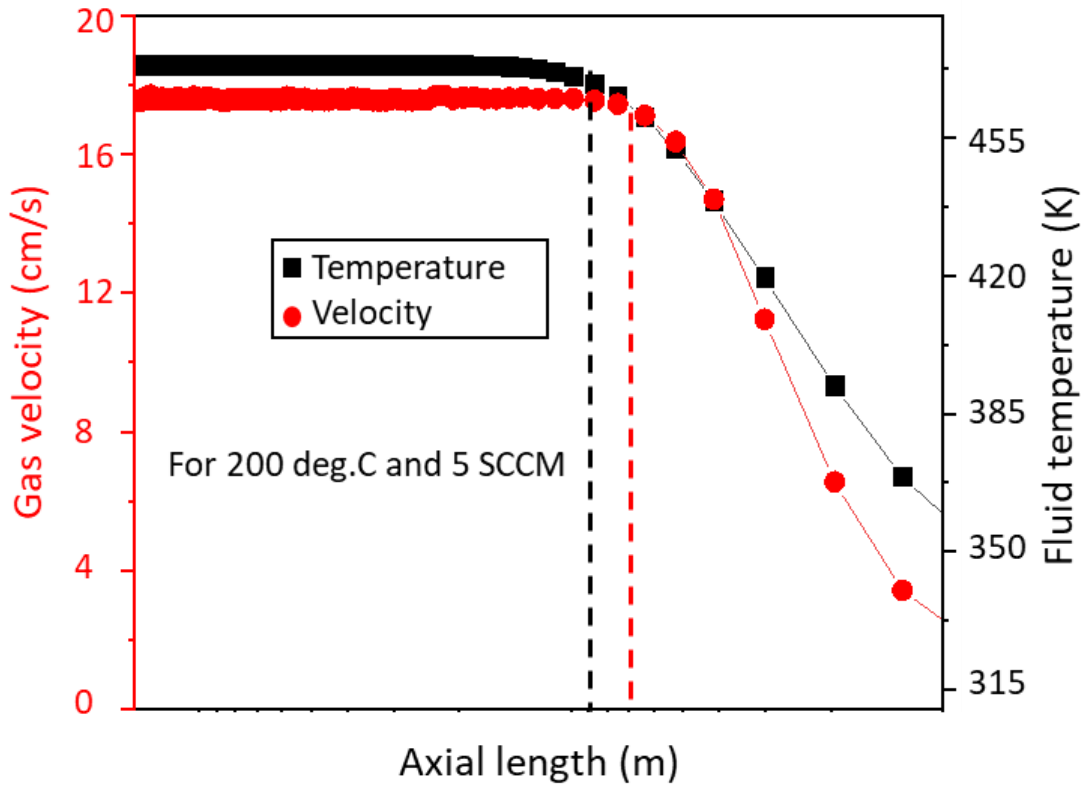
$$\delta_T: \frac{T-T_s}{T_\infty - T_s} = 0.99, \quad \delta_v: \frac{U}{U_\infty} = 0.99$$

$$\delta_T = 10cm, \qquad \delta_v = 7cm$$

Figure 3.3: Axial distribution of vapor temperature and velocity, with the dashed lines indicating thicknesses of the thermal boundary layer (δ_T) and hydrodynamic boundary layer (δ_v) near the cooled substrate held at temperature T_s. Mainstream temperature and velocity are symbolized as T_∞ and U_∞

Figure 3.4 shows the predicted material utilization efficiency and its dependence on substrate size at different evaporation temperatures and base pressures. The results in Figure 3.4 are for diffusion-limited regime, and they reveal two interesting trends.

Firstly, preferential deposition of film on the substrate, and not on the chamber wall is due to the existence of thermal boundary layer near the cooled substrate. Thus, the location of the thermal boundary layer dictates the area where preferential film deposition is realized.

Secondly, our results reveal that material utilization efficiency is majorly driven by the area ratio (substrate to chamber cross section) and depends insignificantly on evaporation temperatures and base pressures for this regime. MUE is predicted to be linearly correlated with area ratio (substrate to chamber cross section) with upper bound value of ~ 60% MUE expected for system configuration where exposed surface of the substrate is parallel to chamber cross section.

These theoretical results predicted from the model are also supported by experimental data (see Figure 3.5). The experimental testing was done by using values from Lunt, et al. [102] as well as experimental data obtained in this project. MUE model trend is experimentally tested by conducting OVPD experiment as described in the project methodology section of 3.4 while numerically testing is implemented by obtaining and visualizing dynamic flow behavior at different substrate size, thereby showing that the model introduced in this work can be used as basis for MUE maximization by increasing the exposed area for vapor condensation relative to the tube cross section. Therefore, it follows from the results presented in Figs. 3.4 and 3.5, that area ratio (substrate to tube cross-section) is the key driving variable influencing MUE in OVPD [108].
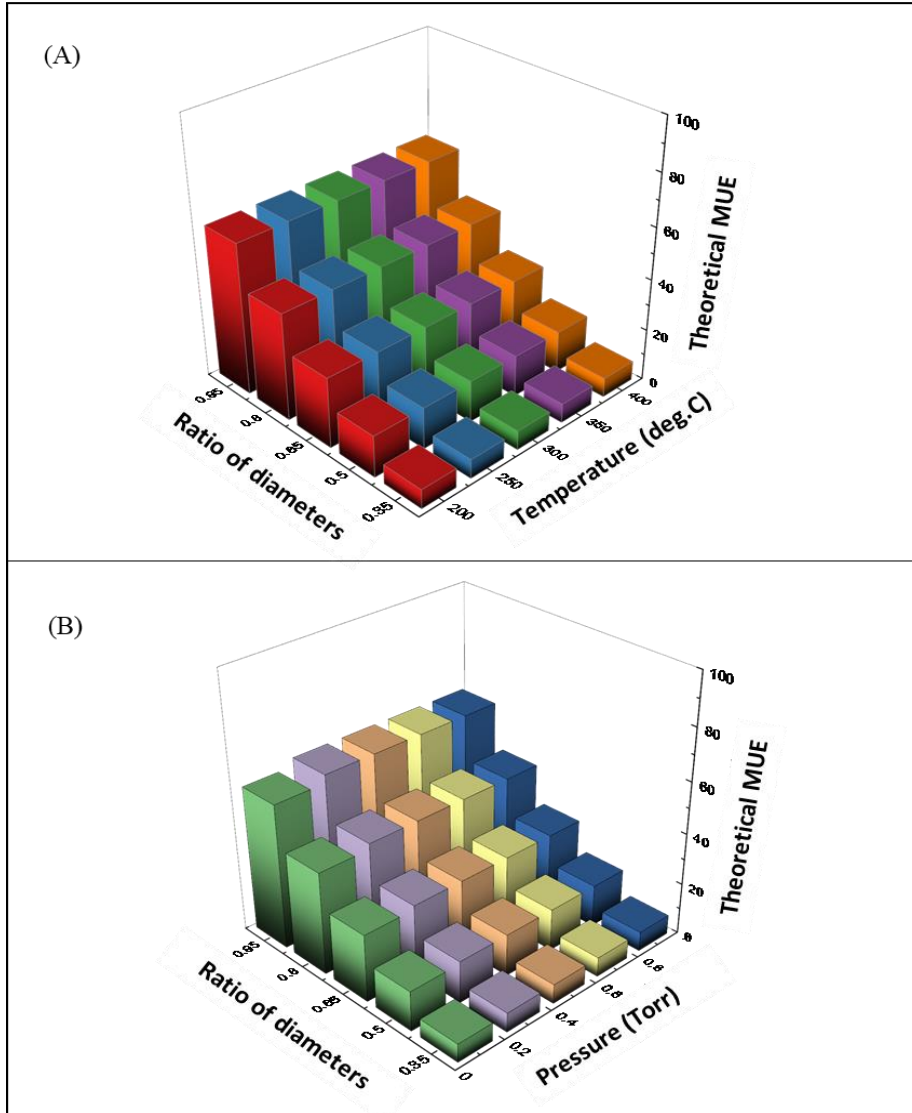
Figure 3.4: Theoretical material utilization efficiency dependence on substrate size at different evaporation temperature (3.4A; obtained at 5 SCCM and 0.1 Torr) and chamber pressure (3.4B; obtained at 5 SCCM and 200 deg. C) with substrate maintained at 15 deg. C. The size of substrate area relative to tube cross section is expressed as a ratio of diameters.

Experimental validation
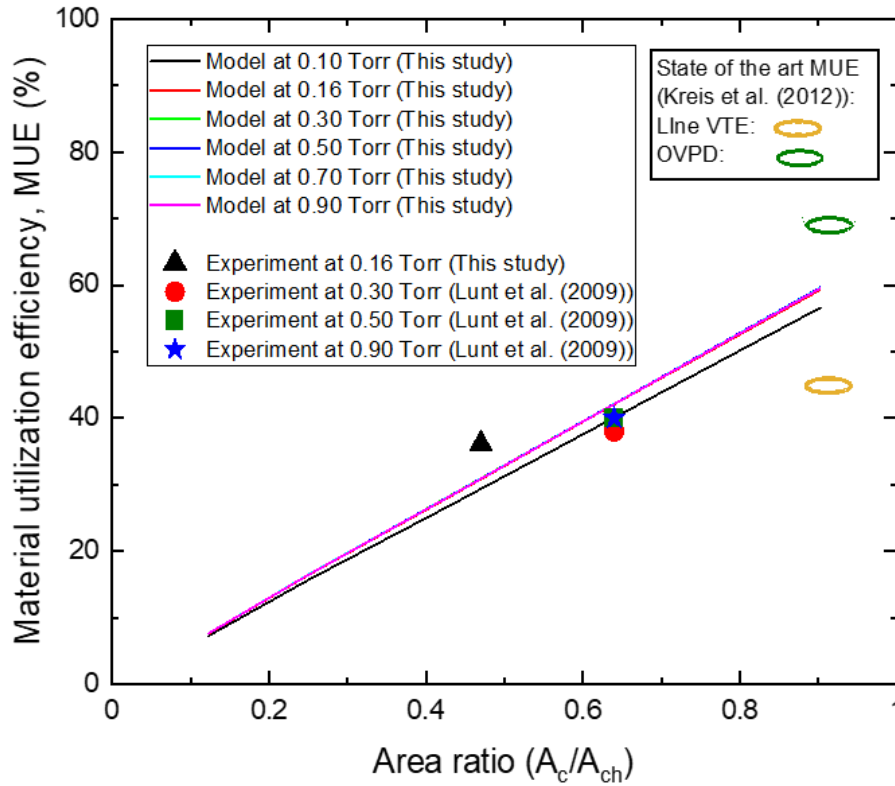
Figure 3.5: Comparison of predicted theoretical MUE with experimental values. Experiment value from the current study is obtained at 20 SCCM, 250 °C evaporation temperature with substrate of exposed area A_c maintained at 15 °C in a 10 cm diameter tube of cross-sectional area A_{ch}. Reported values are from Lunt et al. [102] . *Conditions for reported state of the art MUE are not revealed [109].

Based on the insights from the model and Figs. 3.4 and 3.5, the MUE can be maximized by increasing the area of substrate exposed to organic vapor flow. A practical means of realizing this configuration is by translating substrate over a roll-to-roll (R2R) unit in the OVPD chamber. By translating substrate in a R2R unit, higher MUE can be realized since organic vapor deposits both perpendicularly and coaxially on the substrate.

To obtain coaxial deposition, thermal boundary layer must be engineered to build coaxially on the substrate. To this end we designed and fabricated (See Figure 3.6) for experimental demonstration of tangential deposition.

The cold finger is a 12.5 cm x 3.8 cm aluminum block (See Figure 3.6 A and B) with two parallel channels for feed and return legs of the coolant line. We utilized a block of aluminum material to realize a stage that is light in weight, which also allows efficient heat transfer.

Figure 3.6C shows films of Alq3 deposited on the cold finger, which is realized by engineering the location of the thermal boundary layer as highlighted in the figure. For this strategy of tangential deposition to be practically useful, this coaxial deposition feature must be compatible and realizable on suitable substrates. Further, MUE obtained using this strategy must be quantifiable to measure process performance [108].
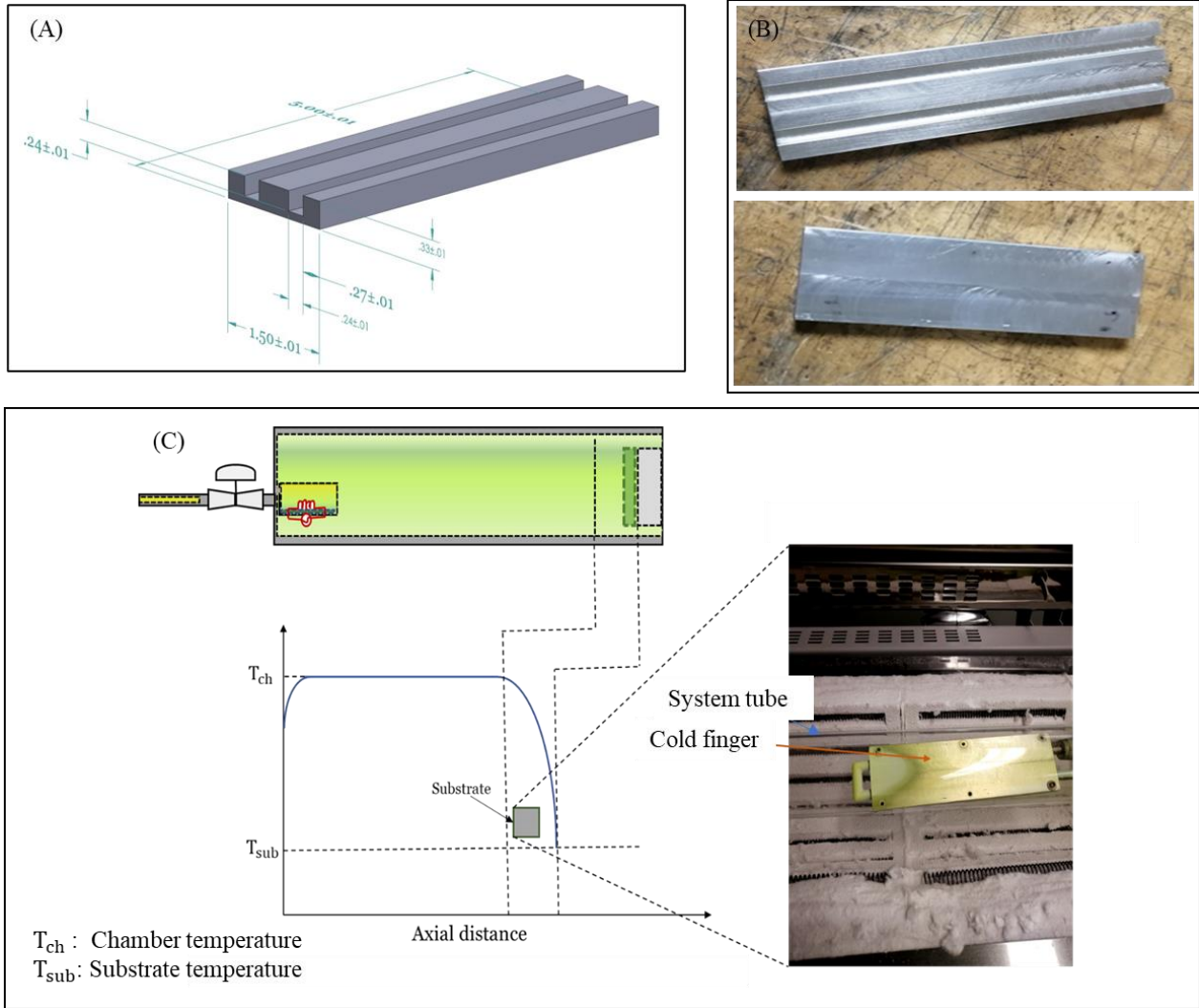
Figure 3.6: Designed (3.6A) and fabricated cold finger (3.6B) used in demonstrating tangential deposition experimentally realized from engineered thermal boundary layer (3.6C).

To measure MUE realized by this tangential deposition, we implement the procedures described in section 3.4. Solutions of known Alq3 concentrations in acetonitrile were prepared and analyzed using spectrophotometric technique at 380 nm wavelength (see Figure 3.7). Absorbance-concentration calibration curve obtained was then utilized to analyze solution obtained by

desorbing Alq3 film in acetonitrile, which enables determination of mass of film deposited and thus MUE.

Figure 3.7 shows the samples all have peak absorbance values at 380 nm with similar spectral shapes showing, with the peak absorbance value increasing with increase in Alq3 concentration. Thus, these results confirm acetonitrile as a suitable solvent for analyzing Alq3 powder and film.
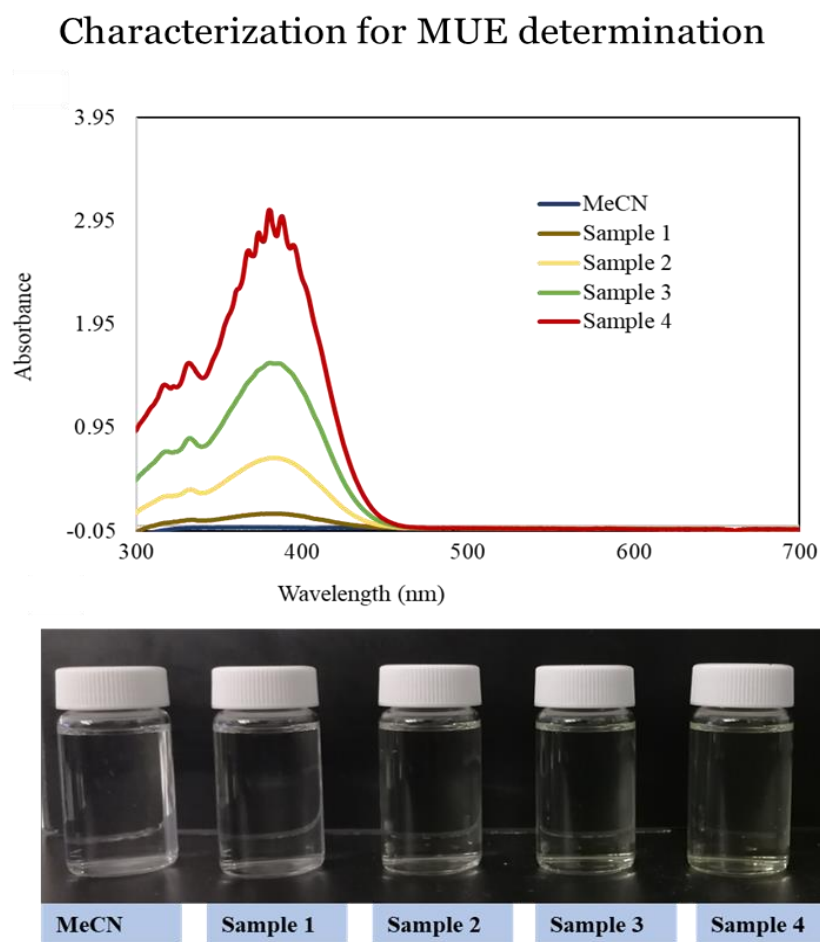
Figure 3.7: Spectrophotometric signals of AlQ_3 solutions of different concentrations used for determining mass of organic film deposited on tangential side of the substrate. Absorbance-concentration calibration curve was obtained at 380 nm wavelength.

Having demonstrated the ability to quantify the deposited film, we now show that this strategy of tangential deposition can be realized on useful substrates.

Figure 3.8 shows the experimental demonstration of tangential deposition by engineering location of thermal boundary layer (A) on useful substrates. The substrates utilized are silicon wafer (B) and (polyimide substrate (C).

This film growth realized by leveraging the engineered thermal boundary layer is demonstrated on both silicon wafer (Figure 3.8B) and polyimide (Figure 3.8C) substrates mounted on a 5 in x 1.5 in cooled finger with the exposed area of the substrate parallel to vapor flow. Corresponding experimental MUEs on these substrates were obtained by spectrophotometry (as described in section 3.4) by using a calibration curve obtained from standard samples of Alq3 in acetonitrile to realize experimental MUE of 9.07% and 11.27%, respectively. It is important to note that, while the studied parameters influence deposition and physical properties of the film, the original chemical functionality of the OVPD grown film is preserved as both the desorbed film and pure sample powder have peak signals at same wavelength after chemical characterization by spectrophotometric technique. Therefore, optimum system configuration can be identified using the insights from the model (Figs. 3.4 and 3.5) and these tangential experimental MUE results (Fig. 3.8), such that efficient film deposition can be realized on continuous basis on a roll-to-roll (R2R) system [108].

Figure 3.9 shows numerical demonstration of thermal boundary gradient near cooled stage realized by coupling cross-sectional and tangential depositions. Expanded view shows substrate translated on a roll-to-roll unit. By this demonstration of thermal boundary layer on a translated substrate, we have shown that continuous printing of organic films can be efficiently realized. Therefore, based on insights from the model (Figs. 3.4 and 3.5), tangential experimental MUE results (Figs. 3.8) and Fig. 3.9, we propose a system configuration (Figure 3.10) that can realize over 75% MUE [108]. The corresponding temperature profile for an OVPD process occurring in this system is also demonstrated in Figure 3.10.
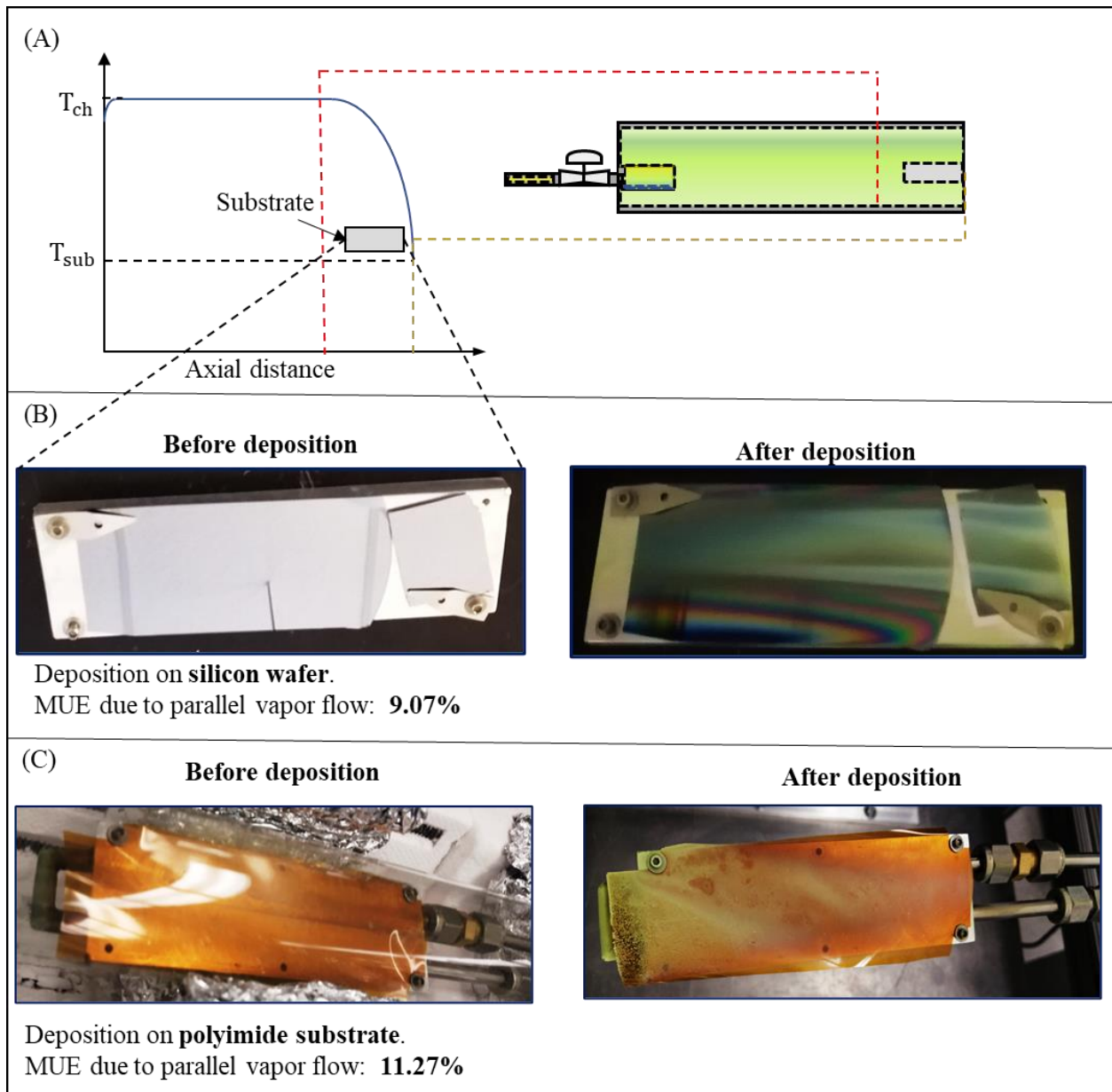
Figure 3.8: Leveraging the engineered thermal boundary layer (3.8A) to experimentally demonstrate tangential film deposition on silicon wafer substrate (3.8B) and on polyimide substrate (3.8C). Realized 10% MUE on each tangential side (with the trend from model results 3.4 and 3.5) demonstrate pathways for record > 75% MUE.
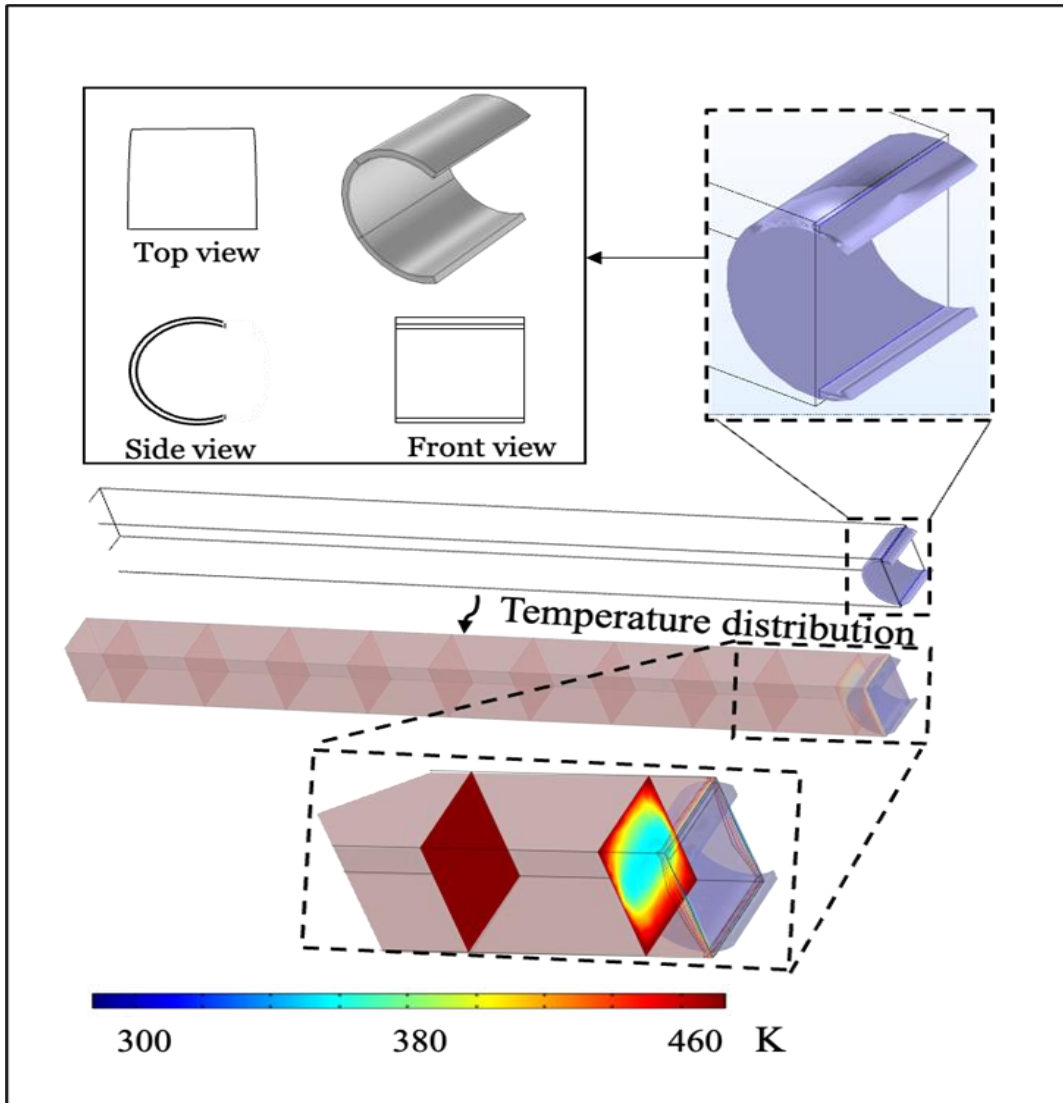
Figure 3.9: Numerical demonstration of thermal boundary gradient near cooled stage realized by coupling cross-sectional and tangential depositions. Expanded view shows substrate translated on a roll-to-roll unit.
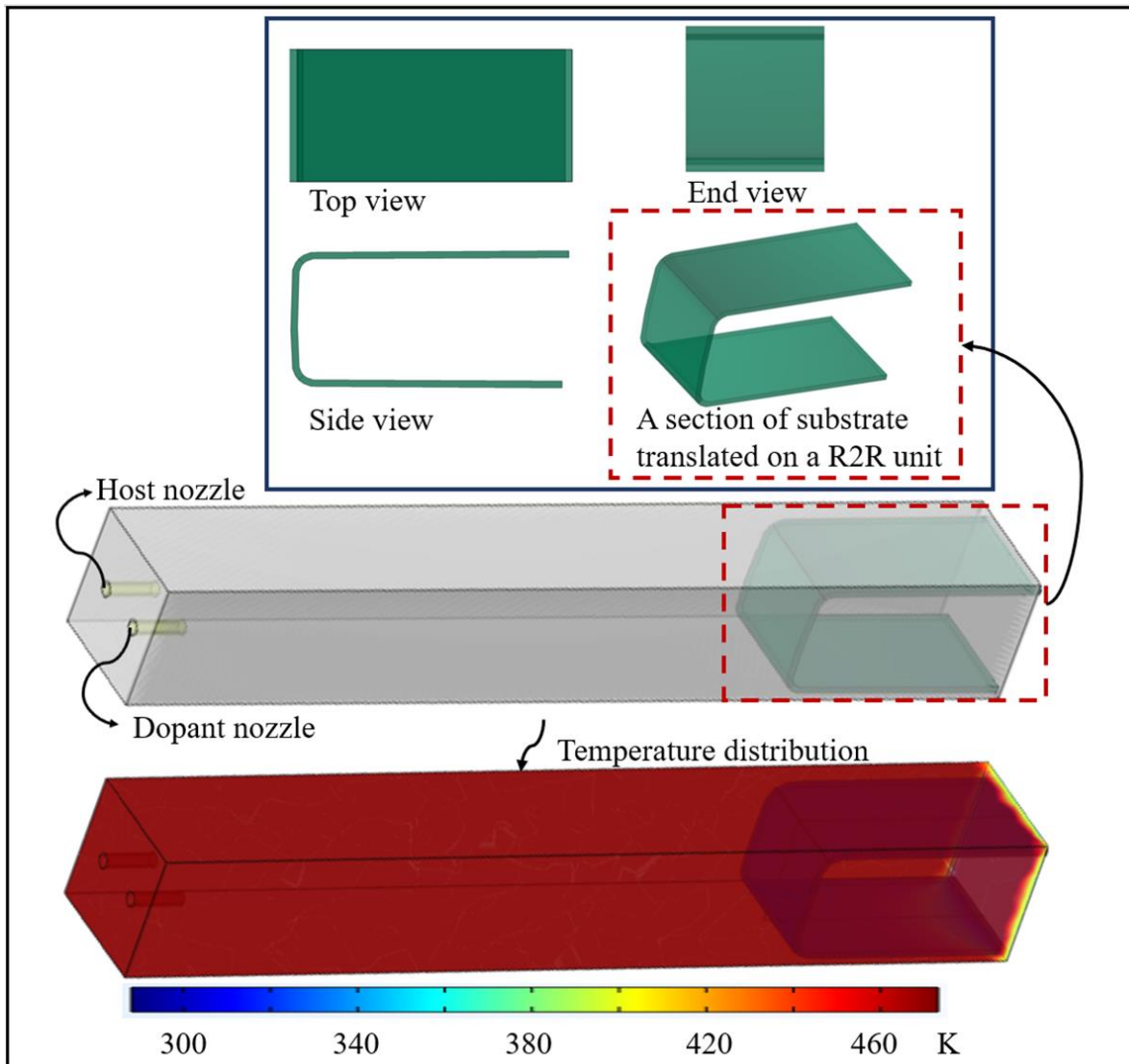
Figure 3.10: Proposed OVPD configuration that can deliver > 75 % MUE, with temperature

profiles demonstrating the existence of thermal boundary layer near the cooled substrate.

3.7 Conclusions

Material utilization efficiency is a critical economic metric that must be enhanced to facilitate wider adoption of organic vapor deposition, especially for manufacturing emerging tandem organic light emitting diodes (OLEDs) intended for general illumination. In this study, we apply a combination of first-principle physics, computational fluid dynamic (CFD) simulation, model development and experimentation to develop a pathway for boosting MUE beyond reported values.

We introduce a simple model that predicts material utilization efficiency in organic vapor phase deposition technique. Our numerically and experimentally supported results reveal area ratio (substrate to chamber cross section) as a key driving variable influencing material utilization efficiency. Further, by leveraging model insights, we show that by engineering location of the thermal boundary layer, organic vapor can deposit on additional planes of the substrate thereby further boosting MUE. This feature was demonstrated on practically useful substrates that can support both batch and continuous manufacturing modes.

Therefore, based on our findings, we propose system configuration that can deliver > 75% MUE. These findings reveal a clear pathway on how OVPD can be efficiently used to print thin film devices. The proposed system can also be used for other large-area applications where high MUE deposition of uniformly mixed vapors of small-molecular materials are desired.

Chapter 4 Analyses of Transport Mechanisms in Organic Vapor Phase Deposition for Material Mixing and Management of Substrate Heating

4.1 Preface:

This chapter is a moderately modified version of the original work published in the Journal of Materials Research and has been reproduced here with the permission of the copyright holder. First published in the Journal of Materials Research, 38, pages 2327–2338 (2023) by Springer Nature. Reproduced with permission from Springer Nature.

4.2 Abstract: Statement of Research Gaps, Hypothesis and Original Contribution

Low-pressure conditions in organic vapor phase deposition (OVPD) allow specie vapor to move with short mean free path thus allowing for decoupling of evaporation, transport and deposition. This process flexibility provides an opportunity for OVPD system to be engineered to realize effective mixing of active emissive organic and host materials. Also, the degree of material mixing influences film morphology and composition, which consequently influence device performance. Further, earlier works in OVPD have shown that evaporation temperature and stage temperature influence film deposition rate and morphology, with resulting tradeoffs as high deposition rate but high energy requirement at high evaporation temperature, and more uniform film but substrate heating and high energy requirement at high stage temperature. Development of hardware design method is crucial for scaling OVPD to realize effective material mixing. To meet this research goal, we hypothesize that if OVPD is adequately modeled, hardware aspect ratio needed to realize

effective vapor mixing can be predicted from vapor transport properties. To this end, we apply a combination of analytical and numerical techniques to investigate effects of process conditions, including evaporation temperature (200 – 400 °C), carrier gas flow rate (5 – 65 SCCM) on vapor transport, as well as synergistic effects of stage temperature (15 – 25 °C) and evaporation temperature (200 – 400 °C) on substrate heating. Our comparative studies on transport mechanisms show that for typical OVPD configuration, diffusion dominates convection at flow rate $\leq$ 5 SCCM while convection is the dominant mechanism at higher flow rates. We further analytically and numerically show that during co-deposition, hardware length needed for effective vapor mixing scales with gas flow rate. Also, our numerical study on synergistic effects of evaporation and stage temperatures on substrate heating reveals that thermal map indicating propensity for substrate heating is majorly controlled by evaporation temperature. Hence, the resultant recommendation is for films to be grown at the highest non-destructive substrate temperature and lowest evaporation temperature that meet target production rate. Therefore, based on these contributions, a scalable method for predicting hardware aspect ratio needed to realize effective vapor mixing was proposed as well as a numerical strategy for assessing likelihood of substrate for target process conditions.

4.3 Introduction and Motivation

In this section, we briefly reintroduce organic vapor phase deposition (OVPD) and discuss practical motivations for project 2, which is to analyze transport mechanisms in OVPD for effective vapor mixing and management of substrate heating.

Organic vapor phase deposition (OVPD), as an evaporation physical vapor depositions (PVD) technique, is attractive where high film deposition rate and simple operating procedures are desired. These two features also make the established PVD technique - vacuum thermal evaporation (VTE) also attractive since they allow convenient fast processing of thin film products. Further, both OVPD and VTE are capable of multilayer deposition with precise control of film thickness and deposition rate, but VTE is limited by suboptimal material utilization efficiency (MUE) and difficulty in creating uniform films over large area substrate. Since VTE system works by utilizing joule heating under hard vacuum (10^{-4} - 10^{-8} Torr) to vaporize source materials, vapors move with long mean free path before condensing on the substrate as thin film. While in OVPD, source materials are typically thermally vaporized in low-pressure (0.01 - 10 Torr) from source cells with carrier gas simultaneously fed through the source tube to support vapor transport towards a cooled substrate where they condense. Thus, in OVPD, vapors have shorter mean free path allowing for process flexibility to enhance MUE. Also, this shorter mean free path of material vapors allows for control in vapor flow direction as well as their mixing during transport.

This process flexibility due to short vapor mean free path and the use of carrier gas supported transport provides opportunity for OVPD system to be engineered to realize effective mixing of active emissive organic and host materials. In its simplest configuration, a length of transport zone will be required to achieve uniform mixing (e.g., by diffusion), in inverse proportion to the rate of carrier gas flow and pressure in the chamber. Downstream, the flow structure can be engineered to achieve uniform coating of the substrate, independent of the evaporation source geometry. Indeed, OVPD has shown controllable material doping [110], while film uniformity > 97.5 % over 200 mm diameter substrates has been shown at 50 % material utilization efficiency [102]. These

parameters are conducive to high speed of production; Qu and coworkers showed that a hybrid OVPD-VTE roll-to-roll system can be used to fabricate organic photovoltaic (OPV) cells on flexible substrates at high rates (e.g., up to 15 Å/s onto a substrate translated at 1.7 cm/s), and > 50 Å/s deposition rate was shown for organic layers for OLEDs [111]. Further, earlier works in OVPD have shown that evaporation temperature and stage temperature influence film deposition rate and morphology, with resulting tradeoffs as high deposition rate but high energy requirement at high evaporation temperature, and more uniform film but substrate heating and high energy requirement at high stage temperature.

Also, the degree of material mixing influences film morphology and composition. The former is affected by OVPD process conditions like evaporation temperature, carrier gas flow rate, chamber base pressure as well as material chemistry while the latter determines nature of deposited film, which consequently influence device performance. Thus, development of hardware design method is crucial for efficient scaling OVPD to realize effective vapor mixing. Therefore, in project 2, we analyze transport mechanisms in OVPD to numerically demonstrate a method for effective vapor mixing and management of substrate heating.

4.4 Chapter Objectives for Project 2 on Analyses of Transport Mechanisms in Organic Vapor Phase Deposition for Effective Material Mixing and Management of Substrate Heating

The research objectives of this project are summarized below:

- Analyze effects of process conditions on vapor transport of small molecular materials and

system temperatures on propensity for substrate heating during organic phase deposition

- Analytically and numerically demonstrate a method for achieving effective vapor mixing for different process conditions.

- Propose scalable method for predicting hardware aspect ratio need to realize effective vapor mixing during co-deposition in organic vapor phase deposition.

4.5 Methodology

The OVPD process involves 3 main stages: 1) evaporation of active material(s), 2) carrier-gas supported transport of the vapor, and 3) deposition onto a cooled substrate. For project 2 on scalable hardware design for effective vapor mixing and substrate heating, we focus on stages 2 and 3. We utilize a combination of first-principle physics, theoretical analyses and numerical modeling for this purpose.

Emissive layers for organic light emitting diodes typically comprise two or more molecular species, requiring mixing of vapor streams from multiple sources. Further, the nature and composition of film affect OLED device. The morphology of this deposited film is also affected by substrate temperature. Thus, effective mixing of vapor streams and management of substrate heating will ultimately translate to devices of improved performance. To this end, as project 2, we analyze vapor transport in OVPD to identify conditions that will result in effective mixing. We further numerically validate these analytical results and propose conditions for better management of substrate heating.

To better understand OVPD process and numerically test analytical results, we adopt a 2D-axisymmetric simulation geometry with a 10 cm diameter substrate, 150 cm long chamber [88, 106] to model the OVPD process, which mimics the geometry of a convenient experimental deposition chamber and heater configuration; upon validation of the model, it can be extended to non-axisymmetric geometries. At steady-state, laminar flow is typically observed (Re < 500) with heat and mass transfer dominated by diffusion of molecular species.

As justified in section 3.4 continuum fluid mechanics is expected in OVPD, such that conservation of momentum is modeled by Navier-Stokes (Eq. 4.1) and energy conservation is Eq. 4.2. It is important to state that, while the Navier-Stokes Equations are commonly used to model viscous liquid flow processes [104, 105], they are also appropriate for modeling gaseous and vapor flow processes where the operating conditions justify the continuum assumptions, especially at high temperatures and low pressures where their viscosities are enhanced.

$$\rho(\mathbf{u} \cdot \nabla)\mathbf{u} = \nabla \cdot (-p\mathbf{I} + \mathbf{K}) + \mathbf{F} + \rho\mathbf{g} \qquad\qquad 4.1$$

$$\rho C_p \mathbf{u} \cdot \nabla T \;\; + \nabla \cdot \mathbf{q} \;\; = \;\; Q \qquad\qquad 4.2$$

where ρ is fluid density, C_p, heat capacity at constant pressure, and T, absolute temperature. Bold letters denote vector quantities where $\mathbf{u}$, velocity vector, $\mathbf{q}$ is heat flux due to conduction. Q is heat input rate from other heat sources, $\mathbf{F}$ is volume force vector, $\mathbf{K}$ vector accounting for constitutive relation between conservation of mass and momentum. We used COMSOL Multiphysics® (COMSOL 5.5) to solve the above Equations using settings and boundary conditions highlighted in section 3.4.

Deposition system configurations typically involve an axisymmetric flow chamber whose length is greater than its cross-section, allowing for adequate mixing of organic vapor streams in the transport zone *en route* to the substrate. This axial distance required for effective mixing of host and dopant vapor streams is hereafter termed Z_{mix}.

We hypothesize that Z_{mix} is the axial distance along the chamber where the lateral spread of the vapor $(= \sqrt{6D_i \tau}) \geq D$, the chamber diameter and τ is the time required to transport the vapors downstream. D_i $(= \frac{\bar{v}\bar{l}}{3})$ is the mass diffusivity of organic species where $\bar{v}$ and $\bar{l}$ are molecular speed and mean free path of the gas, respectively. When convection dominates diffusion, τ is obtained using average velocity, $< U >$; $\tau = \frac{Z_{mix}}{<U>}$. Otherwise transport time is determined from kinetic theory using $\tau = \frac{PMZ_{mix}^2}{2\mu RT}$. Where μ and M are viscosity and molecular weight of the species while P and T are chamber pressure and temperature. Using these parameters, we investigate the effects of process conditions on vapor mixing by identifying dominant mechanism and corresponding Z_{mix} values for different carrier gas flow rates (5 – 65 SCCM) and evaporation temperature (200 – 400 °C). Afterwards, we numerically validate the results by visualizing flow distributions from host and dopant nozzles. We further numerically investigate the synergistic effects of stage temperature (5 - 25 °C) and evaporation temperatures (200 - 400 °C) on substrate heating.

4.6 Results and Discussion

The composition and morphology of deposited film are important factors that influence device performance. These factors are respectively affected by the degree of mixing achieved between

vapor streams as illustrated in Figure 4.1. Further, the degree of vapor mixing is influenced by vapor transport mechanisms, which are determined by the operating process conditions. We therefore model OVPD using computational fluid dynamic simulation, investigating effects of process conditions on vapor transport mechanisms.

Film composition and morphology

Host/dopant

Device performance.

Drive voltage and EQE
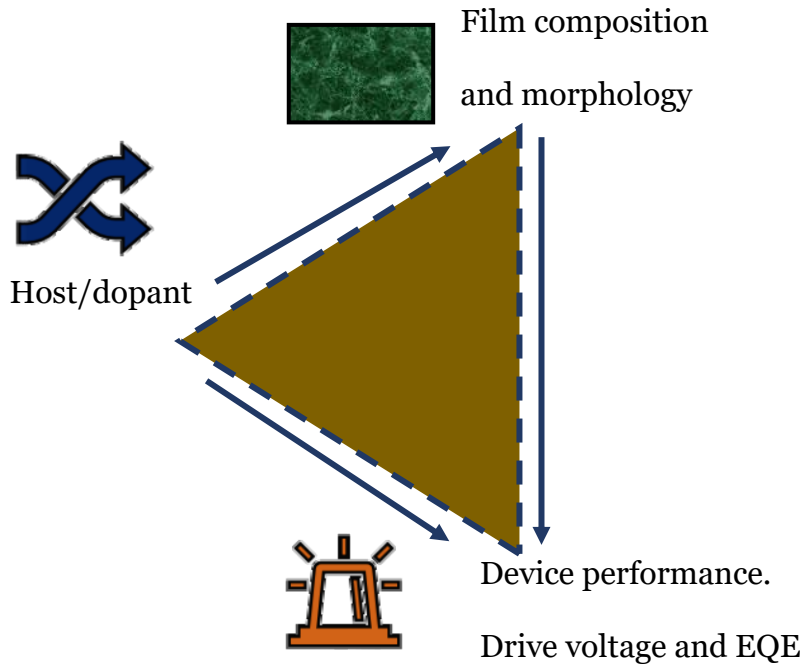
Figure 4.1: Schematic illustrating dependence of device performance on film composition and morphology, and their dependence of vapor mixing.

As discussed in section 4.4, occurrence of molecular flow is not expected since molecular mean free path (mfp) of gases at OVPD condition is far less than diameter of the deposition chamber for pressure $0.01 - < 760$ Torr (This is demonstrated for thirty OLED materials, refer to section 4.7 of Appendices). Flow in the chamber is then by both convection and concentration-driven diffusion.

We numerically investigate how diffusion and convection transport mechanisms compare with each other as well as how they are affected by OVPD process conditions.

Figure 4.2 shows steady state profiles of gas temperature (A) and velocity (B) with axial distributions of these properties along the central axis plotted in Figure 4.2 (C and D). These axial distributions are for different carrier gas flow rates at 200°C evaporation temperature and for different temperatures at 5 SCCM carrier gas flow rate. Expectedly, the results (Figure 4.2 (C and D)) show increase gas temperature and velocity with evaporation temperature and carrier gas flow rate, respectively.

Further, Figure 4.2 shows uniform gas temperature upstream and significant temperature gradient near the substrate. The latter is due to the thermal boundary layer that builds near the cooled substrate, which is responsible for film deposition.

Unlike the trend observed for fluid temperature, magnitude of vapor velocity decreases radially with maximum values along the central axis and minimums along the chamber walls. Nevertheless, the vapors experience significant reduction near the substrate. This reduction in velocity near the substrate indicates the existence of hydrodynamic boundary layer. Therefore, in OVPD conditions and system, both thermal and hydrodynamic boundary layers build near the cooled substrate. For the system configuration and conditions used in this study, the thickness of hydrodynamic boundary layer, δ_h is found to be 7 cm, which is less than that of thermal boundary layer, $\delta_T = 10$ cm. Interestingly, gas velocity is found to be highest aspherical the edges of the substrate. This peak velocity aspherical the edges is attributed to sharp reduction in cross-sectional area where

flow occurs. Indeed, from the continuity equation, an increase in flow velocity is expected when the size of section perpendicular to flow direction is reduced.

It is important to state that source nozzle configuration can impact flow velocity as well as gas temperature. Figure 4.2 shows numerical results demonstrating this trend at @ 200 °C, 0.1 Torr and 5 SCCM. The results show that source configuration impacts gas velocity more than temperature. For the effect on the former, when source configuration is accounted for, a sharper peak in flow velocity is observed at the exit point of the nozzle before steady decline of flow velocity downstream. Nevertheless, source configuration is found to have somewhat minor effect on distribution of gas temperature with rate of decline in gas temperature downstream as the notable distinction between the systems (system A: source configuration accounted for and system B: source configuration not accounted for).
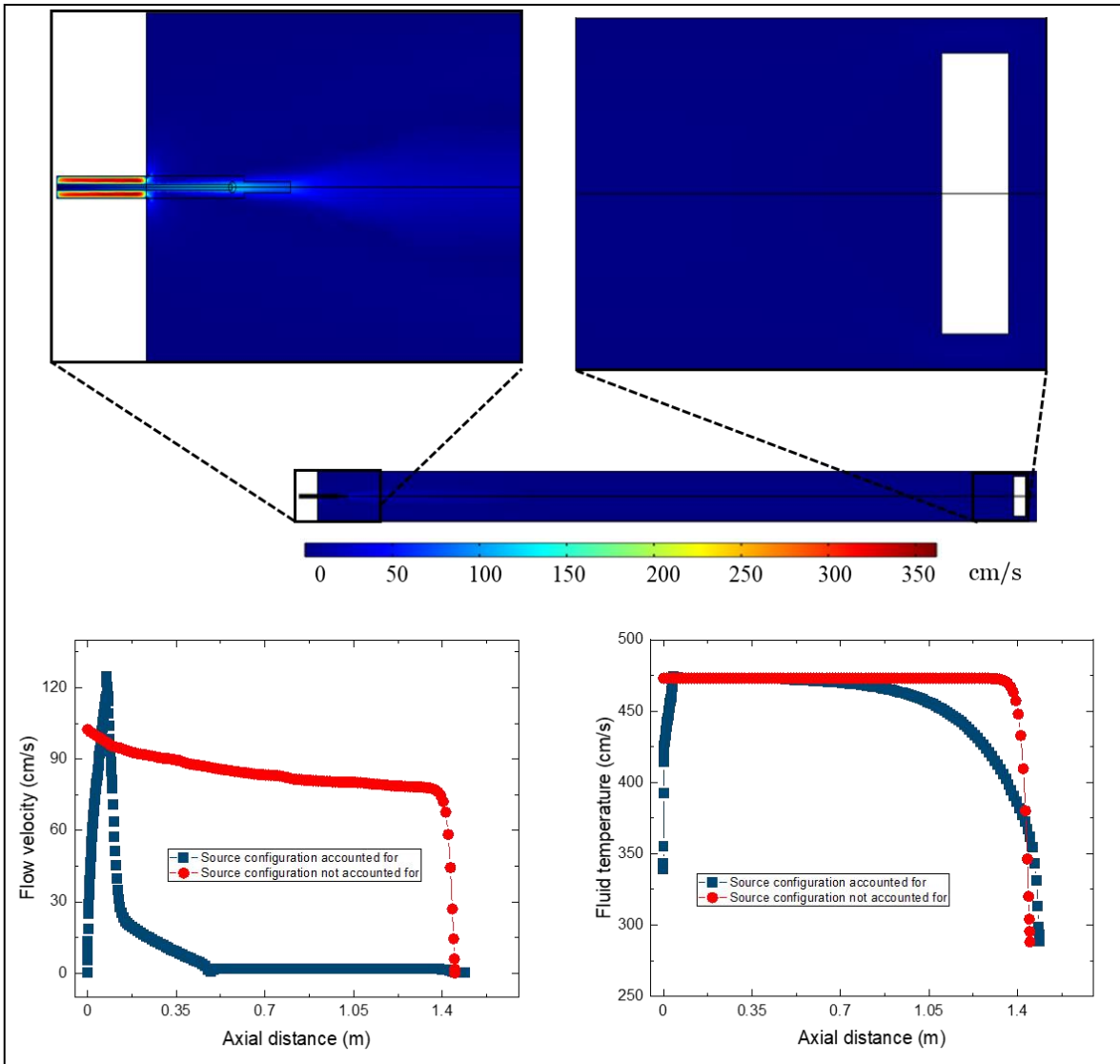
Figure 4.2: Visualizing vapor flow from source nozzle, and effects of nozzle configuration of flow velocity and fluid temperature @ 200 °C, 0.1 Torr and 5 SCCM (≡ 128 cm/s inlet velocity) Data obtained from central axis.
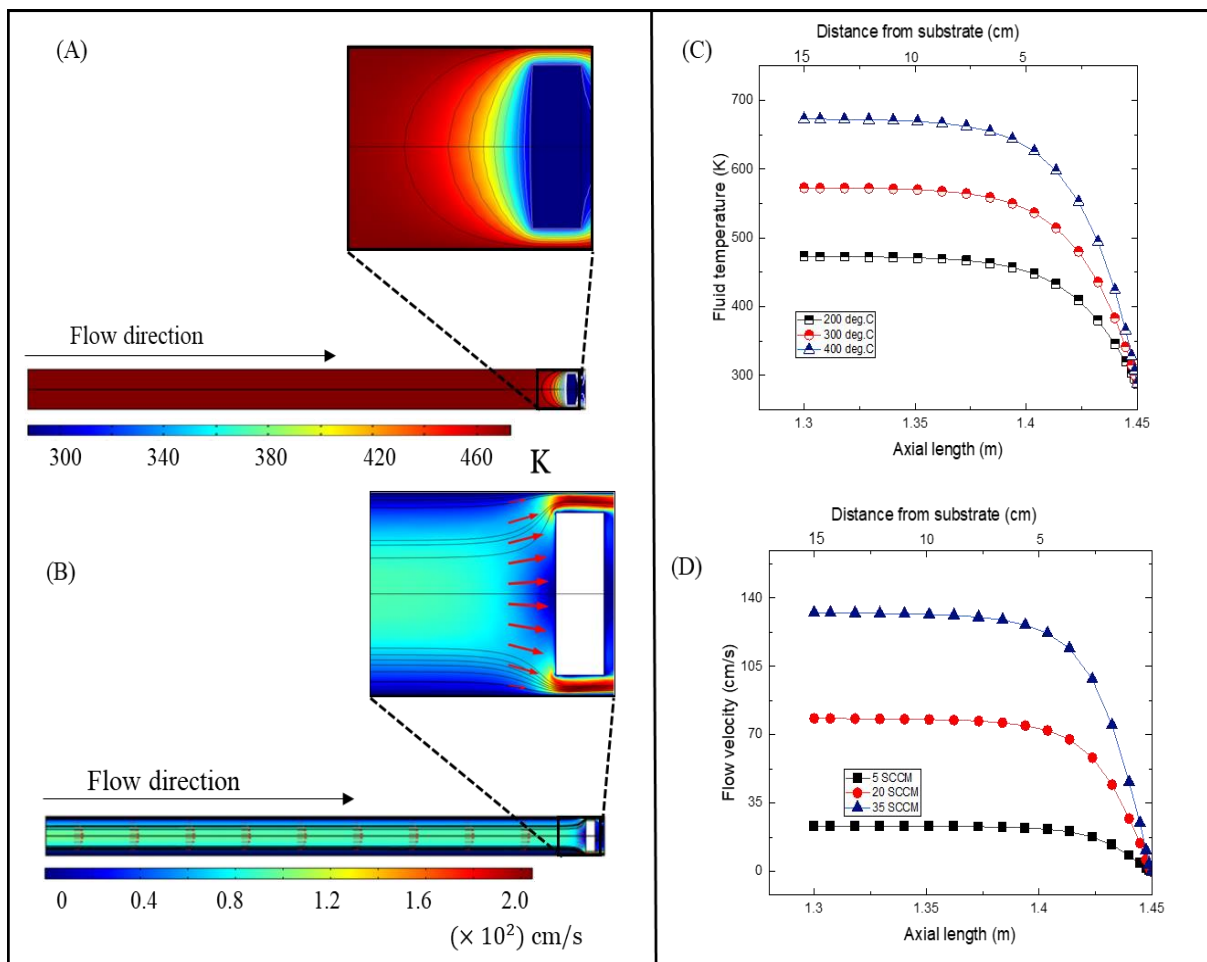
Figure 4.3: Steady state profile of temperature (A) and gas velocity (B). Axial distributions of (C) fluid temperature and (D) flow velocity for different evaporation temperatures and carrier gas flow rates, respectively. For different carrier gas flow rates, evaporation temperature is 200°C (D) while for different evaporation temperatures, carrier gas flow rate is 5 SCCM (C).

These numerical results are needed as inputs for identifying the dominant transport mechanisms, which in turn influence the degree of mixing achievable between organic vapor streams during co-deposition. For this purpose, we assess both mechanisms by determining their transport times, such that the one having shorter transport time dominates since organic vapors would be traveling the fastest by this mode.

Figure 4.4 shows the dependence of minimum axial distance for uniform vapor mixing by interdiffusion (uniform lateral spread), Z_{mix} on different process conditions. These conditions include substrate (8.0cm in diameter) maintained at 15°C in an 10cm diameter OVPD chamber for different evaporation temperatures (200-400 °C) and carrier gas flow rates (5 – 65 SCCM).

This axial distance required for effective mixing of host and dopant vapor streams is hereafter termed Z_{mix}. We hypothesize that Z_{mix} is the axial distance along the chamber where the lateral spread of the vapor $(= \sqrt{6D_i\tau}) \geq D$, the chamber diameter and τ is the time required to transport the vapors downstream. D_i $(= \frac{\bar{v}\bar{l}}{3})$ is the mass diffusivity of organic species where $\bar{v}$ and $\bar{l}$ are molecular speed and mean free path of the gas, respectively. When convection dominates diffusion, τ is obtained using average velocity, $< U >$; $\tau = \frac{Z_{mix}}{<U>}$. Otherwise transport time is determined from kinetic theory using $\tau = \frac{PMZ_{mix}^2}{2\mu RT}$. Where μ and M are viscosity and molecular weight of the species while P and T are chamber pressure and temperature. Using these parameters, we investigate the effects of process conditions on vapor mixing by identifying dominant mechanism and corresponding Z_{mix} values for different carrier gas flow rates (5 – 65 SCCM) and evaporation temperature (200 – 400 °C).

Figure 4.4: Minimum axial distance for uniform vapor mixing by interdiffusion (uniform lateral spread), Z_{mix} at different conditions. Substrate (8.0cm in diameter) is maintained at 15℃ in an 10cm diameter OVPD chamber. Peclet number for mass transfer and ratio of lateral spread width to chamber diameter are mean values obtained for 200-400 ℃ evaporation temperatures. Standard

deviations (not shown) are small (≤ 0.80 for Peclet number and ≤ 0.02 for the ratio). The values of the ratio above red dashed lines indicate that uniform mixing is obtainable at the corresponding conditions. Blue stars show increasing Peclet number for mass transfer with flow rate indicating decreasing dominance of diffusion at the corresponding conditions. Schematic (insert) illustrates regions for vapor mixing and boundary layer near cooled substrate.

We further assess the relative contributions of diffusion and convection using the Peclet number for mass transfer and theoretically assess vapor mixing by determining ratio of lateral spread width to chamber diameter. Further, the corresponding times organic vapors need to traverse this Z_{mix} distance by diffusion and convection mechanisms are plotted in Figure 4.5 and Figure 4.6, respectively.
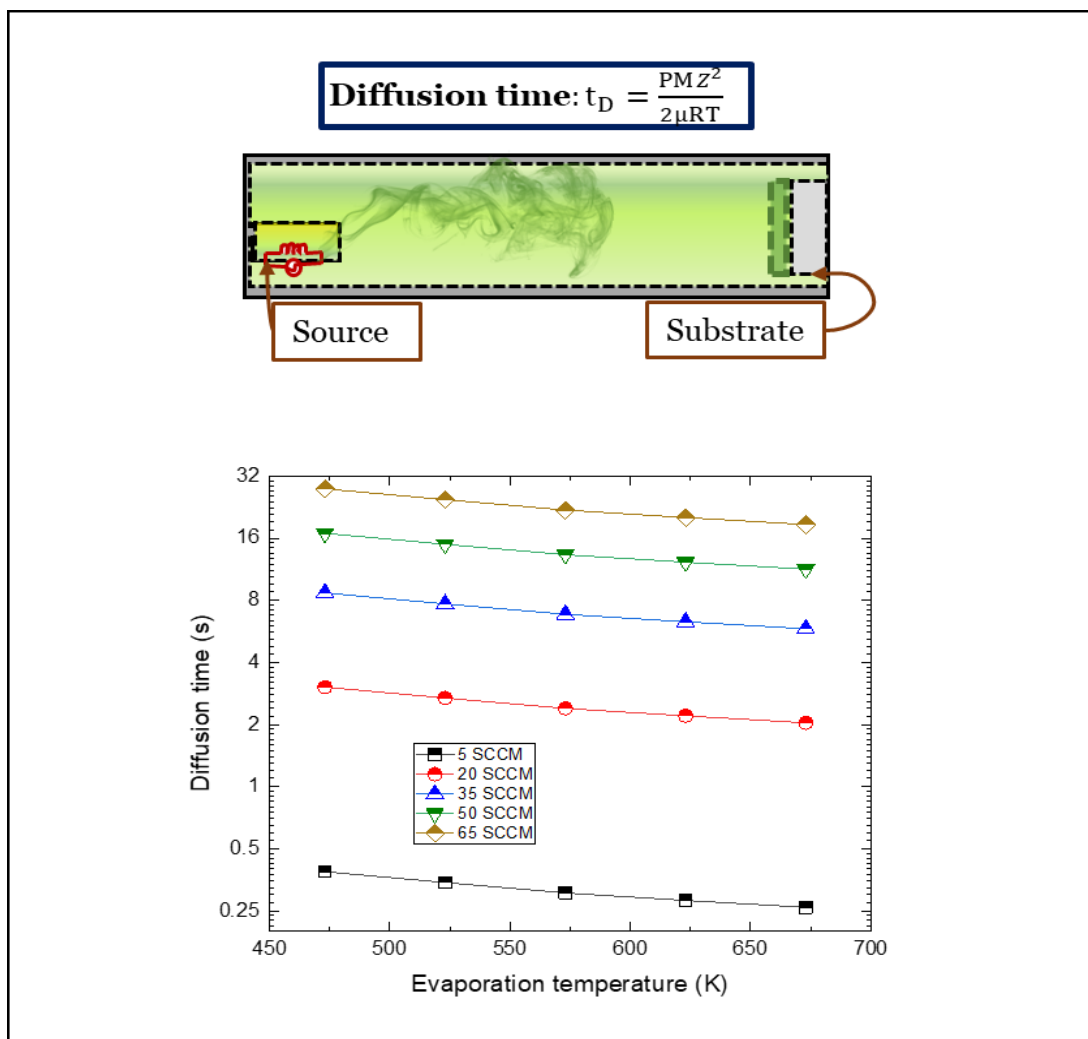
Figure 4.5: Times for uniform lateral spread of vapor to be achieved by diffusion mechanism at different carrier gas flow rates and evaporation temperatures. Substrate (8.0cm in diameter) is maintained at 15℃ in an 10cm diameter OVPD chamber. Schematic (insert) illustrates vapor transport from source boat to substrate by diffusion mechanism. Diffusion time calculated using the indicated Eq., where μ is viscosity, P is chamber base pressure, T, evaporation temperature, M, molecular weight of organic species, Z, axial distance for uniform vapor mixing, and R, the gas constant.
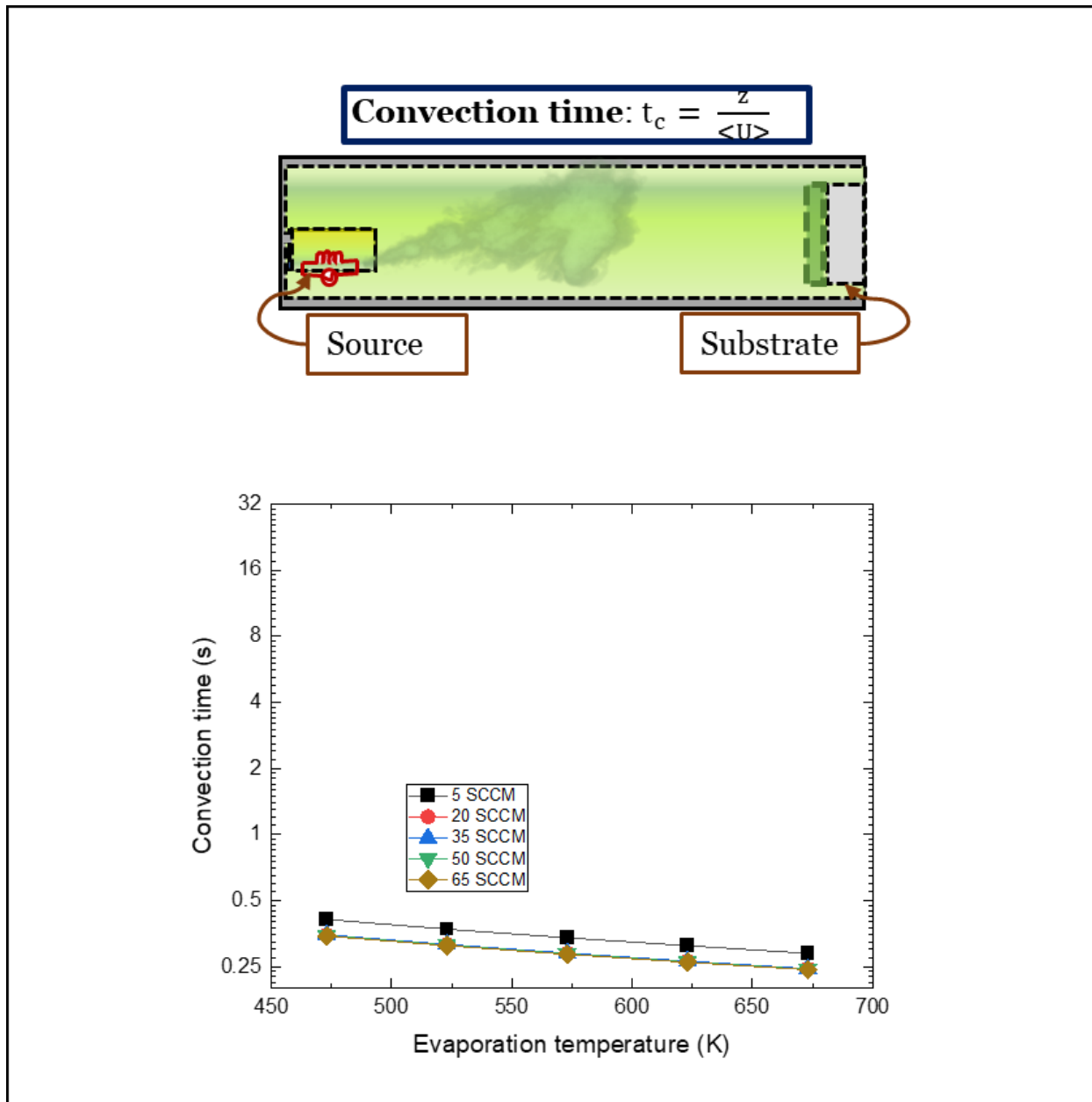
Figure 4.6: Times for uniform lateral spread of vapor to be achieved by convection mechanism at different carrier gas flow rates and evaporation temperatures. Substrate (8.0cm in diameter) is maintained at 15℃ in an 10cm diameter OVPD chamber. Schematic (insert) illustrates vapor transport from source boat to substrate by convection mechanism. Convection time calculated

using the indicated Eq., where <U> is average velocity, and z, axial distance for uniform vapor mixing.

These results illustrate effects of operating evaporation temperature (200 - 400 °C) and carrier gas flow rate (5 – 65 SCCM) on axial distance for interdiffusion, Z_{mix} (Figure 4.4) and associated travel times due to diffusion (Figure 4.5) and convection (Figure 4.6). The analysis approach is detailed in the materials and methods section. Z_{mix} is found to increase from 7.5 cm at 5 SCCM to 63.5 cm at 65 SCCM, indicating that a higher flow rate necessitates a longer mixing length. Further, effectiveness of material mixing at these Z_{mix} values is corroborated by assessing the ratio of vapor lateral spread to chamber diameter (see dashed line of Fig. 4.4) and Peclet number for mass transfer. The dominant mechanism by which organic species intermix at different conditions is ascertained by comparing the transport time for diffusion (Fig. 4.5) and convection (Fig. 4.6), which shows that for all operating temperatures, over a transport distance of Z_{mix}, diffusion dominates at flow rate ≤ 5 SCCM while convection is the prevalent mechanism at higher flow rates (≥ 20 SCCM). Indeed, this trend is corroborated by the increasing value of Peclet number (Pe) for mass transfer (see Fig. 4.4), and it's consistent for different temperatures as supported by their similar Pe values with ≤ 0.80 standard deviation.

Further, for both diffusion and convection, transport times decrease with increase in evaporation temperature showing that higher vapor temperatures improve the kinetic energy of organic molecules, which result in faster transport. On the contrary, carrier gas flow rate has dissimilar effects on the two transport times. Figure 4.5 shows that as flow rate increases, more diffusion time is needed for organic species to travel Z_{mix} distance with the values ranging from 0.3 seconds

at 5 SCCM to 27 seconds at 65 SCCM. This increase in diffusion time is due to the longer axial distance needed for organic molecules to intermix at higher flowrates without any increase in diffusion coefficient. However, as illustrated in Fig. 4.6, flow rate has negligible effects on convection time as values at 5 SCCM and higher flowrates are within the same order of magnitude. This non-dependence of convection time on flow rate is because when the latter increases, bulk flow of organic vapor is proportionally enhanced thereby compensating for longer reactor length needed for interdiffusion.

Also, the predicted Z_{mix} values are numerically validated with Figure 4.7 showing the simulation results for visualizing material mixing. Indeed, increase in Z_{mix} with flow rate predicted in Fig. 4.4 is excellently validated by the mixing profiles of Figure 4.7. Therefore, in terms of practical benefits, this presented method can be used to predetermine hardware aspect ratio needed to achieve effective vapor mixing at target production conditions.
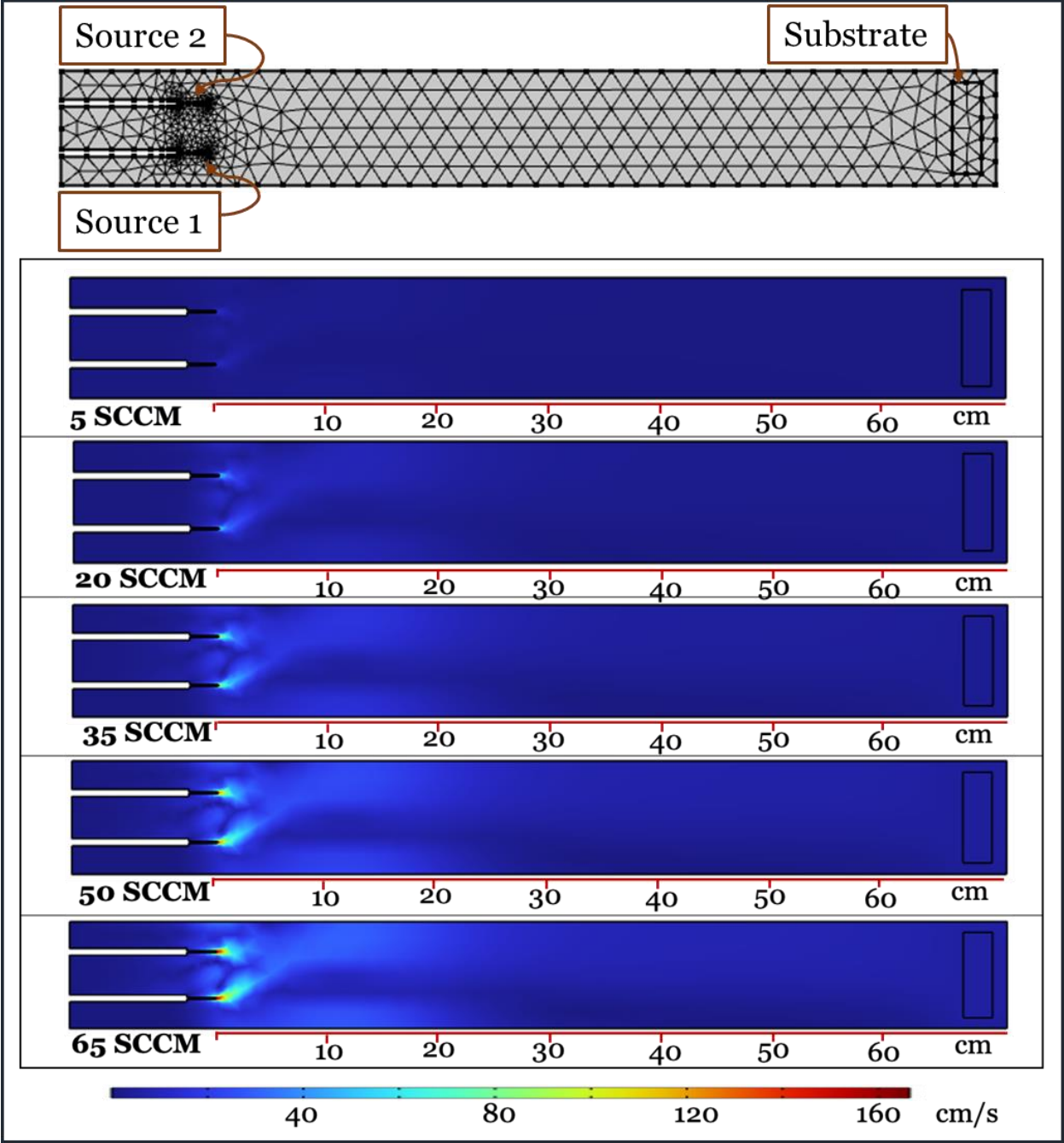
Figure 4.7: Numerical validation of vapor mixing at different conditions (5 – 65 SCCM). Substrate (8.0cm in diameter) is maintained at 15°C in a 10cm diameter OVPD chamber at 0.1 Torr base pressure.

We further show that by leveraging the understanding of process conditions, a higher evaporation rate can be achieved. Figure 4.8 shows experimental results on effects of chamber base pressure on sublimation kinetic of organic vapor. As shown in the figure, a 10X increase in sublimation rate can be achieved by switching from atmospheric sublimation to vacuum sublimation. Specifically at 20 SCCM carrier gas flow rate and 250 °C evaporation temperature, triplicate results obtained at atmospheric pressures of 739, 750 and 764 Torrs have average sublimation rate of 0.008 ± 0.005 mg/min while corresponding triplicate results at low pressure of 4.69, 5.15 and 5.22 Torrs yielded a 10X increase in sublimation rate (0.090 ± 0.030 mg/min). Therefore, in terms of practical benefits, chamber base pressure is another convenient process variable that can be optimized to boost sublimation rate, and subsequently film production rate.
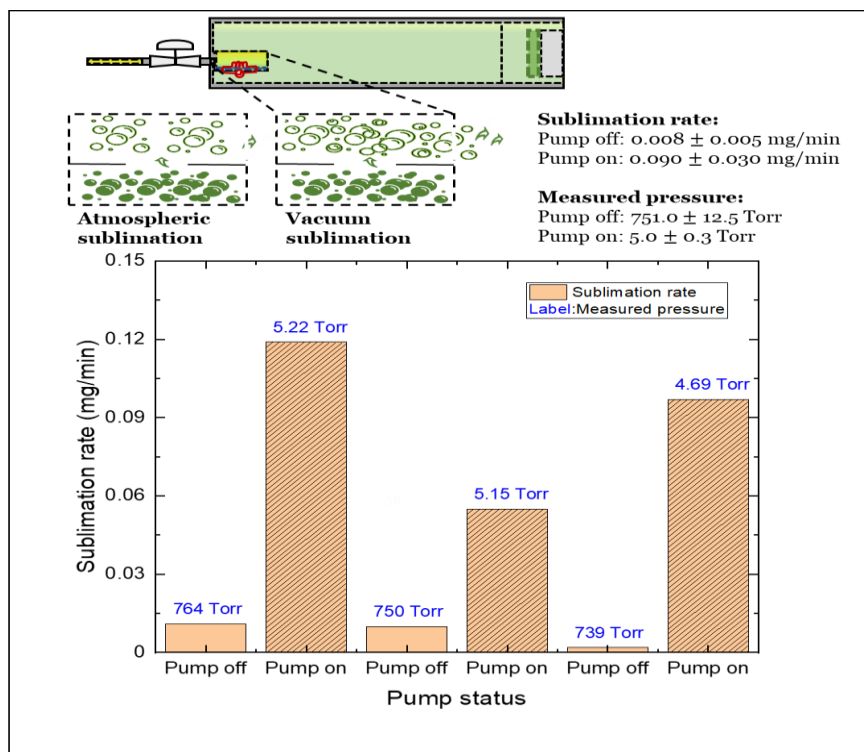
Figure 4.8: Leveraging pressure effect on vapor kinetics to demonstrate 10X increase in sublimation rate in OVPD chamber @ 20 SCCM carrier gas flow rate and 250 °C.

Having demonstrated how hardware aspect ratio can be designed for different operating conditions, we now numerically investigate how stage and evaporation temperatures influence substrate heating.

Figure 4.9 shows effects of substrate temperatures (5 – 25 °C) and evaporation temperatures (200 - 400 °C) on thermal profiles near cooled substrate translated on a R2R unit. The visualizations in Fig. 4.9 reveal thermal maps on the substrate during deposition, indicating propensity of substrate heating and film stress distribution. As shown in Fig. 4.9, at a given substrate temperature, uniformity of thermal distribution on the substrate decreases with evaporation temperature, thereby showing increasing susceptibility of substrate to thermal stress and non-uniformity of film morphology.

Further, Figure 4.9 shows that, at a given evaporation temperature, thermal map of substrate translated on a R2R unit shows little dependence on stage temperature. Thus, the resultant recommendation from the results in Fig. 4.9 is to grow film at highest substrate temperature (without thermally degrading the substrate) and lowest evaporation temperature that meet target production rate.
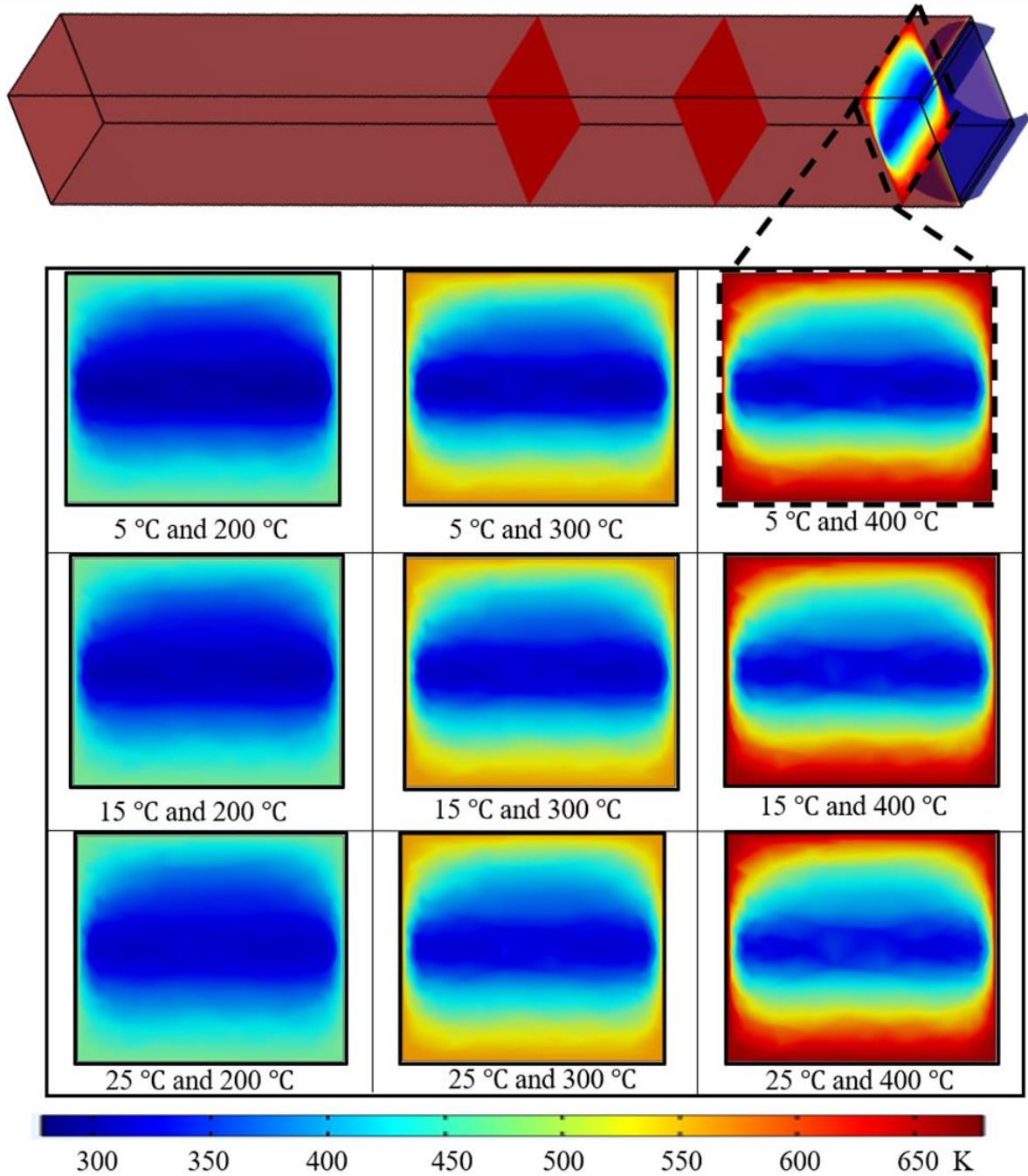
Figure 4.9: Thermal map of OVPD with substrate translated on a roll-to-roll unit. Expanded

visualizations show synergistic effects of evaporation temperature (200 - 400 ℃) and stage

temperature (5 - 25 ℃) on temperature distribution across the cooled stage.

4.7 Conclusions

The ability to scale a process hardware allows for forecastable capital and operating expenditures. Since organic vapor deposition technique is being considered for cost effective volume manufacturing of organic light emitting diodes (OLEDs) for general illumination, OVPD system must allow for attainment of designed device performance. Device performance is influenced by film composition and morphology, which are affected by the degree of material mixing. In this study, we apply a combination of analytical and numerical techniques to analyze vapor transport in OVPD thereby presenting a scalable method for predicting hardware aspect ratio needed to realize.

Analyses on vapor transport mechanisms show that diffusion dominates convection at flow rate ≤ 5 SCCM while convection is the dominant mechanism at higher flow rates. Further, our analytical and numerical results show that during co-deposition, hardware length needed for effective vapor mixing scales with gas flow rate. Also, results from our numerical study show that thermal map indicating propensity for substrate heating is majorly controlled by evaporation temperature. Hence, the resultant recommendation is for films to be grown at the highest non-destructive substrate.

Therefore, based on these contributions, a scalable method for predicting hardware aspect ratio needed to realize effective vapor mixing was proposed as well as a numerical strategy for assessing likelihood of substrate for target process conditions.

4.8 Appendices:

4.8.1 Mean free path and Knudsen number of different OLED materials at OVPD conditions.

Figure 4.10 below shows how the mean free paths of different OLED materials depend on chamber pressure and the corresponding Knudsen numbers of the system at these conditions. These values of Knudsen number (Kn < 1) show that for all small molecular materials (molecular weight < 1 kg/mol), their vapor flow can be conveniently modeled as a continuum flow in OVPD conditions. The properties and functions of these materials are tabulated in Table 4.1 below.

4.7.2 *Thirty common organic light emitting diode materials, their molecular weights, and functions.*
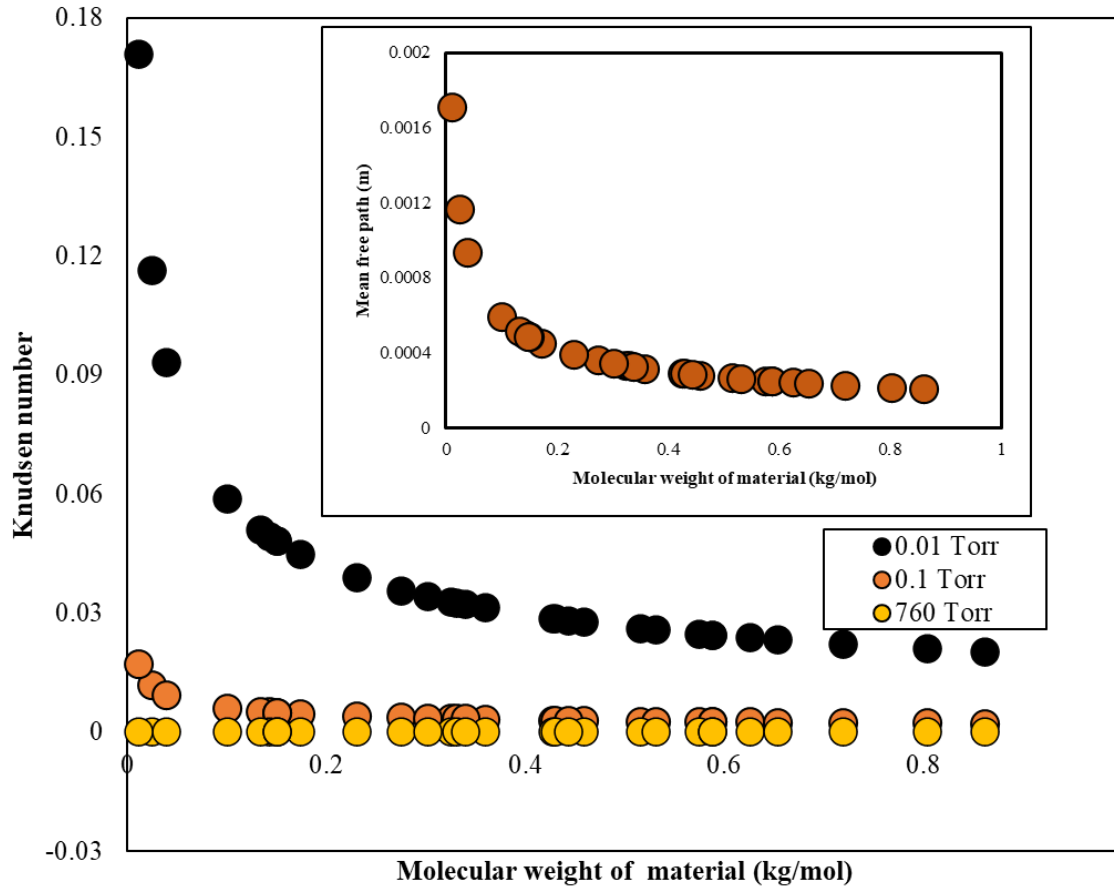
Figure 4.10: Dependence of Knudsen number on molecular weight for thirty common organic light emitting diode materials in nitrogen carrier gas at 250 deg.C evaporation temperature at different bases pressures in a 10-cm diameter chamber. Insert shows dependence of mean free path of these materials at 0.1 Torr.

Table 4.1: Thirty common organic light emitting diode materials, their molecular weights, and functions.

OLED material	OLED material formula	Molecular weight (kg/mol)	Function
tris (8-hydroxyquinoline) aluminum	Alq3	0.45943	Emission, electron transport
lithium fluoride	LiF	0.025939	Electron injection
2,9-dimethyl-4,7-diphenyl-1,10-phenanthroline	BCP	0.36045	Electron transport
magnesium oxide	MgO	0.0403044	cathode material
Alumina	Al_2O_3	0.10196	cathode material
indium thin oxide	ITO	0.42834	Anode material
Graphene	C	0.012	Anode material
copper phthalocyanine	CuPc	0.576082	Hole injection
4,40,4-tristriphenylamine and molybdenum trioxide	MoO_3	0.14394	Hole injection
N,N'-bis(naphthalen-1-yl)-N,N'-bis(phenyl)-benzidine	NPB	0.58874	Hole transport
N,N'-bis(3-methyl phenyl)-N,N'-bis(phenyl)-benzidine	TPD	0.51667	Hole transport
N,N'-Di(1-naphthyl)-N,N'-diphenyl-(1,1'-biphenyl)-4,4'-diamine	NPD	0.58874	Hole transport

1,1-Bis[(di-4-tolylamino)phenyl]cyclohexane	TAPC	0.62687	Hole transport
Caesium carbonate	Cs_2CO_3	0.32582	Electron injection
Tetrafluorotetracyanoquinodimethane	F_4-TCNQ	0.27615	Dopant
2,2',2"-(1,3,5-Benzinetriyl)-tris(1-phenyl-1-H-benzimidazole)	TPBi	0.65476	Electron transport
Cesium azide	CsN_3	0.174926	Dopant
4,4,4 -tris (N-carbazolyl) triphenylamine	Bphen	0.3324	Electron transport and hole blocking
Tungsten trioxide	WO_3	0.23184	Supports charge generation
Fullerene	C_{60}	0.72064	charge transport
Copper hexadecafluorophthalocyanine	F_{16} CuPc	0.862929	Support charge generation
4-*tert*-Butylpyridine	TBP	0.13521	Hole transport
Coumarin 545T	C545T	0.43056	Dopant and electron transport host
N,N'-Dimethylquinacridone	DMQA	0.34037	Dopant
5,6,11,12-tetraphenyltetracene	Rubrene	0.53267	Dopant
4-(Dicyanomethylene)-2-methyl-6-(4-dimethylaminostyryl)-4*H*-pyran	DCM	0.30336	Dopant
Tris(1-phenylisoquinoline)iridium (III)	Ir(piq)3	0.80496	Dopant

			Dopant, electron injection
Cesium fluoride	CsF$_3$	0.1519	injection
8-Hydroxyquinolinolato-lithium	LiQ	0.15109	Electron injection
2-methyl-9,10-bis(naphthalen-2-yl) anthracene	MADN	0.44457	Emission

Chapter 5 Understanding Interaction Energies for Particle Mass Assembling onto Non-conventional Surfaces

5.1 Preface:

Results contained in this chapter are part of unpublished work.

5.2 Abstract: Statement of Research Gaps, Hypothesis and Original Contribution

Understanding particle-surface interaction is important for engineering processing systems used across industries. These interactions are well understood for traditional systems, including a pair of interacting planes, a pair of interacting spherical particles and a particle-planar system. However, for nonconventional scenarios like particle-cavity system, little is known about these interactions, yet understanding these interactions for the latter system is critical for engineering emerging semiconductor systems for particle mass assembling. An example for semiconductor industry is the mass transfer of micro-LED chips onto receiver panel. To develop pathways for assembling particles onto nonconventional surfaces (like cavities on receiver plane), we hypothesize that if the participating interactions can be identified and quantified, their dependence on process conditions can be leveraged to show conditions where it is thermodynamically favorable to realize preferential particle mass assembling. We further fundamentally investigate the behavior of chip-cavity interaction energies, determining contributions of Lifshitz-van der Waals (LW) and electrostatic interactions, entropic contribution and gravity on overall energetics of system, assessing effects of chip size (0.2 - 50.2

μm), particle fill up ratio (0.25 - 0.95), chip shape (cubic chip and spherical chip), and cavity surface potential on the interaction energies while accounting for the interfacial Lewis acid-base (AB) interactions contributions. Our results show greatest energies for all interactions (van der Waals, gravitational, entropic contribution and electrostatic) energies when chip-cavity size ratio is ~1 indicating more favorable interaction between cavity and chip of similar size. We find that interactions due to electrostatics and entropy dominate attractions due to van der Waals and gravitational energies for different chip shapes and sizes. Further, our results show that chip size and shape synergistically influence different contributors to overall energy in a complex manner. Thermodynamic assessment of the processes as quantified by free energies reveal surface energies and cavity surface potential as clear pathways for chip assembling, leveraging dominance of interfacial Lewis acid-base interaction and entropic contribution, respectively. These resulting pathways will benefit the semiconductor industry in cost-effective assembling of micro-LEDs onto receiver planes.

5.3 Introduction and Motivation

Knowledge of interfacial energies between interacting bodies is applied in many industries for designing and operating separation as well as production systems. These interactions are well understood for the well-known Lifshitz-van der Waals (LW), especially for traditional systems like those involving a pair of interacting planes or spheres. However, for nonconventional scenarios like particle-cavity system, little is known about these energies. Yet they hold enormous promise for emerging manufacturing processes. In this section, we introduce and discuss motivations for projects 3. In project 3, we show how understanding interaction energies can facilitate design of systems for efficient micro-LED assembling. Thus project 3 investigates these interaction energies and presents pathways on how they benefit semiconductor industry.

For example, in semiconductor industry, adequate knowledge of interaction energies can be leveraged to engineer cost-effective micro-LED (μLED) assembling systems. Since micro-LED devices can deliver excellent quality performances, including high brightness, high stability, fast response time, infinite contrast ratio and ability to be as flexible and transparent display, they are being considered as befitting display candidates for head-up display, smartphones, and smart glasses, where the above features are required.

However, manufacturing cost of μLED display resulting from suboptimal chip transfer yield and chip assembling rate currently limit wider adoption of this technology [112]. This high cost is due to difficulty in realizing rapid mass-assembling of μLEDs with high yield as millions of chips need to be precisely trapped unto receptor panel with minimal defects. For example, using 5 μm chips,

1.5-in wide smart glass, 3-in wide Head-up display (HUD) and 6-in long cell phone would respectively require over 100 million, 350 million and 450 million chips to be precisely assembled such that ultra-high yield processing system is required for the micro-LED technology to be viable (see Figure 5.1). To solve this critical processing challenge, many µLED mass transfer processes have been developed.

Micro-LED assembling consists mainly of two steps, including epitaxial lift off (to remove the chips from growth substrate) and transfer process to deliver the chips onto receiver substrate. To realize, full color micro-LED display, the transfer process can be done either by sequentially delivering blue, green and red chips onto the receiver substrate [113, 114] or by monolithically delivering only blue chips followed by color conversion [113]. The color conversion can be realized by ink jet printing of quantum dots (QD) [115-117] or light-emitting polymer [118].

In terms of development status, the first step of the assembling process (epitaxial lift off) has advanced from the pioneer chemical lift off (CLO) [113, 119-121] with hydrofluoric acid (HF), through van der Waals epitaxy (VDWE), laser lift off (LLO) [122-124] to more recent selective lift-off techniques [113, 125, 126]. Thus, the first step of the assembling process is sufficiently advanced.

On the other hand, for the second step of the chip assembling process (mass transfer), while significant progress has been made in developing different transfer techniques, no existing chip mass transfer technique currently meets required the yield and throughput requirements. For micro-LED display to be viable for commercialization and wider adoption, an excellent mass

transfer technique needs to meet three key performance and economic requirements, including ability to deliver ultra-high assembly throughout (> 100 million chips/hr., > 99.9999 % yield) [6] as well as high placement accuracy (< 5% of the micro-LED chip size) [113]. The first criterion is necessary in order to transfer millions of chips into the receiver panel within a reasonable process time. The > 99.9999 % yield requirement is essential as a 0.01 % loss in yield could result in thousands of defect counts. Nevertheless, the third criterion allows for attainment of high pixel density and fine pixel pitches, which are critical for potential applications in smartphones and smart glasses. As a result of these mass transfer needs, significant advances have been made in the development of technologies for mass transfer of chips onto receiver substrate.

To date, seven main micro-LED transfer technologies have been developed, including roll-to-roll transfer, electrostatic pick and place, electromagnetic pick and place, elastomeric pick and place, fluidic self-assembly, laser enhanced advanced placement by adhesive ablation, and laser enhanced advanced placement by thermal release. Other chip transfer technologies are microtube transfer [127, 128], and magnetic/electric self-assembly [129] which have driving mechanisms as mechanical force and electromagnetic force, respectively. To better understand the state of progress in advancement of the second assembling step (chip transfer), we now discuss these seven main chip mass transfer processes.

Roll-to-roll transfer works by utilizing soft stamp on rotational unit to pick and imprint chips onto receiver substrate [130-135]. The driving mechanism for this technology is imprinting by van der Waals force. This technology is attractive since its curve roll head allows for more controllable contact with the planar substrate and continuous production [130] and can realize transfer

performance of up to 36 million chips/hr. at 99.9 % yield using < 100 um chips [130, 134, 135].

However, this technology lacks the capability of selective transfer of micro-LED chips [6] and it

is limited by suboptimal transfer yield.

Electrostatic pick and place utilize electrostatic force as the driving mechanism to remove chips

from growth substrate and to deliver them onto receiver substrate by voltage application. This

technology is uniquely attractive since it allows for selective pick and place of individual chips as

well as ease of operation by simple switching between on and off mode [130]. The drawbacks of

electrostatic pick and place technology include, requirement for a complex programmable module,

chip damage due to electric field caused by applied voltage [130] and suboptimal transfer yield

and throughput.

Electromagnetic pick and place utilize magnetic field generated by voltage application to generate

magnetic attraction for picking chips (magnetic property induced by mixing with iron, nickel, and

cobalt) and removal of magnetic force for chip placing on the receiver substrate [130]. The driving

mechanism for this technology is provided by electromagnetic force. Like electrostatic pick and

place method, advantages of this technology include selective pick and place of individual chips

as well as ease of operation by simple switching between on and off mode [130]. Nevertheless,

drawbacks of this technology include requirement for micro-LED chip mixing with ferrous metals

[6], need for a complex programmable module, chip damage due to electric field caused by applied

voltage [130] and suboptimal transfer yield and throughput.

Elastomeric pick and place technology uses adhesion between an elastomeric soft stamp and micro-LED to pick up the latter [136, 137]. The driving mechanism resulting in this adhesion is van der Waals interaction. Since adhesion is rate-dependent [138-140], pick-up of the chips from donor substrate is accomplished at high peeling rate while their placement on the receiver substrate is achieved at low peeling rate [137]. Advantages of this technology include ease of scalability, relatively good transfer yield of 99.99 % [141] and simple mode of operation. However, this technology is limited by suboptimal throughput and transfer yield.

Fluidic self-assembly utilizes a combination of gravity, capillary force and shape recognition to deliver micro-LED chips suspended in a liquid bath onto wells of similar shape in the receiver substrate [142-144]. This transfer technology is attractive since it involves less steps than pick and place counterparts, simple operating method, opportunity to be optimized by mounting navigation keel structure on the chip top to realize suitable placement orientation to achieve electronic connection in the circuit [130, 145], and it can achieve transfer throughput of up to 50 million chips/hr. at a yield of 99.98 % [130, 146, 147]. Nevertheless, this technology is limited by susceptibility to chip damage during parallel collision [130], suboptimal transfer throughput and transfer yield.

The last transfer technologies are laser enhanced advanced placement by adhesive ablation and laser enhanced advanced placement by thermal release. Both techniques of laser enhanced advanced placement (LEAP) utilize irradiation from laser beam to release and place chips onto receiver substrate. The release mechanism can be due to ablation or thermal release effects impacted on photothermal materials [130]. The driving mechanism for the former is laser-induced

96

chemical decomposition of supporting material (gallium nitride (GaN)) while the driving mechanism for the latter is thermal degradation of the sacrificial layer (dynamic release layer) caused by laser-induced physical or chemical changes.

For laser enhanced advanced placement by ablation of adhesive material, decomposition of the supporting material (usually GaN) is induced by laser irradiation with the resulting chemical reaction forming gallium and nitrogen [148]. The formed nitrogen thereby causes the chips to separate from the substrate by reducing the binding force of the former on the latter [130]. For this LEAP method, the applied laser power is the key variable influencing the chip release and needs to be optimized. Optimization of this variable is important since suboptimal laser power results in insufficient chemical decomposition of the gallium nitride supporting material thus no or less desired ablation is realized. On the other hand, too high laser power causes excess gallium to be formed from decomposition of the supporting material (GaN) leading to large contact area and surface area, which anchoring points that impede efficient chip-substrate separation [130].

For laser enhanced advanced placement by thermal release, sacrificial layer is sandwiched between the chips and the laser-transparent carrier such that sacrificial layer is physically or chemically decomposed when irradiated by laser beam thus resulting in chip separation from the carrier. This process typically involves the use of laser-transparent dynamic release layer (the sacrificial layer), such that after the chips are picked from growth substrate by laser lift off [6], the carrier is irradiated by laser beam to partially ablate the dynamic release layer, thus resulting in placement of the chips onto the receiver substrate [149, 150].

These laser enhanced advanced placement technologies are attractive since they allow for fast-response, high-precision positioning [130] and high transfer throughput of 100 million chips/hr. [149]. Nevertheless, complexity of design and maintenance of lasers and suboptimal transfer yield are the drawbacks of this technology.

As at the time this dissertation is written, best reported yield is 99.99 % [130], which is significantly less than the required transfer yield of 99.9999 % [6]. Therefore, to advance current knowledge in μLED assembling processes, project 3 focuses on fundamentally understanding interfacial energies occurring during chip-cavity interaction, determining relative contributions of constituent interactions as well as effect of chip shape and size on the overall energy. We thus demonstrate that by using our strategy of quantifying and assessing the interaction energies, we can show pathways where it is thermodynamically favorable to realize preferential chip-assembly, which will benefit semiconductor industry.
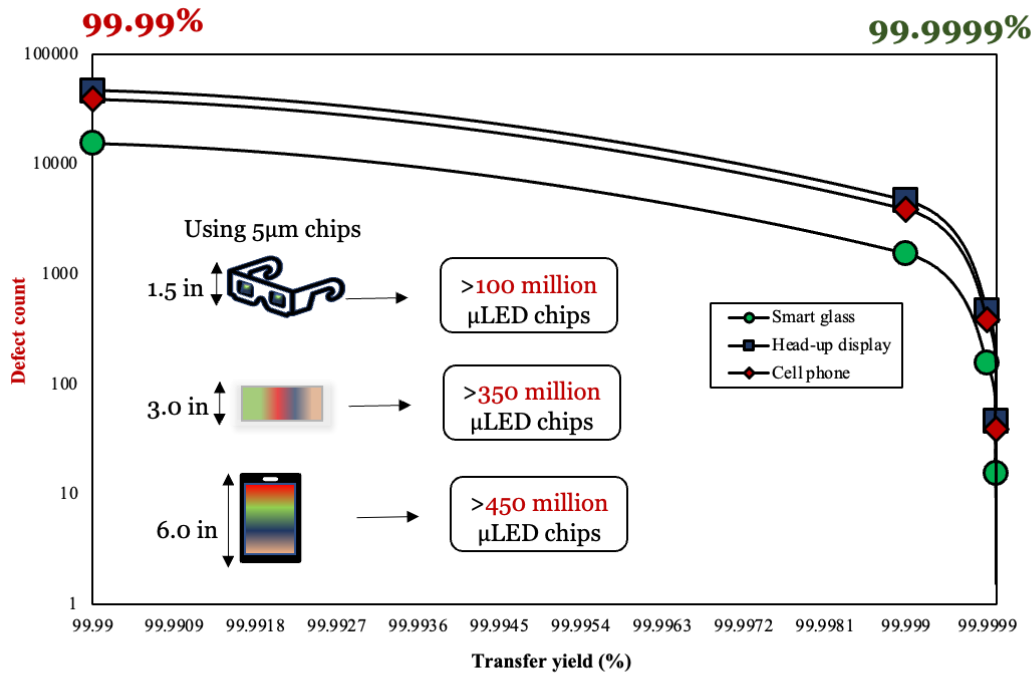
Figure 5.1: Dependence of defect count on chip mass transfer yield, modeling dimensions of smart glass, head-up display and cell phone as well as the number of 5-micron chips needed. 99.99% represents the best reported yield while target yield is 99.9999 %.

5.4 Chapter Objectives for Project 3 on Understanding Interaction Energies for Particle Mass Assembling onto Substrate Cavities

The research objectives of this project are summarized below:

- Critically review existing technologies developed for micro-LED assembling, highlighting their working mechanisms, benefits, and drawbacks in comparison to industry requirements.

- Identify and quantify different interaction energies acting on a suspended microparticle being assembled onto a substrate cavity.

- Determine the effects of process conditions, including particle shape, chip size and fill factor on the identified interaction energies.

- Leverage the understanding of the relative contributions of the interaction energies to propose clear pathways where it is thermodynamically favorable to achieve selective mass assembling of the microparticles.

5.5 Methodology

To engineer processes for efficient assembling of μLED unto receiver panel, different interfacial energies involved during chip-cavity interaction must be identified and understood. In this section, we identify these energies, describe how we quantify them as well as their dependence on process conditions.

For any system of interacting surfaces, the van der Waals interaction is expected. This interaction is due to fixed or momentary polarity within molecules of the interacting bodies. In this research study, we use the Lifshitz-van der Waals (LW) approach, which is a more rigorous form since it accounts for influence of neighboring molecules on interaction between every interacting pair of the interacting surfaces. Also, the energy due to weights of chips must be accounted for to determine the contribution of gravity to the overall energetics of the process.

For chip-cavity interaction in polar media like water, the interfacial Lewis acid-base (AB) interaction energy can be significant and must be accounted for. This AB energy is due to the peculiar effects experienced by surfaces interacting in polar media, which can be attractive (hydrophobic attraction due to cohesive hydrogen bonding of water) or repulsive (hydrophilic repulsion due to polar adhesion of electron donor of particle and electron acceptor of water) [151].

In addition to LW, gravity and AB, we identify electrical double layer interaction which represents electrostatic interaction energy due to charges of interacting surfaces as well as charges of electrolyte ions [152, 153]. Further, by accounting for effects of mixing of ions and charged surfaces and solvent molecules in bulk solution, the entropic contribution must be identified [152, 153].

Surface-surface interactions in liquid medium are well understood for well-known Lifshitz-van der Waals (LW), especially for traditional systems like those involving a pair of interacting planes or spheres [154]. LW interactions is due to fixed or induced dipoles within molecules of the interacting bodies and are described by Eqs. 5.1 and 5.2 for a pair of interacting planes or spheres [154], respectively. Where l is surface-surface separation distance, R_1, R_2, radii of interacting spheres and A_{132} is the Hamaker constant of the system for interaction between surfaces (1 and 2) in a medium (3), defined by Eq. 5.3 [155]:

$$E_{pp}^{LW} = \frac{-A_{132}}{12\pi l^2} \qquad\qquad 5.1$$

$$E_{ss}^{LW}(l) = \frac{-A_{132}}{6l}\left(\frac{R_1 R_2}{R_1 + R_2}\right)$$

$$\text{5.2}$$

$$A_{132} = \left(\sqrt{A_{11}} - \sqrt{A_{33}}\right)\left(\sqrt{A_{22}} - \sqrt{A_{33}}\right)$$

$$\text{5.3}$$

Other straightforward contributors are the gravitational interaction and interaction due to Brownian free energy, which are described per particle as mgl and 1.5 $K_B T$, respectively; where m is particle mass, g, acceleration due to gravity, K_B (= $1.381 \times 10^{-23}\frac{m^2 kg}{s^2 K}$), Boltzmann constant, and T, absolute temperature. However, other more complex interaction energies also acting on particles in suspension include electrostatic interaction energy, entropic contribution and interfacial Lewis acid-base (AB) energy, which require numerical determination, especially for nonconventional scenarios like particle-cavity and particle-rod systems where no approximating analytical expression exist. Electrostatic interaction energy account for contributions from both electrolyte ions and surface charges, and is accurately described for a 3D system by Eq. 5.4, demonstrated by Krishnan [156] and Chen, et al. [152]:

$$E_{ij}^{EL} = \frac{1}{2}\iint \sigma\varphi_s dA + \frac{1}{2}\iiint \rho\varphi dV = \frac{\varepsilon\varepsilon_o}{2}\iiint (\mathbf{E} \cdot \mathbf{E})\, dV$$

$$\text{5.4}$$

Where φ_s is surface potential, σ, charge density, ε, dielectric constant of medium and $\mathbf{E}$, electrostatic field. The local net charge is given as $\rho = c_0 e[\exp(-\phi) - \exp(\phi)]$, where the dimensionless electrostatic potential, $\phi = \frac{e\varphi}{K_B T}$ and C_o, ion concentration. Further, for a 3D system utilizing a monovalent electrolyte of ion concentration, C_o, entropic contribution due to mixing of ions and solvent molecules in suspension can be obtained using Eq. 5.5, which has been used to study the size-selective confinement of nanoparticles on nanocavity (Chen, et al. [152]), and nanoscale object in fluid (Krishnan [156]).

$$\Delta S = 2K_B C_o N_A \iiint [-\phi\sinh(\phi) + \cosh(\phi) - 1]dV \qquad 5.5$$

where ϕ is dimensionless electrostatic potential, and N_A $(= 6.023 \times 10^{23}\ \text{mol}^{-1})$ is Avogadro's number. Thus, the corresponding entropic contribution is given as Eq. 5. 6, with its equivalent in Eq. 5.7. First-principle derivation of this entropic contribution is provided in section 5.6.1 (Appendices).

$$-T\Delta S = -2K_B T n_o N_A \iiint [-\phi\sinh(\phi) + \cosh(\phi) - 1]dV \qquad 5.6$$

$$-T\Delta S = -K_B T \iiint \left[\left(\sum_i n_{io}\left(z_i\phi e^{-z_i\phi} + e^{-z_i\phi} - 1\right)\right)\right]dV \qquad 5.7$$

Where $n_{io}(= n_o N_A)$ is number of ions of type i in bulk solution per unit volume, and z_i is the ion charge.

Further, for surfaces in solvent like water, interfacial Lewis acid-base (AB) interaction also occur, which accounts for peculiar effects experienced by surfaces interacting in polar media, which can be attractive (hydrophobic attraction due to cohesive hydrogen bonding of water) or repulsive (hydrophilic repulsion due to polar adhesion of electron donor of particle and electron acceptor of water) [151].It can be shown that this free energy due to interfacial Lewis acid base interaction for a pair of surfaces (like two particles) (1 and 2) interacting in polar medium (water), 3 is given by Eq. 5.8 [157]:

$$E_{132}^{AB} = 102[\delta_{3w}^{+}(\delta_{1w}^{-} + \delta_{2w}^{-} - \delta_{3w}^{-}) + \delta_{3w}^{+}(\delta_{1w}^{+} + \delta_{2w}^{+} - \delta_{3w}^{+}) \qquad 5.8$$

$$- \delta_{1w}^{+}\delta_{2w}^{-} - \delta_{1w}^{-}\delta_{2w}^{+}]$$

Where the acidic (δ_{iw}^{+}) and basic polarity (δ_{iw}^{-}) ratios are given by Eqs. 5.9 and 5.10 [157] as functions of polar surface energy parameters of each surface (i) and water (w), γ_i^{+}, γ_w^{+} (acidic) and γ_i^{-}, γ_w^{-} (basic).

$$\delta_{iw}^{+} = \sqrt{\frac{\gamma_i^{+}}{\gamma_w^{+}}} \qquad\qquad 5.9$$

$$\delta_{iw}^{-} = \sqrt{\frac{\gamma_i^{-}}{\gamma_w^{-}}} \qquad\qquad 5.10$$

To determine polar surface energy parameters for each interacting surface, the Young and Dupré Eq. is solved using the approach demonstrated by van Oss, Chaudhury, and Good [158, 159]:

$$\frac{1}{2}(1 + \cos\theta)\gamma_L = \sqrt{\gamma_S^{LW}\gamma_L^{LW}} + \sqrt{\gamma_S^{+}\gamma_L^{-}} + \sqrt{\gamma_S^{-}\gamma_L^{+}} \qquad 5.10A$$

The parameters γ_L, γ_L^{LW}, γ_L^{-}, and γ_L^{+} are known for relevant liquids [160] and they represent liquid surface tension, apolar (Lifshitz –van der Waals) parameter, basic polar parameter and acidic polar parameter, respectively. Subscript i (in Eqs. 5.9 and 5.10) denotes S for solid surface in Eq. 5.10A and L for liquid in Eq. 5.10A.

Further, for an apolar liquid ($\gamma_L^{+} = \gamma_L^{-} = 0$), such that the apolar (Lifshitz –van der Waals) surface energy parameter, γ_S^{LW} can be obtained using Eq. 5.10B using measured contact angle of the apolar solvent on the solid surface, θ and the solvent surface tension, γ_L.

$$\gamma_S^{LW} = \left(\frac{1}{2}(1+\cos\theta)\right)^2 \gamma_L \qquad \text{5.10B}$$

Thus, with γ_S^{LW} known, Eq. 5.10A can be rewritten in the form of Eq.5.10.C [160]:

$$\frac{\frac{1}{2}(1+\cos\theta)\gamma_L - \sqrt{\gamma_S^{LW}\gamma_L^{LW}}}{\sqrt{\gamma_L^+}} = \sqrt{\gamma_S^+}\sqrt{\frac{\gamma_L^-}{\gamma_L^+}} + \sqrt{\gamma_S^-} \qquad \text{5.10.C}$$

Since values for all the quantities on the lefthand side of the Eq. can be obtained from experimental measurement and property tables, by measuring contact angles of more than one polar solvents on each interacting surface, Eq.5.10.C can be solved either graphically [160] or by a matrix method [161] to obtain the acidic (γ_S^+) and basic (γ_S^-) solid polar surface energy parameters. A graphical method is convenient when three or more polar solvents are utilized while the matrix method can be used when two polar solvents are used. Thus, the solved polar surface energy parameters for each solid material are used as inputs in Eq. 5.14 (below) to determine the interfacial Lewis acid base interaction energy of the system.

By using the Derjaguin approximation (see section 5.6 for Appendices), we can show that interaction energy between curved surfaces (E_{ij}) can be obtained from that between infinite flat plates (E_{pp}) using Eq. 5.11 [162]:

$$E_{ij} = \int_0^\infty 2\pi E_{pp}\, h\, dh = \Delta_{D-ij} \int_\infty^l E_{pp}\,(l)\, dl \qquad \text{5.11}$$

Such that Δ_{D-ij} for two interacting spherical particles (of radii R_1 and R_2) and of a particle-cavity system (R_p and R_v) are given by Eq.s 5.12 and 5.13, respectively. Detailed derivation of these factors is provided in section 5.6.2 (Appendices).

$$\Delta_{D-ss} = \frac{-2\pi R_1 R_2}{R_1 + R_2} \qquad\qquad 5.12$$

$$\Delta_{D-sv} = \frac{-2\pi R_p R_v}{R_v - R_p} \qquad\qquad 5.13$$

By combining Eqs. 5.8, 5. 12 and 5. 13, we obtain Eq. 5.14, which describes interfacial Lewis acid base interaction for a pair of surfaces (1: particle, and 2: cavity) in polar medium (water), 3:

$$E^{AB}_{132\_sv} = 102\left(\frac{R_p R_v (R_1 + R_2)}{R_1 R_2 (R_v - R_p)}\right)\left[\delta_{3w}{}^{+}(\delta_{1w}{}^{-} + \delta_{2w}{}^{-} - \delta_{3w}{}^{-}) \qquad 5.14\right.$$

$$\left. + \delta_{3w}{}^{+}(\delta_{1w}{}^{+} + \delta_{2w}{}^{+} - \delta_{3w}{}^{+}) - \delta_{1w}{}^{+}\delta_{2w}{}^{-} - \delta_{1w}{}^{-}\delta_{2w}{}^{+}\right]$$

Where R_p and R_v are particle radius and cavity radius, and R_1 and R_2 are radii of two interacting particles of an equivalent system. Therefore, net free energy change of the system is given by Eq. 5.15, as illustrated in Figure 5.2, where interaction due to Brownian free energy, E^{BR}_{ij} is 1.5 $K_B T$ per particle. Mechanisms of these interactions are summarized in Table 5.1.

$$F_{ij} = E^{BR}_{ij} + E^{LW}_{ij} + E^{EL}_{ij} + mgl - T\Delta S + E^{AB}_{ij} \qquad\qquad 5.15$$

Table 5.1: Underlining mechanisms and expected nature of interactions for our study.

Interaction energy	Mechanism (due to)	Nature	Nature in this study
Lifshitz- van der Waals	Fixed or momentary polarity within molecules of interacting bodies	Attractive	Attractive

Interaction due to Brownian free energy	Thermal motion (diffusion) of particles in suspension	Repulsive	Repulsive
Electrical double layer (EL)	Contributions from potentials (charges) of interacting surfaces and electrolyte ions	Attractive, neutral or repulsive	Repulsive
Interfacial Lewis acid-base (AB)	Hydrophobic attraction Cohesive hydrogen bonding of water Hydrophilic repulsion Polar adhesion between electron donor of chip and electron acceptor of water	Attractive, neutral or repulsive	Attractive
Gravity	Weight of chips	Attractive	Attractive
Entropic contribution	Mixing of ions (mainly counterions) and solvent molecules	Attractive, Repulsive	Attractive

To obtain the electrostatic energy and entropic contribution of a system, the distribution of the electrostatic potential must be obtained by solving a system of partial differential equations describing interactions between charged chip and cavity in aqueous suspension. To achieve this

goal, we utilize COMSOL for the computation, and numerically investigate the effects of chip shape and size on interaction profiles of the system. For study A, models illustrating these two scenarios (cubic chip and spherical chip systems) are comprised of a micro-LED chip interacting with the cavity in aqueous medium of constant volume. The same settings were applied on both models such that the Laplace Eq. $(\nabla^2\varphi = 0)$ was implemented on the particle, Poisson–Boltzmann Eq. $\left(\nabla^2\varphi = \dfrac{2n_o eN_A \sinh\left(\frac{e\varphi}{K_B T}\right)}{\epsilon_o \epsilon_r}\right)$ imposed on the ion-containing liquid medium and the region of study held under electrical neutrality $(n \cdot \nabla\varphi = 0)$, where N_A $(= 6.023 \times 10^{23} \text{ mol}^{-1})$ and K_B $(= 1.381 \times 10^{-23} \frac{m^2 kg}{s^2 K})$ are the Avogadro constant and Boltzmann constant, respectively. n_o is the bulk ion concentration (mol/m^3) and T, temperature in Kelvin. For both models, the separation distance between the interacting surfaces is set as two Debye lengths to capture interactions up to diffuse layers of the surfaces, while their potentials are set as φ_p (-34mV) and φ_V (= 26mV) for the particle and cavity, respectively.

First micro-LED models of different shapes (cubic and spherical chips) and different sizes (2.5 – 9.5µm, each interacting with a 10µm cavity of similar shape) were used to study effects of chip size and shape on van der Waals, electrostatic and entropic contributions at different chip-cavity separation distance (10 - 70 nm). By using different chip sizes on a fixed cavity depth, we have also coupled the chip fill ratio as another factor in this study, with it levels corresponding to fill factor of 0.25, 0.50, 0.75 and 0.95. Since gravity terms have a simple scaling relationship with size, the effects of these factors are only tested for statistical significance on van der Waals, electrostatic and entropic energies. For testing the statistical significance of an effect (like fill-factor) whose two samples have unequal variance, the Welch's t-test is sufficient, with the

analysis done by using each pair of the factor settings [105]. This statistical test was implemented on energy data obtained for different chip sizes using both cubic and spherical chip systems. Also, for the effect of chip shape, we perform a similar statistical analysis using data for a cubic chip vs spherical chip system across different particle sizes.

Further, to cover the entire size range of typical Micro-LEDs, we expand our computations to also investigate effects of chip size numerically (0.2 - 50.2 μm) and shape (cubic chip and spherical chip), cavity surface potential (10 – 200 mV) at two Debye length separation distance under this well-matched condition (size ratio of 0.95), and subsequently determine the corresponding energies, including van der Waals, electrostatic, gravity and entropic contributions. Afterwards, we then assess how the dominant contributors can be leveraged to tune the thermodynamic feasibility of chip-cavity interaction.

This computational protocol is also implemented for study B, which models interaction of five particles (each of 500 nm) with a nanowire (40 nm by 100 μm), mimicking the binding of proteins onto DNA strands. Similarly, the corresponding energies, including van der Waals, Brownian, electrostatic, gravity and entropic contributions were determined for this system, and subsequently leveraged to numerically demonstrate dynamic confinement of the particles onto the nanowire. The schematics, physics, settings as well as boundary conditions used in these studies are illustrated in Figure 5.3
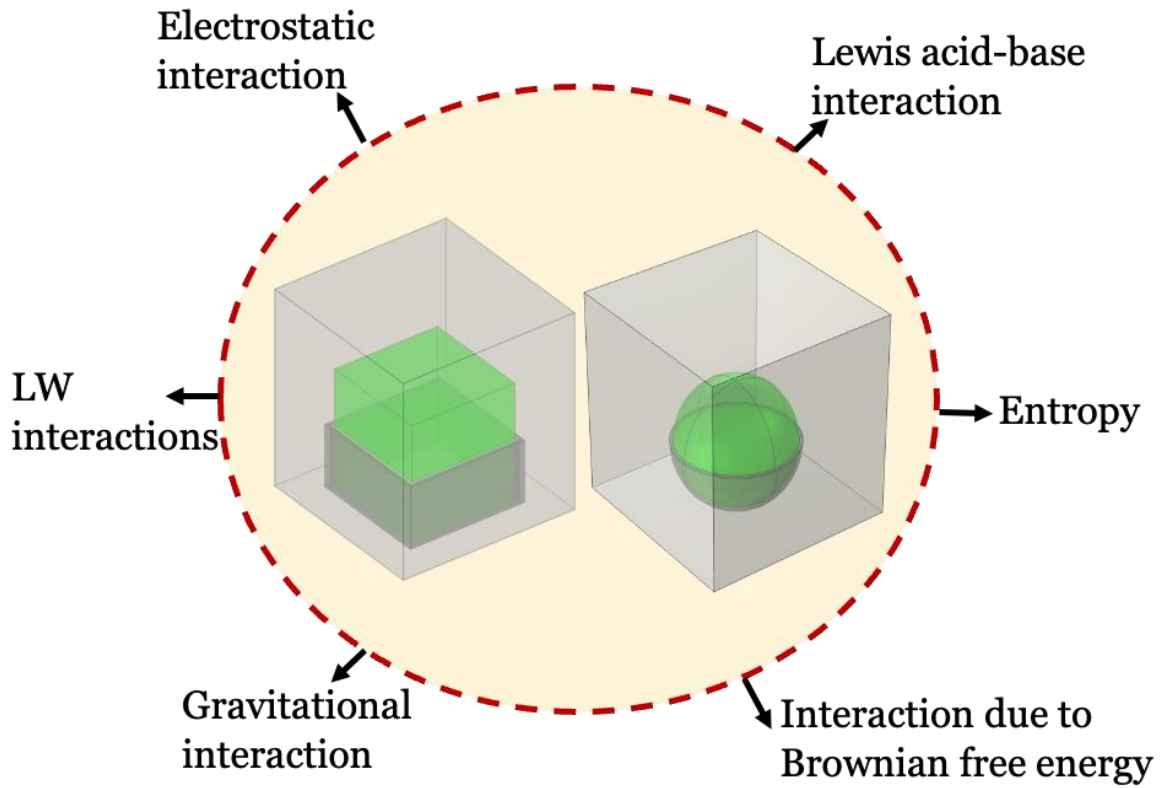
Figure 5.2: Illustration of model cubic and spherical chip systems and six interaction energies acting on the system.
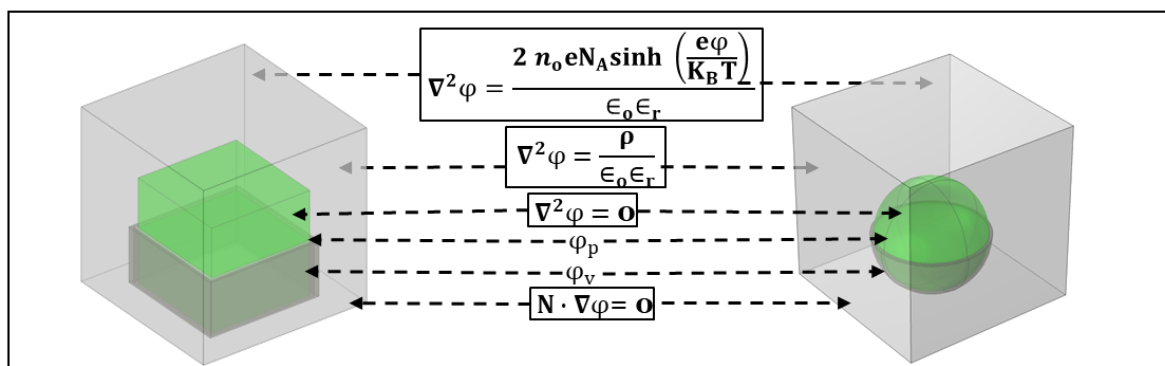
Figure 5.3: Illustration of settings, physics, and boundary conditions used for modeling chip-cavity interaction systems of both particle shapes. N_A is Avogadro's number,

n_0, bulk ion concentration, ρ, local net charge density (which follows Boltzmann distribution, as shown in the figure), z, ion charge and φ, electrostatic potential.

5.6 Results and Discussion

5.6.1 In this section, we discuss these interaction energies as well as their dependences on studied variables (fill factor, particle size and particle shape).

Figure 5.4 shows Lifshitz-van der Waals (LW) energies for interacting particle-cavity surfaces of different size ratio for cubic-chip (5.4 A) and spherical-chip (5.4 B) system. Since LW interaction energy is per unit area, the finite energy of each system is obtained following compensation by multiplying with the contact area between the surfaces. In Fig.5.4 A, LW interaction energy between chip and cavity is shown to be increasingly attractive as the chip size increases relative to the cavity width, with systems having peak energies (at 10nm separation) of -8,300 KT, -33,000 KT, -75,000 KT and -120,000 KT for 2.5um, 5.0um, 7.5um and 9.5um chips, respectively. This trend indicates that LW is favored to be more attractive when the cubic chip is well matched with the cavity size. Similarly, Figure 5.4B shows energies of interaction for spherical chip-cavity for different size ratio. While both systems show attractive LW energies of same order of magnitude, energies of spherical chip systems are less than those of cubic chip systems, with the values of former at 10 nm separation distance corresponding to -4,400 KT, -17,500 KT, -39,300 KT and -63,000 KT for 2.5um, 5.0um, 7.5um and 9.5um chips.

Also, in Fig. 5.4 B, the results show that, as the size ratio increases the magnitude of LW energy also increases thereby indicating increasingly attraction between the chip and cavity. Therefore,

as expected, attraction due to LW interactions have been shown to be more favorable as the chip-cavity size ratio increases for both chip shapes. While these trends are not surprising, it is important to calculate LW energies as they can be significant component of the overall interaction energies.
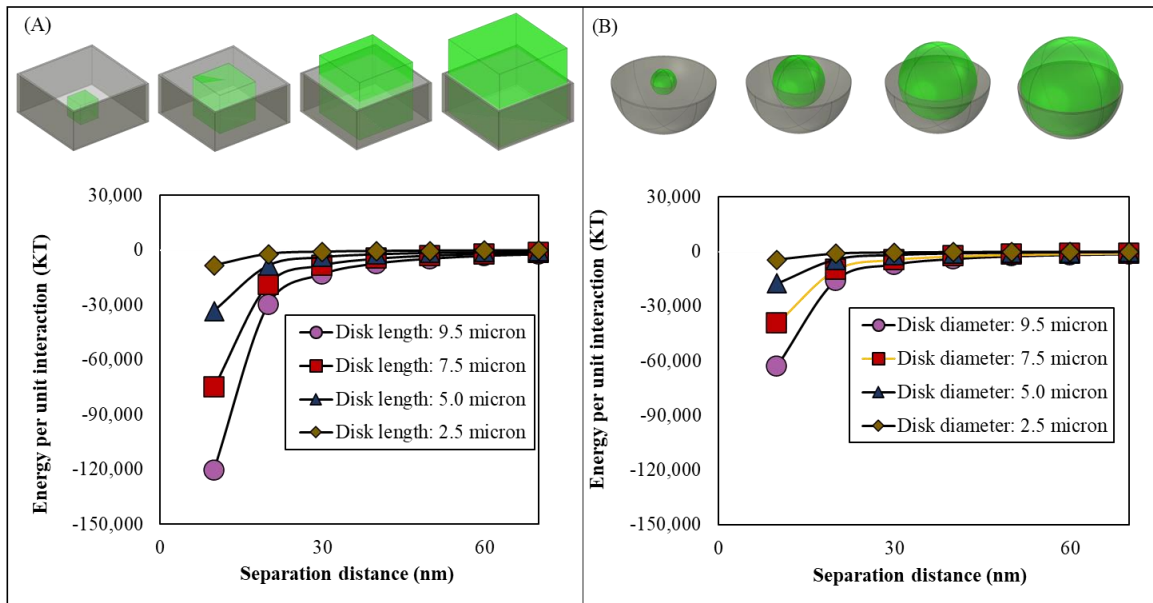
Figure 5.4: Dependence of LW on fill factor for different chip shapes, each in 10-micron cavity.

To obtain electrostatic energy and entropic contribution of the systems, the models were solved as discussed in section 5.4 using the same settings with the boundary, domain, and parameter specifications for both cubic chip and spherical chip systems with both models held under same conditions of surface potentials, electrolyte concentration and two Debye length separation distance, with distributions obtained for electric potential and electric field strength illustrated in Fig. 5.5.
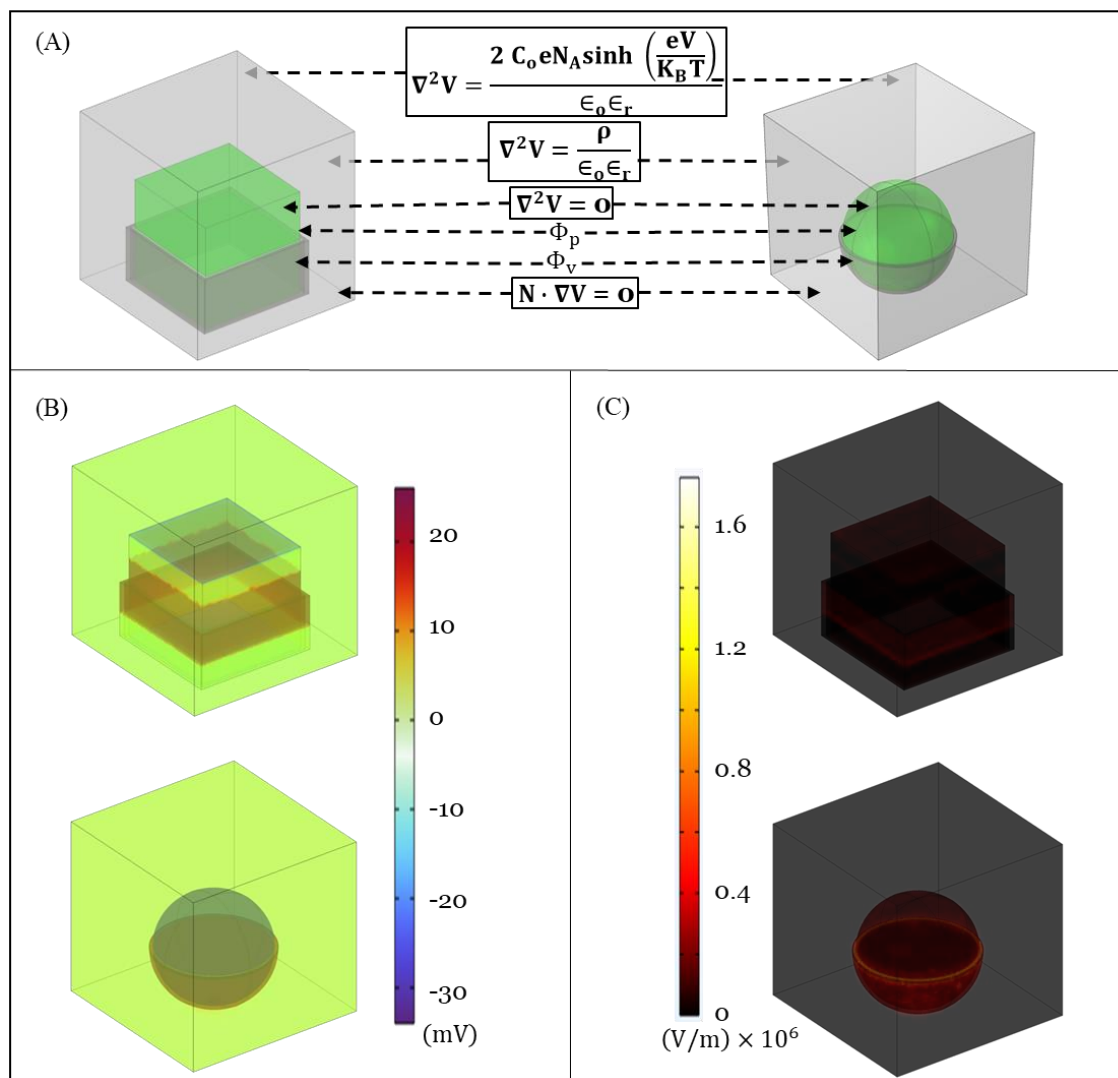
Figure 5.5: Distributions of electric potential and magnitude of electric field. Interaction modeled in 0.0001 M KCl solution using surface potentials of -34 mV for the particle and 26 mV for the cavity at 2 Debye length surface-surface separation distance. Particle size is similar for both cases: 10-micron diameter spherical chip and 10-micron wide cubic chip.

Figure 5.6 illustrates energies for particle-cavity system (cubic chip (5.6A) and spherical chip (5.6B)) of different fill factor (chips of diameter 2.5 – 9.5 microns, each in 10-micron cavity) due to electrostatic interactions. These results directly elucidate shape and fill factor effects on

electrostatic interactions, which is also termed electrostatic potential energy or field energy of a distribution of charges. This energy includes both contributions from electrolyte ions and potentials at the interacting surfaces (as represented by Eq. 5.4 [153]. As shown in Figure 5.6, both systems present repulsive interaction behaviors, which results from significant attraction among the ions leading to net repulsion between the interacting bodies surfaces, as illustrated in Figure 5.7. Another fundamental explanation to the obtained repulsive interaction is that the positive potential on the cavity electrostatically attract negative electrolyte ion (Cl^-) at a rate faster than any rate of adsorption between the particle and positive ion (Na^+), such that negative electrolyte ions in both stern and diffuse layers of the cavity make it to have an effective negative charge, thereby resulting in repulsive behavior. Specifically, chloride ions having larger diffusivity value migrate faster than sodium ions because of their smaller size; Na^+ is more hydrated than Cl^- such that hydrated sodium ion is larger (Na^+ has larger effective (hydrated radius) of 0.36 nm compared to 0.33 nm, the hydrated radius of Cl^-) [154]. Thus, this faster migration rate of Cl^- makes it easier for them to approach and adsorb on the cavity surface at a rate faster than the Na^+ approach the particle.

Figure 5.7 also illustrates the effects of fill factor on how the energies of spherical and cubic chip systems compare with each other. In terms of fill factor effect on electrostatic behavior, two interesting trends are identified from Figure 5.6: i) at fill factor ≤ 0.5, energies of cubic chip system are greater than those of spherical chip systems, and ii) at fill factor > 0.5. Since at fill factor $\leq$ 0.5, double layers are less overlapped, it is intuitive that surface potential contribution becomes significant such that cubic chip systems having more surface area in the double layer region have higher energy than spherical system.
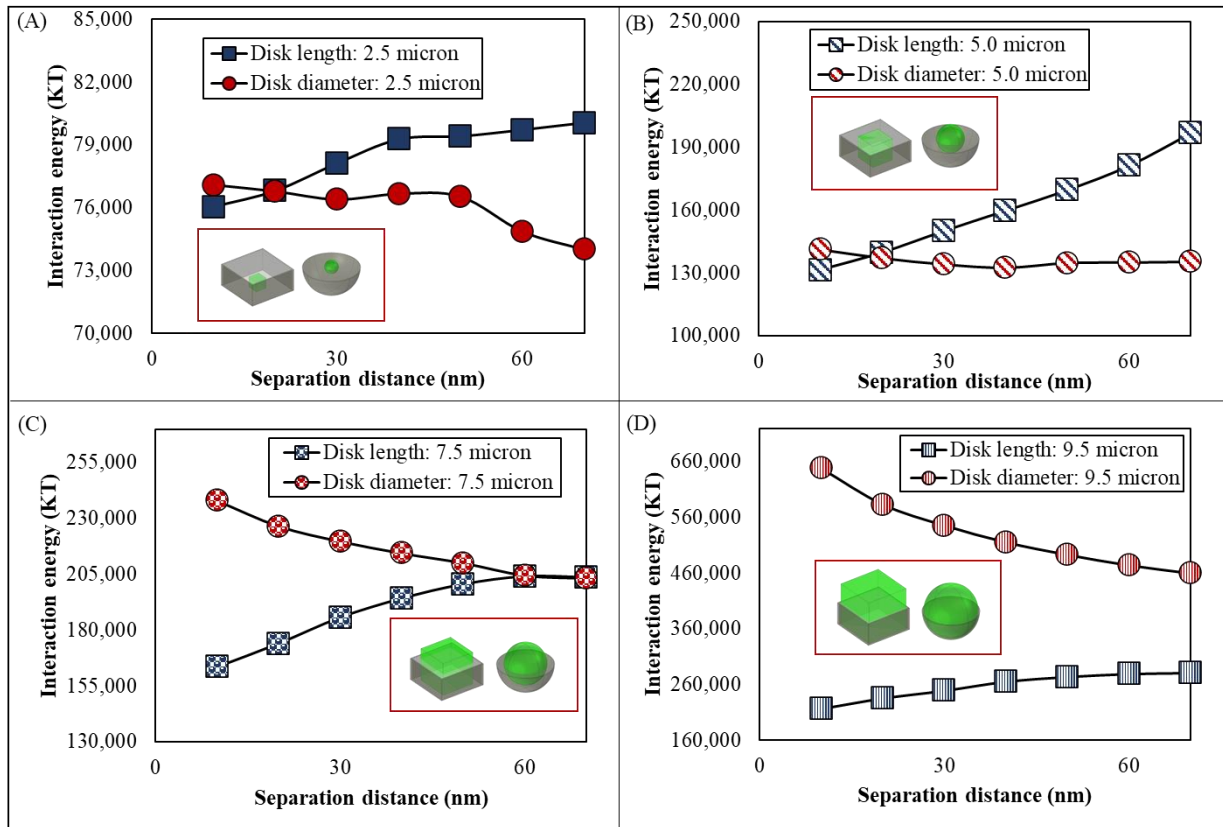
Figure 5.6: Dependence of electrostatic interaction on fill factor for different chip shapes, each on 10-micron cavity.
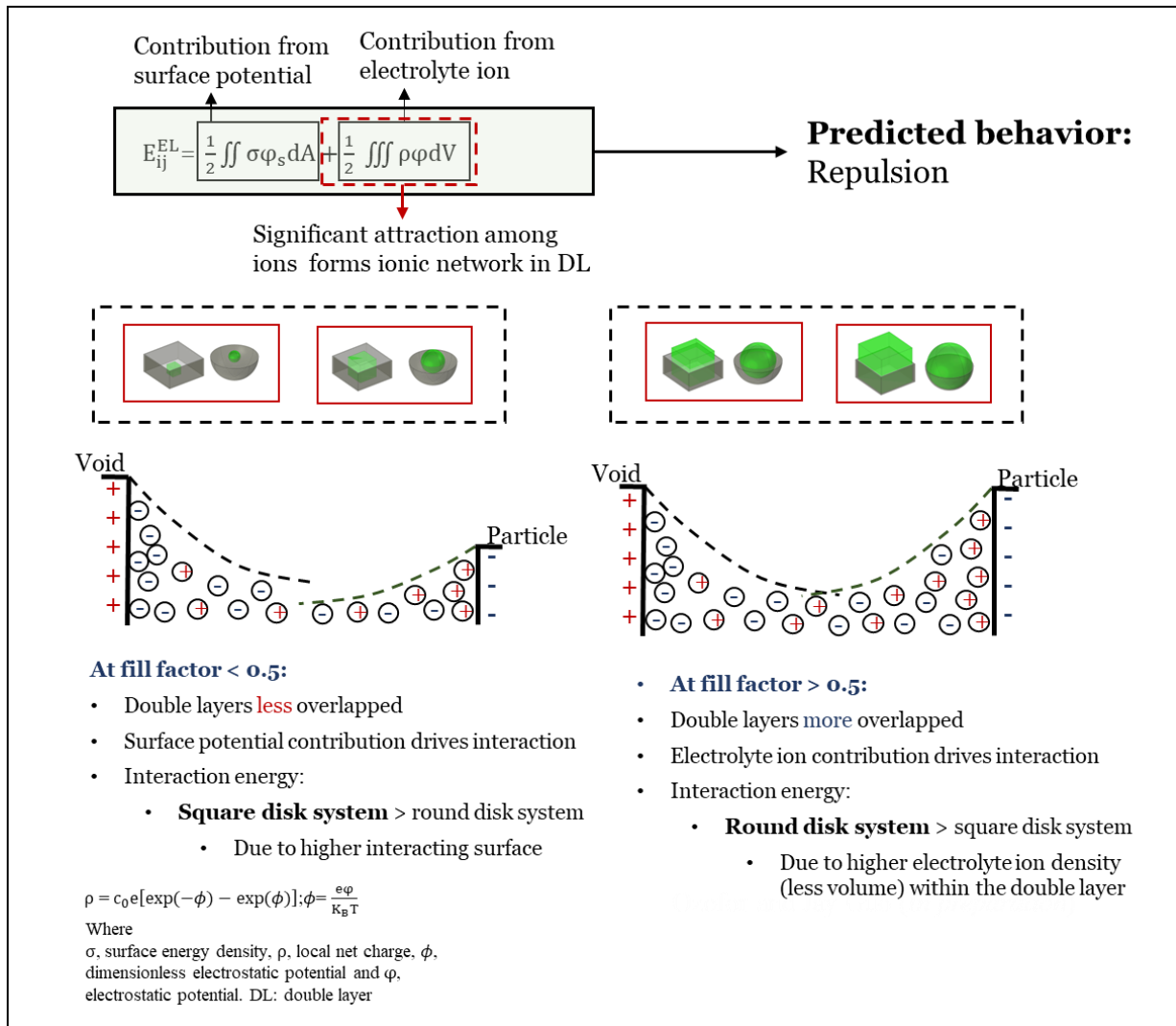
Figure 5.7: Predicting mechanism of electrostatic interaction and its dependence on fill factor.

On the other hand, at fill factor > 0.5, double layers are more overlapped with electrolyte ion contribution becoming significant such that spherical chip systems having higher ion density in the double layer region possess higher interaction energies than cubic chip systems. Hence, it follows fundamentally that, for a given fill factor setting, cubic chip energy is governed by areas of the interacting surfaces while spherical chip energy is governed by ion density in the double layer. This fundamental insight is consistent with how energies of these systems vary with

separation distance (as illustrated in Figure 5.7). Hence, as the separation distance increases, the cubic chip systems possess higher repulsive energies due to an increase in areas of the interacting surfaces. Conversely, as the separation distance increases, spherical chip energies reduce because of reduction in ion density in the double layer. Therefore, the most distinctive repulsive behavior with separation distance for both systems is observed at 0.95 fill factor.

To understand entropic contributions from fundamental perspective, Figure 5.8 shows the predicted entropic behavior from first principle as well as how the entropic change of the cubic system compares with that of spherical system. Detailed derivation of the governing Eq. for entropic contribution is provided in section 5.6.1.
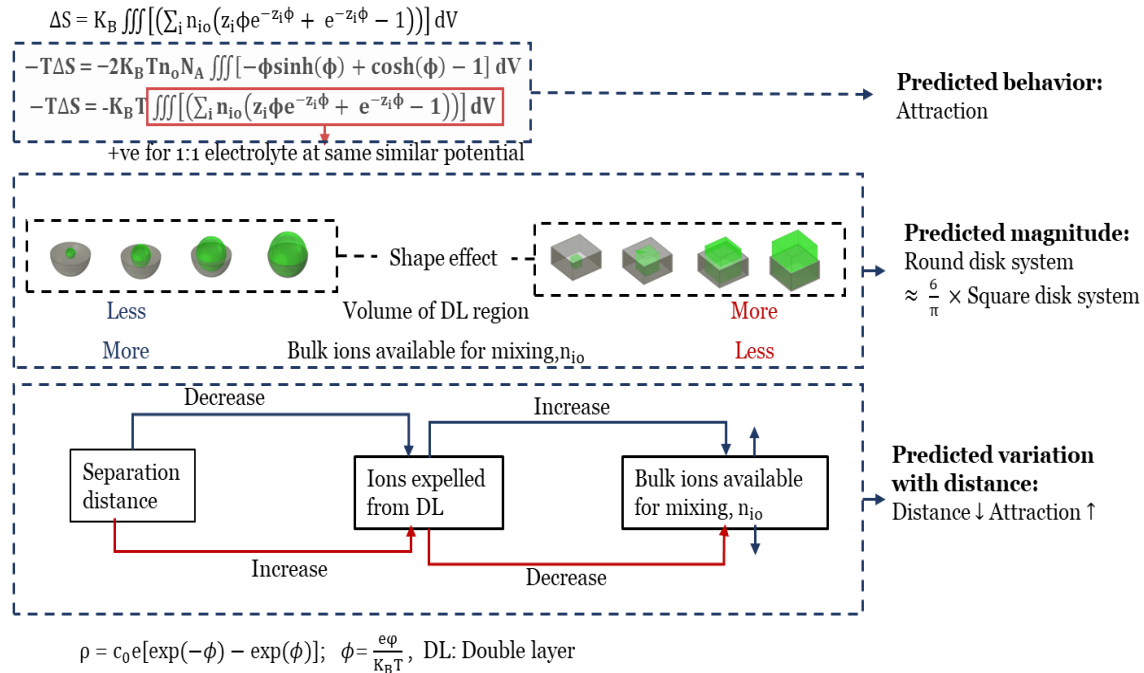
Figure 5.8: Predicting entropic behavior from first principles.

Figure 5.9 shows entropic contributions obtained for different particle-cavity systems (cubic chip (5.9 A) and spherical chip (5.9 B)) of different fill factor (chips of diameter 2.5 – 9.5 microns, each in 10-micron cavity) at different separation distances. These results were obtained by accounting for entropic effects due to distribution of ions and their mixing with solvent molecules in suspension as modeled in Eq. 5.6. As shown in Figs. 5.9A and 5.9B, interaction between chip and cavity due to entropy of mixing is shown to be increasingly attractive as the chip size increases relative to the cavity width, with systems having highest energies (at 10nm separation) of -1,188,300 KT; -3,916,000 KT; -9,191,000 KT and -18, 1720,000 KT for 2.5um, 5.0um, 7.5um and 9.5um cubic chip systems (Fig. 5.9A), and -1,587,000 KT; -10, 891,100 KT; -17,500,000 KT and -29, 200,000 KT respectively for spherical chip systems of same size (Fig. 5.9B). The attractive behavior observed follows fundamentally since volume integral of expression in Eq. 5.7 gives a positive value for similar potentials such that entropic contribution $(-T\Delta S)$ results in negative values of free energies with attraction as the interaction behavior.
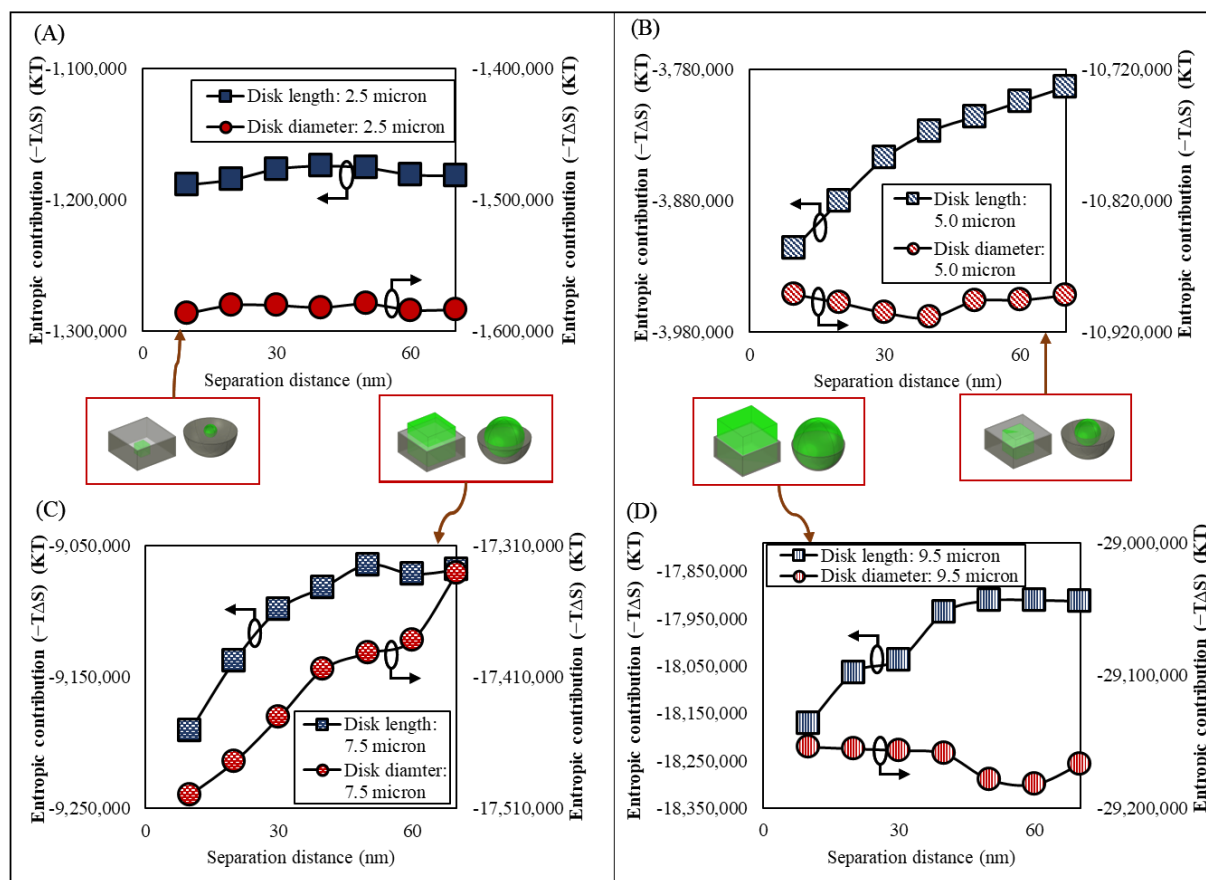
Figure 5.9: Dependence of electrostatic interaction on fill factor for different chip shapes, each on 10-micron cavity.

Secondly, spherical chip systems present more attractive energies due to entropy than cubic chip systems at different fill factor settings (see Figures 5.9 A – 5.9 D). This shape effect on entropic contributions is supported by first-principle physics, since compared to cubic chip system, spherical chip systems have less volume of the double layer region, and thus more ions available in the bulk phase to participate with mixing of solvent molecules.

Further, it is noteworthy to discuss how the entropic energies vary with chip-cavity separation distance. From the first principle (see Figure 5.8), entropic contribution is predicted to increase

119

in magnitude when the particle-cavity separation distance decreases. While this predicted trend is consistent with the results of cubic systems, a somewhat non-monotonic trend is observed for spherical systems. The system under investigation can be conceived as a two-partition system, comprising the double layer region loosely separated from the bulk phase, such that when the separation distance between the interacting surfaces decreases, more ions are expelled from the double layer region, which enter the bulk phase to participate in mixing with solvent molecules, thereby resulting in increase in attraction. This fundamentally predicted behavior is consistent with results obtained for cubic chip systems. However, for spherical chip systems, non-monotonic variations with separation distance are obtained, which we attribute to less stability in number of bulk phase ions caused by more expelled ions reentering the double layer region in the spherical chip system.

Having demonstrated that van der Waals, electrostatic and entropic interactions are most pronounced and distinct for well-matched chip-cavity system, we now investigate their relative contributions on free energies (while also accounting for gravitational energy), and their dependence on chip size typical of micro-LEDs (0.2 - 50.2 µm) and shape (cubic chip and spherical chip) under this well-matched condition (size ratio of 0.95) and at two Debye length separation distance.

Figure 5.10 shows different energies and their dependence on chip size and shape due to (Fig.5.10A) LW interactions, (Fig.5.10B) gravity, (Fig.5.10C) electrostatic potential energy interactions, and (Fig.5.10D) contributions from entropy of mixing. Our calculations (refer to Figure 5.10) show three interesting trends. Firstly, interactions due to electrostatics and entropy

120

of mixing are the two major interaction mechanisms, dominating attractions due to van der Waals and gravitational energies for different chip shapes and sizes studied. Nevertheless, energies from LW and gravitational interactions can be significant as their values can be up to 100, 000 KT (corresponding to 1000s of eV) (see Figs. 5.10A and 5.10B). These results reveal electrostatic and entropic effects as the prevalent interactions and show that gravitational and van der Waals contribution can be neglected unless the particles are large (e.g., tens of microns).
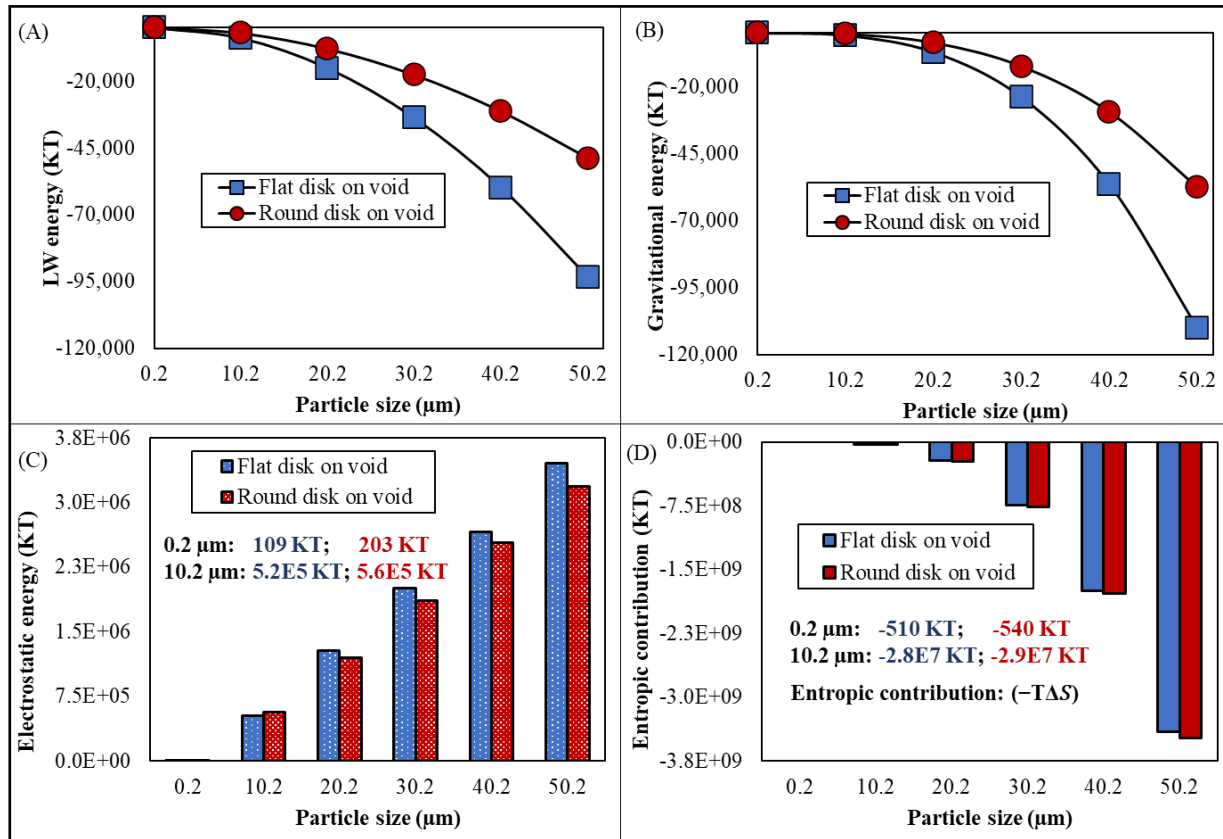
Figure 5.10: Synergistic effects of chip shape and size on different energies, using surface potentials of -34 mV for the particle and 26mV for the cavity, @ 0.95 fill factor and two Debye length separation distance.

Secondly, we find that chip size influences the relative contributions of the energies in a complex manner such that for both cubic and spherical chip systems, the energies are in the order of, 0.2 μm: electrostatic > entropy > LW > gravity; 10.2 - 40.2 μm: entropy > electrostatic > LW > gravity, and for 50.2 μm: entropy > electrostatic > LW > gravity. Therefore, these results numerically confirm chip size as a critical factor influencing the relative contributions of each interaction mechanism to overall chip-cavity energetics, and thus can be optimized for efficient chip assembling.

The last trend from results shown in Figure 5.10 that is noteworthy is the effect of chip shape on the respective energies of the system. For the chip size tested (0.2 - 50.2 µm), gravitational and van der Waals energies of cubic chip system are greater than the corresponding energies of the spherical chip system, while the reverse is the case for entropic contribution, which shows that entropy of mixing in spherical chip system to be greater than those of cubic chip system. Cubic chip systems have more LW and gravity energies due to the higher effective interacting surface and particle mass they possess relative to spherical chip systems. On the other hand, spherical chip systems have larger entropic energies than cubic chip systems since the former have smaller volume of the double layer region, and consequently more ions in bulk phase participating in the mixing with solvent molecules. In terms of chip-shape effect on electrostatic energy, a rather more complex trend is observed. We find that for ≤ 10.2 µm chip, electrostatic energy of spherical chip system is greater than electrostatic energy of cubic chip system, while the reverse trend holds for larger chip size (20.2 - 50.2 µm). Thus, further confirming chip shape and size as key variables influencing the overall energetics of chip cavity interaction. Therefore, as we have demonstrated in Figures 5.7 – 5.10, these variations of different energies with chip geometry and size have confirmed chip shape and size as critical factors thereby validating our hypothesis. We now thermodynamically assess the overall feasibility of the process.

5.6.2 Thermodynamic assessment of overall interaction

Since entropic contribution and electrostatic interactions largely dominant LW, Brownian and gravitational interactions, and these prevalent mechanisms are affected by surface potential of

the cavity, we now theoretically demonstrate how this convenient variable (cavity surface potential) can be leveraged to demonstrate thermodynamic feasibility of chip assembling.

Further, with the five energies (Brownian, LW, gravity, electrostatic and entropy) known, the sixth contributor (due to AB interaction) needed to make the assembling process thermodynamically favorable can be predetermined, which can be realized, in principle by tuning surface energies of the interacting surfaces. By measuring contact angles of appropriate solvents on the interacting surfaces and solving the Young-Dupre Eq., polar surface energy parameters can be obtained, which are inputs for determination of AB energy of the system (from Eq. 5.14), such that the pathways that emerge for chip assembling are cavity surface potential and surface energy parameters. We therefore assess the thermodynamic feasibility of the assembly process for different chip shape and size by quantifying the corresponding free energies of the system, with the results shown in Figures 5.11 and 5.12, leveraging surface potential and surface energy parameters, respectively.

Figures 5.11 and 5.12 show free energy changes of chip-cavity interactions, with most conditions indicating attractive behavior to be thermodynamically favorable. Nevertheless, the net positive free energy changes (indicating attraction to be less thermodynamically favorable) obtained for 0.2 μm chip is because contribution of repulsive electrostatic energy dominates cumulative attractive contributions from entropy, LW and gravity at this chip size. Further, unlike in cubic chip system where positive free energy change is observed for cavity surface potential up to 48mV, these repulsive energies persist for up to 162 mV in spherical chip system, which is due

to the latter system having more repulsive electrostatic energy than the former system at fill factor of 0.95 (see Figure 5.6D).

Further, our results show that free energies of the interaction is strongly dependent on chip size as well as on tuning variable (cavity surface potential in Figure 5.11 and surface energy parameters in Figure 5.12), a trend which holds for both cubic and spherical chip systems as evident on the increasing magnitude of attraction with chip size and the tuning variable. Thus, in terms of practical benefits, these resulting free energies from thermodynamic assessment reveal cavity surface potential and surface energy parameters as pathways for realizing high-yield high-throughput micro-LED assembling.
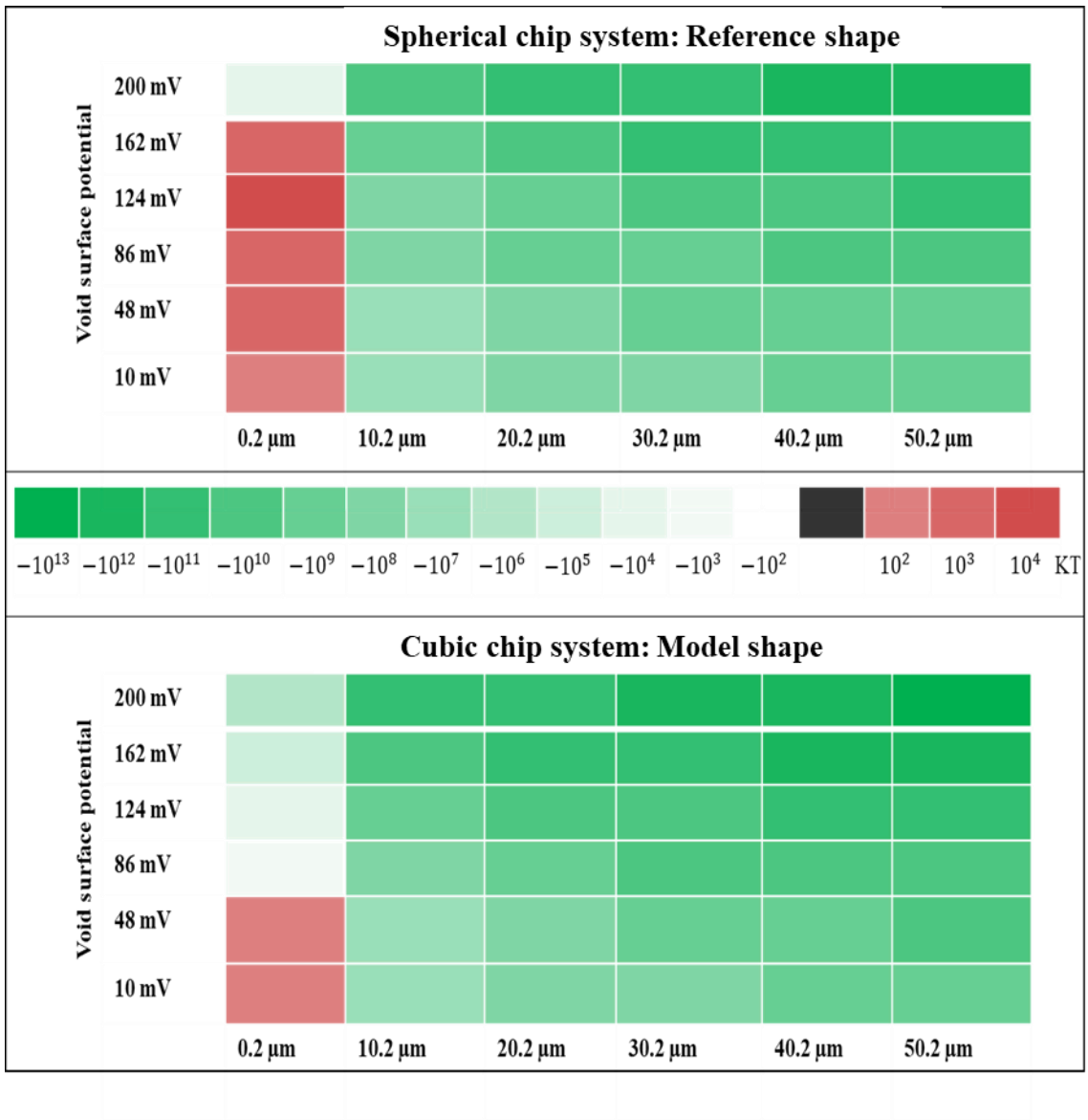
Figure 5.11: Free energies from thermodynamic assessment reveal cavity surface potential as a clear pathway for chip assembling.
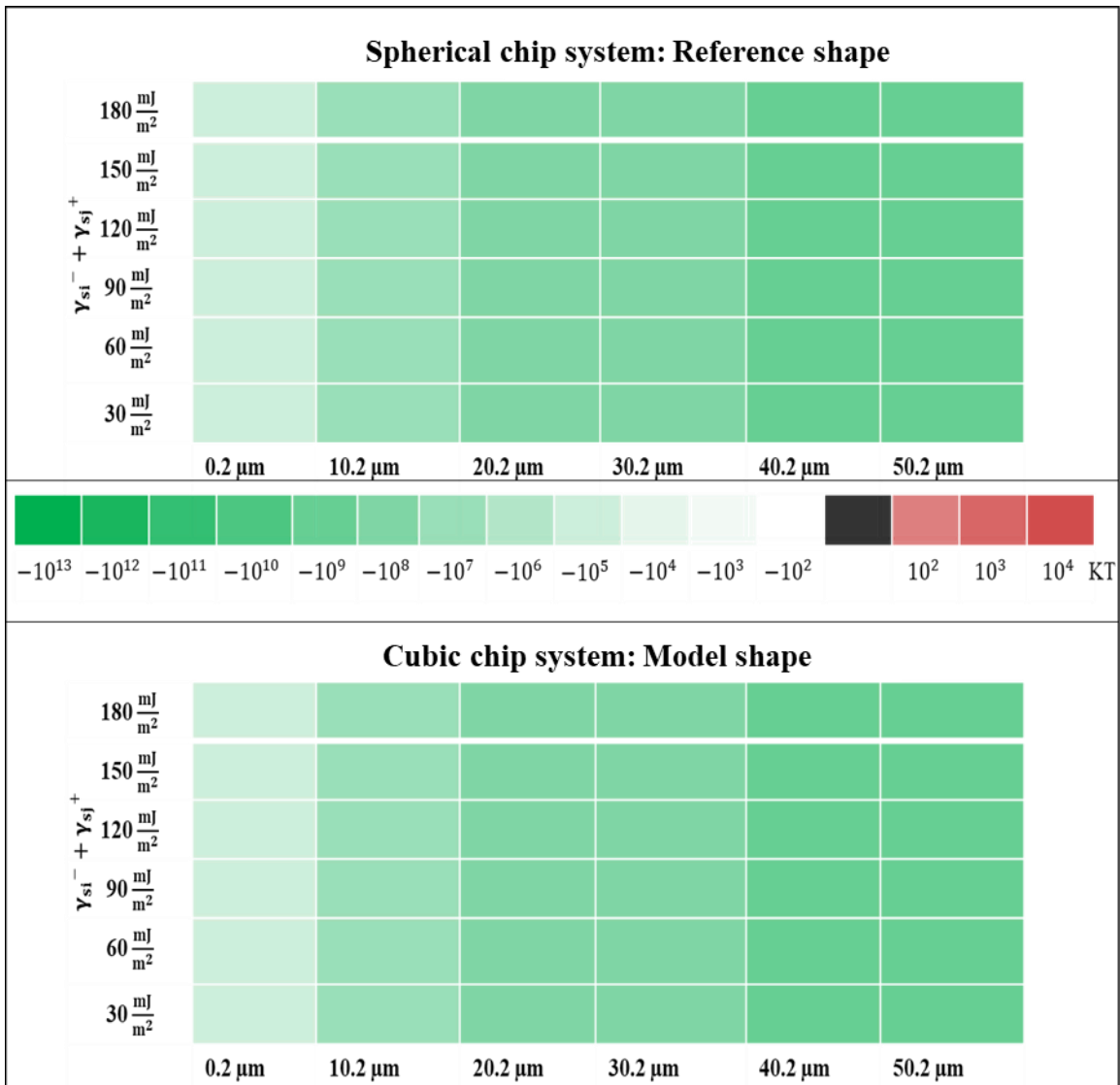
Figure 5.12: Free energies from thermodynamic assessment reveal surface energy as a clear pathway for chip assembling.

5.7 Conclusions

Understanding the energetics of chip-cavity interactions is critical in engineering processing systems for cost-effective assembling of particles onto nonconventional surfaces. In this study, we leverage understanding of interaction energies and their dependence on process conditions to develop pathways where particle mass assembling is thermodynamically favorable.

This energetic strategy is applied to study interaction of a micro-LED chip interacting with a cavity on a receiver plane. The study will benefit semiconductor industry in engineering systems for cost-effective mass assembling of micro-LED chips.

We calculate the contributions of Lifshitz-van der Waals (LW) and electrostatic interactions, entropic contribution and gravity on overall energetics of chip-receiver cavity system, assessing their dependences on process variables, including chip size (0.2 - 50.2 µm), particle fill factor (0.25 - 0.95), and chip shape (cubic chip and spherical chip).We find chip shape and size to influence the energies in a complex manner, such that contributions from electrostatics and entropy of mixing dominate those due to van der Waals and gravity for different chip shapes and sizes, with most distinct interactions observed at fill factor of 0.95. Gravity and electrostatic are respectively the least and most dominant mechanisms for 0.2 µm chip system, while for 50.2 µm chip system, LW and entropy are the smallest and largest contributors. For systems having chips of size 10.2 - 40.2 µm, entropic and gravitational interactions are the prevalent and least

dominant effects, respectively. Further, our calculations further show that for the chip size studied (0.2 - 50.2 μm), while gravitational and van der Waals energies of cubic chip system are greater than corresponding energies of spherical chip system, the reverse is the case for entropic contribution, further confirming chip shape and size as critical factors influencing the assembling process. Importantly, contribution from interfacial Lewis acid base interaction can be the prevalent mechanism, dominating effects due to gravity, LW, and electrostatic effects. Finally, energetic assessment of the process shows assembling can be made thermodynamic favorable by tuning cavity surface potent and surface energies, leveraging entropy and interfacial AB interactions, respectively.

5.8 Appendices:

5.8.1 First-Principle Derivation of Entropic Contribution

1st and 2nd laws of thermodynamics for an ideal gas can be combined to obtain Eq. 5.8.1.1, which is equivalent to 5.8.1.2

$$dE = PdV - TdS = 0 \qquad\qquad 5.8.1.1$$

$$dS = \frac{P}{T}dV = \frac{nR}{V}dV \qquad\qquad 5.8.1.2$$

Such that for binary system of ideal gases, the change of mixing is given by Eq. 5.8.1.3

$$\Delta S_{mix} = n_1 R \ln \left(\frac{1}{X_1}\right) + n_2 R \ln \left(\frac{1}{X_2}\right) = -R \left(n_1 \ln x_1 + n_2 \ln x_2\right)$$

<div align="right">5.8.1.3</div>

Where number of moles and mole fractions are given by n_i and x_i, and gas constant, $R = N_A K_B$ and number of ions = concentration of ion $*$ N_A. N_A ($= 6.023 \times 10^{23}$ mol^{-1}) is Avogadro's number, and K_B ($= 1.381 \times 10^{-23} \frac{m^2 kg}{s^2 K}$), Boltzmann constant.

The system under investigation comprises interactions surfaces in a dilute electrolyte medium, such that entropic contribution of the system (-TΔS) (treated as ideal mixture of ions and solvent molecules) is due to distribution of electrolyte ion (mainly counterion) in the double layer (Eq. 5.8.1.4) and mixing of same ions and solvent molecules in the bulk solution (Eq. 5.8.15). Thus, entropy change of the system is given by (Eq. 5.8.1.6).

$$\Delta S_{DL} = -K_B \iiint \left[\left(\sum_i n_i \ln x_i + n_w \ln x_w \right) \right] dV$$

<div align="right">5.8.1.4</div>

$$\Delta S_{mix,o} = -K_B \iiint \left[\left(\sum_i n_i \ln x_{io} + n_w \ln x_{wo} \right) \right] dV$$

<div align="right">5.8.1.5</div>

$$\Delta S = -K_B \iiint \left[\left(\sum_i n_i \ln \frac{x_i}{x_{io}} + n_w \ln \frac{x_w}{x_{wo}} \right) \right] dV$$

<div align="right">5.8.1.6</div>

Where DL: double layer; n_i : number of ions of type i in the double layer per unit volume = (concentration of i $*$ N_A), n_w : number of water molecules in the double layer = (concentration of

water $* N_A$). Subscript o denotes values in bulk solution. x_{io}, x_{wo} are bulk mole fractions, n_{io} : number of ions of type i in bulk solution per unit volume = ($n_o * N_A$, where n_o : electrolyte ion concentration in the bulk), n_{wo} : number of water molecules in bulk solution.

For dilute electrolyte solution, $x_i \approx \frac{n_i}{n_w}$ and $x_w = 1 - \sum_i x_i$, and $\frac{x_i}{x_{io}} \approx \frac{n_i}{n_{io}}$, such that Eq.5.8.1.6 results.

$$n_w \ln \frac{x_w}{x_{wo}} = n_w \ln \frac{1 - \sum_i x_i}{1 - \sum_i x_{io}} \approx n_w(-\sum_i x_i + \sum_i x_{io}) \approx \sum_i(-n_i + n_{io}) \qquad 5.8.1.7$$

Combining Eqs. 5.8.1.6 and 5.8.17 gives 5.8.1.8 [163]:

$$\Delta S = -K_B \iiint \left[\left(\sum_i n_i \ln \frac{n_i}{n_{io}} + \sum_i(-n_i + n_{io}) \right) \right] dV \qquad 5.8.1.8$$

By applying the Poisson-Boltzmann model ($n_i = n_{io} e^{-z_i \phi}$) to Eq. 5.8.1.8 for ions of charge $z_i e$, we have Eq. 5.8.1.9 for general expression for entropy change of the system.

$$\Delta S = K_B \iiint \left[\left(\sum_i n_{io} \left(z_i \phi e^{-z_i \phi} + e^{-z_i \phi} - 1 \right) \right) \right] dV \qquad 5.8.1.9$$

Where ϕ ($= \frac{e\varphi}{K_B T}$) is dimensionless electrostatic potential, and φ, electrostatic potential. Therefore, for 1:1 electrolyte, and applying hyperbolic cosine and sine functions, we have Eq. 5.8.1.10 for entropy change of the system. Thus, the expression for entropic contribution, which has been described and applied by Chen, et al. [152] and Krishnan [153] is obtained in Eq. 5.8.1.11

$$\Delta S = 2K_B n_o N_A \iiint [-\phi \sinh(\phi) + \cosh(\phi) - 1] \, dV \qquad 5.8.1.10$$

$$-T\Delta S = -2K_B T n_o N_A \iiint [-\phi \sinh(\phi) + \cosh(\phi) - 1] dV \qquad 5.8.1.11$$

5.8.2 Development of Multiplying Factor for Determining Particle-Cavity Energy Based on Derjaguin Approximation

Consider particle-cavity and particle-plane interacting systems shown in Figure 5.8.2.1 (A and B), with the details influencing interactions illustrated in Figures 5.8.2.1.C and D, where variables are as defined in the Figure. The interaction energy between curved surfaces can be obtained from that between infinite flat plates using Eq. 5.8.2.1 [162]:

$$E_{ij} = \int_0^\infty 2\pi E_{pp} \, h \, dh \qquad 5.8.2.1$$
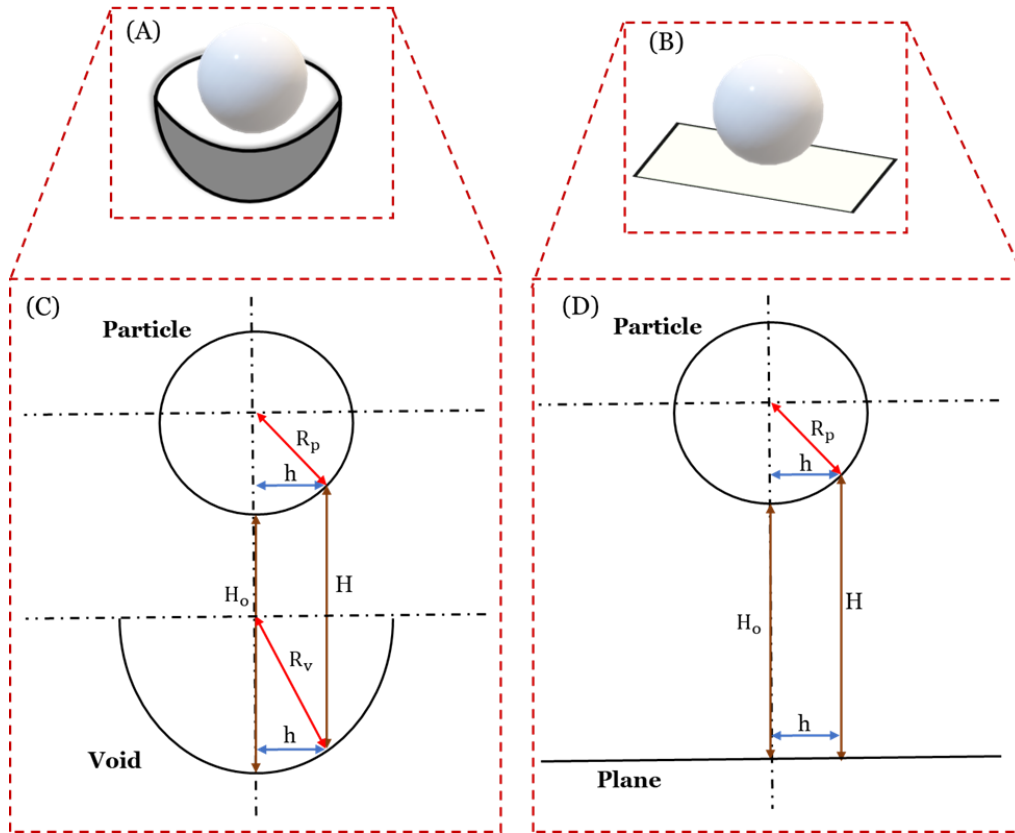
Figure 5.8.2.1: Systems of particle-cavity (A) and particle-plane (B) interactions, and details used in derivation of their transforms (C and D).

From Figure 5.8.2.1.C, we have:

$$H = R_p - \sqrt{(R_p^2 - h^2)} + H_o - \left[R_v - \sqrt{(R_v^2 - h^2)}\right] \qquad 5.8.2.2$$

Similarly, from Figure 5.8.2.1.D, we have:

$$H = H_o + R_p - \sqrt{(R_p^2 - h^2)} \qquad 5.8.2.3$$

The derivative of H with respect to h in Eqs. 5.8.2.2 and 5.8.2.3, gives Eqs. 5.8.2.4 and 5.8.2.5, respectively after rearrangement.

133

$$hdh = dH \left(\frac{1}{(R_p^2 - h^2)^{\frac{1}{2}}} - \frac{1}{(R_v^2 - h^2)^{\frac{1}{2}}} \right)^{-1}$$

<div align="right">5.8.2.4</div>

$$hdh = dH \left(R_p^2 - h^2 \right)^{\frac{1}{2}}$$

<div align="right">5.8.2.5</div>

Since $h \ll R_p$, and $h \ll R_v$, Eqs. 5.8.2.4 and 5.8.2.5 simplify to Eqs. 5.8.2.6 and 5.8.2.7, respectively.

$$hdh = dH \left(\frac{1}{R_p} - \frac{1}{R_v} \right)^{-1} = \frac{R_v R_p}{R_v - R_p} dH$$

<div align="right">5.8.2.6</div>

$$hdh = R_p dH$$

<div align="right">5.8.2.7</div>

Combining Eqs. 5.8.2.1 and 5.8.2.6 give Eq. 5.8.2.8 for particle-cavity system of finite surface-surface separation distance (l):

$$E_{sv}(l) = 2\pi \frac{R_v R_p}{R_v - R_p} \int_0^\infty E_{pp} \, dH = \Delta_{D-sv} \int_\infty^l E_{pp}(l) \, dl$$

<div align="right">5.8.2.8</div>

Where $\Delta_{D-sv} = \frac{-2\pi R_p R_v}{R_v - R_p}$

<div align="right">5.8.2.9</div>

Similarly, combining Eqs. 5.8.2.1 and 5.8.2.7 give Eq. 5.8.2.10 for particle-plane system:

$$E_{sp}(l) = 2\pi R_p \int_0^\infty E_{pp} \, dH = \Delta_{D-sp} \int_\infty^l E_{pp}(l) \, dl$$

<div align="right">5.8.2.10</div>

Therefore, by using Eqs. 5.8.2.8 and 5.8.2.10, we obtain Eq. 5.8.2.11, which relates particle-cavity system (of size ratio $0 < \frac{R_p}{R_v} < 1$) to particle-plane interactions.

$$\frac{\Delta_{D-sv}}{\Delta_{D-sp}} = \frac{R_v}{R_v - R_p} \qquad\qquad 5.8.2.11$$

Similarly, for a system of two interacting spheres of radius (R_1 and R_2), Hogg, et al. [162] showed that the geometric factor is given by Eq. 5.8.2.12

$$\Delta_{D-ss} = \frac{-2\pi R_1 R_2}{R_1 + R_2} \qquad\qquad 5.8.2.12$$

Hence, while the geometric factor for two interacting spheres (Eq. 5.8.2.12) was derived by Hogg and coworkers, the factor for sphere-cavity (Eq. 5.8.2.9) was developed by this study. Thus, both factors can be used to describe particle-cavity system from knowledge of particle-particle system, as demonstrated in this study for $E^{AB}_{132\_sv}$ in Eq. 5.14.

5.9 Chapter Postface: Important remarks on entropic contributions for the systems studied.

Here we provide remarks that address two interesting questions that emerge due to entropic trends obtained from our study.

5.9.1 Given that the interaction energies are somewhat large (in KT) in some cases, when should entropy be important?

When the energies are moderately greater or comparable to KT, thermodynamic consideration of free energies can dictate assembly since thermodynamics can dominate, and in this condition entropic contribution will be important. On the other hand, force balance or energy minimization

(not thermodynamic consideration of free energy) will govern assembly when the energies are incredibly large compared to KT, such that entropy may be insignificant in this scenario. For this latter case, assembly into a local energy minimum (with possibility of multiple energy minima) may be more feasible than through minimization of global free energy minimization. Nevertheless, it is still unknown what this transition value of energy is; below which thermodynamics can dominate, and above which local energy can govern assembly. Since energies are extensive quantities, this limited knowledge can be advanced by theoretical and experimental works investigating effects of chip size (across nanoscale and microscale) on particle assembly.

5.9.2 The interaction energy between the chip and cavity due to entropic contribution is attractive. Is there a physical mechanism by which the chip can be attracted to the cavity due to entropic contribution?

The chips (microparticles) are many orders of magnitude larger than the electrolyte ions such that the former are macroscopic objects to the thousands and millions of latter. Thus, while the chips and electrolyte ions are in contact with the solvent molecules, only the entropic contribution due to redistribution of the millions of electrolyte ions (not the chips) is significant for our system. The translation entropy of the thousands of ions makes that of the chip inconsequential. Such that a suspended chip is at a higher and unstable thermodynamic state than a chip that is attracted to (trapped on) the cavity. Therefore, it is physical that redistributions of the millions of ions can result in spontaneous attraction between the chip and the cavity.

Chapter 6 Understanding Mechanisms of Electrically Directed Particle Trapping on a Charged Line

6.1 Preface:

Results contained in this chapter are part of unpublished work.

6.2 Abstract: Statement of Research Gaps, Hypothesis and Original Contribution

Understanding particle-surface interaction is important for engineering processing systems used across industries. Electrophoretic analyses of dispersed particles and macromolecules have been widely studied and applied under different modes on both two-dimensional and well-formed geometric substrates and support media. However, little is known about electrophoretic process in a non-uniform field no-support medium on a one-dimensional substrate, yet this process provides versatility that allows for specificity and customizability desired in emerging applications. Further, a system of nanoparticles interacting with a charged line can be used to mimic and better understand the binding of ribonucleic acid (RNA) onto deoxyribonucleic acid (DNA) strand. To demonstrate electrically directed particle trapping on a charged line, we hypothesize that if the participating interaction energies and competing forces can be identified and quantified, free energy from the former can be used to do work in confining the particles on the charged line while the effects of the forces can result in capturing the trajectories of the particles during confinement. In this work, we numerically demonstrate dynamic trapping of particles onto a charged line in a non-uniform field without the need for a geometric barrier or support media, with excellent agreement with experimental observation. These confinement

demonstrations will benefit pharmaceutical industry in preferential binding of RNA molecules onto DNA strand. Our demonstrations of actively tunable and reversible particle confinement on a 1-D substrate show that electrophoresis can be conveniently tailored for specific and custom applications.

6.3 Introduction and Motivation

In this section, we introduce and discuss motivations for project 4, which is to understand the mechanism of confinement of nanoparticles on charged lines due to applied electric field. In project 4, we demonstrate electrically directed particle trapping on charged lines, which can facilitate engineering system for custom electrophoresis.

We first review electrophoresis as an established process and discuss it in relation with other electrokinetic processes and then provide motivation for nonconventional electrophoresis as a befitting process that will benefit emerging techniques for customizable, reversible, and dynamic manipulation of particle and macromolecules. By nonconventional electrophoresis, we mean a system where electrophoretic process can be realized using non-uniform field in a no-support media.

Since dielectrophoresis is another electrokinetic process that also involves movement of particles by applying electric field, we briefly discuss this process in relation to electrophoresis before focusing on discussion of the latter.

Dielectrophoresis is the movement of neutral and/or charged particles or solutes using electric field gradient under non-uniform electric field. Basically, for dielectrophoresis, ions under electric field migrate, and their movement induces a dipole in the (neutral) particle, which under a non-uniform electric field cause the particle to experience translational forces resulting in its motion. Since there is non-uniform electric field, a higher force acts on regions of stronger electric field and vice versa such that different magnitudes of force acting on the particle in opposite directions results in a net overall particle motion.

A notable distinction between electrophoresis and dielectrophoresis is the driving mechanism responsible for particle motion. For electrophoresis, this mechanism is the net electrostatic effect experienced by the particle in the system while in dielectrophoresis, this mechanism is due to difference in polarizability of the particles relative to the surrounding medium. This distinction further explains why both charged and neutral particles experience dielectrophoresis while only charged particles experience electrophoresis.

Unlike electrophoresis that is described by electrostatic force, the corresponding expression for dielectrophoretic force (F_{DEP}) is given in Eq. 6.1 below [164, 165] :

$$F_{DEP} = 4\pi R^3 \varepsilon_o \varepsilon_m [CM](\mathbf{E} \cdot \nabla)\mathbf{E} \qquad\qquad 6.1$$

Where R is particle radius, ε_o, ε_m are permittivity of free space and relative permittivity of medium, CM is the Clausius-Mossotti factor $= \left(\frac{\varepsilon_p - \varepsilon_m}{\varepsilon_p + 2\varepsilon_m}\right)$ [164, 165], which is a relative permittivity of the particle, and **E,** electric field strength. Depending on the polarizability of the particle relative to that of the surrounding medium, dielectrophoresis can be positive or negative.

If [CM] is positive, dielectrophoresis is positive, thus the particle's polarizability is greater than that of the medium such that the dielectrophoretic force is directed up a field gradient towards an electrode while when [CM] is negative, the particle's polarizability is less than that of the medium such that the dielectrophoretic force is directed away from an electrode down a field gradient [165]. Thus, from basic electric force Eq., there is no requirement for electric field to be uniform or non-uniform for electrophoretic force to be non-zero. On the contrary, the dielectrophoretic force is zero when the electric field is uniform since $\nabla \mathbf{E} = 0$. Thus, while electrophoresis typically occurs in systems having uniform electric field and can also occur where the electric field is non uniform, dielectrophoresis occurs only in a non-uniform field [165]. Also, while electrophoresis depends directly on charge, inversely on shape and size, and inversely on viscosity of the medium, dielectrophoresis depends on particle volume, particle permittivity and conductivity as well as properties (like polarizability) of the medium. It is important to note that for electrophoresis, Stoke's radius is more appropriate for accounting for size effect, which is the radius of a hard sphere that diffuses at the same rate as the ion/solute.

Having discussed dielectrophoresis in relation to electrophoresis, both resulting in particle motion, it is important to note that suspending medium can also move due to applied electric field. This phenomenon is termed electroosmosis, which is the movement of liquid through a conduit due to applied electric field. Note that for electroosmosis to exist, there must be liquid flow through a conduit due to applied electric field. Thus, in addition to occurring alone in a system, each of electrophoresis and dielectrohoresis can also occur in combination with electroosmosis, such that direction of particle motion is determined by net effect of the two processes. For example, in a system where both electrophoresis and electroosmosis exist, when one-directional electroosmotic

flow velocity is greater than electrophoretic velocity, the particle is trapped along the direction of the former, while when electrophoretic velocity > electroosmotic velocity, the particle is trapped along the direction of dominant electrophoresis direction.

Having distinguished between dielectrophoresis and electrophoresis, we now focus our discussion of electrophoresis.

Electrophoresis is an essential technique that has been widely applied for identification, analyses as well as separation of ionic, macromolecular and particle solutes. These applications utilize applied electric field to preferentially move negatively charged species (anaphoresis) and/or positively charged species (cataphoresis) and this effect is typically realized with supporting media in channels of micro and nano dimensions (capillary electrophoresis) or on one-dimensional and two-dimensional formats (slab electrophoresis). Common support media include paper, agar, agarose, polyacrylamide and starch, and they serve as molecular sieves and adsorption sites as well as to provide support during electrophoresis.

Capillary electrophoresis can be paper electrophoresis or gel electrophoresis while slab electrophoresis' types include zone electrophoresis, isoelectrofocusing and immunoelectrophoresis. Nevertheless, there can be capillary zone electrophoresis, capillary isotacophoresis, and capillary isoelectrofocusing [166], when the processes occur in systems of micro- and nano-dimensional channels.

Paper electrophoresis involves the use of buffer-saturated strip paper as the separation medium, where its ends are typically immersed in buffer reservoirs. Paper electrophoresis have found earlier applications in many industries, including fractionation of serum proteins [167], separation of radioactive products [168], separation of blood clotting factors [169], assaying of pharmaceutical products [170], and more recently for screening of infectious diseases [171], and determination of radiochemical yield [172].

In gel electrophoresis, the medium of separation is a gel, with common examples as agar, agarose, polyacrylamide and starch. Gel electrophoresis has been applied for species analyses, monitoring, assaying and separation that are relevant to several industries, including pharmaceutical [173, 174], agricultural [175, 176], biotechnology [177] and forensic [178]. Emerging applications of gel electrophoresis include utilization of two-dimensional gel electrophoresis (2-DE) with immunoblotting to identify antigenic proteins targeted by the immune system, and selective capture of metal ion-binding proteins with metal ion-embedded gel [179].

Zone electrophoresis comprises analyses and separation of charged species in a system only filled with an electrolyte buffer under an applied electric field. Capillary zone electrophoresis is arguably the most widely applied type of electrophoresis [180]. Applications of capillary zone electrophoresis are ubiquitous, including determination of inorganic ions in food samples [181], analysis of food sample [182], analysis of cephalosporin [183], separation of water-soluble clusters [184], and characterization of human milk sample [185]. Other earlier applications of capillary zone electrophoresis include analysis of vitamin [186, 187], and analysis of small molecular proteins [188]. Nevertheless, capillary zone electrophoresis is also being considered for emerging

use, as its recent applications include, bottom-up analyses of complex proteomes [189], and in combination with mass spectrometry for top-down proteomics [190], bottom-up proteomics [191], and separation of monoclonal antibodies [192]. These recent applications of capillary zone electrophoresis exist in different industrial sectors. For example, in the agricultural sector, they include analysis of tobacco [193], dipeptide monitoring in meat products [194], rapid detection of ion in seafoods [195], and lactose and lactulose quantification in milk [196]. In forensic and pharmaceutical, an example is the proving/disproving sexual assault evidence by analyzing and separating spermatozoa [197], and simultaneous determination of amines in pharmaceutical samples [198] .

While these electrophoretic methods have been widely applied using different support media and under different configurations utilizing both two-dimensional and well-formed three-dimensional geometric wells and pores, little is known about electrophoresis occurring in a no-support-media nonuniform field on a one-dimensional substrate. Yet, emerging applications requiring versatility and customizability can benefit from the latter electrophoretic method. Moreover, eliminating the need for support media can potentially reduce operating costs and simplify analytical procedures. Further, the ability to confine dispersed particles onto one-dimensional substrate can be leveraged to engineer systems for specific and custom-made applications. Thus, in project 4, we show that by utilizing first-principle physics and computational fluid dynamic simulation, we can demonstrate actively tunable, dynamic and reversible electrically directed trapping of particles onto charged lines.

6.4 Chapter Objectives

The research objectives of this project are summarized below:

- Demonstrate the thermodynamic feasibility of electrically directed trapping of nanoparticle onto a charged line by determining the relevant interaction energies.

- Apply all four relevant competing forces to numerically demonstrate the trajectories of particles undergoing electrophoresis in a system of no-support media having non-uniform field.

- Utilize numerical studies to understand the behavior of the nanoparticles, under different process conditions, including bulk behavior during trapping on positive bias, de-trapping on reverse bias, as well as particle trajectories for different number of particles and charged lines.

6.5 Methodology

6.5.1 Methodology for simulation of dynamic confinement of particles: By Interaction Energy

By using this approach of interaction energy, we only aim to find an upper bound solution since the net free energy of a system indicates maximum possible work a system can do spontaneously. In this case, the entropy change is due to mixing of ions and solvent molecules when the ions migrate due to electric field. A more accurate approach needs to capture the trajectories of the particles, and we also demonstrate this using the force approach in section 6.4.1.2.

To better understand the mechanisms of particle confinement on charged line, we model the problem under study as a system of particles (where $n_p = 5$ is the number of particles) interacting with a gold nanowire.

For particles in dilute 1:1 electrolyte medium, we can show for ideal behavior that the entropic contribution of the system is given by Eq. 6.2. This entropic contribution is due to mixing of electrolyte ions and solvent molecules (Chen, et al. [152]; (Krishnan [156]).

$$-T\Delta S = -K_B T \iiint \left[\left(\sum_i n_{io} \left(z_i \phi e^{-z_i \phi} + e^{-z_i \phi} - 1 \right) \right) \right] dV \qquad 6.2$$

Where $n_{io} (= n_o N_A)$ is number of ions of type i in bulk solution per unit volume, and z_i, ion charge. $N_A (= 6.023 \times 10^{23} \text{ mol}^{-1})$ and $K_B (= 1.381 \times 10^{-23} \frac{m^2 kg}{s^2 K})$ are the Avogadro constant and Boltzmann constant, respectively, n_o is bulk ion concentration (mol/ m^3), T, the temperature in Kelvin, $\phi \left(= \frac{e\varphi}{K_B T} \right)$ the dimensionless electrostatic potential, and φ, the electrostatic potential.

Further, electrostatic interaction energy, accounting for the contributions of both surface potential and electrolyte ions can be quantified using Eq. 6.3.

$$E_{ij}^{EL} = \frac{1}{2} \iint \sigma \varphi_s dA + \frac{1}{2} \iiint \rho \varphi dV = \frac{\varepsilon \varepsilon_o}{2} \iiint (\mathbf{E} \cdot \mathbf{E}) \, dV \qquad 6.3$$

Where φ_s is the surface potential, σ, the charge density, ε, the dielectric constant of medium and $\mathbf{E}$, the electrostatic field. The local net charge density is given as $\rho = n_0 e[\exp(-\phi) - \exp(\phi)]$, where the dimensionless electrostatic potential, $\phi = \frac{e\varphi}{K_B T}$.

In addition to electrostatic interaction and entropic contribution, gravitational, Brownian and Lifshitz-van der Waals (LW) interactions also act on the particles. Therefore, accounting for five physical interactions acting on the system, including Lifshitz-van der Waals (LW), gravitational interaction, electrostatic interaction, and entropic contributions gives the net free interaction energy of the system. When thermodynamics dominates, this net free energy can be used to move the particles from their initial positions to a lower thermodynamic state.

We utilize COMSOL for the numerical solution such that the Laplace Eq. ($\nabla^2\varphi = 0$) was implemented on the particles (each of 500 nm) with applied voltage on the nanowire (40 nm by 100 μm), mimicking the binding of proteins onto DNA strands. The Poisson–Boltzmann Eq. $\left(\nabla^2\varphi = \dfrac{2n_0 e N_A \sinh\left(\frac{e\varphi}{K_B T}\right)}{\varepsilon\varepsilon_o}\right)$ is imposed on the ion-containing liquid medium and the region of study held under electrical neutrality ($n \cdot \nabla\varphi = 0$). Further, the potential on a particle was set as -56.4 mV while the bulk medium has conductivity of 3.45 $\frac{\mu}{cm}$ S and ionic concentration of $n_o = 0.1$ $\frac{mmol}{m^3}$ NaCl. The schematics, physics, settings as well as boundary conditions used for these numerical computations are illustrated in Figure 6.1.
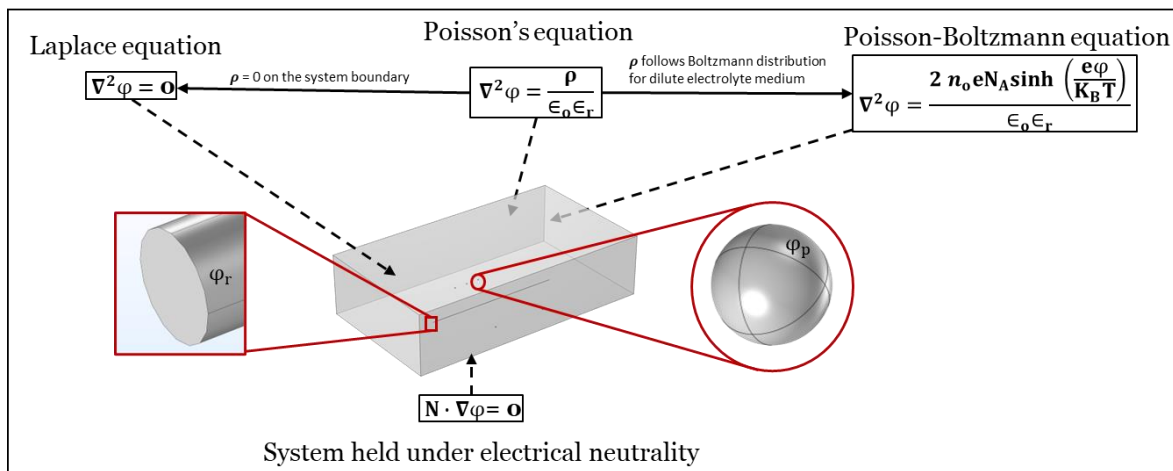
Figure 6.1

Figure 6.1: Illustration of settings, physics, and boundary conditions used for modeling electrically directed particle trapping on charged line. N_A is Avogadro's number, n_0, bulk ion concentration, ρ, local net charge density (which follows Boltzmann distribution, as shown in the figure), z, ion charge and φ, electrostatic potential.

6.5.2 Methodology for simulation of dynamic confinement of particles: By Competing Forces

To better understand the mechanisms of particle confinement on nanowire, we first model the bulk behavior of the system using the Nernst-Planck model (Eq. 6.4) to describe the motion of both electrolyte ions and the particles resulting from different mechanisms. For a system with non-flowing liquid phase where electroosmosis is not expected, the motion of charged species are due to diffusion and electromigration, resulting from concentration gradient and electrophoretic effect, respectively as described by Eq. 6.4.

$$\frac{\partial C_i}{\partial t} = \nabla \cdot \left[D_i C_i + z_i u_{m,i} C_i F \nabla \varphi - C_i \mathbf{v} \right] \qquad 6.4$$

On left hand side of Eq. 6.4 is rate of change of specie i concentration (C_i) while the right-hand side has the diffusive flux, migration flux and convective flux, respectively. D_i, z_i, and $u_{m,i}$ are species i diffusivity, charge number and mobility, and F, φ and $\mathbf{v}$ are Faraday's constant, electric potential, and velocity field.

147

$$\frac{\partial C_i}{\partial t} = \nabla \cdot \left[D_i C_i + z_i \frac{D_i}{RT} C_i F \nabla \varphi \right]$$

6.5

In Eq. 6.5, we utilized the Nernst-Einstein relation to describe specie mobility of sodium and chloride ions in terms of their diffusivities and operating temperature, T. On the other hand, the electrophoretic mobility of a spherical particle for sufficiently small zeta potential (ζ) is given by Henry Equation (Eq. 6.6) [199, 200].

$$\mu = \frac{2\varepsilon\varepsilon_o \zeta}{3\eta} f(\kappa r_p)$$

6.6

Where η, medium viscosity, κ, reciprocal of Debye length and r_p, particle radius. The function $f(\kappa a)$ is generally taken as 1.0 in the Debye–Hückel limit ($\kappa r_p \ll 1$) [199, 200] and 1.5 in Helmholtz-Smoluchowski limit ($\kappa r_p \gg 1$) [199-201]. Since ionic mobility obtained from Nernst-Einstein Eq. $\left(u_{m,i} = \frac{D_i}{RT} \right)$ is in mole basis, for a process where both the ions and particles migrate due applied electric field, electrophoretic mobility of the particle obtained from Eq. 6.6 can be converted to mole basis by dividing with the product of particle charge and Avogadro's number. The diffusivity values of common ions are well known ($D_{Cl} = 2.032 \times 10^{-5}$ (cm^2/s) and $D_K = 1.960 \times 10^{-5}$ (cm^2/s)). For the particle diffusivity, we employ the Stokes-Einstein relation to capture the effect of medium viscosity and particle size, as given by Eq. 6.7.

$$D_i = \frac{K_B T}{6\pi\eta R_h}$$

6.7

Where K_B ($= 1.381 \times 10^{-23} \frac{m^2 kg}{s^2 K}$) is Boltzmann constant, and R_h, particle hydrodynamic radius.

To capture particle dynamics during the process, we further model the problem under study as a system of particles (where $n_p = 5$ is the number of particles) interacting with a charged gold line

under the influence of four forces, including Brownian, electrophoretic, gravitational and drag. Eq. 6.8 describes these forces while Eq. 6.9 models the dynamic electric current physics using transient Eq. of continuity and Ohm's law to obtain the needed inputs.

$$\varsigma \sqrt{\frac{12\pi K_B \eta T r_p}{\Delta t}} + eZ\mathbf{E} + m_p \mathbf{g} \frac{\rho_p - \rho}{\rho_p} + \frac{18\eta}{\rho_p d_p^2} m_p (\mathbf{u} - \mathbf{v}) = \frac{d(m_p \mathbf{v})}{dt} \qquad 6.8$$

Where ς is a dimensionless random number (with zero mean and unit variance), with its independent values chosen in all directions [202], Δt, time step, $\mathbf{E}$, electric field, $\mathbf{g}$, acceleration due to gravity, ρ_p, particle density, ρ, medium density, d_p, particle diameter, m_p, particle mass, $\mathbf{u}$, medium velocity, and $\mathbf{v}$, particle velocity.

$$\nabla \cdot \left[\sigma \mathbf{E} + \frac{\partial \mathbf{D}}{\partial t} + \mathbf{J_e} \right] = Q_{j,v} \qquad 6.9$$

Where σ is electrical conductivity, $\mathbf{D}$ ($= \varepsilon \varepsilon_o \mathbf{E}$), dielectric model parameter, $\mathbf{J_e}$, externally generated current density and $Q_{j,v}$, current source. To visualize bulk distributions of ionic fluxes as well as particle flux and concentration, we utilize COMSOL to solve Eqs. 6.4 – 6.7 for the equivalent 2D model (see Figure 6.2A) with electroneutrality ($\sum_i z_i C_i = 0$) imposed everywhere. For visualizing the particle dynamics, we also use COMSOL to solve Eqs. 6.8 and 6.9 using the settings and conditions in Figure 6.2B.

$$\frac{\partial C_i}{\partial t} = \nabla \cdot \left[D_i C_i + z_i u_{m,i} C_i F \nabla \varphi - C_i \mathbf{v} \right]$$

Nernst-Planck Equations

(A)

Transient equation of continuity and Ohm's law

$$\nabla \cdot \left[\sigma \mathbf{E} + \frac{\partial \mathbf{D}}{\partial t} + \mathbf{J_e} \right] = Q_{j,v}$$

Constituent forces

$$F_B + F_E + F_D + F_G = \frac{d(m_p \mathbf{v})}{dt}$$

(B)

Particle

250 nm;
$\zeta_p = -56.4$ mV

Medium:
3.45 $\frac{\mu}{cm}$ S ;
$n_o = 0.1 \frac{mmol}{m^3}$ NaCl

50 μm

100 μm

180 μm

40 nm

Charged line

100 μm

Boundary (3D)	Setting(s)	Boundary (2D)	Setting(s)
(a) – (d), (f)	$\mathbf{n} \cdot \mathbf{J} = 0$; $\mathbf{v} = \mathbf{v_b}$	(h),(i), (l),(m)	$-\mathbf{n} \cdot \mathbf{i} = 0$
(e)	$\varphi = 0$; $\mathbf{v} = \mathbf{v_b}$	(j)	$\varphi = 0$
(g)	$\varphi =$ Applied voltage; $\mathbf{v} = 0$	(n)	$\varphi =$ Applied voltage;
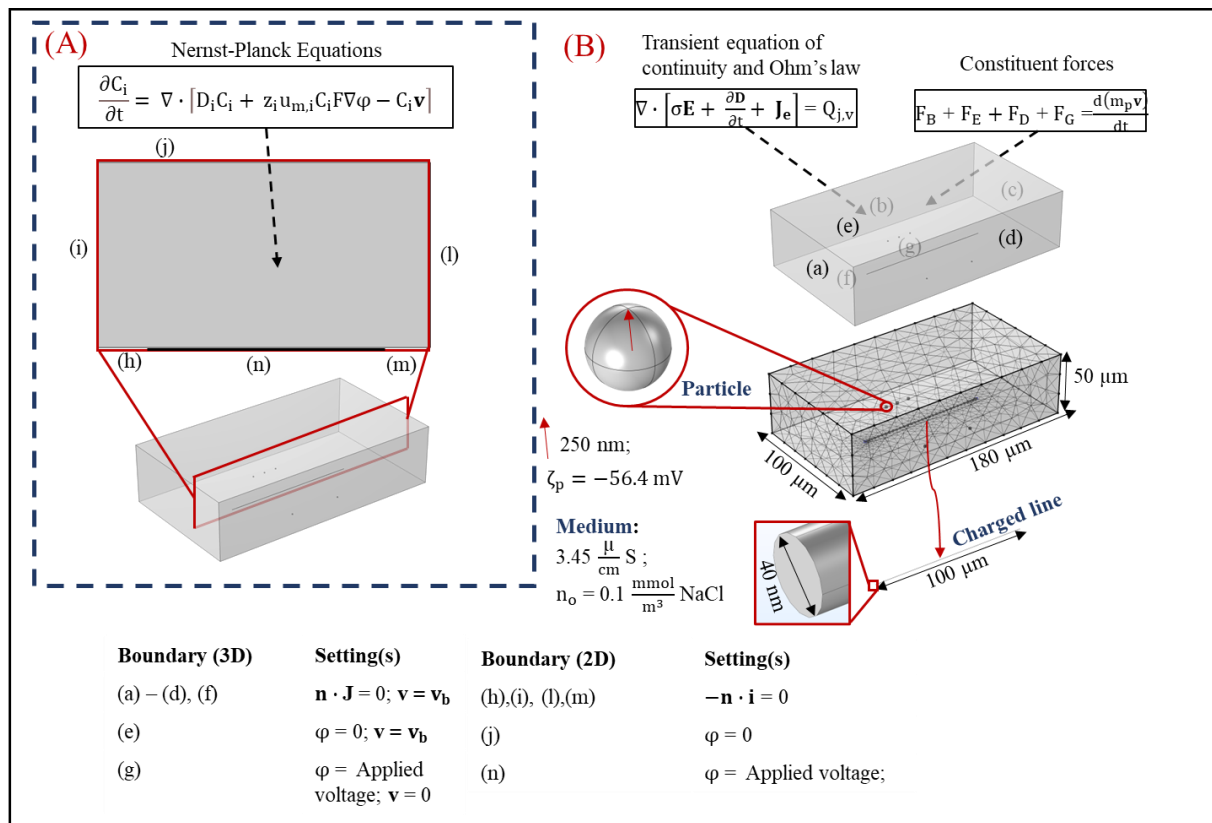
Figure 6.2: Schematics, physics, settings as well as boundary conditions used in numerical solution for electrically particle directed motion by using approach of competing forces. Figure 6.2A shows the 2D model and its physics and settings for understanding bulk behavior of the system while Figure 6.2B shows 3D model and its physics and settings for visualizing particle trajectories. n_0, bulk ion concentrationz, ion charge and φ, electrostatic potential. Electric insulation ($\mathbf{n} \cdot \mathbf{J} =$

0) where $\mathbf{J} = \sigma\mathbf{E} + \frac{\partial \mathbf{D}}{\partial t} + \mathbf{J_e}$; bounce wall condition ($\mathbf{v} = \mathbf{v_b} = \mathbf{v_c} - 2(\mathbf{n} \cdot \mathbf{v_c})\mathbf{n}$), $\mathbf{v}$ is particle velocity. Electric insulation for Nernst-Planck model, $-\mathbf{n} \cdot \mathbf{i} = 0$, where $\mathbf{i} = F\sum_j z_j\left(-D_i\nabla C_i - z_j u_{m,j} C_i F \nabla \varphi\right)$. D_j, z_j, and $u_{m,j}$ are diffusivity, charge number and mobility of specie j. C_i is species diffusivity while φ, electrostatic potential. The competing forces F_B, F_E, F_D, and F_G are Brownian force, electric force, drag force and gravitational force.

6.6 Results and Discussion

Figure 6.3 shows the instantaneous flux distributions of positive (Na^+) and negative (Cl^-) ions during electrically directed particle trapping, which results from positive bias at different applied voltages. These conditions were realized by maintaining the cathode as ground terminal and the anode at 2.0 V (Figures. A and B), 3.5 V (Figures C and D), and 5.0 V (Figures E and F), respectively.

The results show bulk movement of the electrolyte ions to electrodes of opposite terminal on positive bias. Specifically, as shown in Figures 6.3. A, C and E, the positive electrolyte ions (Na^+) migrate in bulk towards the ground terminal at the top (the cathode), while the negative electrolyte ions (Cl^-) migrate towards the charged line (the anode). These opposite directions of the electrolyte ions result from the opposing coulombic or electric forces the ions experience when electric field is applied in the system.
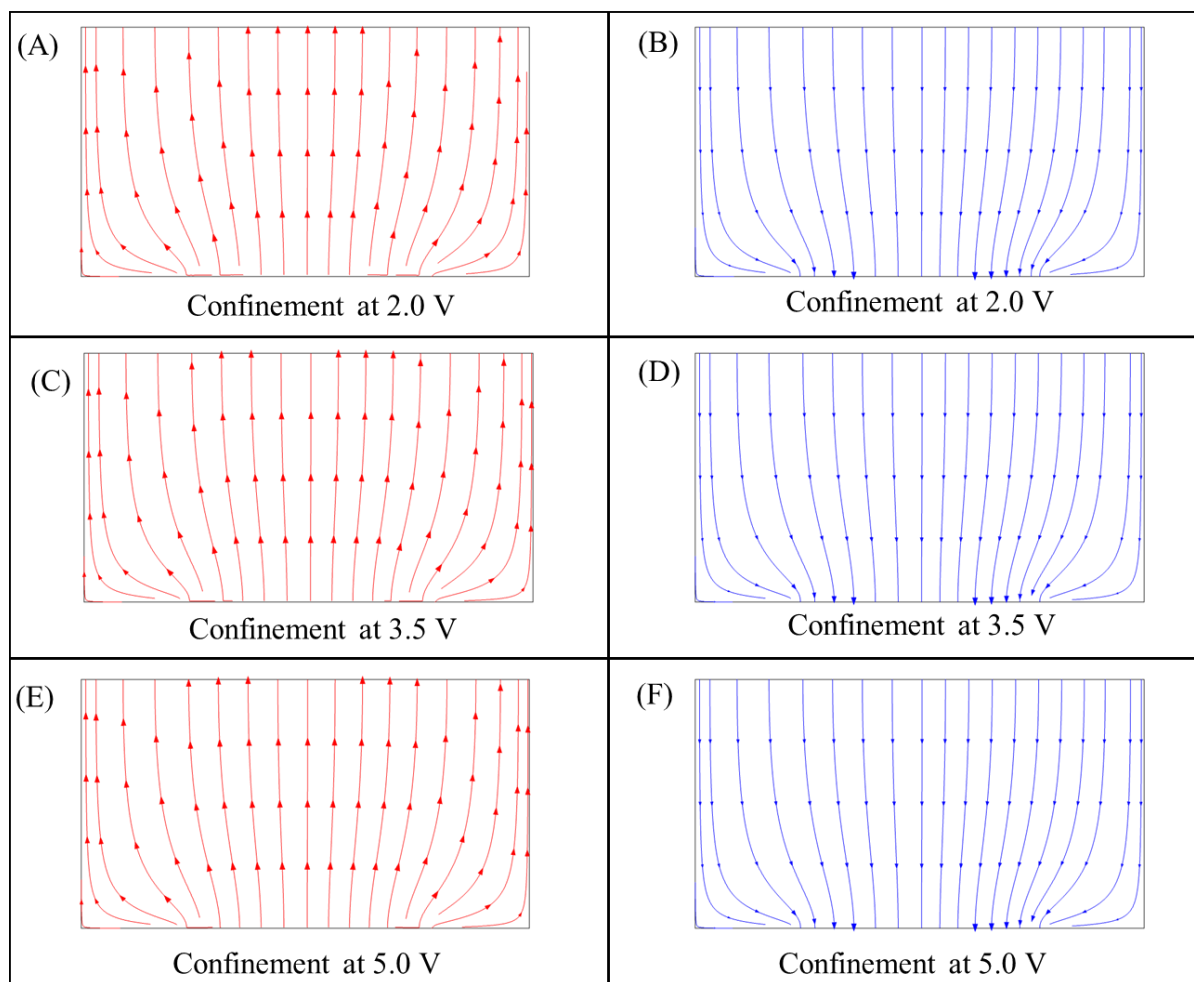
Figure 6.3: Instantaneous flux profiles of positive electrolyte ion (Na^+) (A, C, E) and negative electrolyte ion (Cl^-) (B, D, F) during electrically directed particle trapping process on positive bias using 2.0 V, 3.5 V and 5.0 V. Profiles are obtained at 1 second study time.

Figure 6.4 shows the instantaneous flux distributions of positive (Na^+) and negative (Cl^-) ions during particle de-trapping, which results from reverse bias at different applied voltages. These conditions were realized by maintaining the cathode as groundterminal and the anode at -2.0 V (Figures A and B), -3.5 V (Figures C and D), and -5.0 V (Figures E and F), respectively.

The results show bulk movement of the electrolyte ions to electrodes of opposite terminal on positive bias. Specifically, opposite to the behavior of the electrolyte ions during positive bias, as shown in Figures 6.4. A, C and E, the negative electrolyte ions (Cl^-) migrate in bulk towards the ground terminal at the top (the cathode), while the positive electrolyte ions (Na^+) migrate towards the charged line (the anode). These opposite directions of the electrolyte ions result from the opposing coulombic or electric forces the ions experience when electric field is applied in the system.
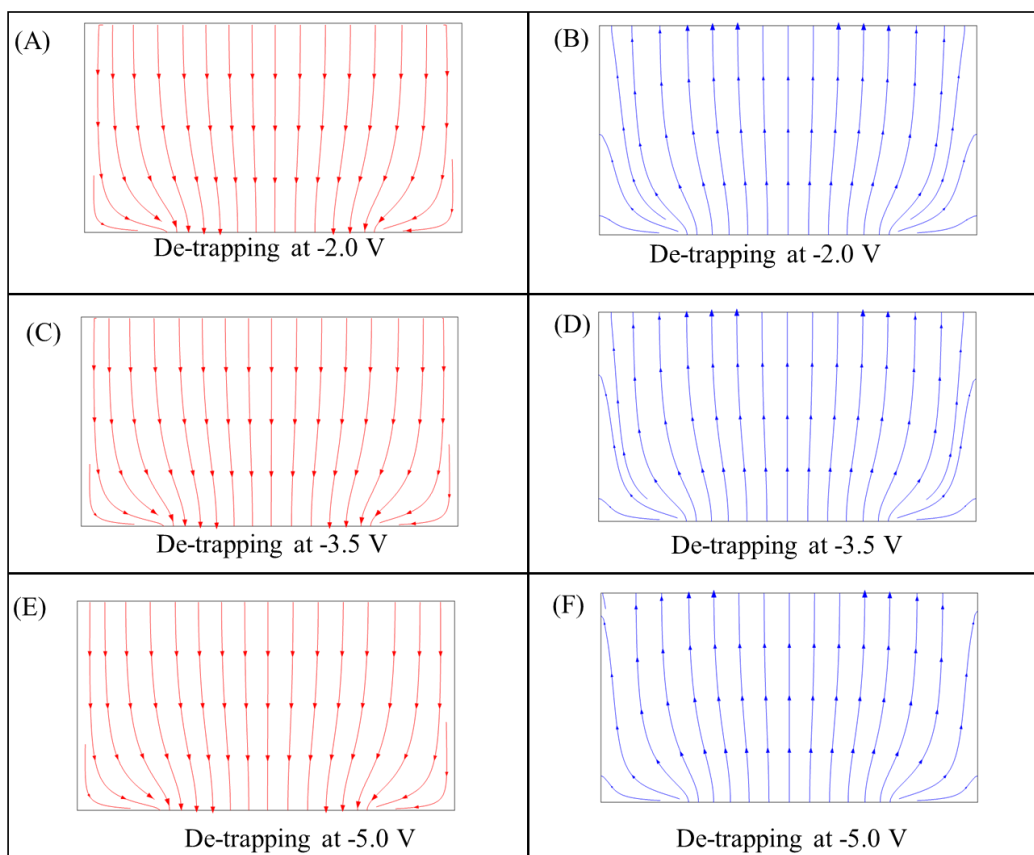
Figure 6.4: Instantaneous flux profiles of positive electrolyte ion (Na^+) (A, C, E) and negative electrolyte ion (Cl^-) (B, D, F) during electrically directed particle trapping process on positive bias using 2.0 V, 3.5 V and 5.0 V. Profiles are obtained at 1 second study time.

In addition to the electrolyte ion, the colloidal particles also experience electrostatic effects when the electric field is applied in the system.

Figure 6.5 shows the Instantaneous flux and concentration profiles of the particles (charge number -0.83) during electrically directed confinement (A, C, E) and de-trapping (B, D, F) using different applied voltages. Streamlines represent flux while color maps indicate spatial concentration distribution. Profiles are obtained at 1 second study time.

The results show bulk movement of particles to the electrode of opposite terminal on both positive and reverse bias, corresponding to particle confinement (Figures A, C, E) and de-trapping (Figures B, D, F). On positive bias, since the particles are negatively charged (charge number of -0.83, which is experimentally determined), particles are expected to be directed to the anode when electric field is applied. Indeed, the direction of streamlines representing the particle flux clearly shows that the applied electric field has a net bulk effect of moving the particles to the anode (charged line). Based on the Nernst-Planck Equation., this flux results from contributions due to electrophoretic and diffusive mechanisms (see Figure 6.7 for details).

Further, also in this positive bias, the instantaneous concentration maps show concentration gradient near the charge line, which further enhances particle trapping on charged line. Since no particle is initially on the charged line, at any time prior to equilibrium state, the number of particles in the bulk medium near the vicinity of the charged line would be greater than number of

particles already trapped on the line, thereby creating a concentration gradient. The evolution of this concentration gradient with time will be discussed later (see Figure 6.7).

Conversely, on reverse bias, since the particles are negatively charged, particles are expected to be directed to the electrode of opposite polarity such that the applied electric field has a net bulk effect of moving the particles to the top terminal (which now has positive polarity). Again, the direction of streamlines representing the particle flux clearly shows that the applied electric field has a net bulk effect of moving the particles to the top terminal (which now has positive polarity). Similarly, also in this reverse bias, the instantaneous concentration maps show concentration gradient building on boundaries other than the charge line. During de-trapping, the number of particles on the charged line continuously decreases, allowing the particles to randomly re-enter the bulk medium before migrating to the top terminal, thereby creating concentration gradient on boundaries other than the charged line.
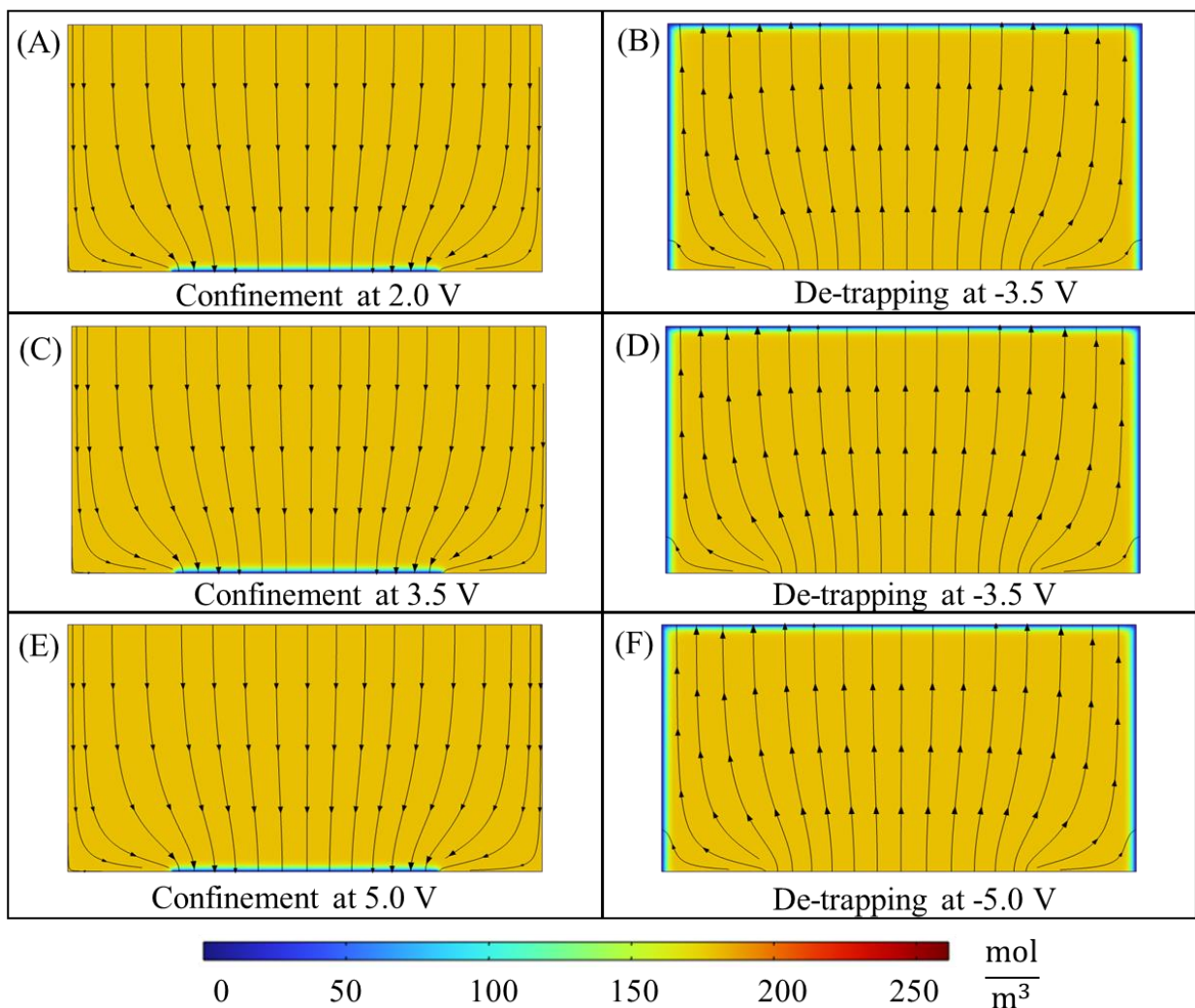
Figure 6.5: Instantaneous flux and concentration profiles of particles (500 nm diameter) of charge number -0.83 during confinement (A, C, E) and de-trapping (B,D,F) using different applied voltages. Streamlines represent flux while color maps indicate spatial concentration distribution. Profiles are obtained at 1 second study time.

Since this electrically directed particle motion is conveniently reversible by changing the polarity of the electrodes through voltage application, we now discuss the extreme ends of this reversible property. Figure 6.6 shows these four scenarios, including behavior at positive bias for particle

trapping (confinement) (A) and reverse bias for de-trapping (B) positive bias after confinement (after charged line is saturated by particles) (C) and reverse bias when no particle is on the charged line (D). Since behaviors of scenarios (A) and (B) have been discussed in the preceding paragraphs (see Figure 6.5), we now attempt to discuss the results of scenarios (C) and (D).

After particle confinement, the charged line is saturated with particles such that on further positive bias, two trends are fundamentally expected. Firstly, since the charged line is saturated, no additional particle can be trapped on the line, thus particle concentration on the line at further positive bias should be same as saturation concentration (bulk concentration). Secondly, since the particles (in the bulk medium) still experience somewhat electrostatic effect due to the polarity of the charge line, the particles still suspended in the medium will migrate towards the charge line but will not be trapped on the line. This effect would result in a decrease in particle concentration at boundaries (other than the charged line) and increase in particle concentration in bulk media near the vicinity of the charged line. As shown in Figure 6.6 C, our numerical result completely validates the first expected behavior. Also, concentration profile from our numerical result (Figure 6.6 C) also corroborate the second hypothesis, as our result clearly shows particle concentration to be lowest at the other boundaries and highest at the bulk medium near the vicinity of the charged line. Nevertheless, our result presents an asymmetric distribution of this highest concentration region with randomly aligned streamlines, which we have not found a fundamental explanation to, but we here attribute this asymmetric behavior to random flocculation of the particles when they cluster near the saturated charged line.

Conversely, prior to particle confinement, no particle is trapped on the charged line such that on further reverse bias, the particles in the bulk region directly overlying the charged line would be easily driven towards the top terminal while the particles in the bulk region aspherical the edges of the charge line will be driven spatially away thereby increasing particle concentration in the vicinity of the boundaries bounding both cross sections of the charged line. As shown in Figure 6.6 D, our numerical result completely validates both expected behaviors as depleted particle concentration is observed directly above the charged line while particle concentration is maximum at the region near the boundaries bounding the cross sections of the charged line.
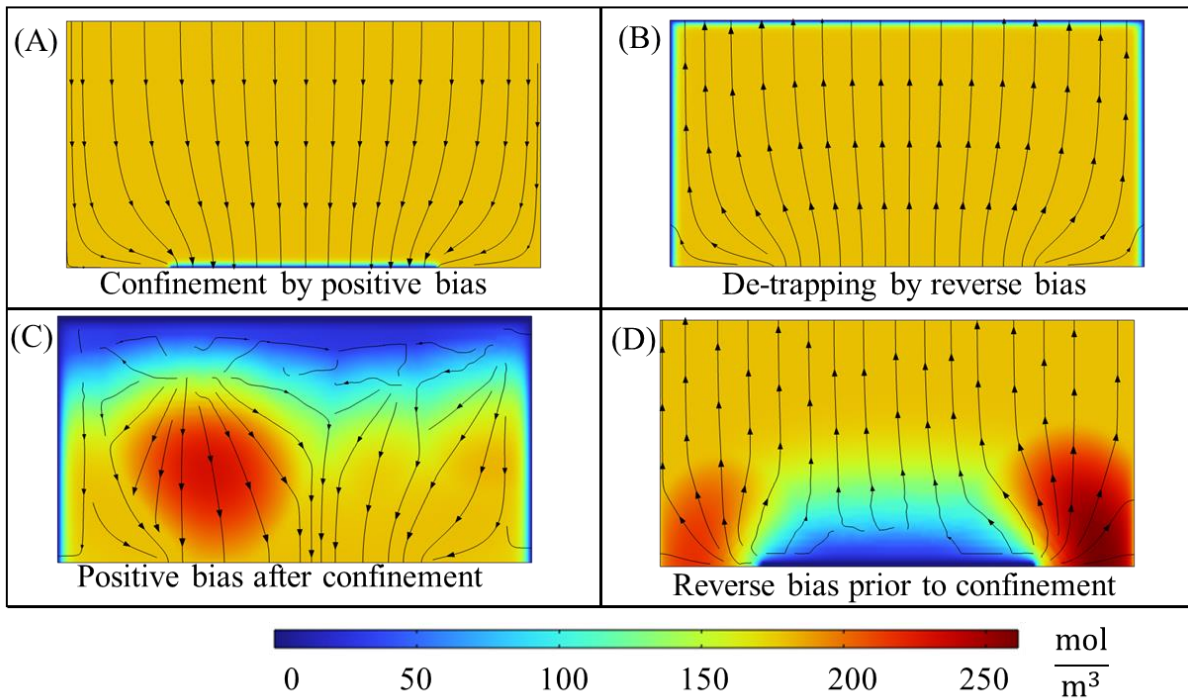
Figure 6.6: Instantaneous flux and concentration profiles of particles (500 nm diameter) of charge number -0.83 during confinement at 5V (A) and de-trapping at -5V (B) as well as distributions for positive bias at 5V after confinement (C) and reverse bias at -5V prior to

158

confinement (D). Streamlines represent flux while color maps indicate spatial concentration distribution. Profiles are obtained at 1 second study time.

Figure 6.7 compares electrophoretic and diffusive fluxes at different distances along a central axis from charge line to top terminal. The results are distributions from top ground terminal to bottom charged line obtained along central axis at 5s study time. The findings are based on modeling the system using the Nernst-Planck model, with non-flowing liquid phase where electroosmosis is not expected and in absence of pressure gradient such that fluxes of the charged species are due to diffusion and electromigration.

The results of Figure 6.7 show two interesting trends corresponding to electrophoresis and diffusion driven regions. Firstly, for the conditions studied, the electrophoretic flux is greater than the diffusive flux in the bulk with both maintaining uniform values. Therefore, this bulk region where electrophoretic flux is greater than diffusive flux can be referred to as the electrophoresis dominant region. Secondly, near the vicinity of the charged line, the diffusive flux becomes greater than the electrophoretic flux with the magnitude of the former decreases with study time. Therefore, this region near the vicinity of the charged line where diffusive flux is greater than electrophoretic flux can be referred to as the diffusion dominant region.

The implication of the first interesting trend is that, for the conditions we studied, electromigration contributes to flux of particles in the bulk region than diffusion. Thus, faster particle flux in the bulk can be engineered by tuning the electric field applied to the system. On the other hand, the implication of the second interesting trend is that, for the studied conditions, diffusion contributes

to flux of particles in the vicinity of charged line than electromigration. Thus, to design a system for efficient utilization of electrically directed particle trapping mechanism, effects of this significant diffusion resulting from random motion of the particles near the vicinity of charged line should be adequately investigated. It is important to state that the reduction in magnitude of diffusive flux as time increases is fundamentally expected since as the process evolves, more particles are trapped on the charged line, thereby resulting in reduction in concentration gradient, and ultimately diffusive flux.
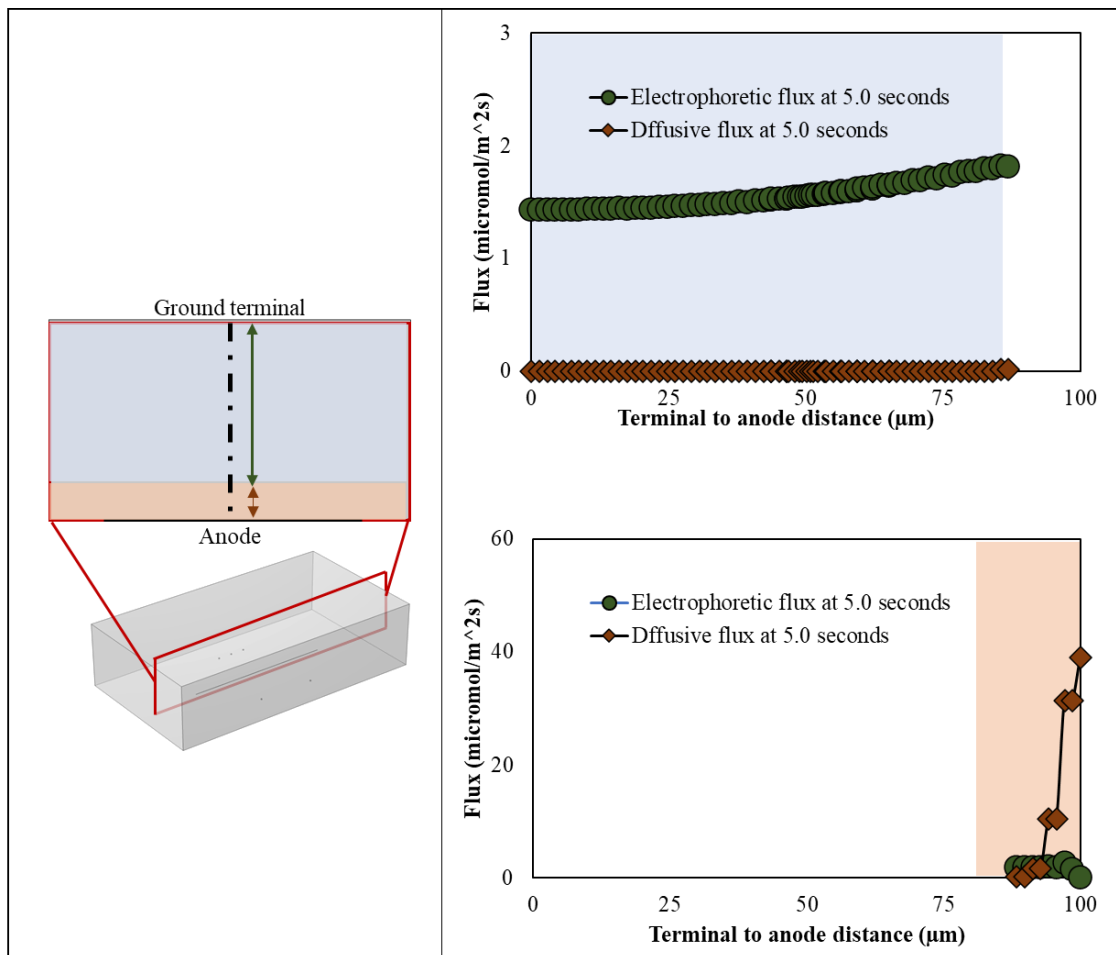
Figure 6.7: Diffusive and electrophoretic fluxes (mol/m^{2}s) of particles (initially dispersed in the suspension) at 5 s study time. Process modeled using 500 nm diameter particles with charge

number -0.83 at 5V applied voltage. Results are distributions from top ground terminal to bottom charged line obtained along central axis. The top ground terminal is origin on x-axis of the plot while upper bound value on the x-axis corresponds to the top surface of charged line facing the medium.

To understand the behavior of the particles under applied electric field, it is important to identify different electrostatic effects experienced by the particle, which are different from Brownian, drag and gravity forces. The net electric force experienced by particle comes from four electrostatic effects.

Figure 6.8 illustrate these effects, which include a) electric or coulombic force on the particle due to its surface charge, b) pull force: experienced by particle due to bulk flux of co-ions (Cl^-) in the electrolyte, during the migration of the latter to electrode of opposite polarity as a result of coulombic interaction, c) push force: experienced by the particle due to bulk flux of counterions (Na^+) in the electrolyte, during the migration of the latter to electrode of opposite polarity as a result of coulombic interaction, and d) electrophoretic retardation force (ERF): viscous stress transferred force experienced by particle due to electric force acting on counterions within the particle double layer. Since this ERF originates from the electrostatic force acting on charges (counterions) in the double layer [203], it has an opposing effect on particle motion, and thus decreases electrophoretic mobility of the particle. This ERF, and thus electrophoretic mobility of the particle depends on particle size and charge, nature of the medium as well as that of the double layer. Where in this case, the double layer generally refers to the fixed surface charge of the particle (which could be due to particle nature or a consequence of ion adsorption [204], constituting the

161

stern layer) and diffuse layer of solvated counterions shielding the particle [205], refer to Figure 6.8.
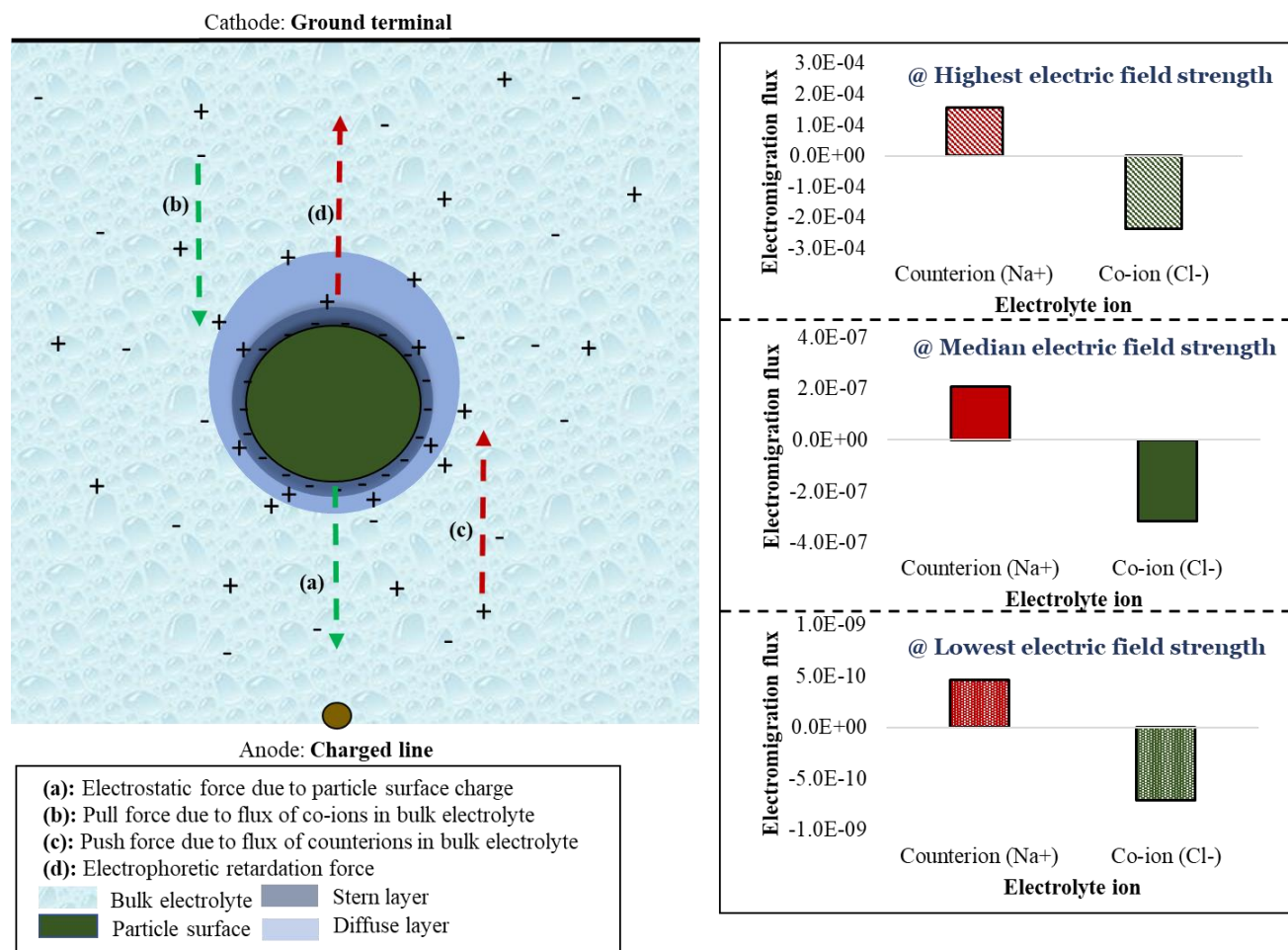
Figure 6.8: Four electrostatic effects experienced by particle in a dilute electrolyte medium due to applied electric field.

Depending on the width of the double layer relative to particle size, we have either Smoluchowski limit or Debye–Hückel limit as unified by Henry (Eq. 6.6, 6.10):

$$\mu = \frac{2\varepsilon\varepsilon_o\zeta}{3\eta}f(\kappa r_p)$$

<div align="right">6.10</div>

Where η, medium viscosity, κ, reciprocal of Debye length and r_p, particle radius. The function $f(\kappa a)$ is generally taken as 1.0 in the Debye–Hückel limit ($\kappa r_p \ll 1$) [199, 200] and 1.5 in Helmholtz-Smoluchowski limit ($\kappa r_p \gg 1$) [199-201]. In the Debye–Hückel limit, particle radius is less than Debye length, such that viscous stress transferred to the particle due to electrostatic effect on the counterion in the double layer (ERF) is reduced. On the other hand, when particle radius >>> Debye length, we have Smoluchowski limit, where ERF is more (compared to the Debye–Hückel limit).

It is noteworthy to mention that forces a) and b) act in same direction (move the particle to the anode; charged line) while forces c) and d) are opposing forces acting in reverse direction (move the particle to the cathode, top ground terminal). Also worthy of note is that drag force experienced by the particle comprises both contributions due to viscosity of the medium and that due to ERF.

The opposite directions of the electrolyte ions result from the opposing coulombic or electric forces the ions experience when electric field is applied in the system. Since the electrolyte ions experience opposing coulombic forces, and thus migrate in opposite directions, it is natural to wonder how the above four electrostatic effects (a, b, c and d) result in the net directional motion experienced by the particles. We have two answers to explain this net directional motion experienced by the particles.

Firstly, this net one-directional motion experienced by the particles results from differences in mobility of the electrolyte ions, which translate to differences in magnitudes of flux experienced by the ions. Since chloride ions having higher diffusivity than sodium ions, the negative electrolyte ions (Cl⁻) migrate faster than the positive electrolyte ions Na⁺ since the former would have higher mobility than the latter according to the Nernst-Einstein Eq. $\left(u_{m,i} = \frac{D_i}{RT}\right)$. Therefore, while positive and negative electrolyte ions are migrating in the opposite directions, the flux of the latter would be greater due to higher mobility resulting in a net one directional motion experienced by the suspended particles.

To understand why chloride ions, migrate faster than sodium ions, we analyze the fluxes of these ions at different electric fields. As shown in Figure 6.8, fluxes of the electrolyte ions are oppositely directed, with the magnitude of the co-ion (Cl⁻) > that of the counterion (Na⁺). Since flux of Cl⁻ > flux of Na⁺ due to the larger diffusivity value of Cl⁻, though Cl⁻ has larger size, the natural question that result is: Why does Cl⁻ diffuse faster than Na⁺ even when Na⁺ is smaller? The answer is that the ions do not behave as isolated ions in aqueous medium. They behave as hydrated ions. So, Na⁺ is more hydrated than Cl⁻ such that hydrated sodium ion is larger than hydrated chloride ion, allowing for the lighter Cl⁻ to diffuse faster. Specifically, Na⁺ is more hydrated with about 4-5 water molecules (Hydration number = 4 ±1) than Cl⁻ (hydration number = 1± 1). Thus, even when the bare (isolated) radius of Cl⁻ (0.181 nm) is larger than that of Na⁺ (0.095 nm), Na⁺ has larger effective (hydrated radius) of 0.36 nm than Cl⁻ (hydrated radius = 0.33 nm) [154]. This more hydration experienced by sodium is because sodium ion has smaller size and thus have more intense electric field, which results in more hydration, compared to chloride ion. The smaller size of Na+ is i) obviously due to its atom having smaller number of electron shells and ii) its ion

164

having a depleted outermost shell. Thus, based on the preceding point ii), cations generally are more solvated than anions, since they are smaller by losing electron [154].

Secondly and finally, for our system, the particles have significant negative surface charge density ($-0.83 \frac{e}{nm^2}$) such that the coulombic or electric force experience by the particles due to their surface charge is also significant. Quantitatively, surface charge density (σ) can be calculated from zeta potential, such that actual charge on particle surface (of radius, a) is proportional to $4\pi a^2 \sigma$ [205]. Therefore, since the electrolyte ions are substantially smaller than the particles (ionic radii of Na^+ and Cl^- are less than 0.3 nm, particle radius: 250 nm), the particles have sufficient negative surface charges that cause them to experience coulombic or electric force that pull them in a net one-directional motion to the positive electrode (the charged line). Therefore, the net one directional motion experienced by the particles is because for our system the combined effects of a) and b) (coulombic force on the particle due to its surface charge and supporting pull force due to bulk flux of co-ions) are greater than those of effects c) and d) (opposing push force due to bulk flux of counterions and electrophoretic retardation force).

Having adequately analyzed and discussed the bulk behavior of the particles, we now discuss the discrete behavior of the particles when they are experiencing electrically directed trapping on a charged line.

Figure 6.9 shows instantaneous locations of particles during confinement at 5.0 V. Particle one-directional motion to the charged line results from net free energy change of the system, whose contributing mechanisms include gravity, van der Waals, Brownian, entropic contribution, and

electrostatic interaction. As shown in Figure 6.9, as the study time increases from $\tau = 0$ through $\tau = 1$, the distance between each particle and the charged line decreases, thereby showing that the particles continuously approach and eventually get confined on the charged line. Nevertheless, since free energy (which is a scalar effect) of the process is being used to do work in moving the particles, only one-directional motion was achieved, which does not adequately describe the trajectories of the particles.

For a more accurate result, particle trajectories during the confinement process must be captured. To that end, we model the behavior of the system under all four relevant forces, including electric force, Brownian force, gravitational force and drag force such that the particle trajectory results from net effects of the competing forces (which is a vector effect). Results obtained that allow visualizations of particle trajectories during the electrically directed particle trapping are presented in Figure 6.10 (for a system of five particles and a charged line), Figure 6.11 (for a system of twenty particles and a charged line) and Figure 6.12 (for a system of twenty particles and five charged lines). These results agree excellently with experimentally observed behavior of the system, as the visualizations show that as study time increases from $\tau = 0$ through $\tau = 1$, the distance between each particle and the charged line decreases while also capturing the trajectories of individual particles. These are illustrated by the results of Figure 6.10 (for a system of five particles and a charged line), Figure 6.11 (for a system of twenty particles and a charged line) and Figure 6.12 (for a system of twenty particles and five charged lines). By the results of Figures 6.11 and 6.12, we have demonstrated that our model is easily scalable to meet target number of particles as well as charged lines, and thus other process conditions.
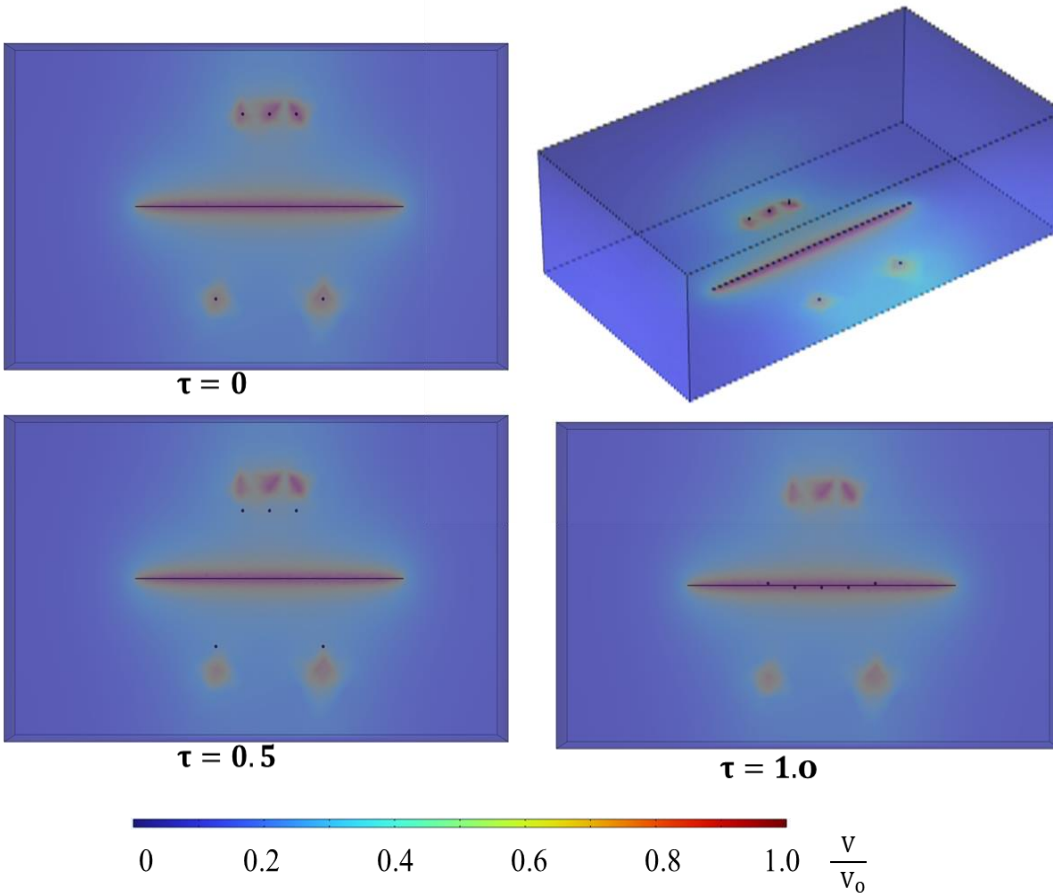
Figure 6.9: Instantaneous location of five 500 nm diameter particles during confinement at applied voltage of 5.0 V. V_0 is voltage needed to assemble n particles, τ, dimensionless time; time relative to time needed to confine the particles on a charged line. Particle one-directional motion to the charged line results from net free energy change of the system, whose contributing mechanisms include gravity, van der Waals, Brownian, entropic contribution, and electrostatic interaction.
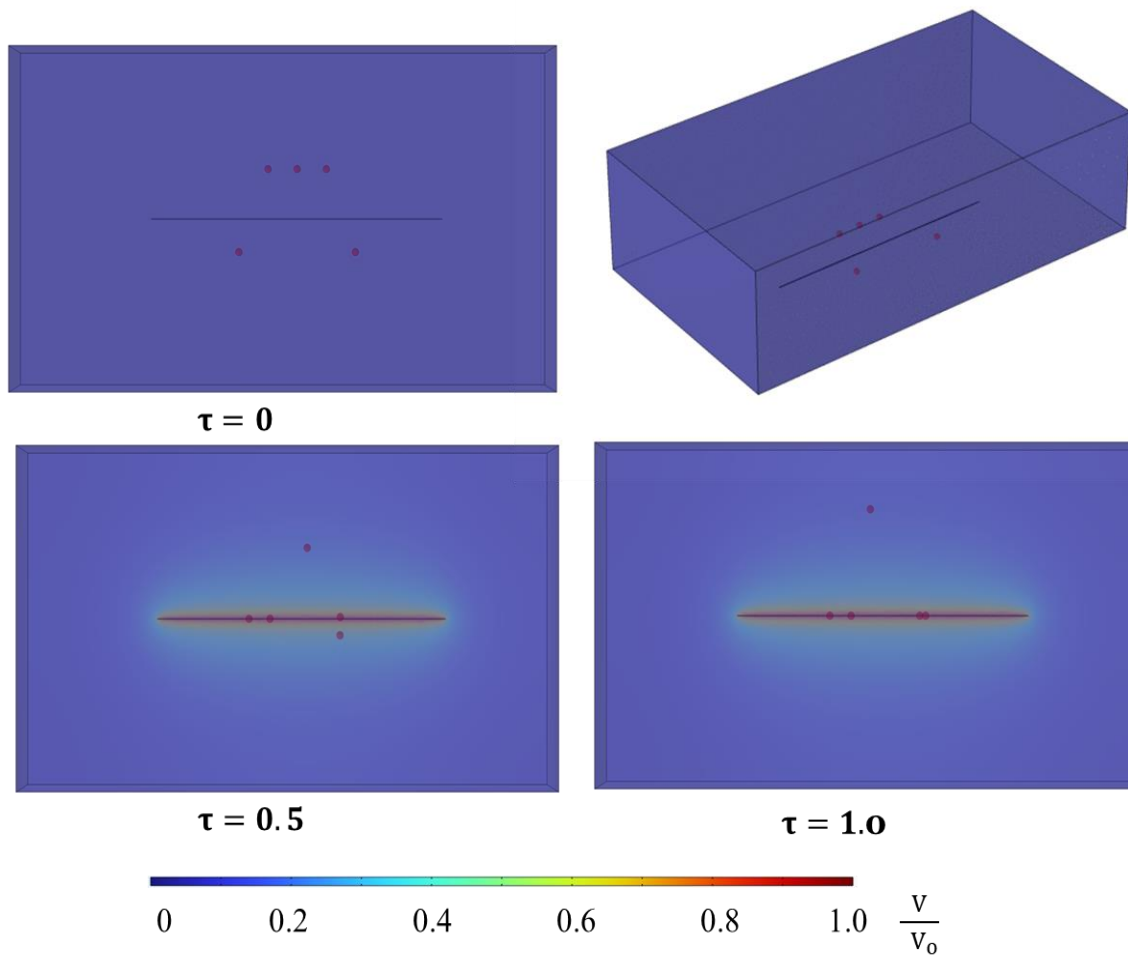
Figure 6.10: Instantaneous location of five 500 nm diameter particles of aqueous charge density - 0.83 $\frac{e}{nm^2}$ during electrically directed particle trapping at 5.0 V. Particle trajectory results from net effects of competing forces, which include electric force, Brownian force, gravity ang drag force. V_0: Applied voltage, τ, dimensionless time; time relative to study time.
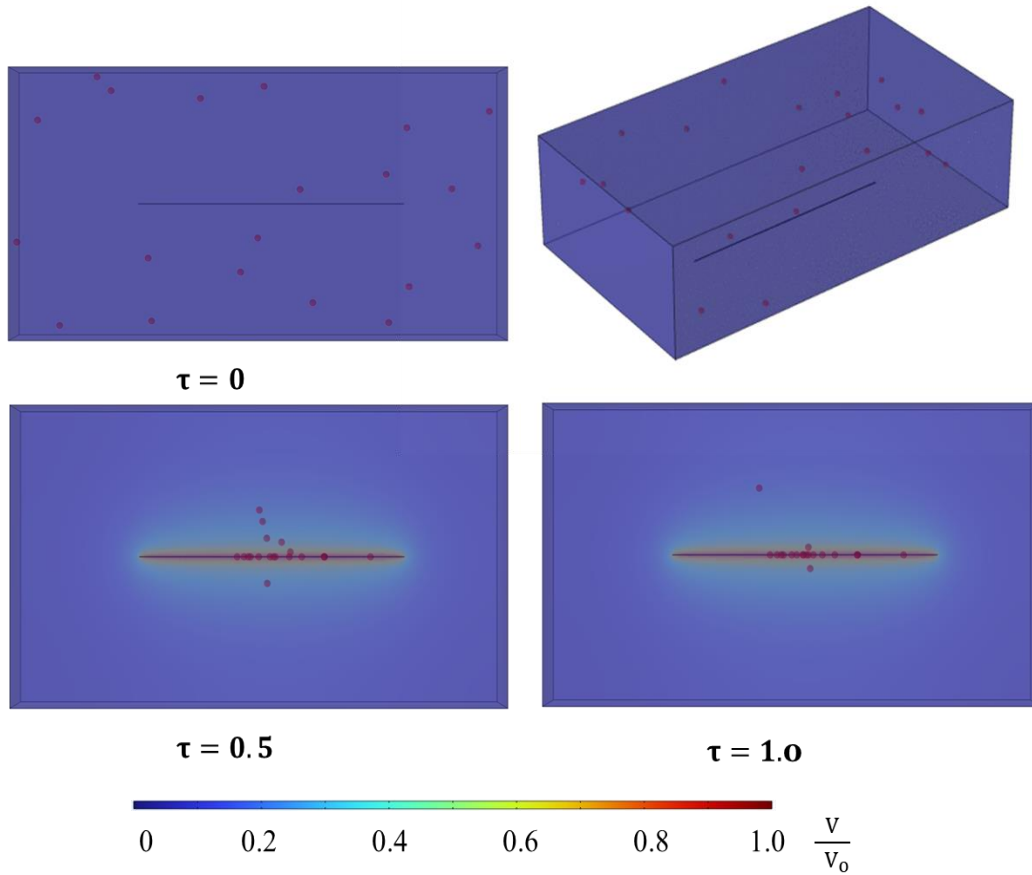
Figure 6.11: Instantaneous location of twenty 500 nm diameter particles of aqueous charge density -0.83 $\frac{e}{nm^2}$ during electrically directed particle trapping at 5.0 V. Particle trajectory results from net effects of competing forces, which include electric force, Brownian force, gravity ang drag force. V_0: Applied voltage, τ, dimensionless time; time relative to study time.
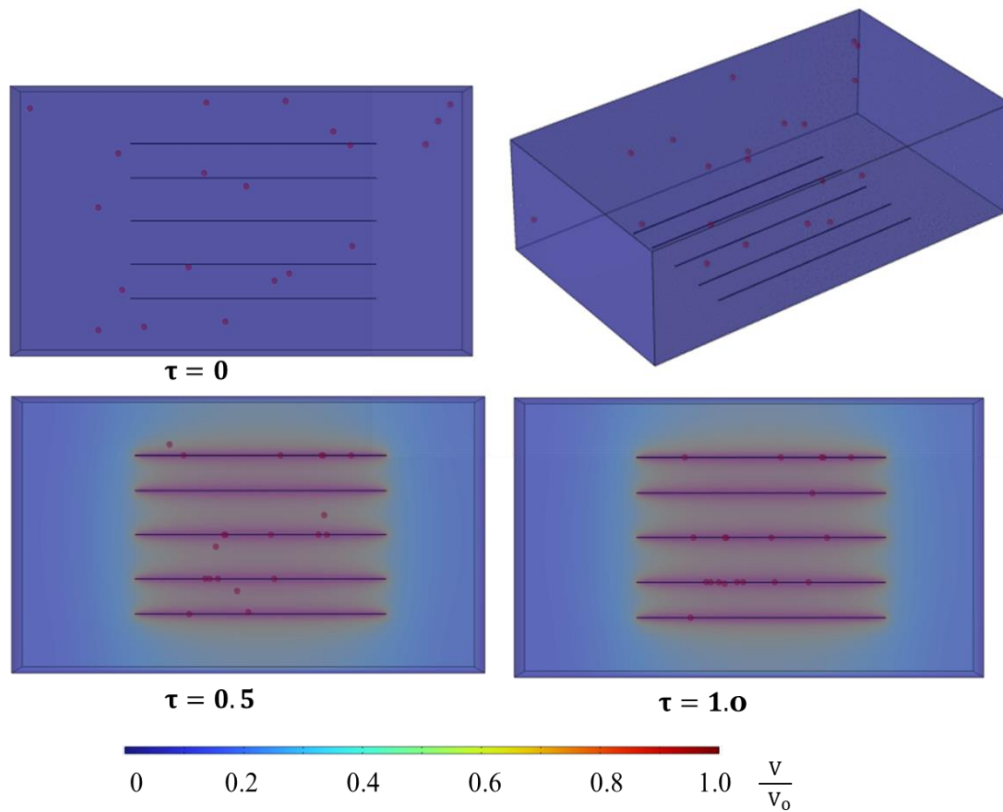
Figure 6.12: Instantaneous location of twenty 500 nm diameter particles of aqueous charge density -0.83 $\frac{e}{nm^2}$ during electrically directed particle trapping on five charged lines at 5.0 V. Particle trajectory results from net effects of competing forces, which include electric force, Brownian force, gravity ang drag force. V_0: Applied voltage, τ, dimensionless time; time relative to study time.

6.7 Conclusions

Understanding underlying mechanisms responsible for electrically directed particle trapping on charged line is important in engineering versatile electrophoretic systems, which require no-support medium and can be operated using a non-uniform electric field. In this work, we numerically demonstrate dynamic trapping of particles onto a charged line in a non-uniform field without the need for a geometric barrier or support media.

We show that electrophoretic flux of the particle is greater than diffuse flux in the bulk phase, with the former resulting as an outcome of electrostatic effects in the system. We identified these four electrostatic effects as electric or coulombic force on the particle due to its surface charge, pull force: experienced by particle due to bulk flux of co-ions in the electrolyte, during the migration of the latter to electrode of opposite polarity as a result of coulombic interaction, push force: experienced by the particle due to bulk flux of counterions in the electrolyte, during the migration of the latter to electrode of opposite polarity as a result of coulombic interaction, and electrophoretic retardation force (ERF), with the first two effects acting in same direction while the last two act in opposing direction. We introduced models to determine the magnitudes of the pull and push forces due to flux of co-ions and counter-ions.

We first quantify different energies participating during interaction of particles and charged line, calculating the contributions due to LW, Brownian, gravity, electrostatic and entropic contribution, and thus leverage this free energy to do work in moving the particles linearly to the charged line. To model the process more accurately, we considered and implemented all the competing forces

171

in the system, including Brownian force, electric force, gravitational force and drag to demonstrate dynamic confinement of the particles on the charged line, capturing the particles trajectories. We further demonstrate process scalability by modeling systems of different numbers of particles and charged lines.

Therefore, our numerical demonstrations of actively tunable and reversible particle trapping on a charged line, which agree excellently with experimental observation can benefit emerging electrophoretic applications where customizability and versatility are desired.

6.8 Appendices

6.8.1 Quantification of pull and push forces due to flux of co-ions and counter-ions.

In section 6.5, we identified four mechanisms resulting in the net electrostatic effect experienced by particle suspended in a dilute-electrolyte medium. As shown in Figure 6.8.1, these effects include a) electric or coulombic force on the particle due to its surface charge, b) electrophoretic retardation force (ERF): viscous stress transferred force experienced by particle due to electric force acting on counterions within the particle double layer, c) pull force: experienced by particle due to bulk flux of co-ions (Cl^-) in the electrolyte, during the migration of the latter to electrode of opposite polarity as a result of coulombic interaction, d) push force: experienced by the particle due to bulk flux of counterions (Na^+) in the electrolyte, during the migration of the latter to electrode of opposite polarity as a result of coulombic interaction. Determination of magnitudes of these effects is important in understanding their relative contribution to the overall effect experienced by particle. Thus, in this section, we calculate and compare the magnitude of forces due to these effects, and how they depend on particle size.

172

Effects of coulombic force on the particle due to its surface charge (effect a) and electrophoretic retardation force (ERF) (effect b) are well understood and their corresponding forces can be determined using Eqs. 6.8.1 and 6.8.2

Effect a): $F = q \, \mathbf{E}$ 6.8.1

Where q is particle charge, which can be estimated from particle size and charge density. $\mathbf{E}$ is the electric field strength. On the other hand, a force balance comprising electrostatic force, hydrodynamic friction and retardation force gives Eq. 6.8.2 for ERF [203]:

Effect b): $ERF = 6\pi\eta r_p \mathbf{E} \, (\mu_{sat} - \mu)$ 6.8.2

Where η is dynamic viscosity of the solvent medium, r_p, particle radius, and μ and μ_{sat} are mobility and saturation mobility of the particle. Determination of the latter requires experimental measurements of mobility and equilibrium mobility μ_o, with their ratio typically in the range of 1 to 4 for a system where a few dc voltages is applied [203]. Since our system under investigation is also biased with a few dc voltages, we utilize a value of 2 for this ratio.

Cathode: **Ground terminal**

Anode: **Charged line**

(a): Electrostatic force due to particle surface charge
(b): Electrophoretic retardation force
(c): Pull force due to flux of co-ions in bulk electrolyte
(d): Push force due to flux of counterions in bulk electrolyte

Bulk electrolyte   Stern layer
Particle surface   Diffuse layer
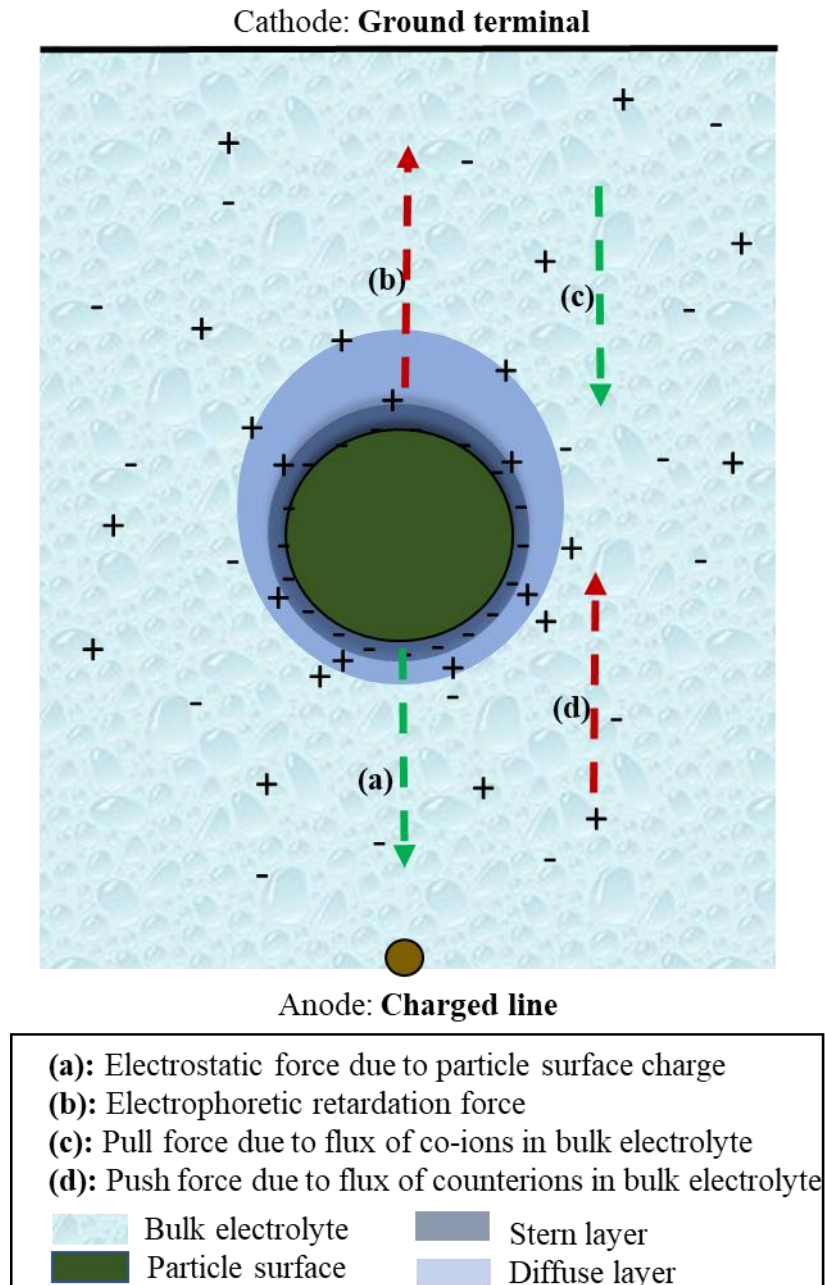
Figure 6.8.1 (Figure 6.8): Four electrostatic effects experienced by particle in a dilute electrolyte medium due to applied electric field.

Unlike effects a) and b) whose forces can be quantified using Eq.s 6.8.1 and 6.8.2, our literature survey shows that there is no reported way of quantifying forces due to effects c) and d). Thus,

174

hereafter we attempt to adapt a convenient flow model to derive a simple Eq. for estimating forces due to flux of co-ions and counter-ions, under relevant assumptions.
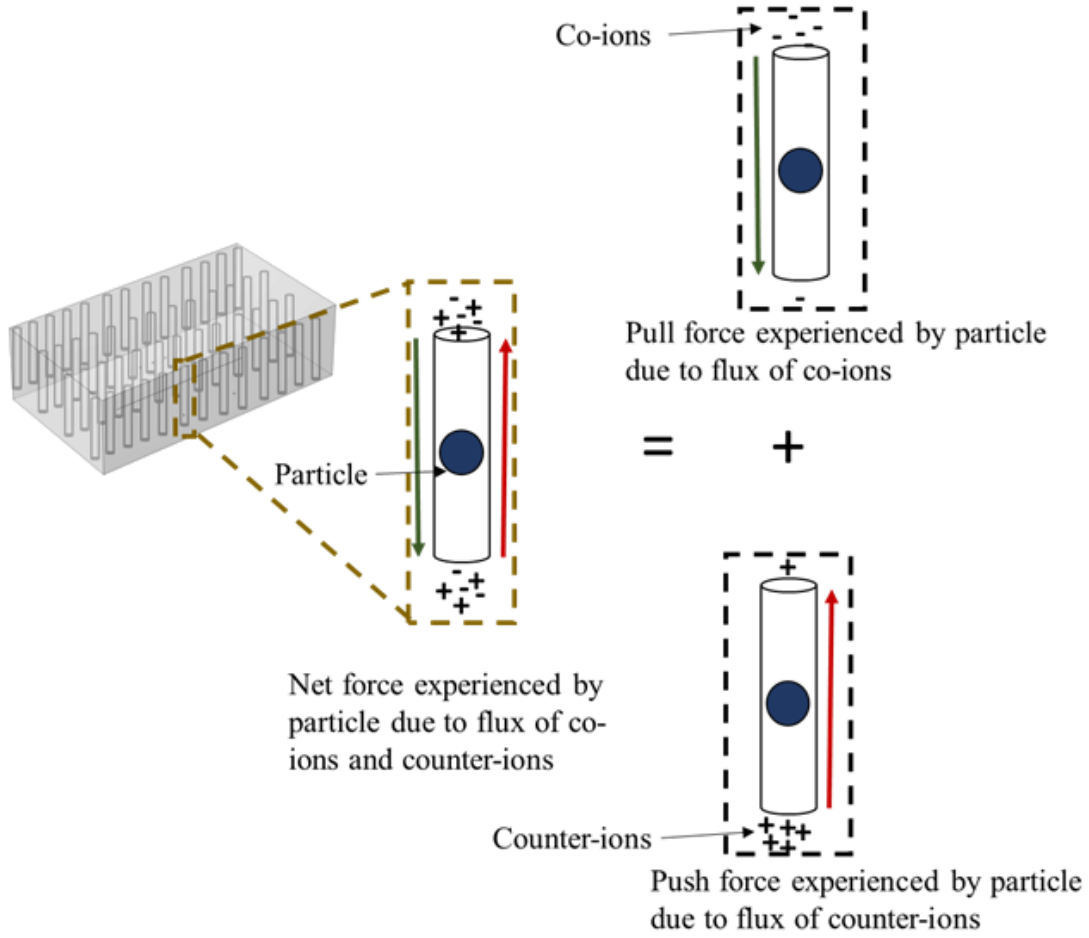
Figure 6.8.2: Schematic of the system modeled as a collection of cylindrical conduits through which the co-ions and counter-ions flow to the bottom and top planes, respectively.

To study the effects on flux of co-ions and counter-ions on a single particle, the system under investigation can be conveniently segmented as cylindrical channels with length equivalent to the distance between plane of the charged line (anode) and top ground terminal (cathode), with each cylinder having a diameter equivalent to particle diameter.

As shown in Figure 6.8.2, the net force experienced by the particle due effects c) and d) is the sum of the pull force due to flux of co-ions and push force due to flux of counter-ions. Where the number of ions (of type i) needed to cover a cross-sectional plane of the particle can be obtained from the hydrated radius of that ion and particle radius as given by Eq. 6.8.3. Such that pull force and push force experienced by the particle due to flux of a collection of co-ions and counter-ions are given by Eq.s 6.8.4 and 6.8.5

$$n_{ion-i} = \frac{d_p}{d_{ion-i}} \qquad\qquad 6.8.3$$

Where d_p is particle diameter, and d_{ion-i} is hydrated diameter of i ion.

$$F_{pull} = n_{Cl} \, \widehat{F}_{pull} \qquad\qquad 6.8.4$$

$$F_{push} = n_{Na} \, \widehat{F}_{push} \qquad\qquad 6.8.5$$

Where $\widehat{F}_{pull}$ and $\widehat{F}_{push}$ are the pull force and push force experienced by the particle due to the flux of a single chloride ion and sodium ion, respectively.

As shown in Figure 6.8.2, the flux of a group of ion each of similar type can be modeled as a laminar flow through a cylindrical conduit connecting the top and bottom planes, such that the pressure drop (ΔP) across each channel can be modeled by the Hagen-Poiseuille Eq. of 6.8.6. By

this approximation, we have assumed that the flow of ions is incompressible and Newtonian, which are pertinent since the ions flow through water.

$$\Delta P = \frac{8\eta LQ}{\pi r_p^4} \qquad\qquad 6.8.6$$

Where Q is volumetric flow rate and L, the length of conduit. Thus, by combining Eqs. 6.8.3 – 6.8.6 and the properties of the system, we obtain Eqs. 6.8.7 and 6.8.8 for pull force and push force acting on a single particle due to flux of co-ions and counter-ions, respectively.

$$F_{pull} = \frac{n_{Cl}8\pi\eta J_{Cl}M_{Cl}L}{\rho} \qquad\qquad 6.8.7$$

$$F_{push} = \frac{n_{Na}8\pi\eta J_{Na}M_{Na}L}{\rho} \qquad\qquad 6.8.8$$

Where J_i and M_i are molar flux and molecular weight of ion i, and ρ is solvent density.

Figure 6.8.3 shows the magnitudes of forces due to these four effects and their dependence on particle size. The results show that, in terms of magnitudes, the forces are in the order of effect A > effect C ~ effect B > effect D, showing that for the particle size range studied, coulombic force due to particle surface charge is the dominant effect with this mechanism contributing attractive forces of -27 pN for 40 nm particle and -4178 pN for 500 nm particle. Nevertheless, since the contribution from effect A can be tuned by particle surface charge density, the contributions from the other effects are not negligible and thus can be made dominant since their values are also in the order of a few picoNewtons. Among these three effects (B, C and D) for the conditions studied, push force due to flux of counterions is the smallest while the pull force and electrophoretic retardation force are comparable in magnitude.

Figure 6.8.3: Forces due to the four electric effects acting on the particle and their dependence on particle size.

Chapter 7 Thesis Summary and Future Directions

7.1 Thesis Summary

In this Ph.D. study, we applied first-principle physics, computational fluid dynamic (CFD) simulation, scientific experimentation, model development and process design to develop scalable pathways for addressing critical constraints of emerging manufacturing processes, which can benefit semiconductor, specialty chemicals and pharmaceutical industries.

We investigate four key objectives, including development of pathway for boosting material utilization efficiency (MUE) in organic vapor phase deposition (OVPD), scalable hardware design for effective vapor mixing and substrate heating management in OVPD, development of pathway for cost-effective micro-LED assembling and understanding interactions energies and numerical demonstration of electrically directed particle trapping on a charged line.

In Chapter 3, we develop and thus introduce a model that predicts material utilization efficiency (MUE) in OVPD, which is numerically and experimentally supported. Our results show that area ratio (substrate to chamber cross section) drives MUE, and that by engineering location of the thermal boundary layer, organic vapor can deposit on additional planes of the substrate thereby further boosting MUE. Our proposed system configuration can deliver > 75 % MUE and be adapted to support both batch and continuous manufacturing modes.

In Chapter 4, we investigate effects of process conditions assessing the influence of carrier gas flow rates and evaporation temperatures on vapor transport mechanisms and demonstrate a method for scalable design of OVPD hardware to realize effective vapor mixing. Our approach can be used to predict hardware aspect ratio needed to achieve effective vapor mixing.

In Chapter 5, we investigate relevant interaction energies affecting mass assembling of microparticles onto substrate cavities, as well as their dependence on fill factor, particle size and particle shape. Our study accounted for contributions due to Lifshitz-van der Waals (LW), electrostatic interactions, entropic contribution, gravity and interfacial Lewis acid base (AB) interaction on overall energetics of micro-LED chip-receiver cavity system. Our assessment of the energies shows preferential mass assembling of the chips can be made thermodynamic favorable by tuning surface potential and surface energy of the substrate cavities, leveraging entropy and interfacial AB interactions, respectively. Our proposed conditions for preferentially chip assembling can inform the system for cost-effective particle assembling.

In Chapter 6, we numerically investigate mechanisms responsible for electrically directed particle trapping on charged lines under the influences of all four competing forces, including electric force, Brownian force, gravitational force and drag force. Our demonstrations of actively tunable and reversible particle confinement on charged lines show that electrophoresis can be conveniently tailored for specific and custom applications. Our numerical model can be easily scaled and used to describe processes where electrically directed trapping or manipulation of particles is desired.

7.2 Future Directions

7.2.1 Emerging Illumination Technology: Proposed System for Organic Vapor Deposition
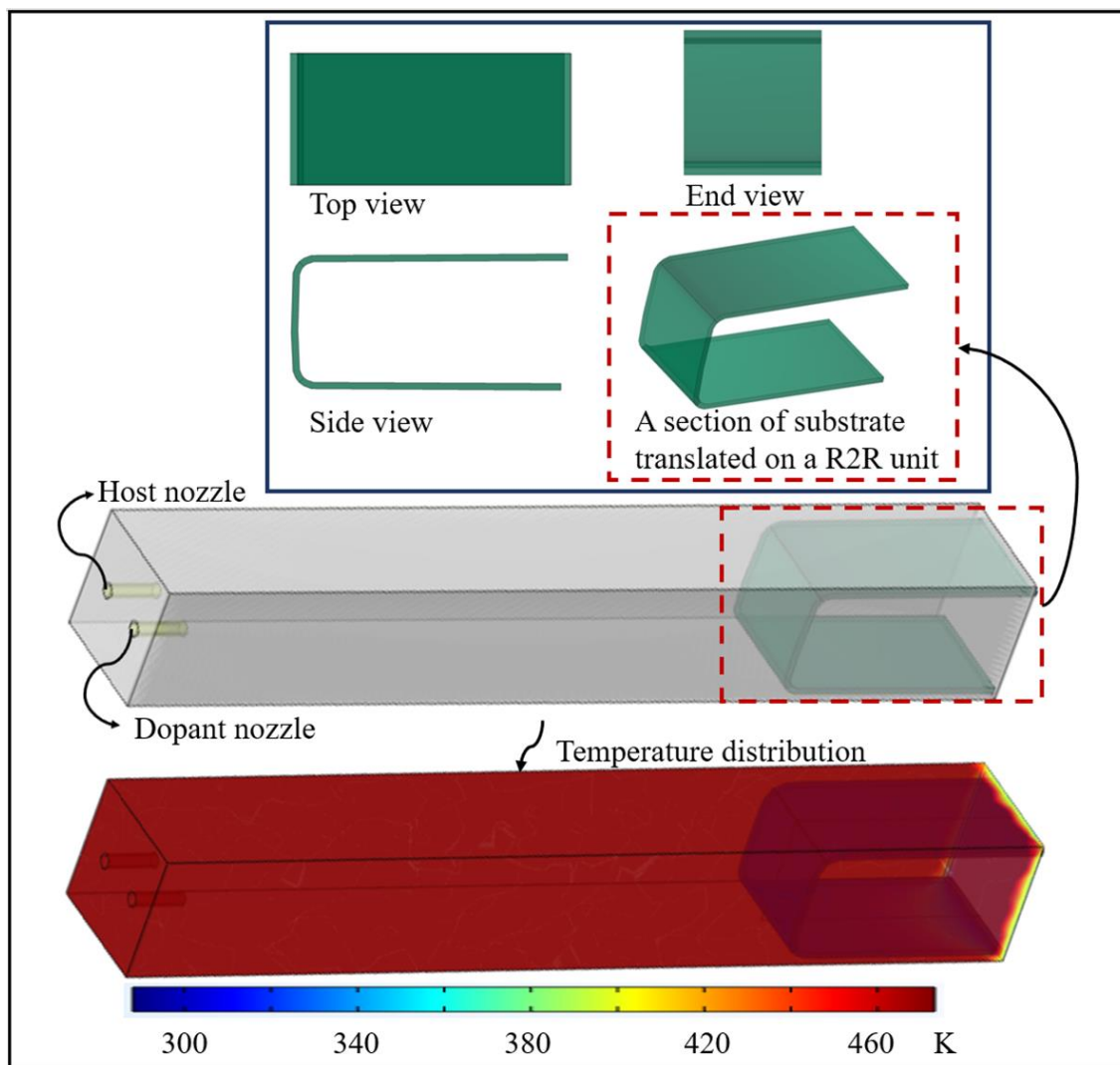
Figure 7.1 (Figure 3.10): Proposed OVPD configuration that can deliver > 75 % MUE, with temperature profiles demonstrating the existence of thermal boundary layer near the cooled substrate.

7.2.2 *Emerging Display Technology: Proposed Conditions for Leveraging Interfacial Energies for Particle Mass Assembly*

(a) $E_{ij}^{FR} > 0$; Non-wetting

(b) (c) (d) $E_{ij}^{FR} < 0$; Wetting

LW interactions

Gravitational interaction

Electrostatic interaction

Reference shape   Model shape

Interaction due to Brownian free energy

Entropy

Lewis acid-base interaction
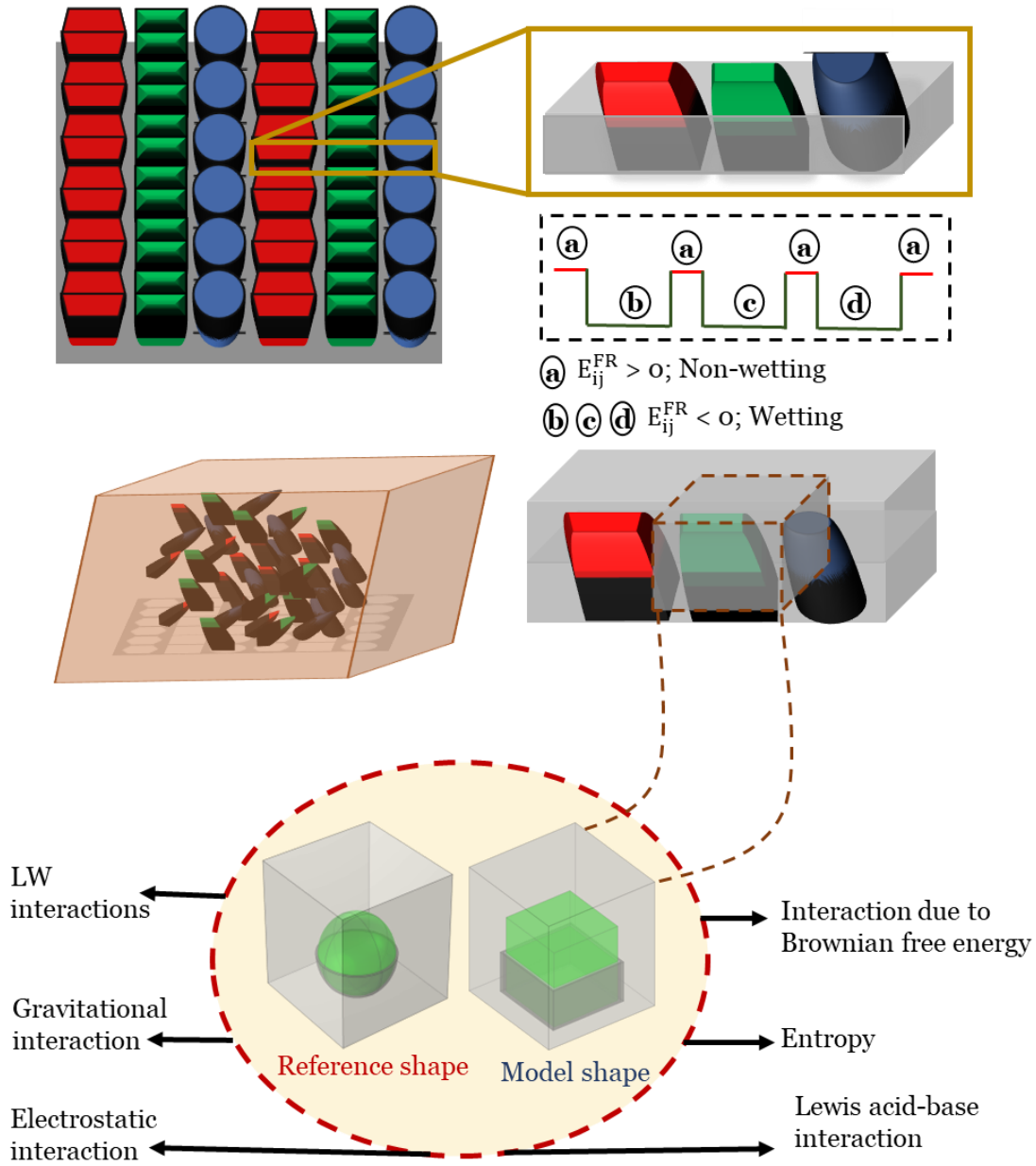
Figure 7.2: Proposed conditions for leveraging entropy, electrostatics as well as and interfacial Lewis acid-base for preferential particle mass assembling.

7.2.3 Recommendations for Future Studies

- In Chapter 3, we find that material utilization efficiency in OVPD is majorly driven by area ratio in the diffusion regime, and further leveraged insights from the MUE model to propose hardware design guideline that can deliver > 75 % MUE. Since high MUE allows for more efficient film deposition as well as reduced operating cost, we therefore recommend future studies to implement our guidelines by experimentally testing MUE with the hardware configuration we designed and proposed, as well as a modification on the introduced MUE model to capture the contributions of the films deposited on the tangential planes.

- In Chapter 4, we demonstrated a method for predicting hardware aspect ratio needed to achieve effective vapor mixing, and experimentally showed that 10X increase in sublimation rate can be achieved by tuning chamber pressure in OVPD. Since sublimation is the upstream process during OVPD, with significant relation with film deposition, we therefore recommend future studies to test and optimize effects of chamber pressure on film deposition rate.

- In Chapter 5, we investigated how different interaction energies affect mass assembling of particles onto non-conventional surfaces, with focus on identifying pathways for cost-effective mass assembling of micro-LED chips on cavities of receiver plane. Our findings showed that preferential mass assembling of particles can be made thermodynamic

favorable by tuning surface potential and surface energies on the receiver plane, leveraging entropy, electrostatics as well as and interfacial Lewis acid-base. Since high-yield mass assembling of micro-LEDs will facilitate wider adoption of micro-LED technology, we therefore recommend future studies to implement our guidelines by experimentally testing particle mass assembling on substrate cavities using the method and conditions we designed and proposed. Since this study investigated spherical (reference) and cubic (model) chips, and chips of other shapes are relevant to the industry, we also recommend future studies to investigate how other particle shapes affect these participating interactions during mass assembling of particles.

- In Chapter 6, we find that, in addition to drag force, gravitational force, and Brownian force, the net electric force experienced by particle in a no-support media electrophoretic system is due to four effects, including a) electric or coulombic force on the particle due to its surface charge, b) pull force: experienced by particle due to bulk flux of co-ions in the electrolyte, during the migration of the latter to electrode of opposite polarity as a result of coulombic interaction, c) push force: experienced by the particle due to bulk flux of counterions in the electrolyte, during the migration of the latter to electrode of opposite polarity as a result of coulombic interaction, and d) electrophoretic retardation force (ERF): viscous stress transferred force experienced by particle due to electric force acting on counterions within the particle double layer. In this study, we adequately quantified and explained the reasons why contribution from effect b) is greater than that from effect c) as well as justified the significance of effect a). However, we know that effect d) can be significant. Thus, we recommend future studies to study the relative contribution and

quantification of effect d) and how it compares among the effects, for different electrolyte concentrations and particle properties. We also recommend experimental testing of the models for pull and push forces introduced in this study.

References

1. D. MacIsaac, Kanner G., and Anderson G., *Basic physics of the incandescent lamp (lightbulb).* The physics teacher, 1999. **37**(9): p. 520-525.
2. J. Coaton and Fitzpatrick J., *Tungsten-halogen lamps and regenerative mechanisms.* IEE Proceedings A (Physical Science, Measurement and Instrumentation, Management and Education, Reviews), 1980. **127**(3): p. 142-148.
3. M. Aman, Jasmon G., Mokhlis H., and Bakar A., *Analysis of the performance of domestic lighting lamps.* Energy policy, 2013. **52**: p. 482-500.
4. W. H. Hayt and Buck J. A., *Engineering electromagnetics*. Vol. 1. 2006: Erlangga.
5. G. Tan, Huang Y., Li M.-C., Lee S.-L., and Wu S.-T., *High dynamic range liquid crystal displays with a mini-LED backlight.* Optics express, 2018. **26**(13): p. 16572-16584.
6. Z. Chen, Yan S., and Danesh C., *MicroLED technologies and applications: characteristics, fabrication, progress, and challenges.* Journal of Physics D: Applied Physics, 2021. **54**(12): p. 123001.
7. D. DiLaura, *A brief history of lighting.* Optics and Photonics News, 2008. **19**(9): p. 22-28.
8. F. Furfari, *A different kind of chemistry: a history of tungsten halogen lamps.* IEEE Industry Applications Magazine, 2001. **7**(6): p. 10-17.
9. G. A. Freeman, *Trends in high-intensity mercury lamps.* Electrical Engineering, 1940. **59**(11): p. 444-447.
10. R. V. Steele, *The story of a new light source.* Nature photonics, 2007. **1**(1): p. 25-26.
11. M. Thumm. *Historical German contributions to physics and applications of electromagnetic oscillations and waves*. in *Proc. Int. Conf. on Progress in Nonlinear Science, Nizhny Novgorod, Rusia*. 2001.
12. P. Sinioros, Anastasatou M., Kavouri S., Lasithiotakis M., and Stamatakis M., *A preliminary study of the concentration of special purpose elements and precious metals in the enriched precipitates produced by a wet method of cathode-ray tube recycling.* Journal of Material Cycles and Waste Management, 2020. **22**: p. 524-535.
13. J.-C. G. Bünzli, *Lanthanide luminescence: from a mystery to rationalization, understanding, and applications*, in *Handbook on the Physics and Chemistry of Rare Earths*. 2016, Elsevier. p. 141-176.
14. E. W. Herold, *A history of color television displays.* Proceedings of the IEEE, 1976. **64**(9): p. 1331-1338.
15. H. Pan, Feng X.-F., and Daly S. *LCD motion blur modeling and analysis*. in *IEEE International Conference on Image Processing 2005*. 2005. IEEE.
16. C. S. Matsumoto, Shinoda K., Matsumoto H., Funada H., Minoda H., and Mizota A., *Liquid crystal display screens as stimulators for visually evoked potentials: flash effect due to delay in luminance changes.* Documenta Ophthalmologica, 2013. **127**: p. 103-112.
17. S. Herat, *Recycling of cathode ray tubes (CRTs) in electronic waste.* CLEAN–Soil, Air, Water, 2008. **36**(1): p. 19-24.

18. A. R. Anwar, Sajjad M. T., Johar M. A., Hernández-Gutiérrez C. A., Usman M., and Łepkowski S., *Recent Progress in Micro-LED-Based Display Technologies.* Laser & Photonics Reviews, 2022. **16**(6): p. 2100427.

19. S. Kobayashi, Mikoshiba S., and Lim S., *LCD backlights*. 2009: John Wiley & Sons.

20. Y. Huang, Hsiang E.-L., Deng M.-Y., and Wu S.-T., *Mini-LED, Micro-LED and OLED displays: present status and future perspectives.* Light: Science & Applications, 2020. **9**(1): p. 105.

21. C.-H. Kim, Kwon I.-E., Park C.-H., Hwang Y.-J., Bae H.-S., Yu B.-Y., Pyun C.-H., and Hong G.-Y., *Phosphors for plasma display panels.* Journal of Alloys and Compounds, 2000. **311**(1): p. 33-39.

22. X. Wu, Li F., Wu W., and Guo T., *Flexible white phosphorescent organic light emitting diodes based on multilayered graphene/PEDOT: PSS transparent conducting film.* Applied surface science, 2014. **295**: p. 214-218.

23. N. T. Kalyani and Dhoble S., *Organic light emitting diodes: Energy saving lighting technology—A review.* Renewable and Sustainable Energy Reviews, 2012. **16**(5): p. 2696-2723.

24. A. Ugale, Kalyani T. N., and Dhoble S. J., *Potential of europium and samarium β-diketonates as red light emitters in organic light-emitting diodes*, in *Lanthanide-Based Multifunctional Materials*. 2018, Elsevier. p. 59-97.

25. B. Geffroy, Le Roy P., and Prat C., *Organic light-emitting diode (OLED) technology: materials, devices and display technologies.* Polymer international, 2006. **55**(6): p. 572-582.

26. H. Kawamoto. *The history of liquid-crystal display and its industry*. in *2012 Third IEEE HISTory of ELectro-Technology CONference (HISTELCON)*. 2012. IEEE.

27. J. Boeuf, *Plasma display panels: physics, recent developments and key issues.* Journal of physics D: Applied physics, 2003. **36**(6): p. R53.

28. A. Laaperi, *OLED lifetime issues from a mobile-phone-industry point of view.* Journal of the Society for Information Display, 2008. **16**(11): p. 1125-1130.

29. D. Chitnis, Swart H., and Dhoble S., *Escalating opportunities in the field of lighting.* Renewable and Sustainable Energy Reviews, 2016. **64**: p. 727-748.

30. S. Pimputkar, Speck J. S., DenBaars S. P., and Nakamura S., *Prospects for LED lighting.* Nature photonics, 2009. **3**(4): p. 180-182.

31. B. W. D'Andrade and Forrest S. R., *White organic light-emitting devices for solid-state lighting.* Advanced Materials, 2004. **16**(18): p. 1585-1595.

32. I. Jun, Han S. J., Shin H.-S., Kim J., Kim E. K., Kim T.-i., Yoon S. C., and Seo K. Y., *Comparison of ophthalmic toxicity of light-emitting diode and organic light-emitting diode light sources.* Scientific reports, 2020. **10**(1): p. 11582.

33. C. Murawski, Leo K., and Gather M. C., *Efficiency roll-off in organic light-emitting diodes.* Advanced Materials, 2013. **25**(47): p. 6801-6827.

34. M. K. Fung, Li Y. Q., and Liao L. S., *Tandem organic light-emitting diodes.* Advanced Materials, 2016. **28**(47): p. 10381-10408.

35. T.-H. Liu, Iou C.-Y., and Chen C. H., *Doped red organic electroluminescent devices based on a cohost emitter system.* Applied physics letters, 2003. **83**(25): p. 5241-5243.

36. X.-Y. Jiang, Zhang Z.-L., Cao J., Khan M., and Zhu W.-Q., *White OLED with high stability and low driving voltage based on a novel buffer layer MoOx.* Journal of Physics D: Applied Physics, 2007. **40**(18): p. 5553.

37.   K. S. Yook, Jeon S. O., Joo C. W., and Lee J. Y., *Correlation of lifetime and recombination zone in green phosphorescent organic light-emitting diodes.* Applied Physics Letters, 2009. **94**(9): p. 093501.

38.   C. Féry, Racine B., Vaufrey D., Doyeux H., and Cinà S., *Physical mechanism responsible for the stretched exponential decay behavior of aging organic light-emitting diodes.* Applied Physics Letters, 2005. **87**(21): p. 213502.

39.   J.-R. Gong, Wan L.-J., Lei S.-B., Bai C.-L., Zhang X.-H., and Lee S.-T., *Direct evidence of molecular aggregation and degradation mechanism of organic light-emitting diodes under joule heating: an STM and photoluminescence study.* The Journal of Physical Chemistry B, 2005. **109**(5): p. 1675-1682.

40.   A. Cester, Bari D., Framarin J., Wrachien N., Meneghesso G., Xia S., Adamovich V., and Brown J., *Thermal and electrical stress effects of electrical and optical characteristics of Alq3/NPD OLED.* Microelectronics Reliability, 2010. **50**(9-11): p. 1866-1870.

41.   K. K. Lin, Chua S. J., Wei-Wang, and Lim S. F., *Influence of electrical stress voltage on cathode degradation of organic light-emitting devices.* Journal of Applied Physics, 2001. **90**(2): p. 976-979.

42.   L.-S. Liao, Slusarek W. K., Hatwar T. K., Ricks M. L., and Comfort D. L., *Tandem organic light-emitting diode using hexaazatriphenylene hexacarbonitrile in the intermediate connector.* Advanced Materials, 2008. **20**(2): p. 324-329.

43.   Y. Miao, Wei X., Gao L., Wang K., Zhao B., Wang Z., Zhao B., Wang H., Wu Y., and Xu B., *Tandem white organic light-emitting diodes stacked with two symmetrical emitting units simultaneously achieving superior efficiency/CRI/color stability.* Nanophotonics, 2019. **8**(10): p. 1783-1794.

44.   S. Lee, Lee J. H., Lee J. H., and Kim J. J., *The mechanism of charge generation in charge-generation units composed of p-doped hole-transporting layer/HATCN/n-doped electron-transporting layers.* Advanced Functional Materials, 2012. **22**(4): p. 855-860.

45.   L. Liao, Klubek K. P., and Tang C. W., *High-efficiency tandem organic light-emitting diodes.* Applied physics letters, 2004. **84**(2): p. 167-169.

46.   H. Kanno, Holmes R. J., Sun Y., Kena-Cohen S., and Forrest S. R., *White stacked electrophosphorescent organic light-emitting devices employing MoO3 as a charge-generation layer.* Advanced Materials, 2006. **18**(3): p. 339-342.

47.   M.-Y. Chan, Lai S.-L., Lau K.-M., Fung M.-K., Lee C.-S., and Lee S.-T., *Influences of connecting unit architecture on the performance of tandem organic light-emitting devices.* Advanced Functional Materials, 2007. **17**(14): p. 2509-2514.

48.   S. Hamwi, Meyer J., Kröger M., Winkler T., Witte M., Riedl T., Kahn A., and Kowalsky W., *The role of transition metal oxides in charge-generation layers for stacked organic light-emitting diodes.* Advanced Functional Materials, 2010. **20**(11): p. 1762-1766.

49.   M. Terai and Tsutsui T., *Electric-field-assisted bipolar charge generation from internal charge separation zone composed of doped organic bilayer.* Applied physics letters, 2007. **90**(8): p. 083502.

50.   D.-S. Leem, Lee J.-H., Kim J.-J., and Kang J.-W., *Highly efficient tandem p-i-n organic light-emitting diodes adopting a low temperature evaporated rhenium oxide interconnecting layer.* Applied Physics Letters, 2008. **93**(10): p. 330.

51.   M. K. Fung, Lau K. M., Lai S., Law C. W., Chan M. Y., Lee C. S., and Lee S. T., *Charge generation layer in stacked organic light-emitting devices.* Journal of Applied Physics, 2008. **104**(3): p. 034509.

52. C. Law, Lau K., Fung M., Chan M., Wong F., Lee C., and Lee S., *Effective organic-based connection unit for stacked organic light-emitting devices.* Applied Physics Letters, 2006. **89**(13): p. 133511.

53. K. S. Yook, Jeon S. O., Min S. Y., Lee J. Y., Yang H. J., Noh T., Kang S. K., and Lee T. W., *Highly efficient p-i-n and tandem organic light-emitting devices using an air-stable and low-temperature-evaporable metal azide as an n-dopant.* Advanced Functional Materials, 2010. **20**(11): p. 1797-1802.

54. C.-W. Chen, Lu Y.-J., Wu C.-C., Wu E. H.-E., Chu C.-W., and Yang Y., *Effective connecting architecture for tandem organic light-emitting devices.* Applied Physics Letters, 2005. **87**(24): p. 241121.

55. T.-W. Lee, Noh T., Choi B.-K., Kim M.-S., Shin D. W., and Kido J., *High-efficiency stacked white organic light-emitting diodes.* Applied physics letters, 2008. **92**(4): p. 26.

56. J. Liu, Wang J., Huang S., Shi X., Wu X., and He G., *A highly efficient, transparent and stable charge generation unit based on a p-doped monolayer.* Organic Electronics, 2013. **14**(5): p. 1337-1343.

57. G. W. Kim, Son Y. H., Yang H. I., Park J. H., Ko I. J., Lampande R., Sakong J., Maeng M.-J., Hong J.-A., and Lee J. Y., *Diphenanthroline electron transport materials for the efficient charge generation unit in tandem organic light-emitting diodes.* Chemistry of Materials, 2017. **29**(19): p. 8299-8312.

58. M. Kröger, Hamwi S., Meyer J., Dobbertin T., Riedl T., Kowalsky W., and Johannes H.-H., *Temperature-independent field-induced charge separation at doped organic/organic interfaces: Experimental modeling of electrical properties.* Physical Review B, 2007. **75**(23): p. 235321.

59. J. Liu, Huang S., Shi X., Wu X., Wang J., and He G., *Charge separation process in an ultrathin electron-injecting bilayer-assisted charge generation unit for tandem organic light-emitting diodes.* The Journal of Physical Chemistry C, 2013. **117**(27): p. 13887-13893.

60. S. Scholz, Lüssem B., and Leo K., *Chemical changes on the green emitter tris (8-hydroxy-quinolinato) aluminum during device aging of p-i-n-structured organic light emitting diodes.* Applied Physics Letters, 2009. **95**(18): p. 293.

61. L. Liao and Klubek K. P., *Power efficiency improvement in a tandem organic light-emitting diode.* Applied Physics Letters, 2008. **92**(22): p. 204.

62. B. Jiao, Wu Z., Yang Z., and Hou X., *Tandem organic light-emitting diodes with an effective nondoped charge-generation unit.* physica status solidi (a), 2013. **210**(12): p. 2583-2587.

63. J. Wang, Wang Y., Qin Y., Li R., An J.-x., Chen Y., Lai W.-Y., Zhang X., and Huang W., *Highly efficient ultra-flexible tandem organic light-emitting diodes adopting a non-doped charge generation unit.* Journal of Materials Chemistry C, 2021. **9**(27): p. 8570-8578.

64. Y. Dai, Zhang H., Zhang Z., Liu Y., Chen J., and Ma D., *Highly efficient and stable tandem organic light-emitting devices based on HAT-CN/HAT-CN: TAPC/TAPC as a charge generation layer.* Journal of Materials Chemistry C, 2015. **3**(26): p. 6809-6814.

65. J. Liu, Shi X., Wu X., Wang J., and He G., *Inverted Tandem Phosphorescence Organic Light-Emitting Diodes Based on $\hbox{MoO}_{3}/\hbox{Al/Cs}_{2}\hbox{CO}_{3}$ Charge Generation Unit.* Journal of Display Technology, 2015. **11**(4): p. 341-345.

66. Y. Yu, Chen X., Jin Y., Wu Z., Yu Y., Lin W., and Yang H., *Electron-transporting layer doped with cesium azide for high-performance phosphorescent and tandem white organic light-emitting devices.* Journal of Physics D: Applied Physics, 2017. **50**(27): p. 275104.

67. X. Zhang, Zhang M., Liu M., Chen Y., Wang J., Zhang X., Zhang J., Lai W.-Y., and Huang W., *Highly efficient tandem organic light-emitting devices adopting a nondoped charge-generation unit and ultrathin emitting layers.* Organic Electronics, 2018. **53**: p. 353-360.

68. T. Chiba, Pu Y.-J., Miyazaki R., Nakayama K.-i., Sasabe H., and Kido J., *Ultra-high efficiency by multiple emission from stacked organic light-emitting devices.* Organic Electronics, 2011. **12**(4): p. 710-715.

69. H. Yang, Yu Y., Wu L., Qu B., Lin W., Yu Y., Wu Z., and Xie W., *Highly efficient tandem organic light-emitting devices employing an easily fabricated charge generation unit.* Applied Physics Express, 2018. **11**(2): p. 022101.

70. H. Zhang, Dai Y., and Ma D., *High efficiency tandem organic light-emitting devices with Al/ WO3/ Au interconnecting layer.* Applied Physics Letters, 2007. **91**(12).

71. J. Sun, Zhu X., Peng H., Wong M., and Kwok H. S., *Effective intermediate layers for highly efficient stacked organic light-emitting devices.* Applied Physics Letters, 2005. **87**(9): p. 093504.

72. Q. Chang, Lü Z., Yin Y., Xiao J., and Wang J., *Highly efficient tandem OLED based on a novel charge generation layer of HAT-CN/CuPc heterojunction.* Displays, 2022. **75**: p. 102306.

73. Y. Qin, Liu C.-Y., Li R.-Q., Wang J., Lu Y.-N., Chen Y.-H., Wang Y.-Z., Xu Y.-N., Zhang X.-W., and Huang W., *Efficient tandem organic light-emitting diodes with non-doped structures.* Optics Letters, 2020. **45**(23): p. 6450-6453.

74. S. Lai, Chan M., Fung M., Lee C., and Lee S., *Copper hexadecafluorophthalocyanine and copper phthalocyanine as a pure organic connecting unit in blue tandem organic light-emitting devices.* Journal of applied physics, 2007. **101**(1): p. 014509.

75. J. E. Ryu, Park S., Park Y., Ryu S. W., Hwang K., and Jang H. W., *Technological breakthroughs in chip fabrication, transfer, and color conversion for high performance micro-LED display.* Advanced Materials, 2022: p. 2204947.

76. Y.-K. Su, Wang H., Lin C., Chen W., and Chen S., *Improvement of AlGaInP light emitting diode by sulfide passivation.* IEEE Photonics Technology Letters, 2003. **15**(10): p. 1345-1347.

77. C. Zhao, Ng T. K., Prabaswara A., Conroy M., Jahangir S., Frost T., O'Connell J., Holmes J. D., Parbrook P. J., and Bhattacharya P., *An enhanced surface passivation effect in InGaN/GaN chip-in-nanowire light emitting diodes for mitigating Shockley–Read–Hall recombination.* Nanoscale, 2015. **7**(40): p. 16658-16665.

78. D.-H. Lee, Lee J.-H., Park J.-S., Seong T.-Y., and Amano H., *Improving the leakage characteristics and efficiency of GaN-based micro-light-emitting diode with optimized passivation.* ECS Journal of Solid State Science and Technology, 2020. **9**(5): p. 055001.

79. M.-C. Choi, Kim Y., and Ha C.-S., *Polymers for flexible displays: From material selection to device applications.* Progress in Polymer Science, 2008. **33**(6): p. 581-630.

80. K. J. Allen, *Reel to real: Prospects for flexible displays.* Proceedings of the IEEE, 2005. **93**(8): p. 1394-1399.

81. F. Peng, Chen H., Gou F., Lee Y.-H., Wand M., Li M.-C., Lee S.-L., and Wu S.-T., *Analytical Eq. for the motion picture response time of display devices.* Journal of applied physics, 2017. **121**(2): p. 023108.

82.	T. Wu, Sher C.-W., Lin Y., Lee C.-F., Liang S., Lu Y., Huang Chen S.-W., Guo W., Kuo H.-C., and Chen Z., *Mini-LED and micro-LED: promising candidates for the next generation display technology.* Applied Sciences, 2018. **8**(9): p. 1557.

83.	M. Schwambera, Meyer N., Gersdorff M., Reinhold M., Strauch G., Beccard R., and Heuken M. *52.3: Invited Paper: OLED Manufacturing by Organic Vapor Phase Deposition.* in *SID Symposium Digest of Technical Papers.* 2003. Wiley Online Library.

84.	M. Schwambera, Meyer N., Leder S., Reinhold M., Dauelsberg M., Strauch G., Heuken M., Juergensen H., Zhou T., and Ngo T. *27.4: Modeling and Fabrication of Organic Vapor Phase Deposition (OVPD) Equipment for OLED Display Manufacturing.* in *SID Symposium Digest of Technical Papers.* 2002. Wiley Online Library.

85.	M. Baldo, Kozlov V., Burrows P., Forrest S., Ban V., Koene B., and Thompson M., *Low pressure organic vapor phase deposition of small molecular weight organic light emitting device structures.* Applied physics letters, 1997. **71**(21): p. 3033-3035.

86.	M. Baldo, Deutsch M., Burrows P., Gossenberger H., Gerstenberg M., Ban V., and Forrest S., *Organic vapor phase deposition.* Advanced Materials, 1998. **10**(18): p. 1505-1514.

87.	T. X. Zhou, Ngo T., Brown J. J., Shtein M., and Forrest S. R., *Stable and efficient electrophosphorescent organic light-emitting devices grown by organic vapor phase deposition.* Applied Physics Letters, 2005. **86**(2): p. 021107.

88.	B. Qu, Ding K., Sun K., Hou S., Morris S., Shtein M., and Forrest S. R., *Fast Organic Vapor Phase Deposition of Thin Films in Light-Emitting Diodes.* ACS nano, 2020. **14**(10): p. 14157-14163.

89.	I. H. Ozofor, *Numerical modeling and investigation of material mixing and utilization during organic vapor phase deposition.* Journal of Materials Research, 2023: p. 1-12.

90.	V.-M. Airaksinen, *Silicon wafer and thin film measurements*, in *Handbook of Silicon Based MEMS Materials and Technologies.* 2015, Elsevier. p. 381-390.

91.	G. E. Jellison Jr, *Data analysis for spectroscopic ellipsometry.* Thin Solid Films, 1993. **234**(1-2): p. 416-422.

92.	C. Huygens, Young T., Fresnel A. J., and Arago F., *The Wave Theory of Light.* 1900: [etc] American book Company.

93.	D. Aspnes, *Spectroscopic ellipsometry—past, present, and future.* Thin Solid Films, 2014. **571**: p. 334-344.

94.	J. Zou, Zhang K., Li J., Zhao Y., Wang Y., Pillai S. K. R., Volkan Demir H., Sun X., Chan-Park M. B., and Zhang Q., *Carbon nanotube driver circuit for 6× 6 organic light emitting diode display.* Scientific reports, 2015. **5**(1): p. 11755.

95.	Y. Wu, Wang S., and Komvopoulos K., *A review of graphene synthesis by indirect and direct deposition methods.* Journal of Materials Research, 2020. **35**(1): p. 76-89.

96.	D. A. A. Trujillo, Iyer A., Hack J., and Opila R. L., *Role of oxide at interface between organic layer and silicon substrate in hybrid solar cells.* 2021.

97.	H. Guo, Wang X., Dupuy A. D., Schoenung J. M., and Bowman W. J., *Growth of nanoporous high-entropy oxide thin films by pulsed laser deposition.* Journal of Materials Research, 2022: p. 1-12.

98.	V. G. Sree, Bathula C., Kadam A. N., Ravindra M., Mahadevan K., Sohn J. I., Kim H.-S., and Im H., *Halogen free solvent processed light-emitting diodes achieving EQE nearly 25% for imidazole-based host materials synthesized by ball milling.* Nano Energy, 2022. **92**: p. 106753.

99. H. Opoku, Choy J.-Y., Kumar A., Kim H.-S., Shrestha N. K., Mane S. D., and Bathula C., *Benzo [1, 2-b: 4, 5-b'] dithiophene-based copolymers as panchromatic light sensors in organic photodiodes application.* Journal of Materials Research and Technology, 2020. **9**(6): p. 15632-15637.

100. H. Opoku, Bathula C., Shin E.-S., Long D. X., Kong H., Jung Y. J., Lim B., and Noh Y.-Y., *Effect of molecular structure of benzo [1, 2-b: 4, 5-b'] dithiophene-based push-pull type donor polymers on performance panchromatic organic photodiodes.* Organic Electronics, 2020. **78**: p. 105580.

101. J. Kreis, Schwambera M., Keiper D., Gersdorff M., Long M., and Heuken M. *Organic Vapor Phase Deposition (OVPD) for efficient OLED manufacturing: The specific advantages and possibilities of carrier-gas enhanced vapor phase deposition for the manufacturing of organic thin film devices.* in *Organic Light Emitting Materials and Devices XVI.* 2012. International Society for Optics and Photonics.

102. R. R. Lunt, Lassiter B. E., Benziger J. B., and Forrest S. R., *Organic vapor phase deposition for the growth of large area organic electronic devices.* Applied Physics Letters, 2009. **95**(23): p. 320.

103. C. Rolin, Song B., and Forrest S. R., *Mass transport through the carrier gas boundary layer in organic vapor phase deposition.* Physical Review Applied, 2014. **1**(3): p. 034002.

104. I. H. Ozofor, *Towards Efficient Water Treatment: Mechanism of Colloidal Fouling of Ultrafiltration Membranes.* 2020, Michigan Technological University.

105. I. H. Ozofor, Tarabara V. V., Da Costa A. R., and Morse A. N., *Analysis of microstructural properties of ultrafiltration cake layer during its early stage formation and growth.* Journal of Membrane Science, 2021. **620**: p. 118903.

106. F. Yang, Shtein M., and Forrest S. R., *Controlled growth of a molecular bulk heterojunction photovoltaic cell.* Nature materials, 2005. **4**(1): p. 37-41.

107. I. Lienhard and John H., *A heat transfer textbook.* 2005: phlogiston press.

108. I. H. Ozofor, *Numerical modeling and investigation of material mixing and utilization during organic vapor phase deposition.* Journal of Materials Research, 2023. **38**(9): p. 2327-2338.

109. J. Kreis, Schwambera M., Keiper D., Gersdorff M., Long M., and Heuken M. *Organic Vapor Phase Deposition (OVPD) for efficient OLED manufacturing: The specific advantages and possibilities of carrier-gas enhanced vapor phase deposition for the manufacturing of organic thin film devices.* in *Organic Light Emitting Materials and Devices XVI.* 2012. SPIE.

110. M. Shtein, Gossenberger H. F., Benziger J. B., and Forrest S. R., *Material transport regimes and mechanisms for growth of molecular organic thin films using low-pressure organic vapor phase deposition.* Journal of Applied Physics, 2001. **89**(2): p. 1470-1476.

111. B. Qu and Forrest S. R., *Continuous roll-to-roll fabrication of organic photovoltaic cells via interconnected high-vacuum and low-pressure organic vapor phase deposition systems.* Applied Physics Letters, 2018. **113**(5): p. 053302.

112. T.-Y. Lee, Chen L.-Y., Lo Y.-Y., Swayamprabha S. S., Kumar A., Huang Y.-M., Chen S.-C., Zan H.-W., Chen F.-C., and Horng R.-H., *Technology and Applications of Micro-LEDs: Their Characteristics, Fabrication, Advancement, and Challenges.* ACS Photonics, 2022. **9**(9): p. 2905-2930.

113.   F. Chen, Bian J., Hu J., Sun N., Yang B., Ling H., Yu H., Wang K., Gai M., and Ma Y., *Mass transfer techniques for large-scale and high-density microLED arrays.* International Journal of Extreme Manufacturing, 2022. **4**(4): p. 042005.

114.   B.-J. Lee and Khang D.-Y., *Non-deterministic transfer-printing of LED chips with controllable pitch using stretchable elastomeric stamps.* Extreme Mechanics Letters, 2021. **45**: p. 101287.

115.   V. L. Colvin, Schlamp M. C., and Alivisatos A. P., *Light-emitting diodes made from cadmium selenide nanocrystals and a semiconducting polymer.* Nature, 1994. **370**(6488): p. 354-357.

116.   Y. Shirasaki, Supran G. J., Bawendi M. G., and Bulović V., *Emergence of colloidal quantum-dot light-emitting technologies.* Nature photonics, 2013. **7**(1): p. 13-23.

117.   H.-V. Han, Lin H.-Y., Lin C.-C., Chong W.-C., Li J.-R., Chen K.-J., Yu P., Chen T.-M., Chen H.-M., and Lau K.-M., *Resonant-enhanced full-color emission of quantum-dot-based micro LED display technology.* Optics express, 2015. **23**(25): p. 32504-32515.

118.   P. Pust, Weiler V., Hecht C., Tücks A., Wochnik A. S., Henß A.-K., Wiechert D., Scheu C., Schmidt P. J., and Schnick W., *Narrow-band red-emitting Sr [LiAl 3 N 4]: Eu 2+ as a next-generation LED-phosphor material.* Nature materials, 2014. **13**(9): p. 891-896.

119.   J.-Y. Kim, Cho Y.-H., Park H.-S., Ryou J.-H., and Kwon M.-K., *Mass transfer of microscale light-emitting diodes to unusual substrates by spontaneously formed vertical tethers during chemical lift-off.* Applied Sciences, 2019. **9**(20): p. 4243.

120.   H. Zhang and Rogers J. A., *Recent advances in flexible inorganic light emitting diodes: From materials design to integrated optoelectronic platforms.* Advanced Optical Materials, 2019. **7**(2): p. 1800936.

121.   M. Konagai, Sugimoto M., and Takahashi K., *High efficiency GaAs thin film solar cells by peeled film technology.* Journal of crystal growth, 1978. **45**: p. 277-280.

122.   W. Wong, Sands T., Cheung N., Kneissl M., Bour D., Mei P., Romano L., and Johnson N., *Fabrication of thin-film InGaN light-emitting diode membranes by laser lift-off.* Applied physics letters, 1999. **75**(10): p. 1360-1362.

123.   A. Koma, *Van der Waals epitaxy—a new epitaxial growth method for a highly lattice-mismatched system.* Thin Solid Films, 1992. **216**(1): p. 72-76.

124.   J. Jeong, Jin D. K., Choi J., Jang J., Kang B. K., Wang Q., Park W. I., Jeong M. S., Bae B.-S., and Yang W. S., *Transferable, flexible white light-emitting diodes of GaN p–n junction microcrystals fabricated by remote epitaxy.* Nano Energy, 2021. **86**: p. 106075.

125.   J. Kim, Kim J.-H., Cho S.-H., and Whang K.-H., *Selective lift-off of GaN light-emitting diode from a sapphire substrate using 266-nm diode-pumped solid-state laser irradiation.* Applied Physics A, 2016. **122**: p. 1-6.

126.   S. Krause, Miclea P.-T., and Seifert G., *Selective femtosecond laser lift-off process for scribing in thin-film photovoltaics.* Journal of Laser Micro Nanoengineering, 2015. **10**(3): p. 274.

127.   J. Bernard, Haas H., Caplet S., Bedoin A., Tournaire M., and Peray P. *18-4: microLED displays based on transfer with microtubes interconnections.* in *SID Symposium Digest of Technical Papers.* 2019. Wiley Online Library.

128.   F. Templier and Bernard J. *18-3: A new approach for fabricating high-performance microLED displays.* in *SID Symposium Digest of Technical Papers.* 2019. Wiley Online Library.

129. M. Durniak, *Methods and systems for parallel assembly, transfer, and bonding of ferromagnetic components*. 2018, Google Patents.

130. G. Zhu, Liu Y., Ming R., Shi F., and Cheng M., *Mass transfer, detection and repair technologies in micro-LED displays.* Science China Materials, 2022. **65**(8): p. 2128-2153.

131. M. D. Bartlett and Crosby A. J., *Material transfer controlled by elastomeric layer thickness.* Materials Horizons, 2014. **1**(5): p. 507-512.

132. S. Bae, Kim H., Lee Y., Xu X., Park J.-S., Zheng Y., Balakrishnan J., Lei T., Ri Kim H., and Song Y. I., *Roll-to-roll production of 30-inch graphene films for transparent electrodes.* Nature nanotechnology, 2010. **5**(8): p. 574-578.

133. Y. Xia, Qin D., and Whitesides G. M., *Microcontact printing with a cylindrical rolling stamp: A practical step toward automatic manufacturing of patterns with submicrometer-sized features.* Advanced Materials, 1996. **8**(12): p. 1015-1017.

134. S. Y. Yang, Carlson A., Cheng H., Yu Q., Ahmed N., Wu J., Kim S., Sitti M., Ferreira P. M., and Huang Y., *Elastomer surfaces with directionally dependent adhesion strength and their use in transfer printing with continuous roll-to-roll applications.* Advanced Materials, 2012. **24**(16): p. 2117-2122.

135. M. Choi, Jang B., Lee W., Lee S., Kim T. W., Lee H. J., Kim J. H., and Ahn J. H., *Stretchable active matrix inorganic light-emitting diode display enabled by overlay-aligned roll-transfer printing.* Advanced Functional Materials, 2017. **27**(11): p. 1606005.

136. R. S. Cok, Meitl M., Rotzoll R., Melnik G., Fecioru A., Trindade A. J., Raymond B., Bonafede S., Gomez D., and Moore T., *Inorganic light-emitting diode displays using micro-transfer printing.* Journal of the Society for Information Display, 2017. **25**(10): p. 589-609.

137. M. A. Meitl, Zhu Z.-T., Kumar V., Lee K. J., Feng X., Huang Y. Y., Adesida I., Nuzzo R. G., and Rogers J. A., *Transfer printing by kinetic control of adhesion to an elastomeric stamp.* Nature materials, 2006. **5**(1): p. 33-38.

138. X. Feng, Meitl M. A., Bowen A. M., Huang Y., Nuzzo R. G., and Rogers J. A., *Competing fracture in kinetically controlled transfer printing.* Langmuir, 2007. **23**(25): p. 12555-12560.

139. H.-J. Kim-Lee, Carlson A., Grierson D., Rogers J., and Turner K., *Interface mechanics of adhesiveless microtransfer printing processes.* Journal of Applied Physics, 2014. **115**(14): p. 143513.

140. A. Luo and Turner K. T., *Mechanics of crack path selection in microtransfer printing: Challenges and opportunities for process control.* Journal of the Mechanics and Physics of Solids, 2020. **143**: p. 104066.

141. D. Gomez, Ghosal K., Moore T., Meitl M. A., Bonafede S., Prevatte C., Radauscher E., Trindade A. J., and Bower C. A. *Scalability and yield in elastomer stamp micro-transfer-printing*. in *2017 IEEE 67th Electronic Components and Technology Conference (ECTC)*. 2017. IEEE.

142. M. Kaltwasser, Schmidt U., Lösing L., Biswas S., Stauden T., Bund A., and Jacobs H. O., *Fluidic self-assembly on electroplated multilayer solder bumps with tailored transformation imprinted melting points.* Scientific reports, 2019. **9**(1): p. 11325.

143. S. Shet, Revero R. D., Booty M. R., Fiory A. T., Lepselter M. P., and Ravindra N. M., *Microassembly techniques: A review.* MATERIALS SCIENCE AND TECHNOLOGY-ASSOCIATION FOR IRON AND STEEL TECHNOLOGY-, 2006. **1**: p. 451.

144. E. Saeedi, Kim S. S., Etzkorn J. R., Meldrum D. R., and Parviz B. A. *Automation and yield of micron-scale self-assembly processes*. in *2007 IEEE International Conference on Automation Science and Engineering*. 2007. IEEE.

145. P. J. Schuele, Zhan C., Sasaki K., Ulmer K., and Lee J.-J., *Emissive display substrate for surface mount micro-LED fluidic assembly*. 2020, Google Patents.

146. X. Zhou, Tian P., Sher C.-W., Wu J., Liu H., Liu R., and Kuo H.-C., *Growth, transfer printing and colour conversion techniques towards full-colour micro-LED display.* Progress in Quantum Electronics, 2020. **71**: p. 100263.

147. C. Ueda, Park J., Hirose K., Konishi S., Ikemoto Y., Osaki M., Yamaguchi H., Harada A., Tanaka M., and Watanabe G., *Behavior of supramolecular cross-links formed by host-guest interactions in hydrogels responding to water contents.* Supramolecular Materials, 2022. **1**: p. 100001.

148. V. Voronenkov, Bochkareva N., Gorbunov R., Zubrilov A., Kogotkov V., Latyshev P., Lelikov Y., Leonidov A., and Shreter Y., *Laser slicing: A thin film lift-off method for GaN-on-GaN technology.* Results in Physics, 2019. **13**: p. 102233.

149. V. R. Marinov. *52-4: Laser-Enabled Extremely-High Rate Technology for μLED Assembly*. in *SID Symposium Digest of Technical Papers*. 2018. Wiley Online Library.

150. D. Lee, Cherekdjian S., Kang S., Mishra K., Ong P., and Xu X. *18-2: Ultra-Fine High Efficiency MicroLEDs with Testability and Transferability Using Layer-Transfer Technology*. in *SID Symposium Digest of Technical Papers*. 2019. Wiley Online Library.

151. C. Van Oss, *Acid—base interfacial interactions in aqueous media.* Colloids and Surfaces A: Physicochemical and Engineering Aspects, 1993. **78**: p. 1-49.

152. L. Chen, Panday A., Park J., Kim M., Oh D. K., Ok J. G., and Guo L. J., *Size-selective sub-micrometer-particle confinement utilizing ionic entropy-directed trapping in inscribed nanocavity patterns.* ACS nano, 2021. **15**(9): p. 14185-14192.

153. M. Krishnan, *Electrostatic free energy for a confined nanoscale object in a fluid.* The Journal of chemical physics, 2013. **138**(11).

154. J. Israelachvili, *Intermolecular and Surface Forces. 3rd edn Academic Press.* San Diego, 2011.

155. N. Zhang, Pang T., Han R., Chen S., Li Z., Yu Y., Shi Z., Liu L., Qu J., and Zhou A., *Interactions between bubble and particles of key minerals of diasporic bauxite through the extended DLVO theory.* International Journal of Mining Science and Technology, 2022. **32**(1): p. 201-214.

156. M. Krishnan, *Electrostatic free energy for a confined nanoscale object in a fluid.* The Journal of Chemical Physics, 2013. **138**(11): p. 114906.

157. C. J. Van Oss, *Interfacial forces in aqueous media*. 2006: CRC press.

158. C. J. van Oss and Good R. J., *Surface tension and the solubility of polymers and biopolymers: the role of polar and apolar interfacial free energies.* Journal of Macromolecular Science—Chemistry, 1989. **26**(8): p. 1183-1203.

159. R. J. Good, *Contact angle, wetting, and adhesion: a critical review.* Journal of adhesion science and technology, 1992. **6**(12): p. 1269-1302.

160. E. McCafferty, *Acid-base effects in polymer adhesion at metal surfaces.* Journal of adhesion science and technology, 2002. **16**(3): p. 239-255.

161. G. Hwang, Lee C.-H., Ahn I.-S., and Mhin B. J., *Determination of reliable Lewis acid–base surface tension components of a solid in LW–AB approach.* Journal of Industrial and Engineering Chemistry, 2011. **17**(1): p. 125-129.

162.   R. Hogg, Healy T. W., and Fuerstenau D. W., *Mutual coagulation of colloidal dispersions.* Transactions of the Faraday society, 1966. **62**: p. 1638-1651.

163.   J. Theodoor and Overbeek G., *The role of energy and entropy in the electrical double layer.* Colloids and Surfaces, 1990. **51**: p. 61-75.

164.   T. B. Jones, *Basic theory of dielectrophoresis and electrorotation.* IEEE Engineering in medicine and Biology Magazine, 2003. **22**(6): p. 33-42.

165.   R. R. Pethig, *Dielectrophoresis: Theory, methodology and biological applications.* 2017: John Wiley & Sons.

166.   I. Messana, Rossetti D. V., Cassiano L., Misiti F., Giardina B., and Castagnola M., *Peptide analysis by capillary (zone) electrophoresis.* Journal of Chromatography B: Biomedical Sciences and Applications, 1997. **699**(1-2): p. 149-171.

167.   F. W. Sunderman Jr and Sunderman F. W., *Clinical applications of the fractionation of serum proteins by paper electrophoresis.* American journal of clinical pathology, 1957. **27**: p. 125-158.

168.   J. Jach, Kawahara H., and Harbottle G., *The application of paper electrophoresis to the separation of radioactive products found in the szilard-chalmers reaction.* Journal of Chromatography A, 1958. **1**: p. 501-507.

169.   C. A. Owen JR and McKenzie B. F., *Application of paper electrophoresis to separation of blood-clotting factors.* Journal of Applied Physiology, 1954. **6**(11): p. 696-700.

170.   H. Schriftman and Shultz R. C., *Application of paper chromatography and electrophoresis to the assay of pharmaceutical products.* Journal of Pharmaceutical Sciences, 1961. **50**(4): p. 332-336.

171.   H. Na, Kang B.-H., Ku J., Kim Y., and Jeong K.-H., *On-chip paper electrophoresis for ultrafast screening of infectious diseases.* BioChip Journal, 2021. **15**(3): p. 305-311.

172.   M. Sanad, Abdelrahim E., Hathout A. S., Hussain O., Rashed M., and Fouzy Ŭ. A., *Distribution of iodine125 labeled parathion and the protective effect of dried banana peel in experimental mice.* Egyptian Journal of Chemistry, 2022. **65**(3): p. 203-214.

173.   M. C. M. Mellado, Franco C., Coelho A., Alves P. M., and Simplício A. L., *Sodium dodecyl sulfate-capillary gel electrophoresis analysis of rotavirus-like particles.* Journal of Chromatography A, 2008. **1192**(1): p. 166-172.

174.   S. Cherkaoui, Bettinger T., Hauwel M., Navetat S., Allémann E., and Schneider M., *Tracking of antibody reduction fragments by capillary gel electrophoresis during the coupling to microparticles surface.* Journal of pharmaceutical and biomedical analysis, 2010. **53**(2): p. 172-178.

175.   R. Müller, Marchetti M., Kratzmeier M., Elgass H., Kuschel M., Zenker A., and Allmaier G., *Comparison of planar SDS-PAGE, CGE-on-a-chip, and MALDI-TOF mass spectrometry for analysis of the enzymatic de-N-glycosylation of antithrombin III and coagulation factor IX with PNGase F.* Analytical and bioanalytical chemistry, 2007. **389**: p. 1859-1868.

176.   M. Marchetti-Deschmann, Lehner A., Peterseil V., Sövegjarto F., Hochegger R., and Allmaier G., *Fast wheat variety classification by capillary gel electrophoresis-on-a-chip after single-step one-grain high molecular weight glutenin extraction.* Analytical and bioanalytical chemistry, 2011. **400**: p. 2403-2414.

177.   M. A. Strege and Lagu A. L., *Capillary electrophoresis of biotechnology-derived proteins.* Electrophoresis, 1997. **18**(12-13): p. 2343-2352.

178. L. A. Johnson and Ferris J. A., *Analysis of postmortem DNA degradation by single-cell gel electrophoresis.* Forensic science international, 2002. **126**(1): p. 43-47.

179. P. Y. Lee, Saraygord-Afshari N., and Low T. Y., *The evolution of two-dimensional gel electrophoresis-from proteomics to emerging alternative applications.* Journal of Chromatography A, 2020. **1615**: p. 460763.

180. J. W. Jorgenson and Lukacs K. D., *Capillary zone electrophoresis.* Science, 1983. **222**(4621): p. 266-272.

181. P. Blatný and Kvasnička F., *Application of capillary isotachophoresis and capillary zone electrophoresis to the determination of inorganic ions in food and feed samples.* Journal of Chromatography A, 1999. **834**(1-2): p. 419-431.

182. C. Corradini and Cavazza A., *Application of capillary zone electrophoresis (CZE) and micellar electrokinetic chromatography (MEKC) in food analysis.* Italian journal of food science, 1998. **10**(4): p. 299-316.

183. Y. Mrestani, Neubert R., Schiewe J., and Härtl A., *Application of capillary zone electrophoresis in cephalosporin analysis.* Journal of Chromatography B: Biomedical Sciences and Applications, 1997. **690**(1-2): p. 321-326.

184. C. K. Lo, Paau M. C., Xiao D., and Choi M. M., *Application of capillary zone electrophoresis for separation of water-soluble gold monolayer-protected clusters.* Electrophoresis, 2008. **29**(11): p. 2330-2339.

185. M. Manso, Miguel M., and López-Fandiño R., *Application of capillary zone electrophoresis to the characterisation of the human milk protein profile and its evolution throughout lactation.* Journal of Chromatography a, 2007. **1146**(1): p. 110-117.

186. J. Schiewe, Mrestani Y., and Neubert R., *Application and optimization of capillary zone electrophoresis in vitamin analysis.* Journal of Chromatography A, 1995. **717**(1-2): p. 255-259.

187. B. L. Ling, Baeyens W., Van Acker P., and Dewaele C., *Determination of ascorbic acid and isoascorbic acid by capillary zone electrophoresis: application to fruit juices and to a pharmaceutical formulation.* Journal of pharmaceutical and biomedical analysis, 1992. **10**(10-12): p. 717-721.

188. G. M. Janini, Fisher R. J., Henderson L. E., and Issaq H. J., *Application of capillary zone electrophoresis for the analysis of proteins, protein-small molecules, and protein-DNA interactions.* Journal of Liquid Chromatography & Related Technologies, 1995. **18**(18-19): p. 3617-3628.

189. L. Sun, Zhu G., Yan X., Zhang Z., Wojcik R., Champion M. M., and Dovichi N. J., *Capillary zone electrophoresis for bottom-up analysis of complex proteomes.* Proteomics, 2016. **16**(2): p. 188-196.

190. X. Shen, Yang Z., McCool E. N., Lubeckyj R. A., Chen D., and Sun L., *Capillary zone electrophoresis-mass spectrometry for top-down proteomics.* TrAC Trends in Analytical Chemistry, 2019. **120**: p. 115644.

191. Z. Zhang, Qu Y., and Dovichi N. J., *Capillary zone electrophoresis-mass spectrometry for bottom-up proteomics.* TrAC Trends in Analytical Chemistry, 2018. **108**: p. 23-37.

192. Y. Zhao, Sun L., Knierman M. D., and Dovichi N. J., *Fast separation and analysis of reduced monoclonal antibodies with capillary zone electrophoresis coupled to mass spectrometry.* Talanta, 2016. **148**: p. 529-533.

193. Z. Li, Wu Q., Zhang X., and Chen G., *Advances in the Applications of Capillary Electrophoresis to Tobacco Analysis.* Current Analytical Chemistry, 2023. **19**(1): p. 77-99.

194. E. Szerdahelyi, Csehi B., Takács K., Korompai E., Nagy A., Gelencsér É., and Friedrich L. F., *Monitoring of imidazole dipeptides in meat products by capillary zone electrophoresis.* Czech Journal of Food Sciences, 2020. **38**(1): p. 36-42.

195. S. Gonçalves, Alves V. R., Pérez S. O., Ferreira M., Daguer H., de Oliveira M. A. L., Micke G. A., and Vitali L., *Rapid method for the determination of citrate, phosphate and sulfite in seafood by capillary zone electrophoresis.* Food chemistry, 2020. **321**: p. 126705.

196. L. N. de Oliveira Neves and de Oliveira M. A. L., *Quantification of lactose and lactulose in hydrolysed-lactose UHT milk using capillary zone electrophoresis.* International Dairy Journal, 2020. **106**: p. 104710.

197. S. N. Wright, Huge B. J., and Dovichi N. J., *Capillary zone electrophoresis separation and collection of spermatozoa for the forensic analysis of sexual assault evidence.* Electrophoresis, 2020. **41**(15): p. 1344-1353.

198. M. M. Ribeiro, Barreto D. N., Petruci J. F. d. S., and Richter E. M., *Simultaneous determination of scopolamine and butylscopolamine in pharmaceutical and beverage samples by capillary zone electrophoresis.* Microchemical Journal, 2022. **172**: p. 106985.

199. P. M. Biesheuvel and Verweij H., *Theory of cast formation in electrophoretic deposition.* Journal of the American Ceramic Society, 1999. **82**(6): p. 1451-1455.

200. R. Sikkema, Baker K., and Zhitomirsky I., *Electrophoretic deposition of polymers and proteins for biomedical applications.* Advances in Colloid and Interface Science, 2020. **284**: p. 102272.

201. A. A. Shah, Kang H., Kohlstedt K. L., Ahn K. H., Glotzer S. C., Monroe C. W., and Solomon M. J., *Liquid crystal order in colloidal suspensions of spheroidal particles by direct current electric field assembly.* Small, 2012. **8**(10): p. 1551-1562.

202. M.-m. Kim and Zydney A. L., *Effect of electrostatic, hydrodynamic, and Brownian forces on particle trajectories and sieving in normal flow filtration.* Journal of Colloid and Interface Science, 2004. **269**(2): p. 425-431.

203. F. Strubbe, Beunis F., Brans T., Karvar M., Woestenborghs W., and Neyts K., *Electrophoretic retardation of colloidal particles in nonpolar liquids.* Physical review X, 2013. **3**(2): p. 021001.

204. D. Tripkovic, Strmcnik D., Van Der Vliet D., Stamenkovic V., and Markovic N., *The role of anions in surface electrochemistry.* Faraday discussions, 2009. **140**: p. 25-40.

205. T. L. Doane, Chuang C.-H., Hill R. J., and Burda C., *Nanoparticle ζ-potentials.* Accounts of chemical research, 2012. **45**(3): p. 317-326.